



LUND UNIVERSITY

Searches for new phenomena in inclusive and tagged dijet distributions at $\sqrt{s} = 13$ TeV

Poulsen, Trine

2020

[Link to publication](#)

Citation for published version (APA):

Poulsen, T. (2020). *Searches for new phenomena in inclusive and tagged dijet distributions at $\sqrt{s} = 13$ TeV*. [Doctoral Thesis (monograph), Department of Physics]. Lund University.

Total number of authors:

1

General rights

Unless other specific re-use rights are stated the following general rights apply:

Copyright and moral rights for the publications made accessible in the public portal are retained by the authors and/or other copyright owners and it is a condition of accessing publications that users recognise and abide by the legal requirements associated with these rights.

- Users may download and print one copy of any publication from the public portal for the purpose of private study or research.
- You may not further distribute the material or use it for any profit-making activity or commercial gain
- You may freely distribute the URL identifying the publication in the public portal

Read more about Creative commons licenses: <https://creativecommons.org/licenses/>

Take down policy

If you believe that this document breaches copyright please contact us providing details, and we will remove access to the work immediately and investigate your claim.

LUND UNIVERSITY

PO Box 117
221 00 Lund
+46 46-222 00 00

Searches for new phenomena in inclusive and tagged dijet distributions at $\sqrt{s} = 13$ TeV

TRINE POULSEN

DEPARTMENT OF PHYSICS | LUND UNIVERSITY





Department of Physics
Particle Physics
ISBN 978-91-7895-616-6



Searches for new phenomena in inclusive and tagged dijet
distributions at $\sqrt{s} = 13$ TeV

Searches for new phenomena in inclusive and tagged dijet distributions at $\sqrt{s} = 13$ TeV

Trine Poulsen



LUND
UNIVERSITY

Thesis submitted for the degree of
Doctor of Philosophy

To be presented, with the permission of the Faculty of Science of Lund University, for public criticism in the Rydberg lecture hall (Rydbergsalen) at the Department of Physics on the 25th of September 2020 at 13:00.

Organization LUND UNIVERSITY Department of Physics Box 118 SE-221 00 LUND Sweden		Document name DOCTORAL DISSERTATION	
		Date of disputation 2020-09-25	
Author(s) Trine Poulsen		Sponsoring organization	
Title and subtitle Searches for new phenomena in inclusive and tagged dijet distributions at $\sqrt{s} = 13 \text{ TeV}$			
Abstract <p>Dijets are produced in abundance at the Large Hadron Collider as predicted by quantum chromodynamics (QCD). However, several theories beyond the Standard Model of Particle Physics predicts new phenomena, which also result in dijet final states. This thesis presents searches for such new phenomena using different techniques. One approach is to look for jets, that originate from top quarks. We know, that the top quark, being the heaviest fundamental particle, has a large coupling to the Higgs field. Therefore, it is appealing to think, that the top quark could play a special role in understanding the fine tuning problem of the Higgs mass. One model of interest is the topcolor assisted technicolor, which predicts a Z'_{TC2} boson, that would appear as a resonance in the invariant mass spectrum. Limits are set on this theory by using the 139 fb^{-1} of data collected at $\sqrt{s} = 13 \text{ TeV}$ by ATLAS.</p> <p>Another approach is to have a more inclusive selection and not only look at the invariant mass spectrum, but also the angular distribution of the two jets. This makes it possible to look for non-resonant signals like those coming from a contact interaction with a compositeness scale, Λ, which is much higher than the center-of-mass energy at the Large Hadron Collider. Limits are set on this theory by using 37 fb^{-1} of data. Studies, conducted to improve this analysis, are also presented.</p> <p>A prerequisite to perform these searches is to have well-calibrated jets. Different methods are used to calibrate the jets at different transverse momentum, p_T, ranges. In order to calibrate high-p_T jets, the calorimeter response to the single particles, that make up the jet, is studied. In this way it is possible to estimate the uncertainty on the jet energy scale at the highest p_T, where there are very few events in data.</p>			
Key words jets, dijets, all-hadronic $\bar{t}\bar{t}$, top quark, angular distribution, resonance, beyond the Standard Model, 13 TeV, contact interaction, Z' boson, topcolor assisted technicolor, dark matter, excited quarks, ATLAS, LHC			
Classification system and/or index terms (if any)			
Supplementary bibliographical information		Language English	
ISSN and key title		ISBN 978-91-7895-616-6 (print) 978-91-7895-617-3 (pdf)	
Recipient's notes		Number of pages 232	Price
		Security classification	

I, the undersigned, being the copyright owner of the abstract of the above-mentioned dissertation, hereby grant to all reference sources the permission to publish and disseminate the abstract of the above-mentioned dissertation.

Signature



Date 2020-08-14

Searches for new phenomena in inclusive and tagged dijet distributions at $\sqrt{s} = 13$ TeV

Trine Poulsen



LUND
UNIVERSITY

© Trine Poulsen 2020

Faculty of Science, Department of Physics

ISBN: 978-91-7895-616-6 (print)

ISBN: 978-91-7895-617-3 (pdf)

Printed in Sweden by Media-Tryck, Lund University, Lund 2020



Media-Tryck is a Nordic Swan Ecolabel certified provider of printed material. Read more about our environmental work at www.mediatryck.lu.se

MADE IN SWEDEN 

Abstract

Dijets are produced in abundance at the Large Hadron Collider as predicted by quantum chromodynamics (QCD). However, several theories beyond the Standard Model of Particle Physics predicts new phenomena, which also result in dijet final states. This thesis presents searches for such new phenomena using different techniques. One approach is to look for jets, that originate from top quarks. We know, that the top quark, being the heaviest fundamental particle, has a large coupling to the Higgs field. Therefore, it is appealing to think, that the top quark could play a special role in understanding the fine tuning problem of the Higgs mass. One model of interest is the topcolor assisted technicolor, which predicts a Z'_{TC2} boson, that would appear as a resonance in the invariant mass spectrum. Limits are set on this theory by using the 139 fb^{-1} of data collected at $\sqrt{s} = 13 \text{ TeV}$ by ATLAS.

Another approach is to have a more inclusive selection and not only look at the invariant mass spectrum, but also the angular distribution of the two jets. This makes it possible to look for non-resonant signals like those coming from a contact interaction with a compositeness scale, Λ , which is much higher than the center-of-mass energy at the Large Hadron Collider. Limits are set on this theory by using 37 fb^{-1} of data. Studies, conducted to improve this analysis, are also presented.

A prerequisite to perform these searches is to have well-calibrated jets. Different methods are used to calibrate the jets at different transverse momentum, p_T , ranges. In order to calibrate high- p_T jets, the calorimeter response to the single particles, that make up the jet, is studied. In this way it is possible to estimate the uncertainty on the jet energy scale at the highest p_T , where there are very few events in data.

Populærvidenskabeligt resumé

Partikelfysikere har igennem de sidste 100 år opnået en imponerende forståelse for de mest fundamentale byggesten og de naturkræfter, der virker imellem dem. De fire naturkræfter er elektromagnetisme, svag kernekraft, stærk kernekraft og gravitation. De tre første af disse kræfter er sammen med de tolv stofpartikler, de fire kraftpartikler samt Higgs partiklen beskrevet af *Standardmodellen*.

Den sidste brik i det store puslespil, som Standardmodellen er, blev lagt i 2012, da ATLAS og CMS eksperimenterne offentliggjorde, at de havde observeret en ny partikel, der var i overensstemmelse med Standardmodellens Higgs partikel. Det har dog ikke fået partikelfysikerne til at ligge på den lade side, da der stadig er mange ting, vi ikke forstår.

Standardmodellen kan for eksempel ikke forklare den store forskel, der er på massen af de forskellige partikler. Den tungeste af de fundamentale partikler er en stofpartikel og hedder top kvarken. Dens store masse gør den særdeles interessant at studere. Top kvarken (og de andre kvarker) opstår i den store partikelaccelerator kaldet Large Hadron Collider, når to protoner kolliderer med hinanden ved meget høj hastighed. Det er dog ikke muligt for disse kvarker at eksistere alene. Derfor omdannes noget af deres bevægelsesenergi til kvark-antikvark par. Denne proces fortsætter indtil energien er kommet under en vis grænse. Resultatet er en kaskade af partikler, der bevæger sig i stort set den samme retning, kaldet en *jet*, som samlet har den samme energi og andre egenskaber, der svarer til det, den oprindelige kvark havde.

Denne afhandling beskriver flere analyser af det data, som ATLAS eksperimentet har samlet fra 2015 til 2018. Disse analyser undersøger, hvorvidt de jet-par, vi observerer, er i overensstemmelse med Standardmodellen eller ej. Håbet er at finde visse afvigelser, da det vil hjælpe os med at forstå, hvordan vi bedre kan beskrive universets mindste byggesten og kræfterne imellem dem. Vi må dog konstatere, at det nuværende data passer fint med Standardmodellen, så yderligere undersøgelser og mere data er nødvendigt.

Acknowledgements

First of all, I want to thank three people, who have played a special role in my professional development. They believed in me and made me believe in myself. Kim Horsevad, my elementary school teacher, who was there to feed my curiosity with printouts from Wikipedia and physics books, when my interest in physics began. You were an exceptional good teacher and I am very grateful for the time you invested in me. Ulrik Uggerhøj, my supervisor at Aarhus University, who, among other things, gave me the opportunity to spend half a year at Lawrence Berkeley National Laboratory (also a special thanks to Spencer Klein for hosting me). Ulrik, you sparked my interest in research and made me believe I could do a PhD. Thank you! Torsten Åkesson, my main supervisor for the PhD, who has been ambitious on my behalf, but also listened and helped me through hard times. You have taught me a lot and it has been a pleasure being your student.

I also want to thank my two co-supervisors, Caterina Doglioni and Johan Rathsmann. Caterina, you were a huge help in the beginning of my PhD. I am thankful for all the time you spend on helping me with my qualification task, teaching me how cool jets are and introduced me to various people in ATLAS. I am still to meet an ATLAS member, who do not know, who you are. You are an amazing physicist and a big role model of mine. Johan, I have been so happy to have you as my theoretical supervisor. It has been a pleasure working with you on the next-to-leading order dijet calculations and I appreciate your effort in explaining particle physics theory in a way that an experimental PhD student can understand. Also thank you for the useful comments on my thesis draft.

A big thanks also goes to my many ATLAS colleagues. In particular, I want to thank the ATLAS groups in Rome, Oslo, Melbourne and Vancouver, which all hosted me for a shorter or longer period during my PhD. My first task in ATLAS was in the Jet/Etmiss performance group, where I met many kind and talented people. In that regard, I would like to thank Max Swiatlowski, Kate Pachal, Chris Young, Steven Schramm, Mark Hodgkinson, Zach Marshall, Bogdan Malaescu, Joakim Olsson and last but not least Millie McDonald.

Through my analysis work, I have also been fortunate to work with many excellent physicists, like Marco Vanadia, Ben Allen, Matteo Bauce and Simone Francescato in the dijet analysis, where I also benefited from the great expertise of Alex Read and Pavel Starovoitov. Many thanks to you all. More recently, I have spent most of my waking hours collaborating with the great people in the all-hadronic $t\bar{t}$ group. Koji Terashi, Aparajita Dattagupta, Hulin Wang, Yu-Heng Chen, Tong Ou, Josu Garcia and Elham Khoda, it has been an absolute pleasure working with you and I am so proud, of what we have achieved together.

It is always scary, when you move to a new place, where you do not know anyone. Therefore, a big thanks to Prim, Juno and Edgar for giving me the best start possible in Lund by becoming my friends. Also a thanks to the *old* PhD students, Lene Kristian, Sasha, Martin,

Tuva, Vytautas and Ben. You showed me that the Lund particle physics PhD students were a group I could be proud of being part of. A special thanks to Lene Kristian for writing a great thesis, which has helped me immensely in understanding the world of dijets. More colleagues and friends have arrived through the years: Katja, Eric, Eva, Caterina, Eleni, Nathan, Alex, Kristian, Will, Geoffrey, Jannik, Saeid, Jonatan, Adrian, Omar, Oliver, Anna and Yosse. You have all made my years in Lund a memorable time, I will look back on with a smile on my face. The Lund particle physics division would also not be the same without the senior scientists. Here I want to give a special thanks to Peter for reading my thesis draft and giving me valuable feedback. Else, Ruth, Oxana and Melissa, I highly appreciate your feedback in the weekly ATLAS Lund meetings. Also a big thanks to Bozena and Florido for keeping the division running in a smooth manner. In short, thank you to everyone, who has been a part of the Lund particle physics division in the last 5 years. I could not have wished for a better working environment.

It is also important to me to thank my fantastic friends in Denmark. Louise, Frederikke, Camilla, Mette, Kathrine, Jakob, Jonas, Jeppe and Chris, your support, friendship and company means the world to me. Thanks for making time to see me, when I am back in Denmark and for reminding me, that there is also a world outside of physics.

Last but not least, I want to express my gratitude to my family. Thanks to my sister and brother-in-law for always welcoming me into their home and my niece and nephew for filling my heart with unconditional love. But most of all, thanks to my parents for letting me know, that I always have a safe place to return to. I cannot begin to explain, how much your support and encouragement means to me. I would not have dared to follow my dreams, if it was not for you. I am eternally grateful.

Contents

Abstract	vii
Populærvidenskabeligt resumé	ix
Acknowledgements	xi
1 Introduction	1
1.1 Particle physics	1
1.2 Popular scientific description and question boxes	2
1.3 Thesis outline	3
1.3.1 Figures	4
1.4 Publications	4
2 Standard Model and Beyond	5
2.1 The Standard Model of Particle Physics	6
2.2 Spontaneous symmetry breaking	8
2.3 Feynman diagrams	10
2.4 Quantum chromodynamics	12
2.4.1 Running of α_s	14
2.4.2 Perturbative QCD	14
2.5 Summary of the Standard Model	15
2.6 Parton distribution function	17
2.7 Factorization theorem	18
2.8 Processes after the collision	20
2.8.1 Parton showers	20
2.8.2 Hadronization	20
2.8.3 Underlying event	22
2.9 Monte Carlo event generators	23
2.10 The top quark	23
2.11 Physics beyond the Standard Model	25
2.11.1 Z' boson	26
2.11.2 Contact Interaction	26
2.11.3 Excited quarks	28
3 Large Hadron Collider	29
3.1 CERN accelerator complex	29

3.2	Run 1 and Run 2 of the LHC	30
3.3	Beam and accelerator parameters	32
3.4	LHC operation	34
4	The ATLAS Experiment	37
4.1	Requirements	38
4.2	Particle identification	39
4.3	The inner detector	40
4.4	The calorimeters	42
4.4.1	EM calorimeter	43
4.4.2	Hadronic calorimeter	44
4.4.3	Energy measurements	47
4.5	Muon spectrometer	49
4.6	Forward detectors	49
4.7	Magnets	50
4.8	Data taking	51
4.8.1	Triggering	52
4.9	Detector simulation	53
4.10	Data processing	54
5	Jets	55
5.1	Reconstruction	56
5.1.1	Topological clusters	56
5.1.2	Tracks from charged particles	57
5.1.3	Combination of topo-cluster and track information	59
5.1.4	Jet algorithms	61
5.1.5	Jets in ATLAS	63
5.2	Calibration	64
5.2.1	Small- R jets	64
5.2.2	Large- R jets	68
5.3	Jet substructure and tagging	70
5.3.1	Substructure variables	72
5.3.2	Top tagging	76
5.3.3	b tagging	84
6	Dijets	87
6.1	Dijet invariant mass distribution	87
6.2	Dijet angular distribution	89
6.3	QCD dijets as background	92
6.3.1	Monte Carlo simulations	92
6.3.2	ABCD method	92
6.3.3	Global fit	94

6.3.4	Sliding Window Fit	94
6.4	Dijet searches	94
6.5	Statistical tools	95
6.5.1	Model-independent resonance search	95
	Pearson's χ^2 test	97
	BUMPHUNTER	97
6.5.2	Model-dependent search	98
6.5.3	Limit setting	100
6.5.4	Wilks' test	101
7	Single Particle Jet Energy Scale Uncertainty	103
7.1	Data sets and object selection	103
7.2	Jet energy response and uncertainty	104
7.2.1	Jet energy scale uncertainty	104
8	All-hadronic $t\bar{t}$ Resonance Analysis	109
8.1	Data and simulation	110
8.1.1	Monte Carlo samples	111
8.1.2	Data samples	112
8.2	Event selection	113
8.2.1	Kinematic selection	113
8.2.2	Top tagging	116
8.2.3	b tagging	117
8.2.4	Summary	117
8.3	Background modeling	118
8.3.1	ABCD method	119
8.3.2	Effective entries	119
8.3.3	Combined multijet sample	121
8.3.4	Fitting range and binning	123
8.3.5	Global fit requirements	125
8.3.6	Pseudo-experiments	126
8.3.7	Choice of fit function	126
8.4	Signal modeling	128
8.4.1	Closure test	134
8.5	Systematic uncertainties	134
8.5.1	Fit parameter uncertainty	134
8.5.2	Spurious signal	139
8.5.3	Large- R jet uncertainties	142
8.5.4	Top and b tagging uncertainties	143
8.5.5	Other uncertainties	143
8.6	Statistical analysis	143
8.6.1	BUMPHUNTER	144

8.6.2	Likelihood	144
8.6.3	Limit setting	144
8.7	Results	145
8.7.1	Model-independent search	145
8.7.2	Model-dependent search	146
8.7.3	Limits	150
8.7.4	Comparison to previous analysis	151
8.8	Discussion	152
8.8.1	Dark matter summary plot	153
9	Dijet Analysis	155
9.1	Angular analysis on 37 fb^{-1}	155
9.1.1	Simulation	156
9.1.2	NLO corrections for signal	156
9.1.3	Event selection	157
9.1.4	Systematic uncertainties	158
9.1.5	Statistical analysis	158
9.1.6	Results	159
9.2	Dijet and di- b -jet resonance search	161
9.2.1	Simulation	162
9.2.2	Event selection	162
9.2.3	Background modeling	163
9.2.4	Resolution study	163
9.2.5	Systematic uncertainties	164
9.2.6	Statistical analysis	165
9.2.7	Results	165
9.3	Initial studies for angular analysis on 139 fb^{-1}	167
9.4	Angular resolution study	167
9.5	QCD NLO corrections	168
9.5.1	NLO k -factors	168
9.5.2	NLO _{JET++}	168
9.5.3	Improvement of NLO calculation	169
9.5.4	Final k -factors	172
9.6	Systematic uncertainties	173
9.6.1	Scale uncertainty	174
9.6.2	PDF uncertainty	175
9.6.3	JES uncertainty	175
9.7	Ratio method	177
9.7.1	Limit setting	178
9.8	Discussion	178
10	Conclusions and Outlook	179

A	Popular Scientific Description	181
B	List of Question Boxes	189
C	Single Particle Uncertainties	193
D	Samples for All-hadronic $t\bar{t}$ Resonance Analysis	197
E	Object Definitions for All-hadronic $t\bar{t}$ Resonance Analysis	201

Introduction

The big hard questions, like “Why are we here?”, “Is the Universe infinite?” and “What is the smallest building blocks of matter?”, has always fascinated me and in that sense, it is not a surprise, that I am now finishing a PhD in particle physics.

1.1 Particle physics

When I was in elementary school, the Large Hadron Collider (LHC) was under construction and even though I did not really understand, how the scientists would be able to unravel some of the mysteries of our Universe by smashing particles together, it was a thrilling thought. So I started reading about particle physics.

I discovered how back in the beginning of the 1930s, we thought, that the most fundamental building blocks were just protons, neutrons and electrons, but that in the following decades several particles were found. The muon was discovered in 1937 [1], even though it was first mistaken for the pion, which was not discovered until 1947 [2, 3]. Then we entered the realm of particle accelerators and many new particles were found in the late 1960s, often referred to as the *particle zoo*. The existence of all these different particles was quite confusing until it was understood, that they all consisted of more fundamental particles, the quarks [4, 5].

Along with the impressive discoveries followed, of course, the theoretical developments, which resulted in the *Standard Model of Particle Physics*. It predicted the existence of a few more fundamental particles, which had not been discovered yet: the top quark, which was later discovered in 1995 [6, 7], the tau neutrino in 2000 [8] and the Higgs boson, which was still not discovered in 2006, when I was finishing elementary school. However, the hope was that with the LHC, we would be able to find it and thereby complete the Standard Model and so we did in 2012 [9, 10].

The history of particle physics is also a history of ever-increasing energies. The W/Z bosons, the top quark and the Higgs boson were all discovered as new particle accelerators made it possible to achieve even higher energy collisions. Higher energy means the possibility of producing more massive particles as stated by Einsteins famous equation $E = mc^2$.

Then a few years later, during my time in high school, I stumbled upon a YouTube video explaining the double slit experiment [11], which demonstrates the concept of particle-wave duality. My first thought was that this could not be true. How could something both be particles and waves? And why did it matter, whether we observed it or not? The topic of quantum mechanics had astonished me for the first time.

Since a particle can also be viewed as a wave, this means, that if we accelerate a particle to a higher energy, we can use it to resolve finer details of the object, we smash it into. This is true, since higher energy means shorter wavelength, which means better resolution.

As a result, the high energy of the LHC, does not only allow us to produce more massive particles than ever before, but it also allows us to look in even finer detail at the particles we already know - or think we know.

1.2 Popular scientific description and question boxes

As you might have realized by now, I was a very curious child and this curious child still lives inside me. I have therefore decided to give her some space in the thesis. My hope is that she can help the reader, who is new to particle physics (like my friends and family) to understand the basics of the research presented in this thesis. This popular scientific description includes a low-level introduction to the Standard Model and explanations to what is presented in each chapter of the thesis. It can be found in Appendix A.

Throughout the chapters you will also find question boxes like the one below.

Question 1.1: What are question boxes?

The question boxes give answers to different questions. It can be all from concepts that are hard to understand to the most basic knowledge in particle physics.

The boxes can be read out of context for the reader, who just want an overview of the topics covered in this thesis, but is also meant as an easy way to look up different concepts. A list of the questions with references to the page is found in Appendix B.

1.3 Thesis outline

The thesis begins, not surprisingly, with a chapter laying out the theoretical foundation, which the rest of the chapters are build upon (Chapter 2). It shortly summarizes the Standard Model of Particle Physics and the processes involved, when two particles collide. It also outlines some of the observations, we have made, which are not in accordance with the Standard Model and a few theories beyond the Standard Model, which might explain some of these observations. Here emphasis is put on the models, which are later used as benchmark models in the physics analyses.

Then two chapters follow, in which the machinery, used to obtain the presented results, is described. First the LHC, which was mentioned above, is introduced (Chapter 3) and then the ATLAS experiment, one of the four big experiments on the LHC ring, is outlined (Chapter 4).

I then focus on one of the main physics objects, which is produced in abundance by the LHC and detected by the ATLAS experiment, the jet (Chapter 5). I will define, what it is and describe how it is calibrated and what it can be used for. When that is covered, I can move on to discuss a system of two jets, called a dijet (Chapter 6). Dijets are of particular interest in this thesis, since they form the basis for the analyses described in the two last chapters.

However, a chapter is first dedicated to the work I have done as part of my *qualification task* (Chapter 7). The qualification task is an assignment, which is for the common good of the collaboration and it consists of at least half a year of full time work. My assignment was to calibrate jets with high transverse momentum using a single particle method.

The first analysis, I will describe, is the all-hadronic $t\bar{t}$ resonance search (Chapter 8). I was one of the main analyzers and I have taken part in all major steps of the analysis. I optimized the event selection in order to improve the sensitivity and I validated the data quality. I improved the signal morphing to minimize the difference to the Monte Carlo samples and tested the background fitting functions on pseudo-experiments to find the best suited function before unblinding the data. I have also estimated the systematic uncertainties related to the background estimation and studied the mass resolution in order to optimize the binning. Furthermore, I have been running the statistical framework and investigated the impact of different systematic uncertainties in order to set limits on the chosen signal model. The chapter goes into quite some detail on the part of these studies, I have deemed interesting.

The second analysis is actually a compilation of several analyses, which I have worked on, but they all have in common, that the final state is dijets (Chapter 9). I have been part of the dijet analysis group, since the beginning of my PhD and I have performed various

studies as well as participated in the weekly meetings. The first analysis introduced is the dijet angular analysis on 37 fb^{-1} of data. I contributed to this analysis by calculating next-to-leading order correction factors for the signal samples. The second analysis is the dijet and di- b -jet resonance search. Here I contributed with a study of the mass resolution. The last part of the chapter shows the various studies, I have performed for the dijet angular search, which have not yet been published, since the analysis of the full Run 2 data set is still ongoing.

1.3.1 Figures

All the figures presented in this thesis, which do not have a citation, are produced by me, except for Figure 8.39, which is produced by Elham Khoda as clearly indicated.

1.4 Publications

Some of the work described in this thesis is also appearing in the following peer-reviewed publications:

- ATLAS Collaboration. Search for $t\bar{t}$ resonances in fully hadronic final states in pp collisions at $\sqrt{s} = 13 \text{ TeV}$ with the ATLAS detector, *submitted to Journal of High Energy Physics*.
- ATLAS Collaboration. Search for new phenomena in dijet events using 37 fb^{-1} of pp collision data collected at $\sqrt{s} = 13 \text{ TeV}$ with the ATLAS detector. *Physical Review D*, 96(5), Sep 2017.
- ATLAS Collaboration. Search for new resonances in mass distributions of jet pairs using 139 fb^{-1} of pp collisions at $\sqrt{s} = 13 \text{ TeV}$ with the ATLAS detector. *Journal of High Energy Physics*, 2020(3), Mar 2020.
- ATLAS Collaboration. High- p_T Jet Energy Scale Uncertainty from single hadron response with the ATLAS detector. *Proceeding of Science LHCP2016* (2016) 212.

Standard Model and Beyond

Particle physics, also called high energy physics, is the field of physics that describes the most fundamental forces and particles of our Universe. There are four fundamental forces of nature: electromagnetism, the weak force, the strong force and gravity.

The four forces have very different range and strength. The strong force is the strongest as the name indicates. Then comes electromagnetism with a strength of only $\frac{1}{137}$ relative to the strong force. The weak force is even weaker with a relative strength of 10^{-6} , but gravity is the absolutely weakest with a relative strength of only 10^{-39} .

This however comes with a caveat. The strengths of the forces depends on the energy, at which they are probed. This is partly due to the *running of the coupling constants*, which we will come back to in Section 2.4.1, but for the weak force, more dominantly, due to the mass of the force mediators. This implies, since the coupling constants do not evolve in the same way, that at some energy the forces unite.

The range of each force is determined by the mass of the force mediator, M_X . By using the Heisenberg uncertainty principle ($\Delta E \Delta t \geq \frac{\hbar}{2}$), it is seen that the range, r , is given by

$$r = c\Delta t \leq \frac{\hbar}{2M_X c} \quad (2.1)$$

where \hbar is the reduced Planck constant and c is the speed of light.

The weak force has massive mediators, which corresponds to a range of approximately 10^{-18} meter. The mediators for electromagnetism and gravity are massless, which gives them infinite range. For the strong force things are a bit more complicated. The mediator, called the gluon, is massless, so we would naively expect an infinite range, but this is not the case, since the gluons are subject to *confinement*, which will be explained in Question 2.4. It leads to a range of approximately 10^{-15} meter for the strong force. This explains why we do not experience the weak and strong forces in everyday life, but clearly see the effect of electromagnetism and gravity.

2.1 The Standard Model of Particle Physics

The knowledge we have about the fundamental constituents and the forces acting on them is summarized in *The Standard Model of Particle Physics* or just the Standard Model for short [12, 13, 14]. It only takes into account the three strongest forces and thereby leaves out gravity. This is not a problem, since gravity has a very small effect on particle interactions. However, the goal is to eventually make a theory, that describes all four forces in a *Theory of Everything*.

In the Standard Model there are two types of particles, fermions and bosons. They are distinguished by their spin, which is the intrinsic angular momentum of the particle. Fermions have half-integer spin, whereas bosons have integer spin. The matter around us is made of fermions, while vector bosons are mediating the fundamental forces and are therefore also called force carrier particles.

Question 2.1: What are the elementary particles?

The elementary fermions of the Standard Model consist of six quarks and six leptons (plus their antiparticles). They are divided into three generations as seen in Figure 2.1. The quarks have fractional electric charge values ($+\frac{2}{3}$ for u , c and t and $-\frac{1}{3}$ for d , s and b) whereas the leptons have integer values (-1 for e^- , μ^- and τ^- and 0 for the neutrinos). All the elementary fermions have a spin value of $\frac{1}{2}$.

The elementary bosons are the mediators of the fundamental forces. Electromagnetism has the photon, the weak force has the Z- and W-bosons and the strong force has the gluon. These are called gauge or vector bosons and have spin 1. The last elementary boson is the Higgs boson, which is a scalar boson with spin 0.

The elementary particles are sketched in Figure 2.1, while their masses and electric charges are seen in Table 2.1. Here the charge is given in units of the elementary charge, e , and the mass in terms of electron volts, eV. An electron gains (or loses) 1 eV in energy, when passing through an electric potential difference of 1 V. In particle physics the electron volt is used as a unit for both energy, mass and momentum. This is possible, since natural units are used, which means the speed of light c is set equal to one such that $E^2 = \vec{p}^2 c^2 + m^2 c^4$ simply becomes $E^2 = \vec{p}^2 + m^2$.

The Standard Model is a quantum field theory (QFT), which in short means that particles are treated as excited states or quanta of their underlying fields. The fields are then seen as the more fundamental parts of nature and they are defined at all points of spacetime. The fields are the following: the fermion fields, ψ ; the electroweak boson fields W_1 , W_2 , W_3 and B ; the gluon fields, G_a ; and the Higgs field, ϕ .

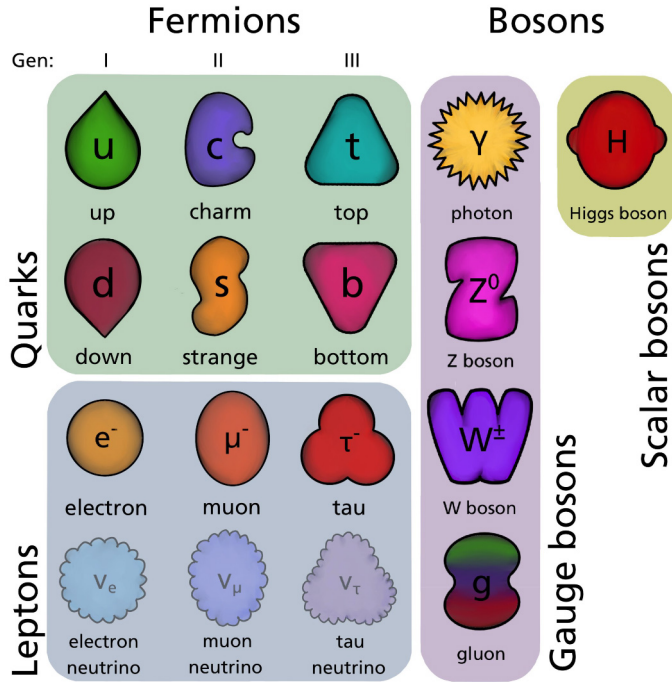


Figure 2.1: The standard model elementary fermions and bosons.

Table 2.1: Masses and electric charges of the elementary particles [15].

	Particle	Mass	Electric charge	Spin
Quarks	up (u)	$2.16^{+0.49}_{-0.26}$ MeV	$+\frac{2}{3}e$	$\frac{1}{2}$
	charm (c)	1.27 ± 0.02 GeV	$+\frac{2}{3}e$	$\frac{1}{2}$
	top (t)	172.9 ± 0.4 GeV	$+\frac{2}{3}e$	$\frac{1}{2}$
	down (d)	$4.67^{+0.48}_{-0.17}$ MeV	$-\frac{1}{3}e$	$\frac{1}{2}$
	strange (s)	93^{+11}_{-5} MeV	$-\frac{1}{3}e$	$\frac{1}{2}$
	bottom (b)	$4.18^{+0.03}_{-0.02}$ GeV	$-\frac{1}{3}e$	$\frac{1}{2}$
Leptons	electron (e)	~ 0.511 MeV	$-1e$	$\frac{1}{2}$
	muon (μ)	~ 105.6 MeV	$-1e$	$\frac{1}{2}$
	tau (τ)	~ 1.777 GeV	$-1e$	$\frac{1}{2}$
	neutrinos (ν_e, ν_μ, ν_τ)	< 2 eV	0	$\frac{1}{2}$
Bosons	photon (γ)	0	0	1
	Z boson (Z^0)	~ 91.2 GeV	0	1
	W boson (W^+, W^-)	~ 80.4 GeV	$\pm 1e$	1
	gluon (g)	0	0	1
	Higgs boson (H)	~ 125 GeV	0	0

The fields are of different types. W_1, W_2, W_3, B and G_a are all vector fields (they transform like four-vectors under Lorentz transformations), whereas ϕ is a scalar field (it is invariant under Lorentz transformations). This explains, why the corresponding bosons are called

vector and scalar bosons. ψ does also transform under Lorentz transformations, but not quite like a four-vector. It only turns by half of the normal angle under a rotation and is therefore instead known as a spinor field (with spin $\frac{1}{2}$).

The Standard Model consists of several parts describing the different forces. Quantum chromodynamics (QCD) describes the strong force and is in itself a QFT with the symmetry group $SU(3)$, which acts on G_a . The electromagnetic and weak forces are described together by electroweak theory (EWT), which is also a QFT with the symmetry group $SU(2) \times U(1)$, where $SU(2)$ acts on W_1, W_2, W_3 and ϕ and $U(1)$ acts on B and ϕ . This means that combined the symmetry group of the Standard Model is $SU(3) \times SU(2) \times U(1)$. However, this symmetry can be broken by so-called spontaneous symmetry breaking.

2.2 Spontaneous symmetry breaking

Spontaneous symmetry breaking results in separating the electromagnetic and weak forces as well as giving the particles mass. The electroweak boson fields W_1, W_2, W_3 and B mix to give the observed massive weak bosons, W^\pm and Z^0 and the massless photon, A :

$$Z^0 = \cos \theta_W W_3 - \sin \theta_W B \quad (2.2)$$

$$A = \sin \theta_W W_3 + \cos \theta_W B \quad (2.3)$$

$$W^\pm = \frac{1}{\sqrt{2}}(W_1 \mp iW_2) \quad (2.4)$$

where θ_W is the Weinberg angle.

This is known as the Brout–Englert–Higgs mechanism [16, 17]. In rough terms, it can be said that the weak bosons gain their mass by absorbing three out of four degrees of freedom of the Higgs field, ϕ . The fourth degree of freedom results in the Higgs boson.

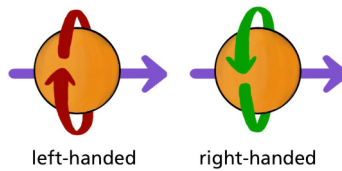
By introducing the Higgs field, not only the weak bosons acquire mass, but also the fermions. This happens through the so-called Yukawa coupling. The size of the coupling to a given fermion is measured experimentally and is so far not explained by theory.

Actually not all the fermions gain mass in the way explained above. This is not the case for the neutrinos, which are assumed to be massless in the Standard Model. To understand why that is, another property needs to be introduced, namely *helicity*.

Question 2.2: What is helicity?

The *helicity* or *handedness* describes the direction of the spin of the particle relative to the direction of motion. If a particle, moving in the direction of the purple arrow, spins as indicated by the red arrow, it is left-handed, since the rotation goes in the same direction as your fingers on the left hand, when your left thumb points in the direction of the purple arrow.

In the same way, the particle is right-handed, if it spins in the opposite direction as indicated by the green arrow, since it is now following the direction of the fingers on your right hand.



Helicity is however not an intrinsic property unless the particle is massless. This can be understood by imagining you are moving slower and faster than a massive particle, respectively. If the helicity is right-handed in the reference frame where you move slower (the particle moves forward relative to you), then it will be left-handed in the reference frame, where you move faster (the particle moves backward relative to you), since that would flip the direction of the purple arrow in the figure above, but not change the spin direction. It is impossible to move faster than a massless particle and its helicity will therefore be the same in all reference frames.

A property, that is intrinsic to all particles, is the chirality, which is closely related to the helicity. In fact it is the same for massless particles. The chirality will be the same, no matter which reference frame you are in and left-chiral and right-chiral particles are therefore fundamentally different.

This difference is of big importance in electroweak theory, since left-chiral and right-chiral particles are not treated the same. Only left-chiral fermions (and right-chiral antifermions) interact with the W^\pm and Z^0 bosons. However, the left-chiral fermions mix with the right-chiral leptons through the Yukawa coupling and thereby gain their mass.

In the Standard Model there are only left-chiral neutrinos, which explains why they are expected to be massless, since they do not have a right-chiral partner to mix with. This is however not, what is observed. Neutrinos can oscillate between the different flavor states (electron-, muon- and tau-flavor) and this is only possible, if they have a mass. This is one of the phenomenon, that tells us, that the Standard Model is not the final story about our Universe.

One possible extension to the Standard Model, which would be able to explain the small, but non-zero, mass of the left-chiral neutrinos, is the introduction of heavy right-chiral neutrinos. These neutrinos, which we have not been able to observe yet, would give mass to the left-chiral Standard Model neutrinos through a so-called *seesaw mechanism* [18]. The heavier the right-chiral neutrinos are, the lighter the Standard Model neutrinos will be.

We have now covered, how the particles get their masses and thereby also discussed electroweak theory. It is therefore natural to move on to quantum chromodynamics, but before doing so, it is useful to introduce a very helpful tool called Feynman diagrams.

2.3 Feynman diagrams

One of the greatest particle physicist of all time, Richard Feynman (May 11, 1918 – February 15, 1988), developed a commonly used graphical representation of particle interactions, which later became known as Feynman diagrams. They are illustrating the mathematical formulas for calculating the probability of different processes, but they are also just great for visualizing the processes. We will focus on the latter here.

The diagrams consists of lines and vertices, where a line represents a particle and a vertex represents an interaction between the particles. Time is going from left to right. Figure 2.2a shows the different lines used for the Standard Model particles. A straight line with the arrow in the time direction represents a fermion, f , whereas a straight line with the arrow against the time direction represents an antifermion, \bar{f} . The wavy line is used for all the electroweak bosons: γ , Z^0 and W^\pm . The gluon is represented by a curly line and the Higgs boson by a dashed line.

Figure 2.2b shows two examples of allowed vertices: A photon (or Z boson) going into a fermion and an antifermion and a gluon going into a quark and an antiquark. These examples show how charge has to be conserved. In the creation of a fermion, an antifermion, with the opposite charge, has to be created as well. This charge conservation is one of many rules, the Standard Model interactions have to obey. One of the strengths of the Feynman diagrams is, that if a certain vertex is allowed, then any rotation or mirroring of it is allowed as well. If the vertices in Figure 2.2b would be vertically mirrored, they would instead represent two particles annihilating and thereby creating a boson.

The simplest Feynman diagrams includes only two vertices, but some have many more. An example of one of the simplest diagrams is shown in Figure 2.3a. An up- and an anti-up-quark annihilates to a photon, which then goes into an electron and positron (antielectron). If this diagram is rotated 90° , it instead shows an electron scattering of an up-quark as is seen in Figure 2.3b. The first one is called a space-like (s-channel) process and the second one a time-like (t-channel) process.

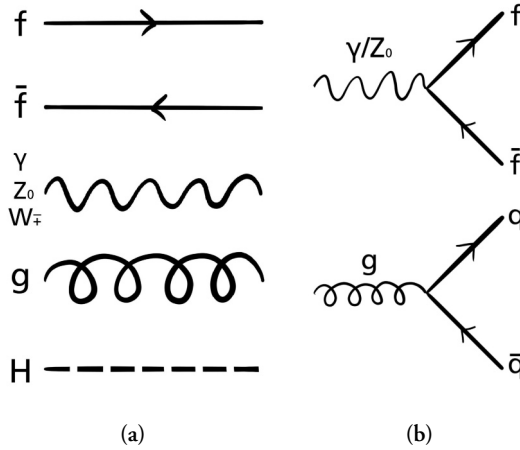


Figure 2.2: Feynman diagrams are made from (a) lines and (b) vertices. The time is going from left to right.

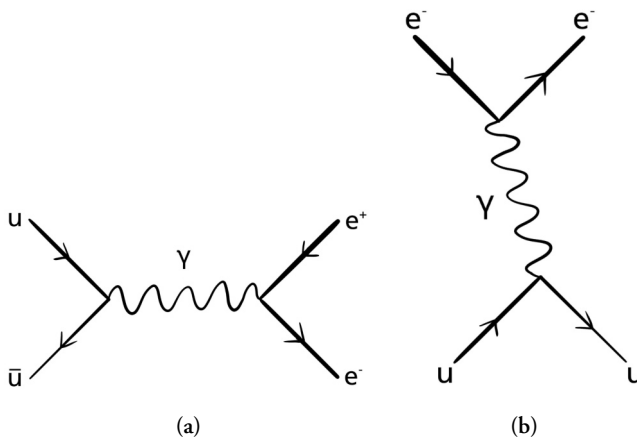


Figure 2.3: Example of simple Feynman diagrams, (a) $u\bar{u} \rightarrow \gamma \rightarrow e^+e^-$ and (b) $ue^- \rightarrow \gamma \rightarrow ue^-$.

Another thing that can be observed from Figure 2.3a is that a quark and an antiquark can turn into a lepton and an antilepton (and vice versa). This is true for all quarks and leptons as long as the initial particles are energetic enough to produce the mass of the final particles. This is true, since the photon does not have any recollection of the flavor of the initial particles. In other words, its flavor quantum number is zero.

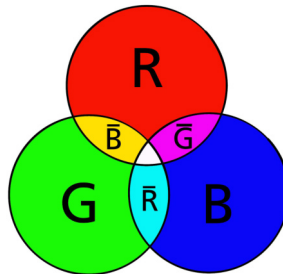
In contrast to the photon that interacts with all the electrically charged fermions, the gluon only interacts with the fermions, that have a color charge, namely the quarks. Which brings us to the topic of quantum chromodynamics.

2.4 Quantum chromodynamics

As mentioned earlier, the strong force is described by quantum chromodynamics (QCD). The name *chromo* comes from the fact, that the important quantum number here is the color charge.

Question 2.3: What is color charge?

Color is the charge of the strong interaction and is similar to the electric charge. As the electric charge can be positive/negative, the color charge can be red/antired, green/antigreen and blue/antiblue. These are just names of the charges and has nothing to do with the everyday concept of color. The name is however used, because adding up the three colors (or anticolors) will give a colorless (white) state, like in the RGB color model. A colorless result is also achieved by adding a color and its anticolor.



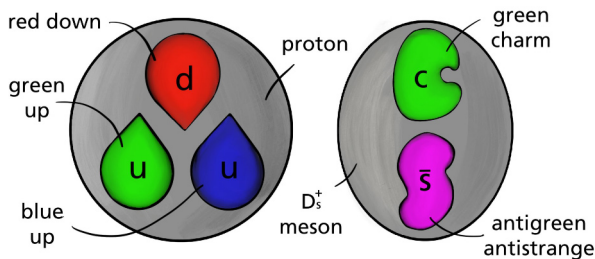
The color charge of a quark can be either red (R), green (G) or blue (B). Whereas for an antiquark it can be either antired (\bar{R}), antigreen (\bar{G}) or antiblue (\bar{B}). A gluon can be thought of as having a color and an anticolor. When a gluon interacts with a quark the color of the quark changes. A red quark could for example emit a red-antiblue gluon, which would make it blue and the gluon could then be absorbed by another blue quark, which would make it red. This way the color charge is conserved.

The combination of a color and an anticolor would naively lead to nine different gluons. That would in fact be the case, if the gauge symmetry of QCD was $U(3)$ and not $SU(3)$. Having a $SU(3)$ gauge symmetry means, there are no color singlet gluons and therefore only eight independent color states (the color octet).

If the color singlet existed as a mediator of the strong force, it would also exist as a free particle, like the photon. This would mean, that the strong force would have infinite range, which is not, what we observe. The gluons from the color octet can, on the contrary, not exist as free particles, which is explained by the concept of confinement.

Question 2.4: What is confinement?

Confinement is the phenomenon, that color charged particles, like quarks and gluons, cannot be isolated and therefore only colorless (color singlet) particles are observed. The observed particles are called hadrons, which are split into two categories: *baryons* consisting of an odd number of quarks, usually three*, and *mesons* consisting of an even number of quarks, usually a quark and an antiquark. The three quarks of the baryon will have red, green and blue color charge, respectively, whereas the meson is made from a color-anticolor combination, like a green quark and an antigreen antiquark.



*When we say that the usual baryon consists of three quarks, it is actually not completely true, since quantum fluctuations occur, where gluons split into quark-antiquark pairs, which then annihilate back into gluons. We however distinguish between these quarks, which we call virtual or sea quarks, and the remaining ones, which we call valance quarks. It is therefore more correct to say the baryon consists of three valance quarks.

Confinement is closely related to the concept of *asymptotic freedom*, which is the property, that the coupling between the quarks becomes weaker at smaller distances, but stronger as the quarks move apart and in that way prevents the separation of individual quarks. This behavior has been ascribed to the fact, that the gluons, which are exchanged between the quarks inside the hadrons, are not neutral, but carry a combination of color and anticolor.

This is in contrast to the photons mediating the electromagnetic force. Photons, emitted from say an electron, can create a virtual electron-positron pair, which can *screen* the charge seen further from the electron. The effect is a smaller effective charge of the electron and therefore a weaker field.

A similar screening is seen from virtual quark-antiquark pairs for the strong force, but the virtual gluons with their color-anticolor combination has the opposite effect. They enhance the color field, which in addition is smeared. Since the virtual quarks and gluons have opposite effects, which one wins is determined by the beta function, which to lowest

nontrivial order for QCD is given by

$$\beta_0(\alpha_s) = -\frac{\alpha_s^2}{4\pi} \left(11 - \frac{2}{3}n_f \right) \quad (2.5)$$

where α_s is the strong coupling constant and n_f is the number of quark flavors. It can be seen that since $n_f = 6$ in the Standard Model, the function is negative, which means the enhancement or *antiscreening* from the gluons wins. This antiscreening gets reduced, as we move closer to the quark, so the effective charge gets smaller, as we get closer. Hence, the coupling increases, as the distance grows.

2.4.1 Running of α_s

What the beta function actually describes, is the dependence of the strong coupling constant on the momentum transfer Q defined as $\beta(\alpha_s) = \frac{\partial \alpha_s}{\partial \ln Q^2}$. If α_s is small, it is possible to integrate this function using only the leading term seen in Equation 2.5. This gives

$$\frac{1}{\alpha_s(Q^2)} = \frac{1}{\alpha_s(\mu_R^2)} + b_0 \ln \left(\frac{Q^2}{\mu_R^2} \right) \quad (2.6)$$

where we have introduced the *renormalization scale* μ_R and $b_0 = \frac{11 - \frac{2}{3}n_f}{4\pi}$. This can be rearranged to give

$$\alpha_s(Q^2) = \frac{\alpha_s(\mu_R^2)}{1 + b_0 \alpha_s(\mu_R^2) \ln(Q^2/\mu_R^2)} \quad (2.7)$$

which shows the *running of α_s* . The agreement of the theory to the measured values of α_s as a function of Q can be seen in Figure 2.4. It is clear that $\alpha_s \rightarrow 0$ as $Q \rightarrow \infty$. The quarks behave like free particles at large momentum transfer (short distances). In this regime it is possible to make perturbative calculations.

2.4.2 Perturbative QCD

Perturbation theory is a methodology, where complicated calculations are split into pieces of increasing precision and starts with the coarsest approximation called leading order (LO). If a more precise result is needed, then next-to-leading order (NLO) calculations can be done as well. Luckily NLO is enough in most cases, since increasing order means an additional factor of α_s , which is small ($\ll 1$), so the importance of the additional terms rapidly decrease. We actually already used this principle, when we were only including the first term for the beta function in Equation 2.5.

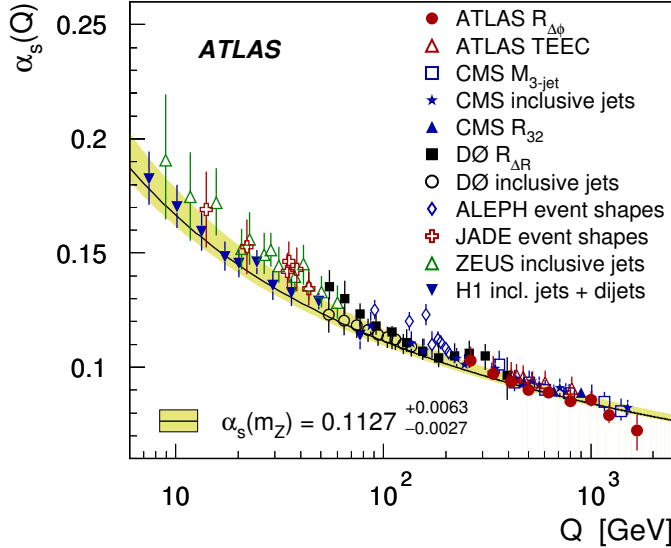


Figure 2.4: The strong coupling constant, α_s , as a function of the momentum transfer, Q [19].

In terms of Feynman diagrams, LO calculations correspond to the simplest, or tree-level, diagrams, whereas NLO diagrams can include a loop (virtual correction) or emission of an additional particle (real correction). Since the loop or emission can be placed in several places, there are a lot more terms to calculate for NLO.

Thus, it is possible to predict the strong interactions between quarks and gluons using perturbative calculations, as long as α_s is small ($Q > 1$ GeV). However, we know, the quarks do not exist as free particles, but are confined inside the hadrons. It is therefore important to understand, how the quarks and gluons are distributed in hadrons, but before we explore that topic, we will first summarize, what we now know about the Standard Model.

2.5 Summary of the Standard Model

The Standard Model particles and the interactions between them are summarized in Figure 2.5. The lines indicate, which particles can interact and it is seen, that the gluon, the Higgs boson and the weak bosons all have lines to themselves. This is not the case for the photon, since it does not have electric charge itself, in contrast to e.g. the gluon, which has color charge and can therefore interact with itself. Similarly, the photon interacts with the W boson, but not the Z boson, due to their electric charges of ± 1 and 0 , respectively.

Mathematically, the Standard Model can be described by a *Lagrangian*.

Question 2.5: What is the Lagrangian of the Standard Model?

The *Lagrangian* or more correctly the Lagrangian density, \mathcal{L} , of the Standard Model describes the kinematics and dynamics of the system of fundamental quantum fields. The full formulation takes up a few pages and will not be given here. However, a very shortened version is given by [20]

$$\begin{aligned}\mathcal{L}_{\text{SM}} = & -\frac{1}{4}F_{\mu\nu}F^{\mu\nu} \\ & + i\bar{\psi}\not{D}\psi + \text{h.c.} \\ & + \psi iy_{ij}\psi_j\phi + \text{h.c.} \\ & + |D_\mu\phi|^2 - V(\phi)\end{aligned}\tag{2.8}$$

which can be understood qualitatively in the following way:

- The first term, $-\frac{1}{4}F_{\mu\nu}F^{\mu\nu}$, is the scalar product of the field strength tensor $F_{\mu\nu}$ containing the mathematical encoding of the gauge bosons, where μ and ν are the Lorentz indices, we also know from four-vectors. The term describes both the existence of the gauge bosons and how they interact with each other.
- The second term, $i\bar{\psi}\not{D}\psi$, describes how the gauge bosons interact with the fermions, ψ . \not{D} is the covariant derivative, featuring the gauge bosons, but now without the self-interactions. So it contains a description of both the electromagnetic, weak and strong interaction.
- The third term, h.c., is the *hermitian conjugate* of the second term, which could actually be omitted, since the second term is self-adjoint. In general the hermitian conjugate is added to ensure that the theory is sound.
- The fourth term, $\psi iy_{ij}\psi_j\phi$, describes how the fermions couple to the Higgs field, ψ , and thereby obtain mass. The entries of the Yukawa matrix, y_{ij} , represent the coupling parameters to the Higgs field.
- The fifth term, h.c., is the hermitian conjugate of the fourth term and is necessary, since the fourth term is not self-adjoint. The fifth term is equivalent to the fourth term, but for anti-fermions instead of fermions.
- The sixth term, $|D_\mu\phi|^2$, describes how the gauge bosons couple to the Higgs field. This only applies to the weak gauge bosons.
- The seventh and last term, $-V(\phi)$, describes the potential of the Higgs field and how the Higgs boson couples to itself.

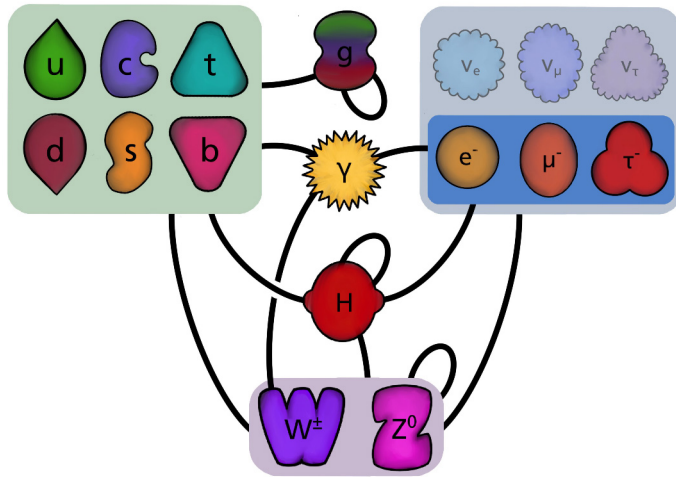


Figure 2.5: Sketch showing how the Standard Model particles interact with each other.

2.6 Parton distribution function

To describe the distribution of partons (quarks and gluons) inside the hadrons, we use so-called parton distribution functions (PDFs). The PDFs are studied by scattering experiments like deep inelastic scattering of electrons off protons. The most studied PDFs are in fact those of the proton, which consists of two up valance quarks and one down valance quark, as we saw in the figure in Question 2.4.

Figure 2.6 shows the Bjorken x times the PDF, $xf(x, Q)$, as a function of the Bjorken x . The Bjorken x is the longitudinal momentum fraction carried by the parton and Q is the energy scale, which is (a) 2 GeV and (b) 1 TeV. The figures shows that if the parton carries more than 20% of the longitudinal momentum (high Bjorken x), it is most likely an up quark, but could also be a down quark or a gluon. It is much more unlikely to be an antiquark or one of the heavier quarks.

At low Bjorken x the sea quarks dominate and the PDFs are more dependent on Q . For $Q = 2$ GeV, up and down quarks as well as their antiquarks are as likely, whereas the heavier quarks (strange and charm) are less likely. If we look at low Bjorken x for $Q = 1$ TeV, there are more sea quarks of any flavor as well as more gluons, than at $Q = 2$ GeV.

If the PDFs are measured at a given Q , it is possible to predict them at another value of Q using the Dokshitzer-Gribov-Lipatov-Altarelli-Parisi (DGLAP) equations. These equations are only valid, where perturbative calculations can be used ($\alpha_s \ll 1$). In fact, perturbative calculations of the hard scattering of two partons and the PDFs are the two crucial components in order to calculate the *cross section* for a hard scattering in a hadronic collision.

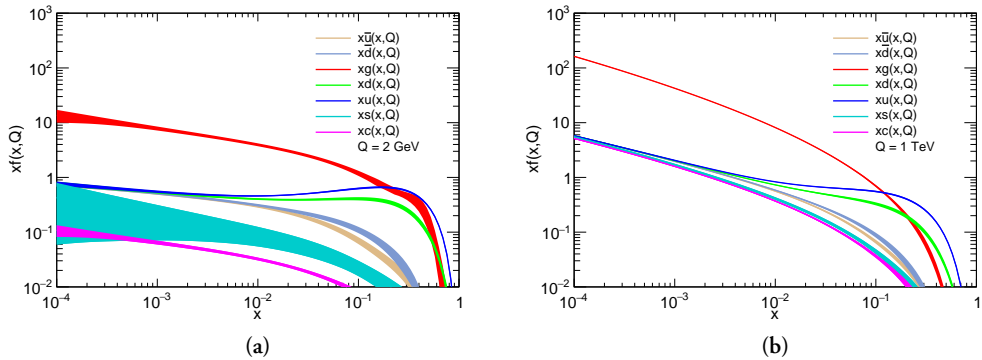


Figure 2.6: Parton distribution function for the proton with (a) $Q = 2 \text{ GeV}$ and (b) $Q = 1 \text{ TeV}$. The width of the functions shows the 1σ band. The figures are generated with *APFEL 2.7.1 Web* [21, 22] using the *NNPDF2.3 LO* PDF set [23].

Question 2.6: What is a cross section?

The *cross section* tells you the probability, that a given process will happen in the collision of two particles. The weird naming, which we usually use for a slice of an object, came to be for historical reasons, since back in the days, physicists believed particles to be small unbreakable balls. It is therefore easy to imagine, that the probability, that two balls would hit each other, would depend on their size or cross section. Today we know, that particles are actually wave packets and not solid balls with a fixed cross-sectional area. However, the term *cross section* is still used.

We use the Greek letter σ to denote the cross section and *barn*, b for the unit, which is a tiny area as $1 \text{ b} = 10^{-28} \text{ m}^2$. In fact we often talk about processes with cross sections as small as pico-barns ($\text{pb} = 10^{-12} \text{ b}$)!

2.7 Factorization theorem

To calculate the cross section of a given process in the collision of two protons with momentum P_1 and P_2 , we can use the *factorization theorem* [24], which allows us to factorize the cross section into the PDFs for the protons (f_i and f_j) and the hard-scattering partonic cross section $\hat{\sigma}_{i,j}$. The indices i and j indicates the two interacting partons. In order to make this factorization, we need to introduce a *factorization scale*, μ_F . Below this scale, the process is described by the non-perturbative PDF and above, by the perturbative hard-scattering cross section. Therefore, we must have $1 \text{ GeV}^2 \leq \mu_F < Q^2$ in order for the perturbative

calculations to be valid. The factorization theorem now reads

$$\sigma(P_1, P_2) = \sum_{ij} \int dx_1 f_i(x_1, \mu_F^2) \int dx_2 f_j(x_2, \mu_F^2) \hat{\sigma}_{ij}(x_1, x_2, \mu_R^2, \mu_F^2) \quad (2.9)$$

where x_1 and x_2 are the respective Bjorken x for the two participating partons. The theorem can also be illustrated schematically. This is seen in Figure 2.7.

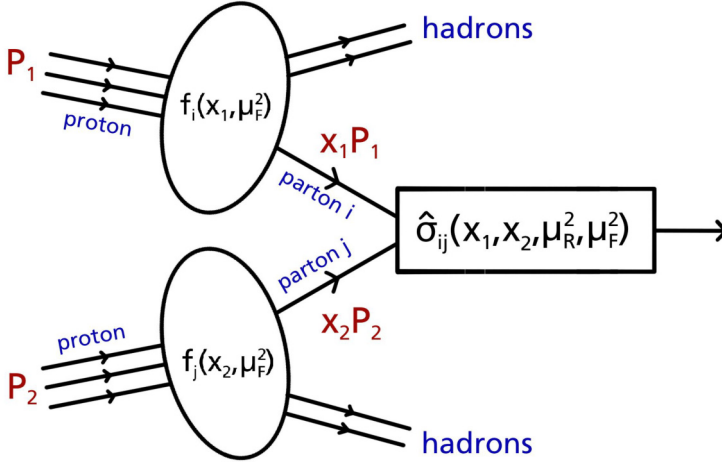


Figure 2.7: Schematic illustration of the factorization theorem.

We also notice, that the hard-scattering cross section $\hat{\sigma}_{ij}$ not only depends on μ_F , but also μ_R , which was introduced, when we discussed the running of α_s . These two scales are actually introduced in order to cure the divergences in the calculations of $\hat{\sigma}_{ij}$.

There are two types of divergences: ultraviolet (UV) and infrared (IR). The UV divergences appear because of large momentum of virtual particles and are cured by introducing the renormalization scale μ_R , which in turn results in the energy dependence of α_s . The IR (or collinear) divergences appear because of massless particles and are cured by introducing the factorization scale μ_F . In this case, it results in the DGLAP equations for the PDFs.

It is important to understand that ideally $\hat{\sigma}_{ij}$ should not depend on the values of these scales. This would indeed be true, if we could sum the entire perturbation series, which is of course not possible. However, as we go to next-to-leading order (NLO) or next-to-next-to-leading order (NNLO), the dependence decreases. Due to the remaining dependence, it is essential to choose the right value for μ_R and μ_F and calculate the uncertainty on the result arising from this choice.

We now have the tools to predict, what happens up until the collision of the partons inside two protons. The next step is therefore to describe, what happens after the collision.

2.8 Processes after the collision

After the hard-scattering collision, which by definition involves large momentum transfer, the two outgoing partons are heavily accelerated. This leads to emission of gluons, which, due to their color charge, can emit further radiation, leading to *parton showers*¹.

2.8.1 Parton showers

In principle, these showers are higher order corrections to the hard-scattering partonic cross section. It is however not possible to calculate these precisely, so instead, only the dominant contributions, which are associated with collinear parton splittings and soft gluon emissions, are included.

The collinear parton splittings are described by fragmentation functions, which are similar to the PDFs. Whereas, the soft gluon emissions can be handled by choosing an appropriate *evolution variable*. A good choice is a variable related to the opening angle of the splitting, θ , which would lead to an angular-ordered parton shower.

Another interesting approach to describe parton showers is dipole showering. In this approach each quark or antiquark are connected to a color partner, whereas a gluon is connected to two color partners. Then each pair of color partners forms a dipole and the emission of a gluon is equivalent to a dipole splitting into two. This gives a parton shower order in transverse momentum, so the angular ordering comes for free.

The emission of gluons continues, until we reach the scale, where perturbation theory is no longer valid, $Q < 1$ GeV. As we have seen, below this scale α_s becomes large and the quarks can no longer be considered free. They hadronize.

2.8.2 Hadronization

Hadronization is in the non-perturbative regime, which means we can not calculate it from first principle, but need to come up with a model. The two models, that are mostly used, are the Lund string model [25] and the cluster model [26]. Here we will focus on the former, which is used by the PYTHIA event generator [27], which we will come back to later.

The Lund string model is quite similar to the dipole picture in the perturbative regime. Imagine two quarks moving away from each other. The color field lines between the two quarks will be attracted to each other due to the gluon self-coupling, resulting in a tube-like

¹It should be noted that on top of final-state radiation, initial-state radiation happening before the collision exists as well.

structure or a *string*. This is in contrast to the radial electric field lines, which are spread out, since the photon does not interact with itself. This is seen in Figure 2.8.

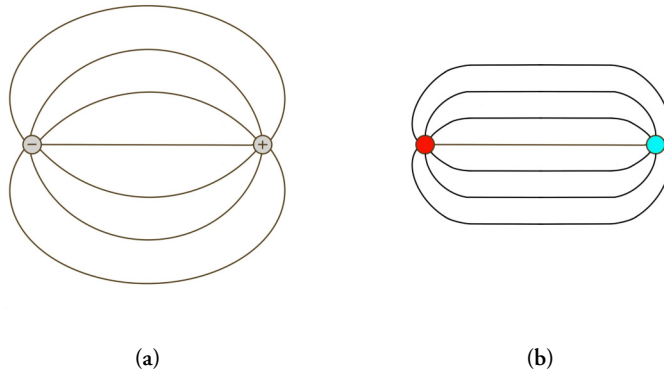


Figure 2.8: The difference between (a) electric and (b) color field lines.

When the two quarks are moving apart, the gluonic string is stretched between them and the kinetic energy of the quarks is transformed into potential energy of the string. When this energy exceeds the mass of a quark-antiquark pair, it becomes energetically favorable for the string to break into two, resulting in two strings with a quark at one end and an antiquark at the other.

The new strings then starts to stretch and break again. This process continues until all the potential energy in the strings is converted into quarks and we are left with quark-antiquark pairs with small strings between them, which can be regarded as hadrons. The hadron type depends on the flavor of the quark-antiquark pairs, that are created in the breaking. The same is true for the momentum distribution. Since the breaking can be thought of as arising from vacuum fluctuations, the creation of low-mass quarks with small transverse momentum with respect to the string axis is the most probable.

One of the most characteristic features of the Lund string model is the way gluons are treated, leading to the *string effect* [25]. Gluons are seen as kinks on the strings. Higher momentum gluons results in sharper kinks. If we consider a quark-antiquark-gluon system in the center-of-mass frame, we would see more hadrons produced in the angular region between the quark and the gluon and the gluon and the antiquark, but less in the region between the quark and the antiquark. This behavior is confirmed experimentally and should be seen in contrast to a quark-antiquark-photon system, where no enhancement is seen in the direction of the photon. It does not create a kink in the string.

At high energies, the result of the hadronization is a cone of particles moving in approximately the same direction. This is called a *jet*.

Question 2.7: What is a jet?

As colored objects, like quarks and gluons, cannot exist in free form due to confinement, the result of a fragmented hadron, which contains quarks and gluons, is the creation of additional quarks and gluons in order to form colorless objects (hadronization). The collection of these colorless objects is called a *jet*. More information about jets will be given in Chapter 5.

On top of the hadrons described by the parton shower and hadronization, we observe some additional hadrons, which come from the so-called *underlying event*.

2.8.3 Underlying event

We call the observed hadrons, which are not coming from the hard scattering, the underlying event. It is seen experimentally, that this additional activity is greater, than what is seen in *minimum-bias events*.

Question 2.8: What is an event?

In particle physics, an *event* is the interaction or particle collision, which is observed by a detector. These collisions can be either elastic or inelastic. The elastic collisions are common, but since the protons do not dissociate and no new particles are created, these are not counted as events in this work. In inelastic collisions, one or both of the colliding protons are dissociated and new particles are created. These are the collisions that will be detected and leading to an event being recorded. So-called *minimum-bias events* are inelastic events, which are triggered in a way, where as little bias as possible is introduced by missing or statistically enhancing certain final states. The definition of minimum-bias is detector-dependent.

The underlying event is believed to come from the partons in the hadrons, that do not directly participate in the hard scattering. This is also indicated for the proton remnants in Figure 2.7.

It is possible, and actually highly probable, to have *multiple parton interactions*, which however has a relatively small momentum transfer. The probability of such additional interactions depend on the *impact parameter*, which describes how big an overlap there is between the protons in the collision. The smaller the impact parameter is, the more probable both the hard-scattering interaction and multiple interactions are. Therefore it is not surprising that a higher level of underlying event activity is seen in presence of a hard-scattering interaction.

2.9 Monte Carlo event generators

In order to see if the experimental results are in agreement with the Standard Model or not, we need to have some theory prediction to compare to. In some cases, it might be possible to calculate a parametric function, which a certain distribution should follow, but in general, as we have seen, the collision of hadrons is very complicated and involves many different processes. Therefore, a very useful tool is Monte Carlo event generators.

There are three major event generators on the market: PYTHIA [27], HERWIG [28] and SHERPA [29]. These three general-purpose event generators have much in common. They all use pseudo-random numbers in order to get the fluctuations seen from event to event, which are dictated by quantum processes. They model the hard-scattering interaction, the parton shower and hadronization as well as the underlying event. However, they are using different assumptions and models in order to do so, which of course leads to different results.

HERWIG is using angular-ordered parton showers, whereas the newest version of PYTHIA as well as SHERPA are based on dipole showering. Regarding hadronization, both HERWIG and SHERPA are using the cluster model, whereas PYTHIA is using the Lund string model.

2.10 The top quark

Since the top quark is of particular interest in this thesis, an overview of the particle seems appropriate. As we saw in Table 2.1, the top quark is the heaviest elementary particle discovered so far [15]. At the LHC, the production of top quark pairs ($t\bar{t}$) is happening via the strong interaction and is primarily coming from gluon-gluon fusion, whereas quark annihilation is less common. The corresponding Feynman diagrams are seen in Figure 2.9.

Single top quark production is less common, being produced through the weak interaction and is primarily driven by t-channel exchange of a W boson. Other sizable contributions come from the s-channel and tW production as seen in Figure 2.10.

Being the only quark, that is heavier than the W boson, it can decay into another quark by emitting a real W boson. From that follows, that it has a very short lifetime ($\sim 5 \cdot 10^{-25}$ s) and that it decays, before it can hadronize. The top quark is usually assumed to exclusively decay to a W boson and a b quark ($t \rightarrow W^+ b$). This can be tested by measuring the ratio R given by

$$R = B(t \rightarrow W^+ b) / B(t \rightarrow W^+ q) \quad (2.10)$$

where $q = d, s, b$. The CMS experiment finds $R = 1.014 \pm 0.003(\text{stat.}) \pm 0.032(\text{syst.})$, which is consistent with a $\sim 100\%$ branching ratio to a W boson and a b quark [30]. Since

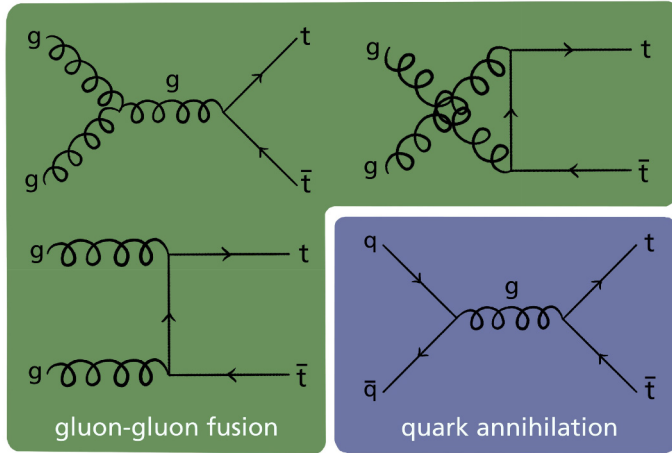


Figure 2.9: Top quark pairs are produced from gluon-gluon fusion and quark annihilation.

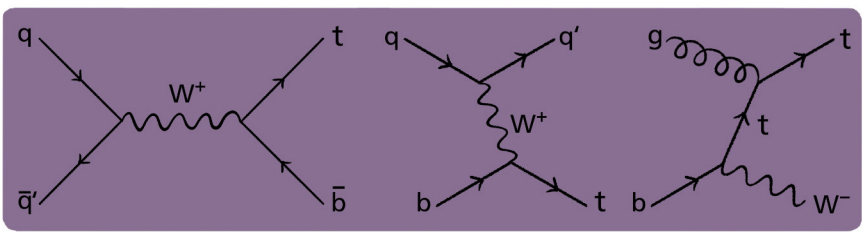


Figure 2.10: Single top quarks are coming from s-channel, t-channel and tW production.

the W boson can decay either hadronically ($W^+ \rightarrow q\bar{q}'$) or leptonically ($W^+ \rightarrow l^+\nu_l$), this means there are three different final states for top quark pair production: the all-hadronic, lepton+jets and dilepton channels. The branching ratios are 45.7%, 43.8% and 10.5%, respectively.

The property of the top quark, which we have measured most precisely, is its mass. It has been measured in all three decay channels, where the most precise measurement is coming from the lepton+jets channel. This is due to a good signal to background ratio, which is much worse for the all-hadronic channel and the presence of only a single neutrino in the final state, in contrast to the dilepton channel.

The top quark is of special importance both when studying the Standard Model, e.g. due to its large coupling to the Higgs field, but also when searching for new phenomena beyond the Standard Model. The latter is the topic of the last section of this chapter.

2.11 Physics beyond the Standard Model

Even though the Standard Model has done a great job describing particle physics phenomena, it has a number of shortcomings. We have already discussed, that it does not include the fourth fundamental force of nature, gravity. We have also seen that the Standard Model predicts massless neutrinos, which is not what we observe experimentally. However, these are not the only weaknesses.

A topic that puzzles many particle physicists is that of *dark matter*. Various astrophysical observations suggest, that the normal matter, explained by the Standard Model, only makes up approximately 15% of the total matter in the Universe; the rest is dark matter. It is called dark, since it does not seem to interact electromagnetically. The only reason we know it exists is through its gravitational interactions.

Another mystery is the abundance of matter over antimatter. It is believed that equal amounts of matter and antimatter was created in the Big Bang, but today all the visible Universe is made up of matter. The Standard Model actually allows for CP violation, which means that charge conjugation parity symmetry is broken. The charge conjugate of a particle is its antiparticle and switching the parity means inverting the spatial coordinates or taking the mirror image. This means, the physics is not the same for a particle and the mirror image of its antiparticle. CP violation is currently only observed in weak interactions and is explained by the presence of a complex phase in the *Cabibbo–Kobayashi–Maskawa matrix*, which describes the quark mixing. However, the violation is not happening to a degree that can explain why we see so much more matter than anti-matter.

CP violation is also, in principle, allowed in strong interactions, but is so far not observed. Actually very strict limits are set on it from measurements of the electric dipole moment of the neutron. This leads to a so-called fine tuning problem called the strong CP problem. It seems unnatural why the CP violating term in strong interactions should be so small.

Another fine tuning problem is why the Higgs mass is so low. It seems, the bare Higgs mass must be extremely large in order to cancel out the quantum corrections, which are of the order of 10^{18} GeV to give the observed Higgs mass of 125 GeV. The hope is, that we will discover the underlying reason for this fine tuning someday, so it will no longer seem unnatural. Studying the top quark in detail might be a rewarding path to follow, since it, with its large mass, could play a special role in the theory of electroweak symmetry breaking.

2.11.1 Z' boson

Various theories beyond the Standard Model predict different kinds of new Z' gauge bosons [31]. One of these models is called *topcolor assisted technicolor* [32, 33, 34]. This model predicts a Z' boson, which strongly and preferentially couples to the top quark. It is a model of dynamical electroweak symmetry breaking, where the Higgs boson is a composite state of a top and an antitop quark. This model aims to explain why the mass of the top is so large, as well as solve the fine tuning problem for the Higgs mass. This leptophobic Z' boson is usually denoted as Z'_{TC2} .

Other models, which introduce Z' bosons are focusing on explaining dark matter [35, 36, 37]. In these models, the Z' boson is the dark matter mediator, which couples the Standard Model particles to the dark matter particles. Such a Z' could be produced in the collision of quarks and could then either decay into dark matter particles, which we would not be able to directly detect or back into Standard Model particles, which we would be able to detect. The Z' boson is a so-called *resonance*.

Question 2.9: What is a resonance?

A *resonance* is an extremely short lived particle, that decays before it can move very far. A resonance is seen as a peak in the energy (or mass) distribution, since the cross section is larger at the mass of the particle. Actually the peak is seen as evidence for the presence of the resonance, which is just as real as other particles. The only difference is the lifetime.

The lifetime, τ , can be found easily by measuring the width of the resonance, Γ , and using the relation

$$\tau = \frac{\hbar}{\Gamma} \quad (2.11)$$

where \hbar is the reduced Planck constant.

Hence, the Z' boson would lead to a bump in an otherwise smooth invariant mass distribution, since the decay products of it will all have the same invariant mass, $m_{Z'}$, and that the production of the Z' increases at that invariant mass of the incoming colliding partons. We will come back to this in Chapter 6.

2.11.2 Contact Interaction

Looking back at the history, it is reasonable to think, that we will gain additional understanding of the fundamental structure of our Universe. It could be, that the particles, we

call fundamental today, are in fact composite. We have just not reached the necessary energy scale in order to resolve them yet.

An example of this is the Fermi theory of β decay. In order to explain β decay, Fermi proposed a four-point interaction, where the neutron is directly coupled to a proton, an electron and a neutrino, which later turned out to be an antineutrino. This is illustrated by the Feynman diagram in Figure 2.11a, where the four-point interaction is labeled CI for contact interaction. Of course now we know, that what happens is one of the down quarks in the neutron is converted to an up quark by emitting a W^- boson, which then decays into an electron and an antineutrino. However, Fermi's theory still works as a low-energy *effective field theory*.

Question 2.10: What is an effective field theory?

An *effective field theory (EFT)* is an approximation used at long distances (or low energy), where the energy is not high enough to resolve, what is happening at small distances. In this kind of theory an energy scale Λ is introduced. This scale tells us at which energy, we no longer can use the EFT, but what happens inside the circle, the contact interaction, will be resolved.

This kind of theory is useful if we want to look for compositeness of quarks [38, 39]. Even though we might not be able to resolve the constituents with energies below Λ , we could still be able to see an effect on the kinematic distributions of the interaction. An example of a $q\bar{q}$ contact interaction is seen in Figure 2.11b.

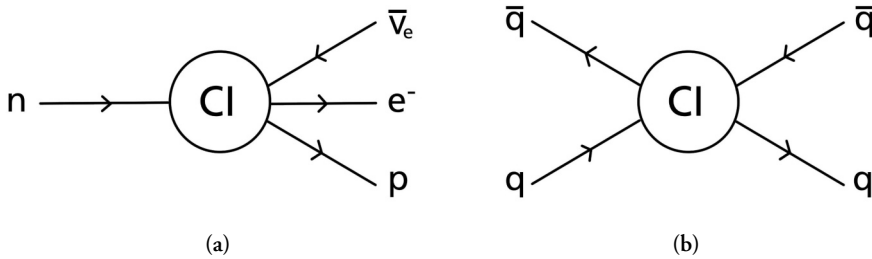


Figure 2.11: Feynman diagrams illustrating (a) the beta decay and (b) an unresolved interaction leading to $q\bar{q}$ production.

The contact interaction can be described by the Lagrangian

$$\mathcal{L}_{CI}(\Lambda) = \frac{g_s^2}{2\Lambda^2} [\eta_{LL} (\bar{q}_L \gamma^\mu q_L) (\bar{q}_L \gamma_\mu q_L) + \eta_{RR} (\bar{q}_R \gamma^\mu q_R) (\bar{q}_R \gamma_\mu q_R) + 2\eta_{RL} (\bar{q}_R \gamma^\mu q_R) (\bar{q}_L \gamma_\mu q_L)] \quad (2.12)$$

where the quark fields q_i have left and right chiral projections ($i = L,R$), g_s is the strong

coupling constant and $\eta_{ij} = 0, \pm 1$ represents the sign of the interference between the contact interaction and the Standard Model two-quark initial and final states. Here, a bit counter-intuitively, $\eta_{ij} = -1$ gives a constructive interference, whereas $\eta_{ij} = +1$ gives a destructive interference.

This kind of model is particularly interesting when searching for new phenomena at the LHC, since we have not seen any resonances (beyond the Standard Model) appear yet, which could mean that even higher energy is needed to resolve them. In Section 6.2, we will see how angular distributions can be useful to detect this kind of non-resonant signal.

2.11.3 Excited quarks

A natural consequence of the compositeness of quarks is the existence of excited quark states [40, 41]. Similarly to excitation of atoms, it would be possible to excite a quark, if it is composite, by transferring energy to it by the absorption of a gluon. The quark would then go back to its ground state by emitting a gluon as seen from the Feynman diagram in Figure 2.12. Like with atoms, only certain states would be allowed, which would result in a resonance at the invariant mass of the decay products.

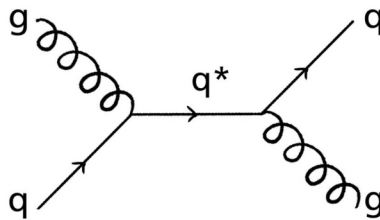


Figure 2.12: Feynman diagram illustrating the excited quark production and decay.

Large Hadron Collider

The world's most energetic accelerator is placed approximately 100 meters under the ground at the French-Swiss border outside Geneva, Switzerland. It is called the Large Hadron Collider (LHC) and it was constructed in order to investigate the smallest parts of our Universe [42, 43]. It is placed in the tunnel, that was used for the Large Electron-Positron (LEP) collider [44] giving it a circumference of 27 km.

The purpose of the LHC is to accelerate beams of protons (or heavy ions) to high energy and then collide them at four interaction points. At each of these interaction points one of the major experiments are placed. These are ATLAS [45], CMS [46], LHCb [47] and ALICE [48]. Whereas ATLAS and CMS are general-purpose detectors, LHCb is specializing in *b*-physics to study the matter-antimatter asymmetry and ALICE is build to study heavy ion collisions.

3.1 CERN accelerator complex

In order to get the protons to the extreme energies, which are obtained in the LHC, several acceleration steps are needed. The proton beam is produced by stripping the electrons from a hydrogen gas. The beam is firstly accelerated in the linear accelerator *Linac 2* (up to 50 MeV), which is however now being replace by *Linac 4* in order to eventually increase the *luminosity* of the LHC.

Question 3.1: What is luminosity?

In accelerator physics, the *luminosity*, \mathcal{L} , is a measure of the interaction probability in the colliding beams and is therefore the main variable determining the performance of the accelerator. It depends purely on the beam parameters and is given by [49]

$$\mathcal{L} = \frac{N_b^2 n_b f_{\text{rev}} \gamma_r}{4\pi \epsilon_n \beta^*} F \quad (3.1)$$

where N_b is the number of particles per bunch, n_b the number of bunches per beam, $f_{\text{rev}} = 11.25\text{kHz}$ the revolution frequency, γ_r the relativistic gamma factor, ϵ_n the normalized transverse beam emittance, β^* the beta function at the collision point and F the geometric luminosity reduction factor due to the crossing angle at the interaction point. Both ATLAS and CMS originally aimed for a peak luminosity of $10^{34}\text{cm}^{-2}\text{s}^{-1}$ as seen in Table 3.1, where also a number of the other observables are given.

If the luminosity is multiplied by the cross section, σ , of a given process, we get the rate, R , of that process.

From the linear accelerator, the protons enter the Proton Synchrotron Booster (up to 1.4 GeV), followed by the Proton Synchrotron (up to 25 GeV) and the Super Proton Synchrotron (up to 450 GeV), before it finally enters the LHC as seen in Figure 3.1, which shows the CERN accelerator complex.

The two beams in the LHC are accelerated in opposite directions, one going clockwise and the other going counterclockwise, in each their vacuum tube, that only intersect at the four collision points. The beams are not a continuous flow of protons, but consists of bunches with certain spacing between them, which is usually measured in nanoseconds.

3.2 Run 1 and Run 2 of the LHC

LHC produced the first high-energy particle collisions with a center-of-mass energy of $\sqrt{s} = 7\text{TeV}$, corresponding to 3.5 TeV per beam, in 2010. This was a world record, which was surpassed in 2012, where a beam energy of 4 TeV was achieved. The LHC was then shut down in the beginning of 2013, marking the end of *Run 1*, to allow for a 2-year long pause, *Long Shutdown 1*, where work on the accelerator was performed in order to achieve even higher beam energies.

The CERN accelerator complex *Complexe des accélérateurs du CERN*

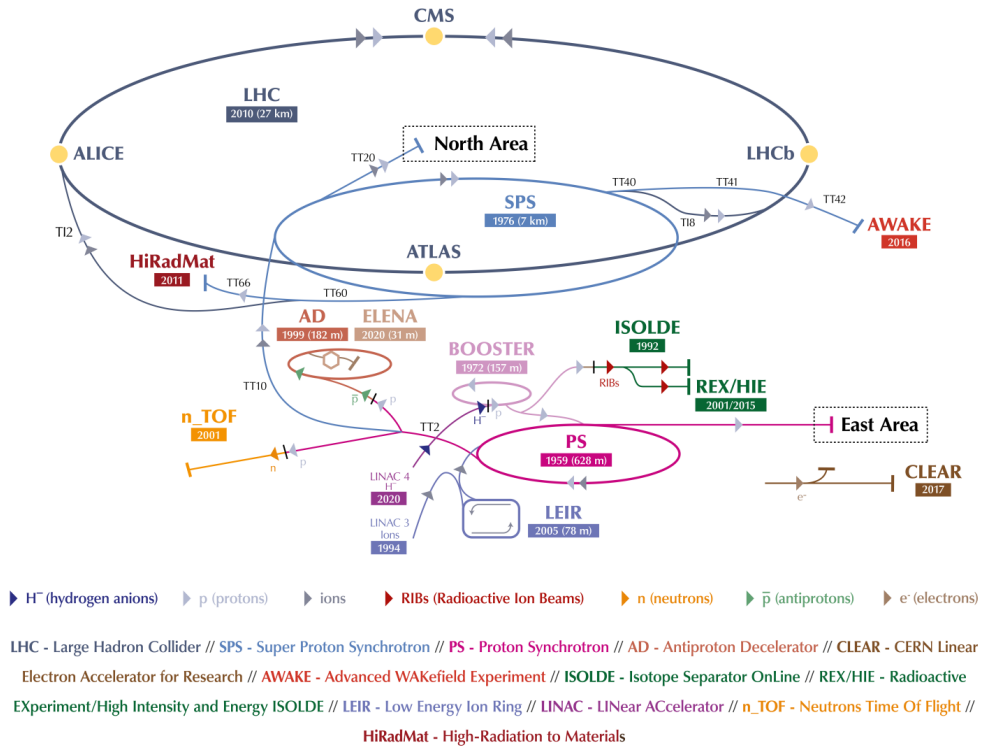


Figure 3.1: Sketch of the CERN accelerator complex [50].

In 2015, *Run 2* started with a beam energy of 6.5 TeV breaking the record once again. The goal of achieving a high luminosity could be achieved in several ways as seen in Equation 3.1. If the number of bunches per beam should be kept low as in Run 1, equivalent to a bunch spacing of 50 ns, this would need to be compensated by having more collisions per bunch crossing. However, this would also lead to a higher number of inelastic collisions per bunch crossing (called *pile-up* as explained below), which is undesirable. Therefore, the LHC experiments had a strong preference for having a bunch spacing of 25 ns instead of 50 ns to minimize pile-up. In order to tune the accelerator to the new bunch spacing of 25 ns, 2015 became a learning year, allowing to prepare the accelerator to provide the full luminosity for the rest of Run 2 (2016-2018). This can be seen in Figure 3.2, which shows the peak luminosity during Run 1 and Run 2.

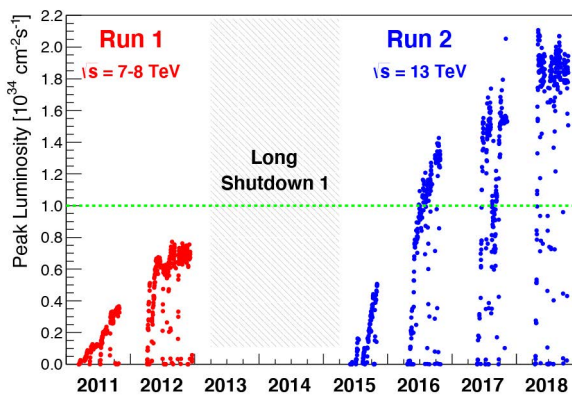


Figure 3.2: Peak luminosity as a function of time for the ATLAS and CMS experiments. The green dashed line shows the design luminosity [49].

3.3 Beam and accelerator parameters

Table 3.1 summarizes the main beam and accelerator parameters for the LHC for 2016-2018 in Run 2, compared to 2012 in Run 1 and the design values. It is seen that the beam energy is still a bit below the design value of 7 TeV. However, the hope is to achieve this during *Run 3*, which will start after the *Long Shutdown 2*, that is currently taking place from November 2018 to May 2021¹. From the minimum bunch spacing of 25 ns, the maximal number of bunches per beam is given, which is 2808. The transverse beam size is given from the function $\beta(z)$ and the emittance, ϵ , by [51]

$$\sigma(z) = \sqrt{\epsilon\beta(z)} \quad (3.2)$$

¹The starting date for Run 3 is subject to some uncertainty due to the COVID-19 pandemic.

Table 3.1: Beam and machine parameters for the LHC for different years compared to the design values [49].

Parameter	Design	2012	2016	2017	2018
Beam energy [TeV]	7	4	6.5	6.5	6.5
Bunch spacing [ns]	25	50	25	25	25
β^* CMS/ATLAS [cm]	55	60	40	40/30	30 – 25
Crossing angle [μ rad]	285	290	370/280	300 – 240	320 – 260
Bunch population [10^{11} ppb]	1.15	1.65	1.1	1.15	1.15
Normalized emittance [μ m]	3.75	2.5	2.2	2.2	2.0
Number of bunches per beam	2808	1374	2220	2556	2556
Peak luminosity [10^{34} cm $^{-2}$ s $^{-1}$]	1	0.75	1.4	2.05	2.01
Peak average event pile-up	~ 20	~ 35	~ 50	~ 55	~ 60
Peak stored energy [MJ]	360	145	270	320	340

where z is the distance along the nominal beam direction. The value of the beta function at an interaction point is called β^* and is usually the minimal value of the function to maximize the luminosity as seen in Equation 3.1. It is seen in Table 3.1 that a smaller value, than the design β^* was obtained in Run 2, which together with a normalized emittance, $\epsilon_n = \beta\gamma\epsilon$, which was also smaller than the design value, lead to a peak luminosity, which was twice as big as the design goal.

In order to avoid collisions outside of the collision points in the roughly 100 m long vacuum chambers, that is shared by both beams at each experimental site, a crossing angle is introduced. This however comes with a price of a reduced luminosity given by the factor F , which was approximately 0.6 in 2018.

The bunch population or intensity is given in units of 10^{11} protons per beam (ppb) and was in 2016 a bit smaller than in 2017 and 2018, where the design value was used. With so many protons squeezed so tight together, it is not surprising that more than one proton interact in each bunch crossing, leading to so-called *pile-up*.

Question 3.2: What is pile-up?

Pile-up refers to the additional proton-proton interactions, which happens on top of the interaction of interest. It can be divided in two categories: *in-time* pile-up and *out-of-time* pile-up.

In-time pile-up is when multiple simultaneous proton-proton interactions happen in the same bunch crossing and is usually given as the mean number of interactions per bunch crossing, μ , which is seen for the different years in Run 2 in Figure 3.3. Out-of-time pile-up is due to the interactions, that happen in the bunch crossings just before and after the one of interest. Some detector parts are more sensitive to out-of-time pile-up than others due to different response time constants, which exceeds the bunch spacing of 25 ns.

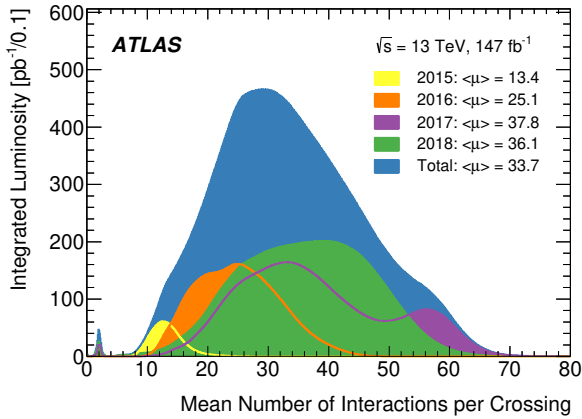


Figure 3.3: The integrated luminosity as a function of the mean number of interactions per bunch crossing, μ . The peak at low μ corresponds to dedicated data-taking periods useful for e.g. high precision W boson measurements [52].

It is therefore unavoidable to have pile-up, when a high luminosity is wanted and we want that, since it increase the chance of discovering new phenomena by increasing the number of events. If we have an interesting process with a cross section, σ , then the number of events is given by

$$N = \sigma \int \mathcal{L} dt \quad (3.3)$$

where the integral is denoted the integrated luminosity, which is a measure of the amount of data provided by the accelerator. The integrated luminosity as function of time is seen in Figure 3.4. If we know the integrated luminosity and the number of events, we can therefore estimate the cross section and compare it to theory. Here it is important to notice, that the number of events produced by the accelerator are not necessarily the number of events, we have left after performing an analysis, since the geometrical acceptance of the detector, A , and the efficiency, ϵ , are both less than unity.

3.4 LHC operation

A typical LHC *fill* goes as follows [53]

Injection \rightarrow Prepare Ramp \rightarrow Ramp \rightarrow Flattop \rightarrow Squeeze
 \rightarrow Adjust \rightarrow Stable Beams \rightarrow Beam Dump \rightarrow Ramp Down

The fill starts with protons being injected into the accelerator and ends, when the beam is dumped. Here *stable beams* is the mode of highest interest for the experiments. It is in

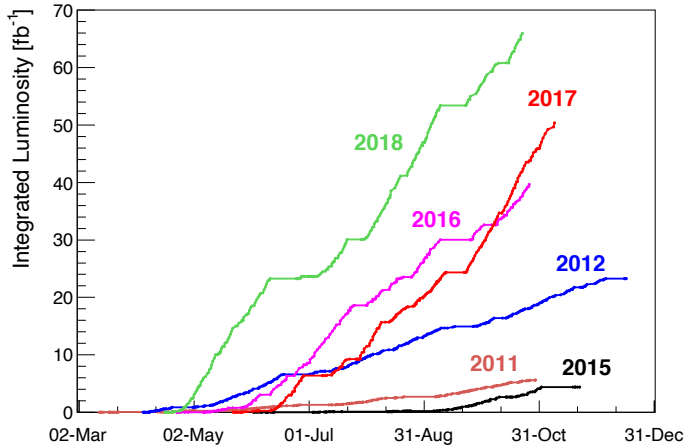


Figure 3.4: The integrated luminosity as a function of time for the different data-taking years [49].

this mode, the valuable collision data taking is happening. This mode can be sustained for several hours, but the luminosity will gradually decrease, mainly due to losses during collisions. It is however possible to slightly increase the luminosity by so-called *anti-leveling* by reducing the crossing angle and β^* value. This is an advantage, because it means that the data will be more similar during a fill (e.g. the pile-up conditions) and so it will be easier to analyze. The effect is seen in Figure 3.5, which shows the luminosity evolution of a typical fill during 2018 data taking.

Figure 3.5 also shows the drastically smaller luminosity at LHCb compared to ATLAS and CMS. As LHCb is optimized for precision physics with b quarks, they do not require the same high luminosity, but instead want pile-up to be low. The luminosity is adjusted by using a larger β^* at the interaction point of LHCb. This kind of *leveling* of the luminosity can also be done for ATLAS and CMS in case the luminosity is so high, that it is leading to pile-up conditions, that cannot be handled by the experiments.

It is clear, that the achievements of the LHC are very impressive, but they would not be of much use, if it was not for the four major experiments measuring the collisions in order to investigate the universe, we live in. In the next chapter, we will therefore describe one of these experiments, ATLAS, which was used to obtain the data used in this thesis.

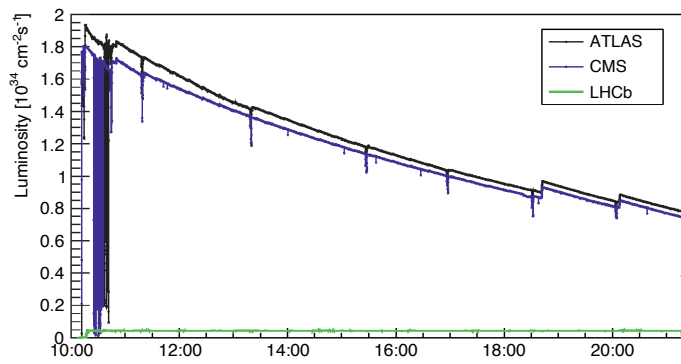


Figure 3.5: Example of the luminosity evolution as a function of time in a typical fill [49].

The ATLAS Experiment

The ATLAS (A Toroidal LHC ApparatuS) experiment [45] is the largest of the four LHC experiments with a diameter of 25 m, a length of 44 m and a weight of 7000 tonnes. It has a cylindrical shape, which is forward-backward symmetric, with the particles colliding in the center of the detector and it consists of several subdetectors, which have each their specific purpose. A sketch of the full detector with all its subdetectors is shown in Figure 4.1.

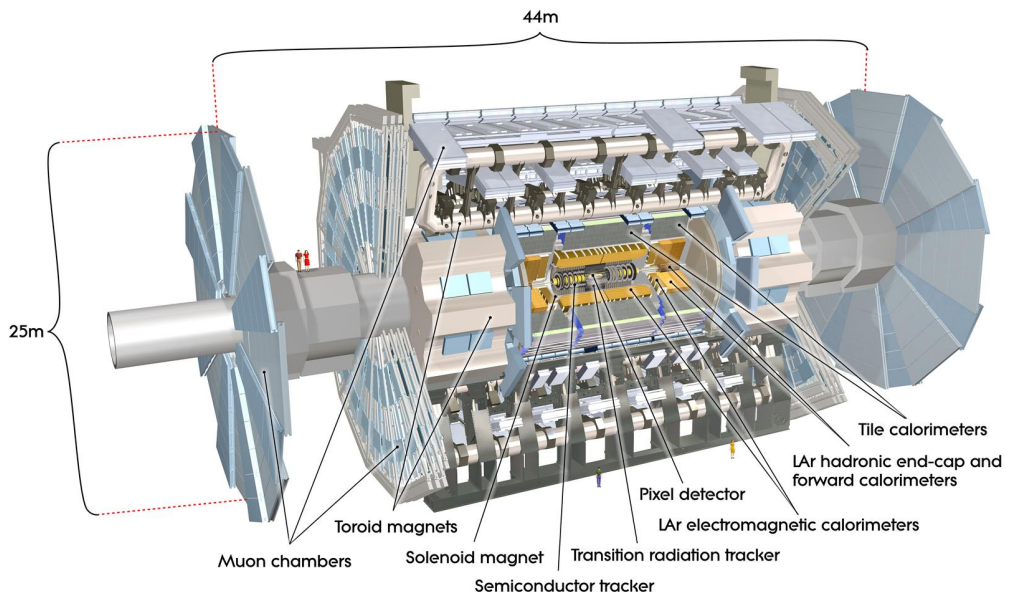


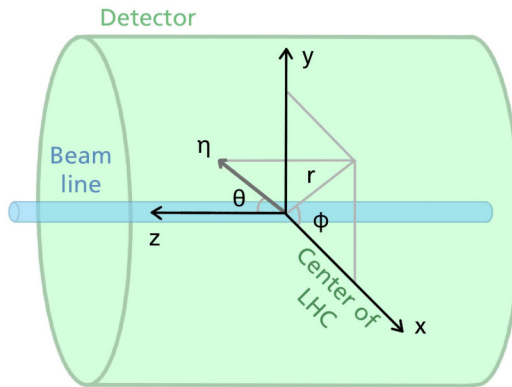
Figure 4.1: Sketch of the ATLAS detector [54].

4.1 Requirements

ATLAS is a general-purpose detector, which means it is build to investigate a wide range of different physics. From that follows, that it has to perform well on many different parameters. First of all, it has to have a large acceptance in pseudorapidity, η , with almost full azimuthal angle, ϕ , coverage, in order to detect as many of the outgoing particles as possible. This brings us to the ATLAS coordinate system.

Question 4.1: Which coordinate system does ATLAS use?

The ATLAS coordinate system is sketched below. It is right-handed and has its origin at the nominal interaction point in the center of the detector and the z-axis goes along the beam pipe. The x-axis points from the interaction point to the center of the LHC ring, whereas the y-axis points upwards. Cylindrical coordinates (r, ϕ) are used in the transverse plane, where ϕ is the azimuthal angle around the z-axis and r is the radius. The pseudorapidity, η , is defined in terms of the polar angle θ as $\eta = -\ln \tan(\theta/2)$. Finally, the angular distance can be measured in units of $\Delta R = \sqrt{(\Delta\eta)^2 + (\Delta\phi)^2}$.



Furthermore, a good charged-particle momentum resolution and reconstruction efficiency in the inner detector is important to provide efficient *vertex finding*. The inner detector should also be able to observe *secondary vertices* in order to identify e.g. *b*-jets. We will come back to the topic of vertices in Section 4.3.

In order to identify electrons and photons, a very good electromagnetic (EM) calorimeter is also needed. That has to be complemented by a hadronic calorimeter for precise jet and missing transverse energy, E_T^{miss} , measurements.

Question 4.2: What is missing transverse energy?

Missing transverse energy, E_T^{miss} , or MET is a measure of the energy, that is not detected, but is expected due to energy and momentum conservation. In a proton-proton collider the energy in a hard-scatter process is not known, since the partons inside the protons are sharing, and constantly exchanging, the energy. However, the transverse energy, the fraction of energy that is perpendicular to the beam axis, is expected to be approximately zero. It is therefore possible to identify any energy missing in the transverse direction.

A big missing transverse energy is implying the presence of a particle, that only interacts weakly, like neutrinos, but it could also be a sign of more exotic particles in theories beyond the Standard Model, e.g. Dark Matter candidates. It is however a difficult quantity to measure, since it relies on very precise energy reconstruction of all the detectable particles produced in the collision.

On top of this, because of the extreme environments created by the LHC, the detectors are required to have fast, radiation-hard electronics and sensors. Due to the many particles created in the collisions as well as additional pile-up contributions, a high granularity, especially in the inner detector, is crucial to distinguish the different particles.

The ability to detect and distinguish the different types of particles is helped by the *onion design* of the ATLAS detector. The different detector types are placed radially outwards from the interaction point, with the most fine-grained trackers closest to the middle and the more coarse-grained calorimeters further out. A cross-sectional view of the detector showing this is seen in Figure 4.2.

4.2 Particle identification

Figure 4.2 illustrates, how different kinds of particles interact in the various subdetectors, making it possible to do particle identification. Whereas only charged particles will leave a track in the inner detector parts, both photons and electrons will deposit their energy in the electromagnetic calorimeter. Heavier particles, like protons and neutrons, will on the other hand mostly deposit their energy in the hadronic calorimeter, whereas muons will not interact much with the calorimeter volumes and can therefore proceed all the way to the outermost part of the detector, the muon spectrometer. Neutrinos interact extremely weakly and will therefore travel across the detector undetected. Their presence can however be inferred through the missing transverse energy as explained in Question 4.2.

Being able to distinguish different particles from each other is of tremendous importance for the discovery potential of a general-purpose experiment as ATLAS, since it allows us

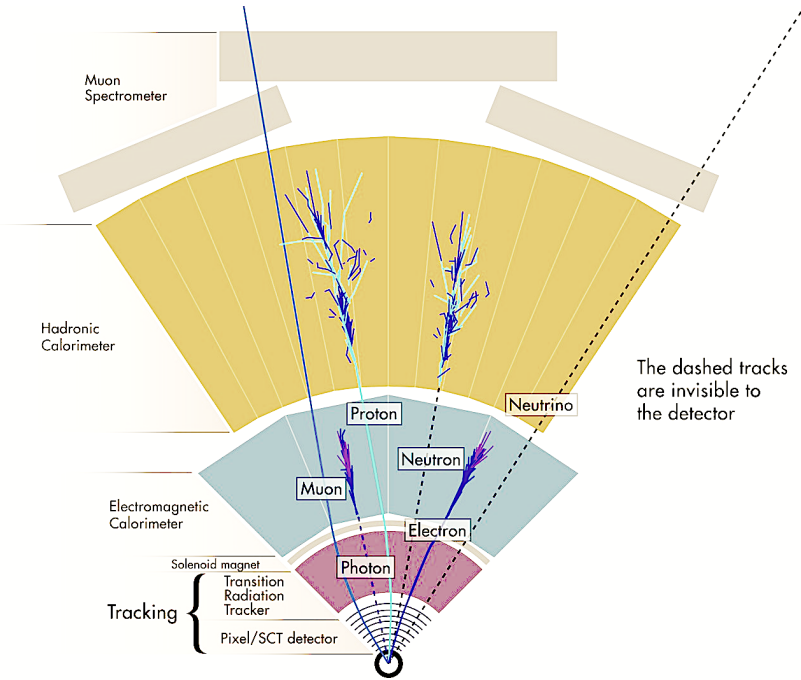


Figure 4.2: Sketch of the ATLAS subdetectors and their particle identification abilities (adapted from [55]).

to measure the cross section for different final states. It has therefore had a big impact in the design process of the detector. We will now go through the various subdetectors in a bit more detail with more emphasis on the parts, that are important for the measurements presented in this thesis. For a more thorough review of the detector see [45] and for the phase-II upgrade see [56].

4.3 The inner detector

The main purpose of the inner detector is to provide accurate tracking information of charged particles with transverse momentum $p_T > 0.5$ GeV in order to determine their charge, momentum and origin, which is also called a *vertex*.

Question 4.3: What is a vertex?

A *vertex* is the place, where two or more tracks intersect. The *primary vertex* is the reconstructed location of the proton-proton collision. As described earlier, several proton-proton interactions happen per bunch crossing (pile-up), which means a given event will have more than one primary vertex, however in ATLAS the vertex with the highest $\sum p_T^2$, where the sum is over the tracks associated to the vertex, is getting labeled as the primary vertex.

A *secondary vertex* can occur when a particle travels a measurable distance, before it decays. This is true for e.g. *b*-hadrons, which means the identification of secondary vertices is crucial for *b*-tagging (see Section 5.3.3).

The inner detector originally consisted of the pixel detector, the SemiConductor Tracker (SCT) and the Transition Radiation Tracker (TRT), but in the first long shutdown the Insertable B-Layer (IBL) was installed closest to the beam pipe [57]. A sketch of the different layers in the inner detector can be seen in Figure 4.3.

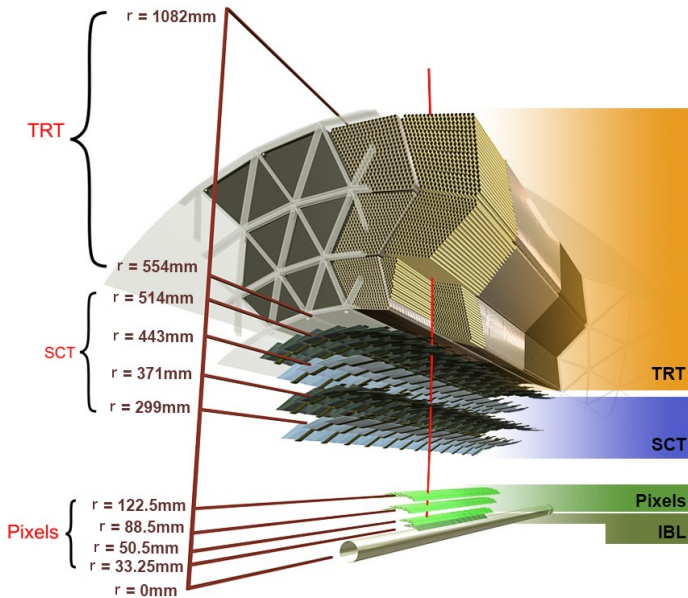


Figure 4.3: Sketch of the ATLAS inner detector [58].

The pixel detector and SCT are precision tracking detectors and have a coverage of $|\eta| < 2.5$. They both have silicon as the active material and were designed to be operated at a temperature of -7°C in order to minimize the impact of radiation damage by greatly reducing the leakage current. The pixel detector consists of approximately 80.4 million pixels, each corresponding to a readout channel, whereas the SCT consists of strips with

approximately 6.3 million readout channels. The pixels are placed on 3 concentric cylinders around the beam pipe in the *barrel region* and on 3 disks perpendicular to the beam in the *end-cap regions*, while the strips of the SCT are placed on 4 cylinders and 9 disks for each endcap. The intrinsic accuracy in $r\text{-}\phi$ is 10 μm for the pixel detector and 17 μm for the SCT.

The IBL was installed between Run 1 and Run 2 of the LHC together with a new beam pipe with a smaller radius. It consists of another 12 million pixels and is complementing the inner layer of the pixel detector by improving the vertex resolution and maintaining the performance at the high luminosity of Run 2 despite of the radiation damage.

The TRT has a lower resolution than the silicon detectors, with an intrinsic accuracy of 130 μm in $r\text{-}\phi$ and it only has a coverage of $|\eta| < 2.0$. However, approximately 36 hits are expected per track, which significantly improves the momentum measurement especially at high p_{T} , since the lower precision per point, σ , is compensated by the large number of points, N , and longer measured track length, L , as seen by the Glückstern formula for the momentum resolution [59, 60]

$$\frac{\sigma_{p_{\text{T}}}}{p_{\text{T}}} = \frac{p_{\text{T}}\sigma}{0.3L^2B} \sqrt{\frac{720}{N+4}} \quad (4.1)$$

where the magnetic field, B , is measured in Tesla, σ and L in meters and p_{T} in GeV.

The TRT consists of nearly 300.000 4 mm thin-walled drift tubes and the spaces between the tubes are filled with a radiator material, which create the transition radiation. It should also be mentioned that the TRT is substantially cheaper than the silicon detectors, so it is a desirable choice, when wanting to cover large volumes in order to get a longer lever arm for the track measurements.

With the described layout of the inner detector, the ATLAS experiment is able to reconstruct the tracks of approximately 1000 particles, that emerge within $|\eta| < 2.5$ from the collision point for every bunch crossing. The way the tracks are reconstructed will be described in Subsection 5.1.2.

4.4 The calorimeters

The primary goal of the calorimeters is to fully absorb and measure the energy of the particles created in the collision. This means, the calorimeter shower must be contained and the *punch-through* into the outermost subdetector, the muon spectrometer, should be minimal. The ATLAS calorimeter system consist of several parts as seen in Figure 4.4, but can roughly be divided in the electromagnetic (EM) and hadronic calorimeter. They are both *sampling calorimeters*.

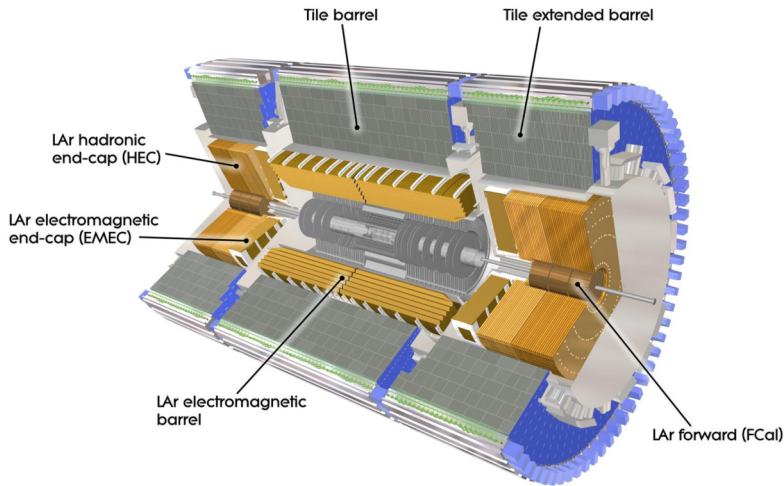


Figure 4.4: Sketch of the ATLAS calorimeters [61].

Question 4.4: What is a sampling calorimeter?

A *sampling calorimeter* consists of a dense *absorber*, that gives rise to a large energy loss and an *active medium*, which measures the energy through ionization or scintillation.

The absorber is usually a material with a high atomic number, Z , since the cross section of electromagnetic processes is proportional to Z^2 and the cross section of hadronic processes depend on the size of the nuclei. This means, that less high- Z material is needed, in order to absorb the particle energy, than low- Z material.

The active medium on the other hand is made of a material, where the energy deposits can easily be measured.

4.4.1 EM calorimeter

The electromagnetic calorimeter is finely-grained in the $|\eta|$ range of the inner detector in order to make precise measurements of electrons and photons and covers the $|\eta| < 3.2$ region. It is using lead ($Z = 82$) as the absorber material and liquid argon (LAr) as the active medium and is therefore often referred to as the LAr calorimeter. As the inner detector, it consists of a barrel (EMB, $|\eta| < 1.475$) and two end-cap regions (EMEC, $1.375 < |\eta| < 3.2$), which each contain two coaxial wheels. Since argon has a boiling point of 87 K, the barrel and the two end-caps are placed in each their cryostat.

The lead absorber plates are interleaved with readout electrodes and are accordion-shaped as seen in Figure 4.5. Each module has three layers, where the first consists of strip cells, which are finely-grained in η with a size of $\Delta\phi \times \Delta\eta = 0.098 \times 0.0031$, whereas the cells in the second and third layer have a size of $\Delta\phi \times \Delta\eta = 0.0245 \times 0.025$ and $\Delta\phi \times \Delta\eta = 0.0245 \times 0.05$, respectively. This architecture of the first layer is chosen to get precise measurements of the particle position in order to distinguish neutral mesons like π^0 from photons. The purpose of the second layer is to collect the main part of the electromagnetic shower, such that only the highest energy electrons reach the third layer, which can therefore be more coarsely segmented. The first and second layer are very valuable for identifying photon vertices, since photons are not leaving any tracks in the inner detector.

The depth of the different layers of the calorimeter in Figure 4.5 are not only given in mm, but also in terms of the *radiation length*, X_0 .

Question 4.5: What is the radiation length?

The *radiation length*, X_0 , of a material is the mean length to reduce the energy of an electron by a factor $1/e$, where $e \approx 2.71828$ is the base of the natural logarithm. The radiation length can be approximated by [62]

$$X_0 = \frac{716.4 \cdot A}{Z(Z+1) \ln \frac{287}{\sqrt{Z}}} \text{g} \cdot \text{cm}^{-2} \quad (4.2)$$

where A is the atomic weight in g/mol and Z is the atomic number.

The radiation length is often given in $\text{g} \cdot \text{cm}^{-2}$, but can be converted to cm by dividing with the density of the material.

The mean free path for pair-production by a high-energy photon, is related to the radiation length by $\lambda_\gamma = \frac{9}{7}X_0$. So through bremsstrahlung and pair-production, an electromagnetic shower will build up in the EM calorimeter and due to the depth of more than $22X_0$ it will be (almost always) fully contained.

Due to the energy loss of the electrons and photons in the material before the EM calorimeter, a presampler detector is used to make up for this. The presampler is placed right before the EM calorimeter in the $|\eta| < 1.8$ region and consist of a 1.1 cm (0.5 cm) active LAr layer in the barrel (end-cap) region.

4.4.2 Hadronic calorimeter

The hadronic calorimeter in ATLAS consists of three parts: the scintillator tile calorimeter, the LAr hadronic end-cap (HEC) and the LAr forward calorimeter (FCal).

pions decay into photon pairs, $\pi^0 \rightarrow \gamma\gamma$, resulting in an electromagnetic component of the hadronic shower.

The hadronic component of the shower includes undetectable or *invisible energy* from breaking of nuclear bonds (binding energy and short-range nuclear fragments, that are mostly absorbed before reaching the active medium), long-lived or stable particles that escape (neutrons, long-lived neutral kaons and neutrinos) and muons from pion and kaon decays, that almost do not interact in the calorimeters.

From this it is clear, that the response to electrons and hadrons is very different. Due to the invisible component of the hadronic shower, the ratio of the energy deposits of an electron-initiated shower and a hadron-initiated shower, where the electron and hadron has the same initial energy, will be bigger than one ($\frac{e}{h} > 1$). The ATLAS hadronic calorimeter are not able to *compensate* for this difference and are therefore called *non-compensating* calorimeters.

Question 4.7: What is a compensating calorimeter?

A *compensating calorimeter* is able to make up for the invisible energy in the hadronic shower and thereby get $\frac{e}{h} \simeq 1$. This is done by either reducing the response to the electromagnetic component (e.g. using a high- Z absorber material) or increasing the response to the hadronic component (e.g. using an active medium with a lot of hydrogen).

One of the challenges with non-compensating calorimeters is that the response will depend on the energy of the hadron (non-linearity). We will come back to how the non-compensating nature of the hadronic calorimeter is treated in Chapter 5.

The hadronic end-cap calorimeter (HEC) consists of two wheels in each end-cap, which are located right behind the EM end-caps and are sharing the same cryostats. It covers the region $1.5 < |\eta| < 3.2$. The absorber is made of copper ($Z = 29$) and the active medium is as in the EM calorimeter LAr.

The last calorimeter is the forward calorimeter (FCal), which covers $3.1 < |\eta| < 4.9$. It consists of three modules in each end-cap, where the first, which is made of copper, is optimized for electromagnetic showers, whereas the second and third, which are made of tungsten ($Z = 74$), are measuring mainly the energy of the hadronic interactions.

The absorption length throughout the detector is seen in Figure 4.6. The figure gives a good overview of the range, the different calorimeters cover and it is seen that they overlap, such that the *dead* material in any η direction is minimal.

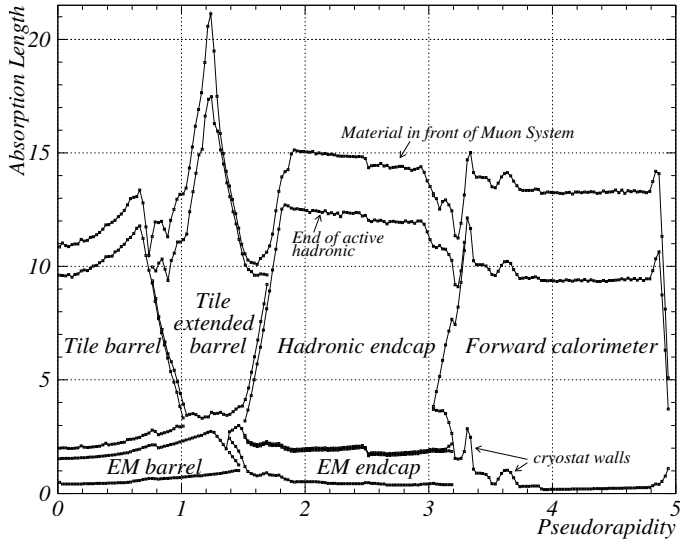


Figure 4.6: The absorption length, λ , as a function of pseudorapidity, η [45].

4.4.3 Energy measurements

In LAr calorimeters, when a particle initiates an electromagnetic shower in the absorber, it will lead to ionization of the liquid argon atoms in between the absorber plates. These ions will induce a current, that is collected by the readout electrodes. This gives a triangular pulse, that is then amplified and shaped by the front-end-board (FEB). The now bipolar shaped signal is *sampled* at 40 MHz (corresponding to the 25 ns bunch spacing used in Run 2). This is seen in Figure 4.7, which also shows that the bipolar shaped signal consist of a positive part, that is short and high, and a negative tail, that is long and shallow. The net integral over the signal is zero and since the number of samples used is only four, the signal and correspondingly energy can be negative. This is only the case for the LAr calorimeters, where the drift time leads to the long pulses of many bunch spaces as seen in the figure. In the Tile calorimeter a scintillating medium is used as the active material, which gives a much shorter pulse length. Therefore, a unipolar shaping can be used, which is never negative.

The bipolar signal shape helps to minimize the contribution from pile-up. Since out-of-time pile-up mostly will contribute with negative signals, whereas in-time pile-up will contribute with positive signals. However, the pile-up will vary from event to event and is therefore leading to an uncertainty in the measured energy, worsening the energy resolution.

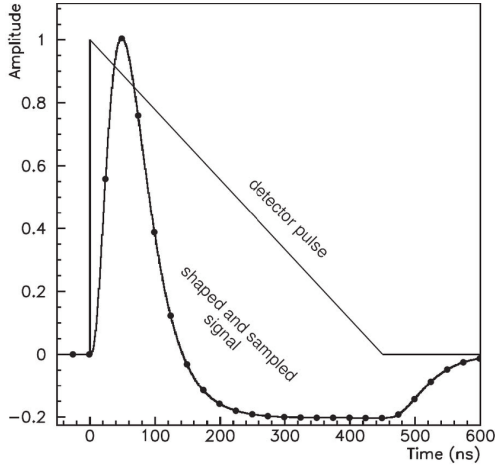


Figure 4.7: Example of amplitude as a function of time for the triangular detector pulse and the bipolar shaped signal from the front-end board in the EMB. The dots indicate samples of 25 ns spacing corresponding to the bunch spacing in LHC in Run 2 [63].

Question 4.8: What is the energy resolution of the ATLAS calorimeter?

The relative energy resolution improves as a function of energy, measured in GeV, and is given by

$$\frac{\sigma_E}{E} = \frac{a}{E} \oplus \frac{b}{\sqrt{E}} \oplus c \quad (4.3)$$

where the first term is the *noise term*, the second is the *sampling term* and the third is the *constant term*.

The noise term takes into account the effect of electronic noise as well as pile-up, whereas the sampling term is dependent on the material choice and thickness. The constant term, which dominates at high energy, depends on the detector geometry and design, like the number of radiation/absorption lengths and the amount of dead material. The energy resolution varies greatly for the different calorimeters as seen in the table below [64]. The noise term, which depends on pile-up is not included.

Calorimeter	Energy resolution $\frac{\sigma_E}{E}$
EMB	$\frac{10\%}{\sqrt{E}} \oplus 0.7\%$
EMEC	$\frac{10\%}{\sqrt{E}} \oplus 0.7\%$
HEC	$\frac{50\%}{\sqrt{E}} \oplus 3\%$
FCal	$\frac{100\%}{\sqrt{E}} \oplus 10\%$
Tile	$\frac{50\%}{\sqrt{E}} \oplus 3\%$

4.5 Muon spectrometer

The outermost layer of the detector is the muon spectrometer. It will almost exclusively measure muons, since it is the only charged particle, that can make it so far out in the detector. It covers the range $|\eta| < 2.7$ and has three layers of chambers in both the barrel and the end-caps. It uses four different technologies in order to detect the muons: thin gap chambers (TGC), resistive plate chambers (RPC), monitored drift tubes (MDT) and cathode strip chambers (CSC).

The main purpose of the TGC in the end-caps and the RPC in the barrel region is to deliver tracking information within a few tens of nanoseconds in order to be able to trigger on muon events. We will come back to the concept of triggering in Subsection 4.8.1.

The purpose of the MDT, which are used over the whole η range, and the CSC in the end-cap is to make precision-measurements of the track and thereby the muon momentum.

4.6 Forward detectors

A few more ATLAS subdetectors, which are not part of the main cylinder, but are placed in the forward direction along the beam pipe, should be mentioned as well. They are called LUCID, ALFA and ZDC.

The LUMinosity measurement using Cherenkov Integrating Detector (LUCID) is placed at ± 17 m from the interaction point. It is the main online relative-luminosity monitor for ATLAS and it measures the instantaneous luminosity by detecting the inelastic proton-proton scattering in the forward direction. It was upgraded before Run 2 to the LUCID-2 detector [65], which consists of several small Cherenkov detectors. It uses thin quartz windows as Cherenkov medium and small amounts of radioactive ^{207}Bi sources placed on to these windows to monitor the gain stability of the photomultipliers. This gives a fast and precise luminosity measurement, which can be kept stable during many months of data taking.

The Absolute Luminosity For ATLAS (ALFA) detector is located even further down the beam pipe, ± 240 m from the interaction point. It consists of four Roman pots with scintillating-fiber trackers, that can be moved as close to the beam as 1 mm. It is designed to measure the total proton-proton cross section as well as the luminosity. It does this by measuring the proton scattering at very small angles and using the optical theorem, which relates the total cross section to the forward elastic scattering amplitude. The operation of ALFA requires special run conditions [66] with high β^* and low emittance, which is also used for calibration of LUCID.

The last forward detector is the Zero Degree Calorimeter (ZDC), which consist of two sampling calorimeter modules, that are placed at ± 140 m from the interaction point. It uses tungsten as the absorber and quartz rods as the active medium. It is measuring neutral particles up to $|\eta| \leq 8.2$ and plays a key role in determining the centrality in heavy ion collisions. During low-luminosity proton-proton collisions it can also be used for triggering of minimum-bias events.

4.7 Magnets

A last but very important part of the ATLAS detector is the magnet system. Without a magnetic field it would not be possible to measure the momentum of the charged particles with the inner detector and the muon spectrometer. The ATLAS magnet system consist of four big superconducting magnets, a central solenoid, a barrel toroid and two end-cap toroids, as seen in Figure 4.8.

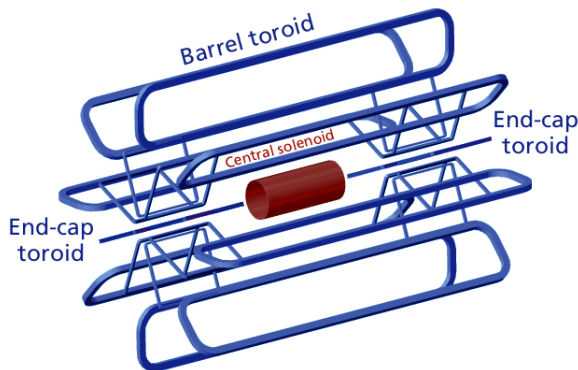


Figure 4.8: Sketch of the ATLAS magnet system. In red the central solenoid and in blue the barrel toroid and the two end-cap toroids.

The solenoid is placed right outside the TRT, but before the EM calorimeter. It is aligned with the beam axis and provides a 2 T axial magnetic field for the inner detector. The layout was optimized to keep the material thickness in front of the EM calorimeter minimal in order to minimize the energy deposited before the calorimeter. Therefore, the calorimeter and the solenoid windings also share a common vacuum vessel and thereby eliminating two vacuum walls.

The three toroid magnets are providing a magnetic field of approximately 0.5 T and 1 T for the muon detectors in the central and end-cap regions, respectively. They each consist of eight coils.

4.8 Data taking

Recording the information from the various subdetectors and transforming it into useful data requires several steps. As discussed in Chapter 3, the LHC has gone through two major data taking periods so far, Run 1 with a center-of-mass energy of $\sqrt{s} = 7$ and 8 TeV and Run 2 with $\sqrt{s} = 13$ TeV.

In ATLAS, the LHC runs are divided into data taking periods, which are denoted by letters (A,B,C,...). Each of these periods consist of a number of sub-periods, which again contain several runs, where the conditions are very similar. The runs should not be confused with the LHC runs, but are continuous periods of ATLAS data recording. They usually corresponds to a single LHC fill and the run number is unique, such that a given event always can be identified by its event and run number. Each run is divided in minute-long luminosity blocks for which the luminosity is known.

These luminosity blocks makes it possible to generate a list of good-quality data and a whole run does not need to be discarded, if a problem occurs in the detector for part of the run. In this manner, the *good run list (GRL)* specifies the luminosity blocks, that are suitable for data analysis. This can vary for different analyses and therefore several GRLs exist. This also means that the integrated luminosity, that is available for data analysis, is less than the integrated luminosity delivered by the LHC. In Run 2, LHC delivered 156 fb^{-1} of data of which 147 fb^{-1} was recorded by ATLAS and only 139 fb^{-1} was suitable for physics analysis as seen in Figure 4.9.

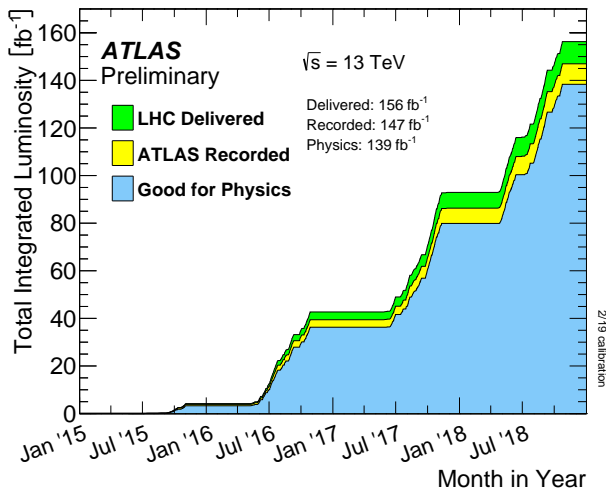


Figure 4.9: Total integrated luminosity in Run 2 [67].

4.8.1 Triggering

In the LHC, the proton bunches cross at a rate of 40 MHz. That is 40 million events per second! Luckily most of these collisions are not interesting and do not need to be saved. In order to make sure that the interesting events are saved, we use *triggers*.

Question 4.9: What is a trigger?

A *trigger* is a system, that quickly decides whether an event, should be saved or not, by checking whether a number of criteria are met. This can e.g. be a requirement on the minimum energy deposited in the calorimeter.

The event rate is brought down from 40 million per second to approximately 1000 per second, which are saved, using the trigger and data acquisition (TDAQ) system. The ATLAS trigger system [68] was upgraded between Run 1 and Run 2 to be able to handle the increased center-of-mass energy and pile-up. It consists of a hardware-based first-level trigger (L1) and a software-based high-level trigger (HLT). The central trigger processor (CTP) makes the L1 trigger decision based on inputs from several subsystems, like the L1 calorimeter triggers and the ZDC. If an event is accepted by the L1 trigger system, it is buffered in the read-out system (ROS) and processed by the HLT. The L1 trigger is reducing the event rate to approximately 80.000 events per second.

In the HLT, tracks are reconstructed in the inner detector and the muon spectrometer, whereas several physics objects are reconstructed in the calorimeter. This includes electron, photon, tau and jet candidates as well as missing transverse energy, E_T^{miss} . It is therefore possible to trigger on different physics objects making it possible to optimize the triggering for specific analyses.

The *trigger menu* outlines the list of L1 and HLT triggers. The composition and trigger thresholds are optimized for various luminosities such that the physics output is maximized within the limits of the bandwidth of detector and the TDAQ system. In order to achieve the optimal trigger menu within the rate constrains, *prescale factors* can be applied to the L1 and HLT triggers.

Question 4.10: What is a prescaled trigger?

A *prescaled* trigger is a trigger, which is only used a fraction of the time, such that e.g. only 50% of a certain kind of events are accepted. Prescales are use in order to not overload the system and can be changed during the data-taking e.g. when the luminosity gets below a certain threshold. A trigger, where no prescale is applied, is called an *unprescaled* trigger and are usually used for physics analyses.

Many triggers, like jet triggers, has a p_T threshold, such that only jets above this threshold is saved. However, due to resolution inefficiencies and differences between the trigger and offline level, this threshold is not leading to a abrupt turn-on of the trigger at this value, but a rather smooth transition, that can be described by an error function. This is called a *turn-on curve* and some examples for L1 single-jet triggers are seen in Figure 4.10. In analyses it is common to apply a cut on the offline p_T , where the *plateau* is reached, such that the turn-on region is not affecting the distributions.

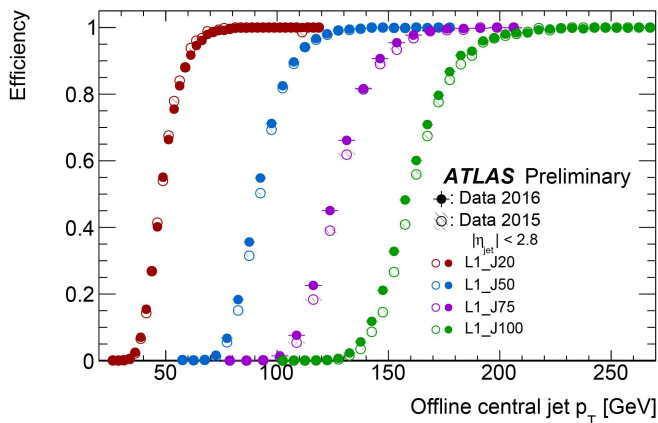


Figure 4.10: Examples of turn-on curves for single-jet triggers with different requirements on the jet E_T [69].

We have now covered, how the data is collected in ATLAS, but to be able to compare the collected data to the Monte Carlo simulations, a good detector simulation is needed as well.

4.9 Detector simulation

We have previously discussed, how the proton-proton collisions are simulated with Monte Carlo event generators (see Section 2.9), but the output from these will be on the *truth* level. In order to compare the simulations to our data, we need it to be on the *reconstructed* level, which takes into account any detector effects, like the coverage and acceptance of the detector, but also the energy losses in dead material and smearing of the particle direction. The effects are simulated with the GEANT4 detector simulation [70], where a full model of ATLAS is build, including the geometry and the different detector materials.

4.10 Data processing

Immense computing resources are needed in order to save, process and analysis the extensive amount of data collected by ATLAS. For that purpose, the Worldwide LHC Computing Grid (WLCG) is used. *The grid* links thousands of computers, which are located all over the world.

The computer centers are divided into different *tiers*, where Tier 0 is located at CERN and is responsible for storing and distributing the primary data files as well as the initial processing. The Tier 1 facilities also store each their part of the primary data files as well as process it to provide high-level data files, which are then further distributed to the Tier 2 centers. On these regional centers, the analysis scripts, which are submitted to the grid by the users, are mostly run. For further information on computing in ATLAS see [71].

Jets

A theorist, a phenomenologist and an experimentalist will all give you a different answer to the question: *What is a jet?* The theorist will tell you, that it originates from the outgoing partons in a Feynman diagram. We will call this a *parton jet*. The phenomenologist will be more concerned with what happens after the hard scatter and would tell you, that a jet is the spray of particles, that arise from the parton shower and hadronization processes. This we name a *particle jet*. The experimentalist on the other hand, will be focusing on what can be measured in the experiment. Namely, the tracks and energy deposits from which we can form a jet with an algorithm. We call this a *reconstructed jet*. These different types of jets are sketched in Figure 5.1.

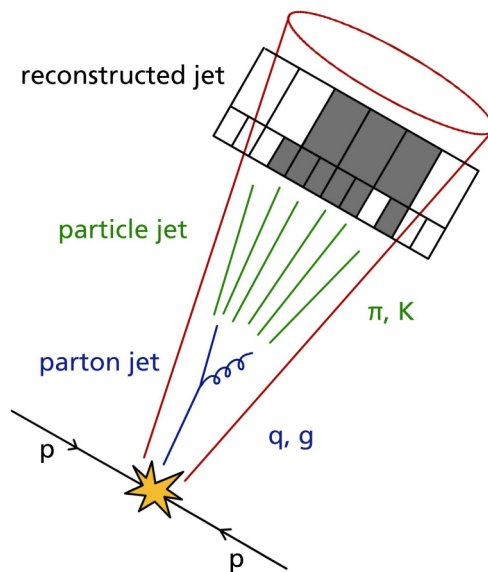


Figure 5.1: Sketch showing the different definitions of jets.

Any hard-scatter interaction, that have quarks or gluons in the final state, will result in jets as explained in Chapter 2. Since the analyses presented in this thesis are indeed looking for new phenomena, that have final states with quarks or gluons, it is of great importance to understand the jets. When we are searching for a new resonance, that goes into either a hadronically decaying top-quark pair, as in Chapter 8, or a b -quark pair, as in Section 9.2, jet substructure comes in handy, as we will see in Section 5.3.

5.1 Reconstruction

Reconstructed jets can be created from any four-vector objects. In ATLAS, both energy deposits in the calorimeter, tracks from charged particles in the inner detector and combinations of the two are used as input to the reconstruction algorithms. It should be mentioned, that at the truth level, using Monte Carlo samples, it is also possible to use the four-vectors of the individual particles directly instead of the reconstructed signal in the detector.

5.1.1 Topological clusters

The energy deposits in the calorimeters are clustered by taking advantage of the high granularity of the calorimeters. The cell signals are clustered based on the ratio of the measured energy, E_{cell} , to the average expected noise in the cell, $\sigma_{\text{noise,cell}}$, forming topological clusters, or *topo-clusters* [72].

First cells with $|E_{\text{cell}}| > 4\sigma_{\text{noise,cell}}$ are selected by the algorithm. Each of these seed cells forms a *proto-cluster*, which grows at the next stage of the algorithm. If the neighboring cell (in all three dimensions) has $|E_{\text{cell}}| > 2\sigma_{\text{noise,cell}}$, it is added to the proto-cluster and the neighbors of this cell is checked as well. This step continues until no more cells fulfill the requirement. If the neighboring cell is a seed cell the two proto-clusters are merged. As a last step all neighbors with $|E_{\text{cell}}| > 0\sigma_{\text{noise,cell}}$ are added as well. This is illustrated in Figure 5.2.

The result of this algorithm is a core of cells with highly significant signals surrounded by an envelope of less significant signal cells. The “420 scheme” as described above was derived from optimizations of the response and the relative energy resolution for charged pions in test-beam experiments using ATLAS calorimeter prototypes. The algorithm is implicitly noise suppressing, but large negative and positive signal fluctuations introduced by pile-up can still remain, such that there will be a pile-up dependence.

Recently, an *origin correction* is applied to the topo-clusters on an event-by-event basis to account for the position of the primary vertex [73]. Earlier, this correction was instead

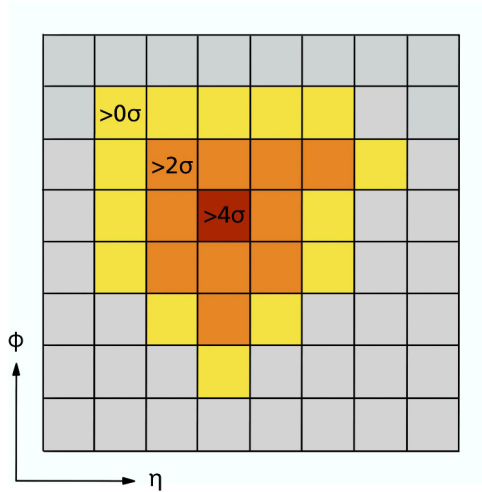


Figure 5.2: Illustration of the topo-cluster algorithm, where each square represents a cell and the red cell is the seed cell with $|E_{\text{cell}}| > 4\sigma_{\text{noise,cell}}$.

applied to the entire jet. Furthermore, only positive energy topo-clusters are used as input for jets.

5.1.2 Tracks from charged particles

Jets can also be reconstructed from the tracks left by charged particles in the inner detector. Reconstructing these tracks is a complicated matter. The primary-track reconstruction happens in the pixel and SCT detectors [74]. It starts by constructing clusters from the raw measurements in pixels and strips with common edges or corners, which are above a given threshold. Three-dimensional measurements called *space-points* are created from the clusters. In the pixel detector each cluster corresponds to one space-point, while in the SCT a cluster on both sides of a strip is needed to create a space-point.

Track seeds are created from sets of three space-points, which allows for a crude momentum estimate, while still having a very high efficiency. A number of requirements are placed on the track seeds to maximize the purity. Those include momentum and impact parameter cuts and the criteria, that an additional space-point is compatible with the particle's trajectory estimated from the seed. If the seed requirements are fulfilled, a combinatorial Kalman filter [75] is used to build track candidates. This results in a number of realistic combinations of space-points. To have a large tracking efficiency, some track candidates will have wrongly assigned space-points and sometimes share several space-points with other track candidates. Therefore, an ambiguity-solving stage is necessary.

The ambiguity solver is ranking the track candidates by calculating a *track score*. This score is based on simple track quality requirements. For instance, a cluster assigned to the track is increasing the score, whereas a missing cluster in a layer (a hole) reduces the score. The χ^2 of the track fit is also taken into account, as well as the logarithm of the track momentum. After calculating the score, the next step is to deal with clusters assigned to multiple track candidates. It is not unlikely, that a cluster can include energy deposits from several particles, since the distance between the charged particles can be very small in the core of highly energetic jets.

An artificial neural network is trained to identify such *merged clusters*. It uses information of the measured charge, which is proportional to the deposited energy and the relative position of pixels in the cluster, as well as the particle's predicted incident angle. The identification efficiency for merged clusters with two (three) participating particles is 90% (85%). Whereas only a few percent of *single particle clusters* are misidentified as originating from two particles. The number of misidentified clusters coming from three particles is negligible.

It is therefore not a problem for multiple track candidates to share a cluster as long as it is *identified as merged*. The clusters, which are not identified as merged, but are used in multiple track candidates, are called *shared clusters*. Such clusters are likely to be wrongly assigned to one of the track candidates. Therefore, clusters can only be shared by two tracks and a track can maximally have two shared clusters. As a consequence, a cluster can be removed from a track, if the requirements are not met and the track score is recalculated.

The ambiguity solver rejects track candidates, if they do not fulfill the following quality criteria:

- $p_T > 400 \text{ MeV}$
- $|\eta| < 2.5$
- ≥ 7 pixel and SCT clusters
- No more than either one shared pixel cluster or two shared SCT clusters on the same layer
- ≤ 2 holes in total in the pixel and SCT detectors
- ≤ 1 hole in the pixel detector
- $|d_0^{\text{BL}}| < 2.0 \text{ mm}$
- $|z_0^{\text{BL}} \sin \theta| < 3.0 \text{ mm}$

where d_0^{BL} is the transverse impact parameter calculated with respect to the measured beam-line (BL) position, z_0^{BL} is the longitudinal difference along the beam line between the point where d_0^{BL} is measured and the primary vertex and θ is the polar angle of the track.

The track candidates, that fulfill these requirements, are used as inputs for a high-resolution fit, which takes into account all available information. In these fits, the position and uncertainty of each cluster is determined by additional neural networks. Only after this step a track extension is done to include the hits in the TRT [76] and thereby finalize the *inside-out* track reconstruction.

Another *outside-in* track reconstruction is done on the hits, that have not already been assigned to a track. This sequence start by a global pattern recognition in the TRT, in order to find tracks that did not have sufficient, if any, hits in the silicon detectors. After constructing a track segment in the TRT, the track is followed backwards into the silicon detector. This allows for additional tracks to be created, which were missed by the inside-out sequence.

5.1.3 Combination of topo-cluster and track information

The topo-clusters and tracks, described above, can be used directly as an input for the jet algorithms, but it is also possible to combined the signals in so-called *particle flow* objects [77]. This approach has several advantages. First of all the momentum resolution of the inner detector is significantly better than the energy resolution of the calorimeter for low-energy charged particles, whereas the opposite is true at high energy. Including the track information is also improving the acceptance of soft particles, due to the low p_{T} requirement of $p_{\text{T}} > 400$ MeV. Such particles would typically not exceed the noise threshold required to seed a topo-cluster. Furthermore, the angular resolution of the inner detector is much better than that of the calorimeter. The great angular resolution also makes it possible to associate the track with a vertex and thereby reject signals originating from pile-up vertices. Another advantage is the ability to cluster low- p_{T} charged particles into the jet by using the track's azimuthal coordinate at the perigee, which would otherwise have been swept out of the jet cone by the magnetic field before reaching the calorimeter.

However, the gain comes with a complication. It is not possible to directly combine the topo-cluster and track information, since it would lead to a double-counting of the energy. Therefore, it is necessary to correctly identify the signal in the calorimeter left by a particle, whose track is going to be used, such that this can be subtracted. The ability to correctly remove all the energy left by a single particle, without removing any additional energy deposited by other particles, serve as the main performance criterion upon which the algorithm is optimized.

A number of additional requirements are placed on the tracks compared to those outlined in Section 5.1.2. This selection is referred to as the *tight selection* and include a criteria of at least nine hits in the silicon detectors and no holes in the pixel detector. In addition, it is required that $p_T > 500$ MeV, which significantly reduces the computing time without affecting the jet resolution, since such low- p_T tracks has a small contribution to the total jet p_T . An upper limit of $p_T < 40$ GeV is also implemented, since such energetic particles are often poorly isolated from nearby activity and thereby complicate the subtraction of the energy in the calorimeter. Consequently, there is no advantage of using the track information in such cases.

The particle flow algorithm provides a list of these well-measured tracks, a list of topo-clusters before subtraction and a list of topo-clusters after subtraction. The algorithm first tries to match each track to a single topo-cluster. Then the expected energy in the calorimeter, from the particle that also created the track, is calculated based on the topo-cluster position and the track momentum. Since it is relatively common for a single particle to deposit energy in multiple topo-clusters, the algorithm evaluates the probability that this is the case for each track/topo-cluster system. If it is the case, additional topo-clusters are added. Then the expected energy deposited in the calorimeter is subtracted cell by cell. If the remaining energy in the topo-cluster is consistent with fluctuations of a single particle's signal, the whole topo-cluster is removed.

Another approach to combined the calorimeter and inner detector information is the so-called *track-caloclusters (TCC)* [78]. Where the particle flow algorithm improves the jet reconstruction performance at low energy, the TCC approach is optimized to improve the performance at high energy, where the jets become so collimated, that the calorimeter has too low angular resolution to be able to resolve the structure inside the jet. Therefore, the 4-vector construction and energy sharing procedures are very different. The TCC algorithm uses the spatial coordinates of the tracking detector and the energy scale of the calorimeter, whereas the particle flow algorithm described above let the tracking information correct the full 4-vector.

There is a number of additional differences due to the different energy regimes, for which they are optimized, like the way the matching of tracks and topo-cluster is done. However, the main goal of both is to improve the understanding of hadronic showers in the detector.

Having gone through the different possible input objects, it is now time to discuss, how these are combined to give jets.

5.1.4 Jet algorithms

A variety of jet algorithms exists, but here we will focus on a class called *sequential recombination algorithms*. A given jet algorithm has to fulfill two major requirements; it has to be both infrared and collinear safe.

Question 5.1: What is infrared and collinear safety?

A jet algorithm is *infrared* safe, if the emission of a soft (low energy) gluon is not changing the outcome. In addition, it is *collinear* safe, if the splitting of a parton into two collinear partons is also not changing the outcome.

This is true for the sequential recombination algorithms [79]. These algorithms are based on the two distance parameters

$$d_{ij} = \min \left(p_{\Gamma i}^{2a}, p_{\Gamma j}^{2a} \right) \frac{\Delta R_{ij}^2}{R^2} \quad (5.1)$$

$$d_{iB} = p_{\Gamma i}^{2a} \quad (5.2)$$

where $p_{\Gamma i}$ and $p_{\Gamma j}$ are the transverse momenta of object i and j , respectively, whereas B indicates the beam. R is the distance parameter of the algorithm and $\Delta R_{ij}^2 = (\Delta\eta_{ij})^2 + (\Delta\phi_{ij})^2$ is the distance between object i and j . The value of the exponent $a \in \{-1, 0, 1\}$ is determining which algorithm we have at hand. The algorithms work as follows:

1. d_{ij} and d_{iB} are computed for all objects i and j and ordered by increasing value.
2. If the smallest value is a d_{ij} , the four-vectors of object i and j are combined into a proto-jet.
3. If the smallest value is a d_{iB} , object i is marked a jet and is not considered further¹.
4. The procedure is repeated until no more objects j fulfill $d_{ij} < d_{iB}$.

As mentioned above, the value of a is different for the different algorithms. We have that $a = 1$ for the k_{Γ} algorithm [80, 81], which means that p_{Γ} enters as a numerator, whereas $a = -1$ for the anti- k_{Γ} algorithm [82], which means it enters as a denominator. For the Cambridge-Aachen algorithm [83, 84] $a = 0$, so the p_{Γ} of the objects do not enter at all.

¹This is true for the *inclusive* algorithm, whereas for the *exclusive* algorithm the object is instead considered to be part of the *beam jet*. In this case the procedure is repeated until the smallest d_{ij} or d_{iB} is above some threshold d_{cut} .

This means that for the k_T algorithm, the lowest p_T object will be the starting point for the algorithm, whereas it will be the highest p_T object for the anti- k_T algorithm. For the Cambridge-Aachen algorithm only the distance between the objects matter.

It should also be made clear, that the distance parameter, R , determines how far from the jet axis, an object is considered for inclusion in the proto-jet. If $\Delta R_{ij}^2 > R$ then the ratio is larger than unity and it is more likely that $d_{ij} > d_{iB}$ and the object will be included.

Since the jet axis will move as new objects are added to the proto-jet, it is possible that the reach of the jet algorithm will be bigger than R . Especially the k_T algorithm can stretch over large areas, since it adds up the soft objects first, but the direction of the jet axis is dominated by the high p_T objects. The jet axis is therefore not moving as much around for the anti- k_T algorithm, which starts with the highest p_T object. The jet axis can also move somewhat around, when using the Cambridge-Aachen algorithm.

A comparison of the three algorithms can be seen in Figure 5.3. It is clear that the anti- k_T algorithm results in rather circular high p_T jets, which is expected since everything within R from the highest p_T object will be added to that proto-jet before the algorithm moves on to the next-highest p_T object.

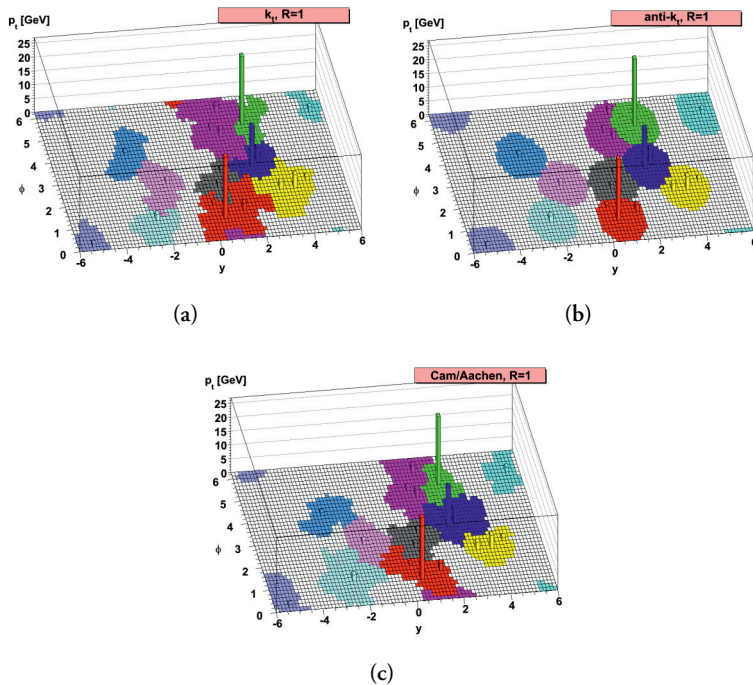


Figure 5.3: Example of how the jet algorithms work on a simulated event for the (a) k_T , (b) anti- k_T and (c) Cambridge-Aachen algorithms [82].

5.1.5 Jets in ATLAS

As we have seen, several different objects can be used as input for the jet algorithms. The combination of different input objects, distance parameters R and jet algorithms lead to a number of different *jet definitions*. Here we will only cover the ones, that are used in the analyses presented in this thesis.

Common for them all is, that the jet clustering framework FASTJET [85] is used to find the jets using the anti- k_T algorithm. The jets can be on two different energy scales: *electromagnetic* (EM) or *local hadronic cell weighting* (LCW).

Question 5.2: What is EM and LCW scale?

Jets in ATLAS are either on the *EM* or *LCW* scale. This depends on, whether the energy deposits in the cells are calibrated to match, what is expected from an electromagnetic (EM) shower or a hadronic shower. The EM scale is the default. An additional local hadronic cell weighting (LCW) calibration can be applied to bring the cell energy to the correct scale for charged pions produced at the interaction point.

This includes corrections for the non-compensating nature of the calorimeters. This means, the signal from hadrons will be smaller than the one from electrons and photons or in other words $\frac{\epsilon}{b} > 1$. The correction aims to get this ratio close to unity, which improves the linearity of the response and the resolution for jets consisting of a mixture of electromagnetic and hadronic signals.

It also corrects for the signal losses due to the noise threshold in the clustering algorithm, which depends on the pile-up conditions. The last correction is for the signal losses due to energy deposited outside the active calorimeter regions, in the so-called dead material.

The corrections depend on the probability $0 \leq \mathcal{P}_{\text{clus}}^{\text{EM}} \leq 1$ that a given topo-cluster is generated by an electromagnetic shower such that the weight is given by [72]

$$w_{\text{cell}}^{\text{cal}} = \mathcal{P}_{\text{clus}}^{\text{EM}} \cdot w_{\text{cell}}^{\text{em-cal}} + (1 - \mathcal{P}_{\text{clus}}^{\text{EM}}) \cdot w_{\text{cell}}^{\text{had-cal}} \quad (5.3)$$

where $w_{\text{cell}}^{\text{em-cal}}$ and $w_{\text{cell}}^{\text{had-cal}}$ are the factors applied to the cell signal by the electromagnetic and hadronic calibrations, respectively.

The value of the distance parameter R is depending on the kind of physics object, you want to capture. For normal QCD jets a value of $R = 0.4$ is used, whereas for jets with an expected substructure $R = 1.0$ is used. These are referred to as small- R and large- R jets, respectively. It is also possible to have a variable R value in the algorithm. This is the case for variable-radius jets [86], where the radius scales as $1/p_T$. In ATLAS, variable-radius

track jets [87] fulfill the requirement

$$R_{\text{eff}}(p_{\text{T}}) = \begin{cases} R_{\text{max}}, & \text{if } \rho/p_{\text{T}} > R_{\text{max}} \\ \rho/p_{\text{T}}, & \text{if } R_{\text{min}} < \rho/p_{\text{T}} < R_{\text{max}} \\ R_{\text{min}}, & \text{if } \rho/p_{\text{T}} < R_{\text{min}} \end{cases} \quad (5.4)$$

where $\rho = 30$ GeV, $R_{\text{max}} = 0.4$ and $R_{\text{min}} = 0.02$. The jets are required to have at least two constituent tracks, $p_{\text{T}} > 10$ GeV and $|\eta| < 2.5$.

In addition to the variable-radius track jets, we will in this thesis also use small- R topo-cluster jets on the EM scale, as well as large- R topo-cluster jets on the LCW scale. As mention earlier it is also possible to create jets from the stable particles in a Monte Carlo sample using the same jet algorithm. These *truth jets* can be useful, when wanting to e.g. calibrate jets, as we will see in the next section and in Chapter 7.

5.2 Calibration

Measurements of the energy scale and resolution of the jets are essential for both precision measurements of the Standard Model and searches for new physics beyond it. The jet energy scale (JES) calibration brings the jet energy to that of jets reconstructed at the particle level. These calibrations varies for different jet definition. We will first look at the calibration of small- R topo-cluster and particle flow jets on the EM scale.

5.2.1 Small- R jets

The calibration applied to EM topo-cluster jet and EM particle flow jets is quite similar. The entire chain of corrections is sketched in Figure 5.4. Each step is correcting the four-momentum by scaling the jet p_{T} , energy and mass [73].

The first step is pile-up corrections to remove the excess energy not coming from the primary interaction. First a correction based on the jet area, A , and median p_{T} density ρ of the event is applied. This correction is a subtraction of p_{T} and does not affect the jet η and ϕ .

Then a residual correction, which is derived from a Monte Carlo simulation and parametrized as a function of the mean number of interactions per bunch crossing, μ , and the number of reconstructed primary vertices in the event, N_{PV} . The residual p_{T} dependence on N_{PV} (α) and μ (β) are seen to be fairly linear and independent of one another, such that the fully corrected p_{T} can be described by

$$p_{\text{T}}^{\text{corr}} = p_{\text{T}}^{\text{reco}} - \rho \cdot A - \alpha \cdot (N_{\text{PV}} - 1) - \beta \cdot \mu \quad (5.5)$$

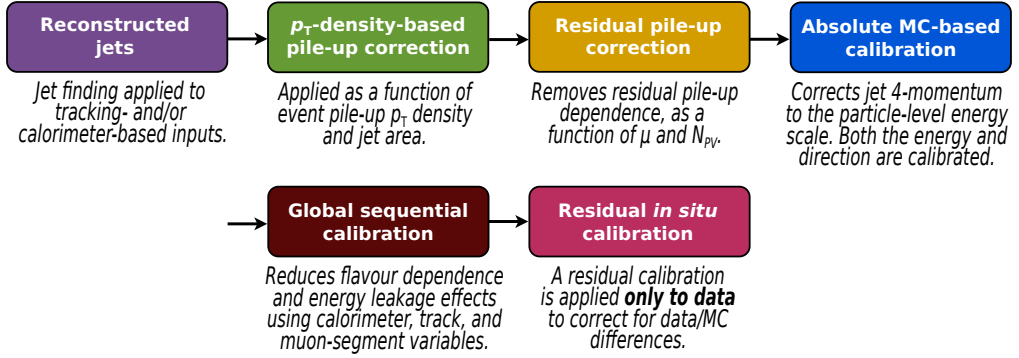


Figure 5.4: The different stages of the jet energy scale calibration for small- R jets [73].

where p_T^{reco} is the reconstructed jet p_T before any pile-up corrections.

The next step is the absolute jet energy scale and η calibrations, which aim to correct the reconstructed jet four-momentum to the particle-level energy scale. This is done by accounting for the non-compensating calorimeter response, out-of-cone effects, energy loss in dead material and biases in the jet η reconstruction, by matching reconstructed jets to truth jets with $\Delta R < 0.3$. This is a purely Monte Carlo based correction.

After this step, there is still a dependence on e.g. the flavor and energy distribution of the jet constituent particles for a given (p_T, η) bin. To account for this, the global sequential calibration (GSC) applies a series of multiplicative corrections to reduce the effect of these fluctuations and improve the jet resolution, σ_R , without changing the average jet energy response. The standard deviation of a Gaussian fit to the jet response distribution is giving σ_R . The GSC is based on global jet observables such as the longitudinal structure of the energy deposits within the calorimeters, the tracking information and information from the muon chambers behind the jet. Also here the reconstructed jets are geometrically matched to truth jets, making it a Monte Carlo based calibration.

The last step of the chain is to take into account the difference between data and Monte Carlo simulations in a so-called *in situ* calibration. The differences are a result of imperfect simulation of both the detector materials and response, as well as the physics processes involved, such as the hard scatter and underlying event, the jet formation, pile-up and the particle interactions with the detector. The calibration takes the ratio of the response in data to the response in Monte Carlo and apply it as an additional correction in data.

The response is calculated by balancing the p_T of a jet against the p_T of a well-calibrated reference object. This can either be a Z boson or photon or at high p_T a system of well-calibrated low p_T jets. The *in situ* calibration has three stages, where the first is the η

intercalibration, which corrects the energy scale of the forward jets ($0.8 \leq |\eta| < 4.5$) to match that of central jets ($|\eta| < 0.8$). This is obtained by using the p_T balance in dijet events. The second step is the balancing against well-calibrated Z bosons or photons. Only after this, high- p_T jets can be calibrated against the now well-calibrated low- p_T jets in the third step.

Finally, the measurements are combined using second-order polynomial splines to provide a single smooth calibration applicable across the full p_T range as seen in Figure 5.5. A χ^2 minimization is performed in each bin, such that the measurements with the smallest statistical and systematic uncertainties dominate the estimate of the response ratio in that bin. It is seen in Figure 5.5a, that Z +jet events dominates at low p_T and γ +jet events dominate at medium p_T , whereas only multijet events are available at high p_T . Figure 5.5b shows a comparison of the combination result for particle flow and EM topo-cluster jets. It is clear the uncertainty is significantly smaller for particle flow jets at low and medium p_T .

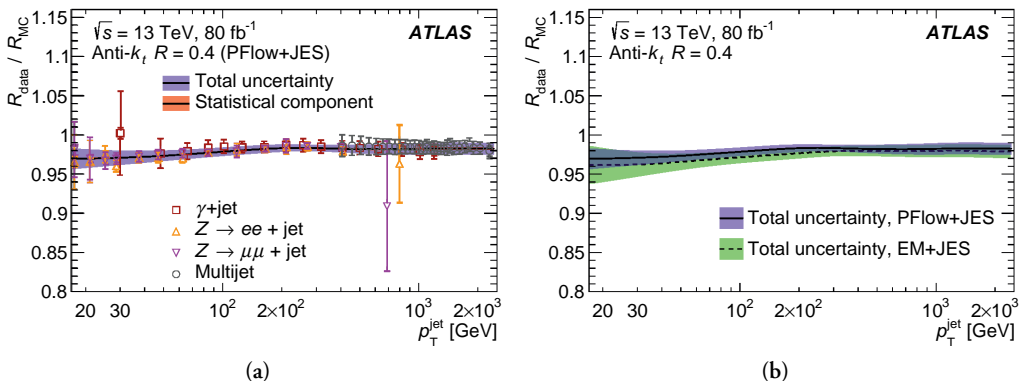


Figure 5.5: Combination of in situ measurements leading to a smooth correction factor (a) for particle flow jets and (b) comparison of particle flow and EM topo-cluster jets [73].

The jet energy scale calibration clearly comes with an uncertainty attached to it. This uncertainty varies as a function of jet p_T and η as seen in Figure 5.6 for particle flow and topo-cluster jets, respectively. It is seen, that the uncertainty is slightly bigger for the particle flow jets at low p_T , due to a bigger pile-up uncertainty, which is caused by the impact of the underlying event.

The kinks around $|\eta| = 2.5$ is caused by the difficulty in modeling the response in the region due to change of detector type. Whereas, the big rise in the uncertainty at high p_T is caused by a change in method, since the in situ measurements are running out of statistics at such high p_T . This new method will be discussed in Chapter 7.

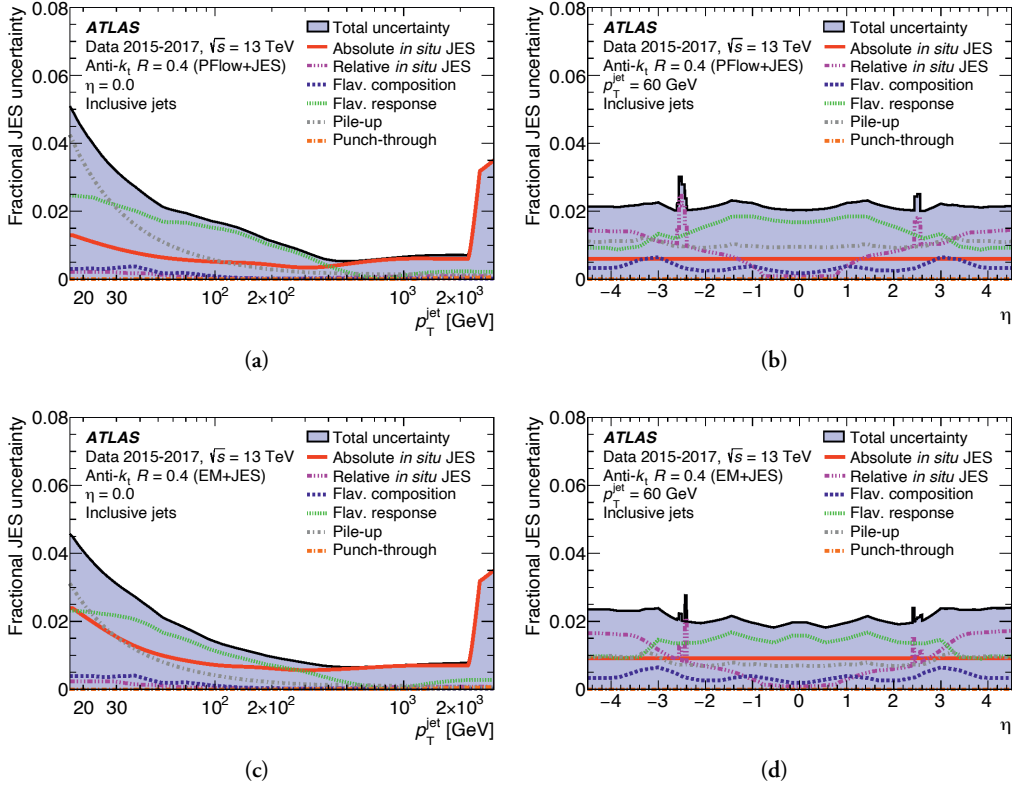


Figure 5.6: Fractional jet energy scale uncertainty for particle flow jets as a function of (a) jet p_T and (b) η and for EM topo-cluster jets as a function of (c) jet p_T and (d) η [73].

The jet energy resolution (JER), $\frac{\sigma_{p_T}}{p_T}$, is expected to be dependent on p_T in accordance with Equation 4.3 for the calorimeter resolution, so we have

$$\frac{\sigma_{p_T}}{p_T} = \frac{a}{p_T} \oplus \frac{b}{\sqrt{p_T}} \oplus c \quad (5.6)$$

where a is the noise term, b is the sampling term and c is the constant term as explained in Question 4.8.

The JER is measured using a *dijet balance method*, which relies on the scalar balance between the p_T of the two leading jets. The exact details of the method can be found in [73], which also describes how the contribution to the resolution from the noise term, a , due to pile-up and electronics, is found. The result is seen in Figure 5.7, which shows a comparison of the JER for particle flow and EM topo-cluster jets.

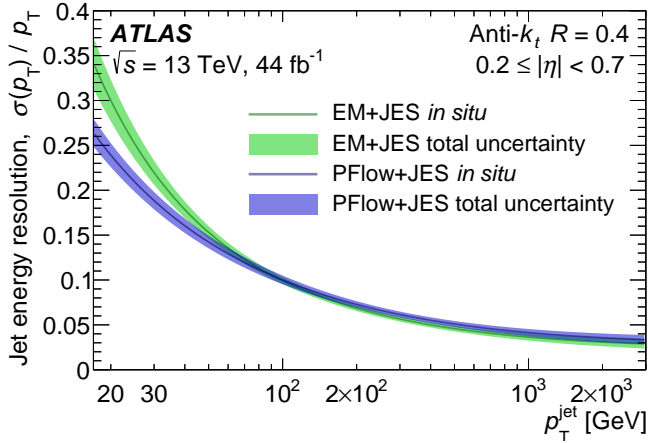


Figure 5.7: The jet energy resolution for small- R jets [73].

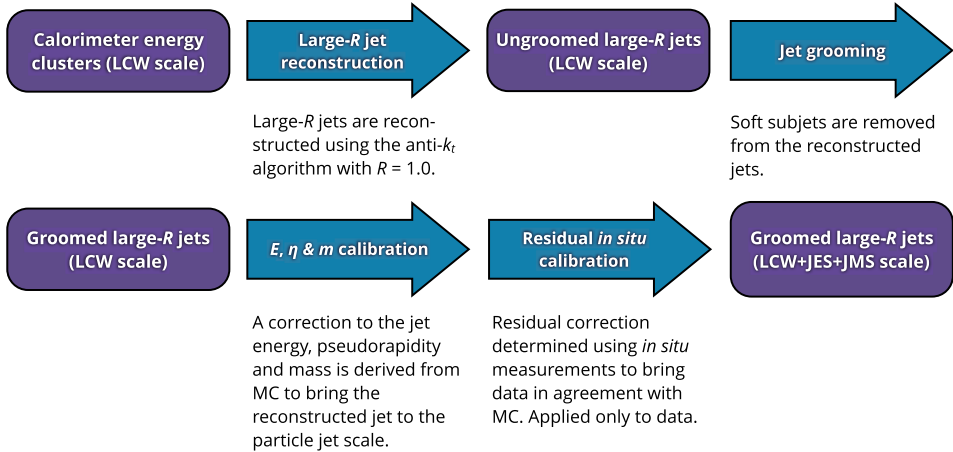


Figure 5.8: The different stages of the reconstruction and calibration of large- R jets [88].

5.2.2 Large- R jets

The calibration of large- R topo-cluster jets [88] is to a large extent equal to that of the small- R jets, so only the main differences will be discussed here. The full reconstruction and calibration chain is seen in Figure 5.8.

First of all the large- R jets are on the LCW scale, which means, as discussed earlier, that corrections have been applied to the topo-clusters to take into account the non-compensating nature of the calorimeter, as well as the signal loss due to the noise threshold of the clustering and energy deposited in the dead material. Therefore such corrections should not be applied again to the jet.

After the jets have been reconstructed using the anti- k_t algorithm with $R = 1.0$, they are groomed in order to reduce the impact from pile-up, soft emission and the underlying event. The grooming algorithm reclusters the jet constituents of each jet using the k_t algorithm and $R_{\text{sub}} = 0.2$, producing a number of subjets for each large- R jet. The subjets with $p_{\text{T}}^i/p_{\text{T}}^{\text{jet}} < f_{\text{cut}} = 0.05$ are removed and the large- R jet four-momentum is recalculated. This improves the energy and mass resolution as well as the ability to see the substructure of the jet, as we will see in Section 5.3.1.

As for the small- R jets, the reconstructed jets are matched to truth jets, which are created with the same algorithm and groomed as the reconstructed jets. Corrections are applied to the reconstructed jets to bring them to the particle-level energy scale and η . This corresponds to the absolute MC-based calibration for the small- R jets, but for the large- R jets an additional correction is applied to the jet invariant mass. This is important for analyses using the jet mass, since the mass is more sensitive than the p_{T} to e.g. soft, wide-angle contributions and to cluster merging and splitting.

Similar to the small- R jet calibration, the last step is an in situ calibration, where the first step is the η intercalibration, followed by a correction to the p_{T} response from the balancing of jets with well-calibrated objects. For large- R jets an in situ measurement of the mass response is also performed. It consists of two different methods: the R_{trk} method and forward folding.

The R_{trk} method is taking advantage of the fact, that the ATLAS detector provides two independent measurements of the properties of the same jet from the calorimeter and the inner detector. Where the jets formed from tracks only take into account the hits from their charge-particle constituents, the calibrated topo-cluster jets measure the properties from the full shower. The double ratio of $R_{\text{trk}} = \langle p_{\text{T}}^{\text{calo}}/p_{\text{T}}^{\text{track}} \rangle$ in simulation and data should be equal to unity for well-modeled observables, so any deviation is taken as a scale uncertainty in the measurement.

Forward folding is using a high-purity signal sample of large- R jets with high- p_{T} , hadronically decaying W bosons and top quarks. It is measuring the response for jets in signal-like topologies, which contain jets consisting of multiple regions of high energy density. It determines the jet mass response by fitting the W boson and top-quark mass peaks in the large- R jet invariant mass distribution of the hadronically decaying top-quark candidate. This is used to give the relative energy and mass scales and resolutions between data and simulation.

Also here the in situ measurements needs to be combined, which is done with first- or second-order spline as seen in Figure 5.9 for the large- R jet p_{T} and mass response, respectively. Also the jet energy scale uncertainty has been derived for the large- R jets as function of p_{T} as seen in Figure 5.10.

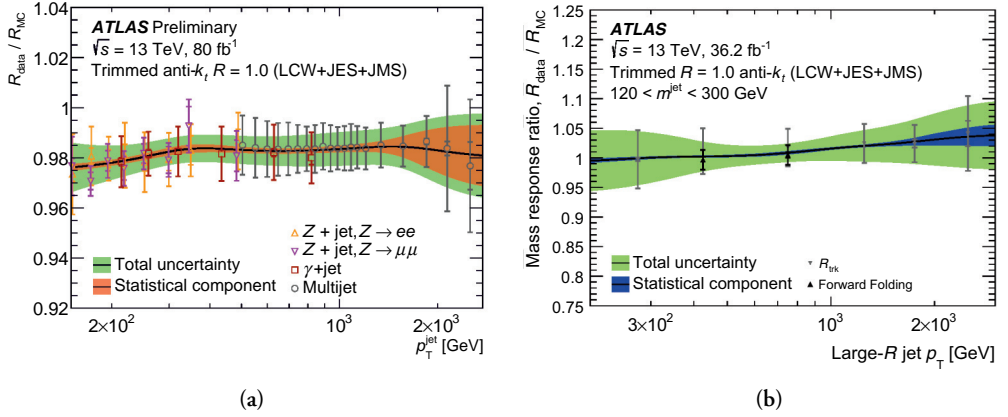


Figure 5.9: Combination of in situ measurements leading to a smooth correction factor for large- R jet (a) p_T [89] and (b) mass response [88].

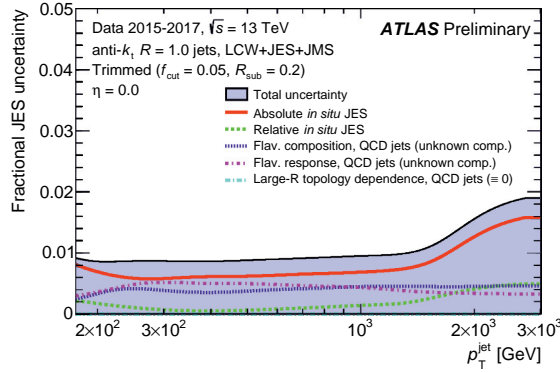


Figure 5.10: The large- R fractional JES uncertainty as a function of p_T [89].

The now well-calibrated large- R jets are very important objects, when searching for final states including W bosons and top quarks, since we can exploit the *substructure* of such jets, which is the topic of the next section.

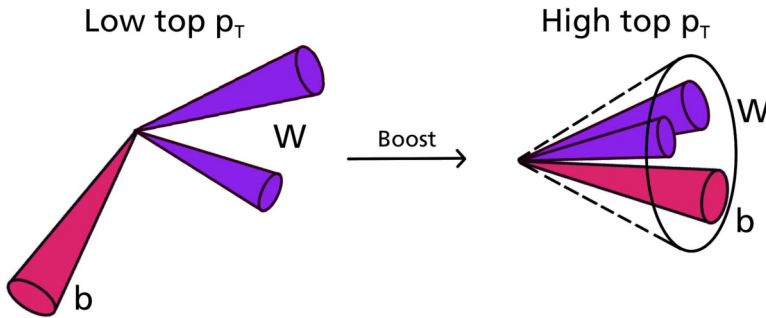
5.3 Jet substructure and tagging

Jet substructure is generally useful for disentangling jets originating from different particles. It is used for separating quark and gluon-initiated jets and isolating boosted W , Z and Higgs boson jets as well as boosted top-quark jets [90]. The focus here will be on jets originating from top quarks, since these are the main interest of this thesis, but similar substructure

variables are used for e.g. W boson tagging. But before we immerse into the specifics of the substructure variables and tagging algorithms used in ATLAS, we will start by introducing the main terms.

Question 5.3: What is jet substructure?

The aim of *jet substructure* is to study the internal kinematic properties of high- p_T jets to determine, whether it has certain structures, that are consistent with originating from a specific particle. When for example a top quark decays hadronically ($t \rightarrow W^+ b \rightarrow q\bar{q}' b$) it will result in three small- R jets, however if the top quark is *boosted* (has high p_T) these three jets will merge together into one large- R jet, which has three prongs as seen in the sketch below. The ability to extract this substructure information of the jet is the key to distinguish e.g. top-quark jets from light-quark jets.



Question 5.4: What is jet tagging?

With jet tagging we are able to say, with a certain probability, that a jet originates from a specific particle. Therefore, when a jet is e.g. *top tagged* it is not necessarily coming from a top quark, since it could be *mistagged*. This also means, that not all jets, that do originate from a top quark, will be tagged as such.

Jet tagging can be divided in several groups: q/g tagging (light quarks and gluons), flavor tagging (tau and b quark) and heavy resonance tagging (W , Z , Higgs and top quark). For the first two usually jets with small R are used, whereas for the latter jets with larger R are preferred.

To be able to evaluate the performance of a jet tagger, it is necessary to know the true origin of a jet, which is done by *labeling* it. This can only be done with Monte Carlo simulation. For signal jets, like top jets, this labeling is based on the partonic decay products of the top in a three-step procedure [91].

First, reconstructed jets j_{reco} are matched to truth jets j_{true} with a criterion of $\Delta R(j_{\text{reco}}, j_{\text{true}}) < 0.75$. Then the truth jets are matched to top quarks, t , again with a criterion of $\Delta R(j_{\text{true}}, t) < 0.75$. Finally, the partonic decay products of the parent top quark (two quarks from the hadronically decaying W boson and an additional b quark) are matched to the reconstructed jet. The reconstructed jet is labeled as a top-quark jet, if the top and all its direct decay products are contained within a region in (η, ϕ) with $\Delta R < 0.75 \cdot R_{\text{jet}}$, where R_{jet} is the jet distance parameter. The value of $0.75 \cdot R_{\text{jet}}$ was chosen as a compromise between the resulting labeling efficiency and the resolution of the top-quark jet mass peak.

Whether all the decay products are contained is seen to depend heavily on the p_{T} of the top quark as expected. Even at a $p_{\text{T}} = 1000$ GeV the top-quark jet labeling efficiency is less than 90% as seen in Figure 5.11.

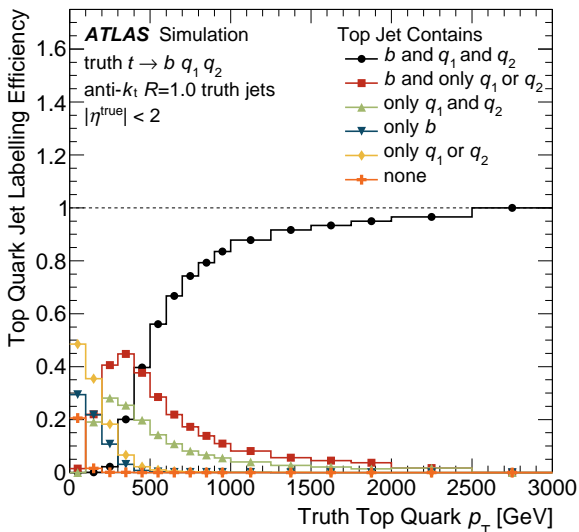


Figure 5.11: Top quark jet labeling efficiency as a function of the truth top quark p_{T} [91].

In order to recognize whether a given jet is likely to originate from a top quark, a number of substructure variables are useful. These can be combined in simple cut-based taggers or used as inputs to more complex machine learning algorithms. We will start by describing the variables and afterwards cover the top taggers making use of them. Finally, the b tagging algorithm used in this thesis is outlined.

5.3.1 Substructure variables

As mentioned above, many different substructure variables exist, which are useful when wanting to uncover jets originating from top quarks. The variables are, in ATLAS, cal-

culated from large- R jets, which are groomed, as it was explained in the previous section. The grooming algorithm, called *trimming*, is of particular importance, when it comes to jet substructure, since the substructure variables are calculated from the remaining set of constituents. The constituents can be either topo-clusters, tracks or truth particles. As an example, it can be easier to see the three-prong structure of the top quark jet after trimming is applied as seen on the sketch in Figure 5.12.

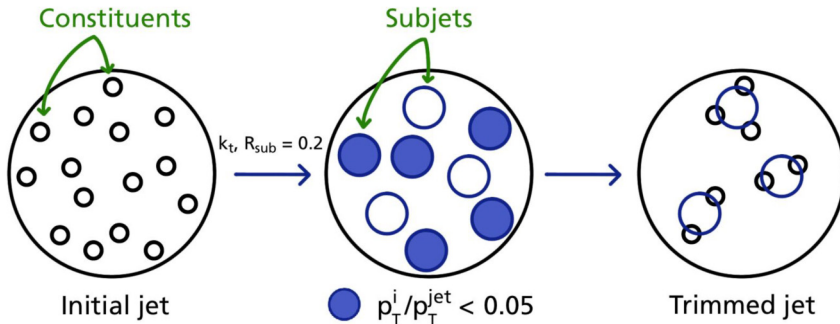


Figure 5.12: The different steps of the default grooming procedure in ATLAS called trimming.

The first group of variables is the kinematics of the calibrated large- R jet. This include the jet p_T and not surprisingly the jet mass. The mass can be calculated either from the calorimeter information, m^{calo} , assisted by the tracks in the inner detector, m^{TA} or a combination of the two, m^{comb} [92].

The calorimeter-based jet mass is given by

$$m^{\text{calo}} = \sqrt{\left(\sum_{i \in J} E_i\right)^2 - \left(\sum_{i \in J} \vec{p}_i\right)^2} \quad (5.7)$$

where J is the jet with topo-cluster constituents i , which have energy E_i and momentum \vec{p}_i , where $|\vec{p}_i| = E_i$. The track-assisted mass, on the other hand, is given by

$$m^{\text{TA}} = \frac{p_T^{\text{calo}}}{p_T^{\text{track}}} \times m^{\text{track}} \quad (5.8)$$

where p_T^{calo} is the transverse momentum of a large- R calorimeter jet, p_T^{track} is the transverse momentum of the four-vector sum of tracks associated to the large- R calorimeter jet, and m^{track} is the invariant mass of this four-vector sum (the track mass is set to m_π). The ratio of p_T^{calo} to p_T^{track} corrects for charged-to-neutral fluctuations, which gives m^{TA} a better resolution, than what is provided by the track-only mass, m^{track} .

The combined mass, m^{comb} , is calculated as a weighted average of m^{calo} and m^{TA} , where the weights are given by the inverse of the mass resolutions. This leads to a good resolution over the whole range, since m^{calo} has a great resolution at low p_T and m^{TA} is performing better at high p_T as seen in Figure 5.13.

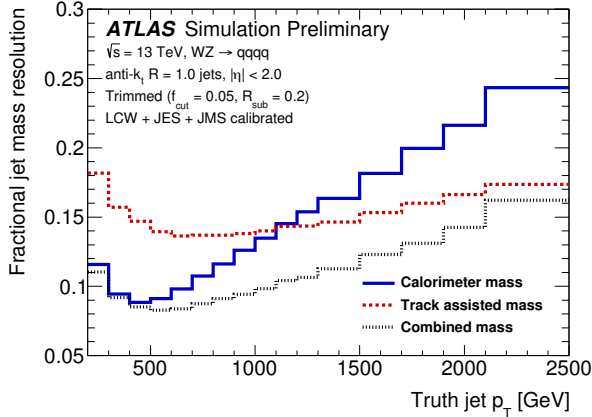


Figure 5.13: The fractional jet mass resolution as a function of the truth jet p_T for the different mass variables [93].

The second group of variables is the energy correlation ratios. A number of generalized energy correlation functions are introduced [94, 95] in order to identify N -prong jet substructure without requiring a subjet finding procedure. These variables only use information about the energies and pair-wise angles of the jet constituents, i , within the jets, J , and are given by

$$E_{\text{CF1}} = \sum_{i \in J} p_{Ti}, \quad (5.9)$$

$$E_{\text{CF2}}(\beta) = \sum_{i < j \in J} p_{Ti} p_{Tj} (R_{ij})^\beta, \quad (5.10)$$

$$E_{\text{CF3}}(\beta) = \sum_{i < j < k \in J} p_{Ti} p_{Tj} p_{Tk} (R_{ij} R_{ik} R_{jk})^\beta, \quad (5.11)$$

where β is used to give weight to the angular separation of the jet constituents and R_{ij} is the distance between constituent i and j . We can now define the ratios

$$e_2^{(\beta)} = \frac{E_{\text{CF2}}(\beta)}{E_{\text{CF1}}^2}, \quad (5.12)$$

$$e_3^{(\beta)} = \frac{E_{\text{CF3}}(\beta)}{E_{\text{CF1}}^3}, \quad (5.13)$$

which can further be used to form the variables

$$C_2^{(\beta)} = \frac{e_3^{(\beta)}}{(e_2^{(\beta)})^2}, \quad (5.14)$$

$$D_2^{(\beta)} = \frac{e_3^{(\beta)}}{(e_2^{(\beta)})^3}, \quad (5.15)$$

which have been shown to be particularly useful in identifying two-body structures within jets. However, both $e_3^{(\beta=1)}$, $C_2^{(\beta=1)}$ and $D_2^{(\beta=1)}$ are seen to have some discriminating power for both W boson and top tagging [91]. Figure 5.14 shows the $(e_2^{(\beta)}, e_3^{(\beta)})$ phase space, which is divided into 1- and 2-prong regions, with the boundary between them corresponding to $e_3^{(\beta)} = (e_2^{(\beta)})^3$. It also shows contours of constant $C_2^{(\beta)}$ and $D_2^{(\beta)}$.

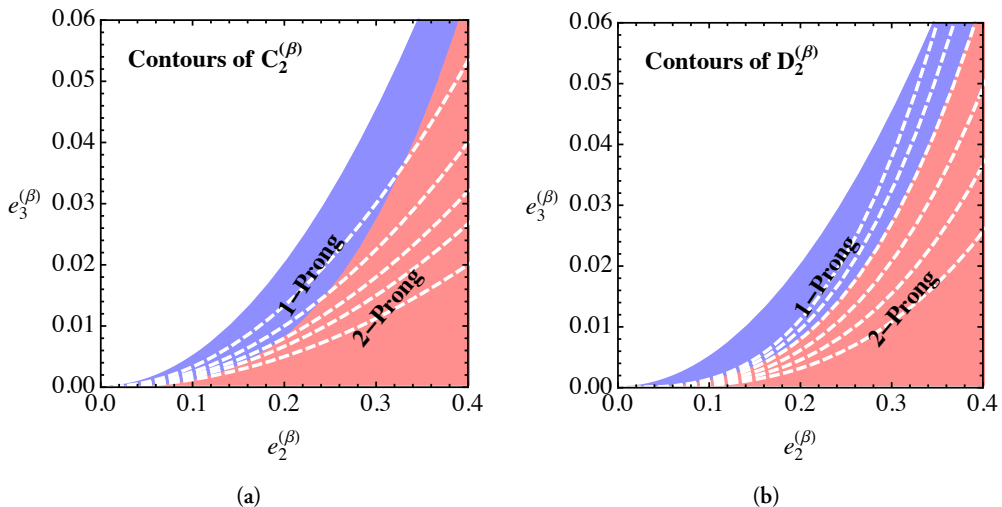


Figure 5.14: Phase space defined by $e_2^{(\beta)}$ and $e_3^{(\beta)}$ with contours of constant (a) $C_2^{(\beta)}$ and (b) $D_2^{(\beta)}$ [95].

The next group of variables is similar in nature, but rely on the subjet information and is called N -subjettiness [96, 97]. The variable τ_N quantifies how well a jet can be described by having N or fewer subjets. The axes within the jet are defined by the N subjets found by an exclusive k_t algorithm on the constituents of the trimmed large- R jet. The variable is defined as

$$\tau_N = \frac{1}{d_0} \sum_{i \in J} p_{Ti} \cdot \Delta R_i^{\min} \quad \text{with} \quad d_0 = \sum_{i \in J} p_{Ti} \cdot R, \quad (5.16)$$

where p_{Ti} is the transverse momentum of constituent i , ΔR_i^{\min} is the distance between constituent i and the axis of the closest subjet and $R = 1$ is the large- R jet distance parameter.

τ_1 , τ_2 and τ_3 are in themselves useful, but the ratios $\tau_{21} = \tau_2/\tau_1$ and $\tau_{32} = \tau_3/\tau_2$ are better. Especially τ_{32} is effective for top tagging, since it quantifies, how likely it is for the large- R jet to have three prongs and not two. This is seen in Figure 5.15, which also shows the (τ_2, τ_3) plane for top jets and QCD jets.

Another related group is the splitting scales $\sqrt{d_{12}}$ and $\sqrt{d_{23}}$ [98]. By taking the square root of Equation 5.1 and setting $R = 1$ and $a = 1$ equivalent to the k_T algorithm for large- R jets, we get

$$\sqrt{d_{ij}} = \min(p_{Ti}, p_{Tj}) \Delta R_{ij}, \quad (5.17)$$

where $\sqrt{d_{12}}$ is the splitting scale of the last merging step and $\sqrt{d_{23}}$ corresponds to the second-to-last merging. For hadronic top-quark decays, which are fully contained in a large- R jet, the expected value of $\sqrt{d_{12}}$ is approximately half the top quark mass, $m_t/2$, whereas $\sqrt{d_{23}}$ targets the hadronic decay of the W boson and therefore has an expected value of $m_W/2$. This is contrary to QCD radiation from light-quark or gluon jets, which will lead to smaller values of the splitting scales as is seen in Figure 5.16.

In a similar way, the last substructure variable used for top tagging in ATLAS is taking advantage of the fact that a boosted top has an *on-shell* W boson inside the jet [99]. By calculating the minimum pair-wise invariant mass of the last three constituents, Q_w , it is possible to see, if it adds up to the mass of the W boson. This will typically be the case for top quark jets, whereas for QCD jets the distribution will peak at lower values.

We have now covered the various substructure variables, that are useful for top tagging, which brings us to how this information is combined in the different taggers.

5.3.2 Top tagging

The simplest top tagger is based on selection cuts on just two variables. Studies have showed, that one-sided cuts on m^{comb} and τ_{32} are effective separating top and QCD jets [91]. The most optimal cut value is found by looking at all combinations of cuts on the two variables, that give the wanted signal efficiency and then choose the combination, that gives the largest background rejection. This is done as a function of p_T and the wanted signal efficiency for top tagging is chosen to be 80%. This high value is chosen since the background events to the interesting process, which includes top quarks, often also include real top quarks. This is e.g. the case for the all-hadronic $t\bar{t}$ resonance analysis in Chapter 8. For W boson tagging on the other hand, the main background is light-quark jets and a better background rejection is therefore needed, which means a lower signal efficiency, which is typically 50%.

Not surprisingly, it is possible to get better discriminating power, if more of the substructure variables, described above, are included in the top tagger. The performance of both a

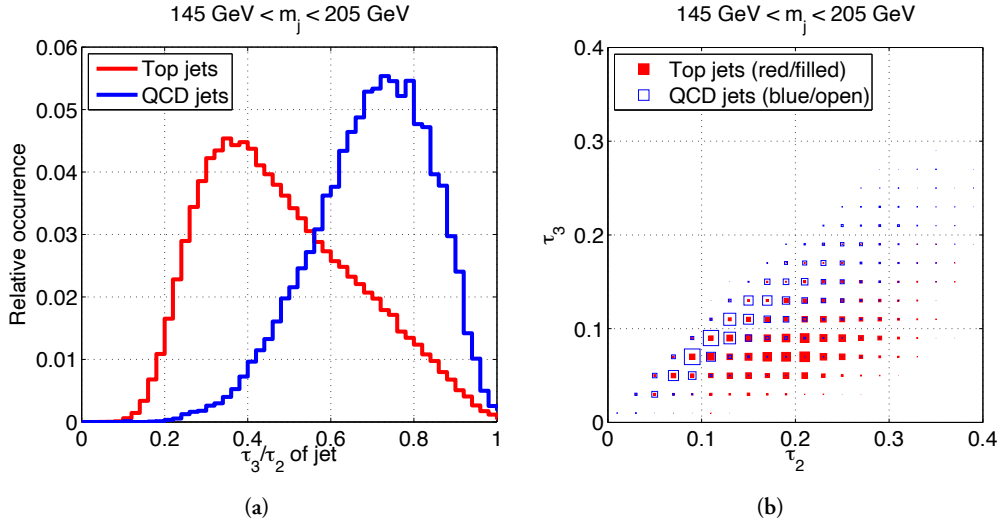


Figure 5.15: Discriminating power of (a) $\tau_{32} = \tau_3/\tau_2$ and (b) the (τ_2, τ_3) plane for top jets versus QCD jets [96].

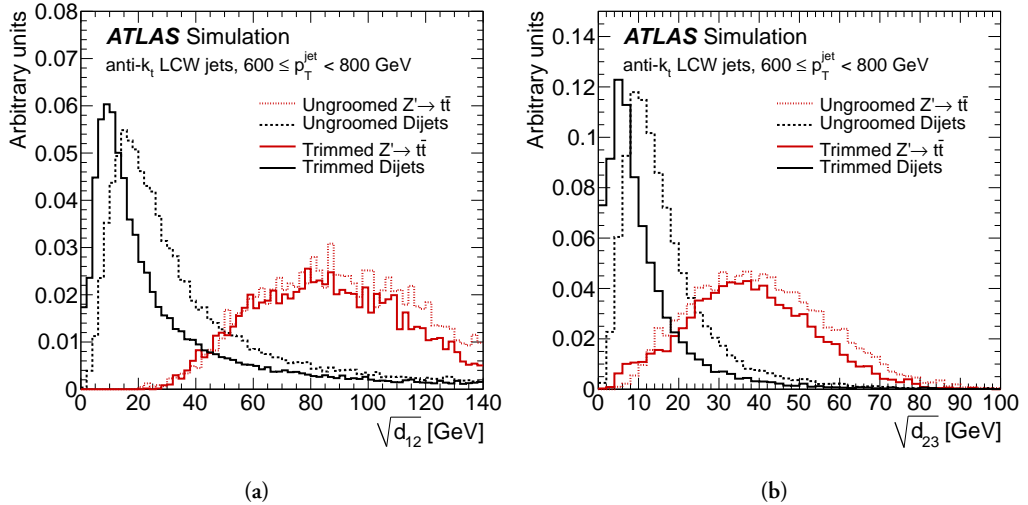


Figure 5.16: Discriminating power of (a) $\sqrt{d_{12}}$ and (b) $\sqrt{d_{23}}$ for $Z' \rightarrow t\bar{t}$ versus dijet events measured at $\sqrt{s} = 7$ TeV [100].

boosted decision tree (BDT) and a deep neural network (DNN), which provide a single top tagging discriminant, has been investigated [91]. For the DNN, the background rejection is calculated for nine different groups of substructure variables, which are seen in Table 5.1 together with the chosen variables for the DNN and BDT. For the BDT, the variables are added one at a time, with the most discriminating ones added first.

Table 5.1: Variables used in the DNN test groups and the final selection of variables for the BDT and DNN (adapted from [91]).

Observable	DNN test group									Chosen inputs	
	1	2	3	4	5	6	7	8	9	BDT	DNN
m^{comb}		○	○	○		○	○	○	○	○	○
p_T			○	○			○	○	○	○	○
e_3				○			○		○	○	○
C_2	○	○	○		○	○		○	○	○	○
D_2	○	○	○		○	○		○	○	○	○
τ_1				○			○		○	○	○
τ_2				○			○		○	○	○
τ_3				○			○		○	○	○
τ_{21}	○	○	○		○	○		○	○	○	○
τ_{32}	○	○	○		○	○		○	○	○	○
$\sqrt{d_{12}}$					○	○	○	○	○	○	○
$\sqrt{d_{23}}$					○	○	○	○	○	○	○
Q_w					○	○	○	○	○	○	○

The relative background rejection is the inverse of the relative background efficiency $1/\epsilon_{\text{bkg}}^{\text{rel}}$, which is given by

$$\epsilon_{\text{bkg}}^{\text{rel}} = \frac{N_{\text{bkg}, m^{\text{comb}} > 40 \text{ GeV}}^{\text{tagged}}}{N_{\text{bkg}, m^{\text{comb}} > 40 \text{ GeV}}^{\text{tagged}} + N_{\text{bkg}, m^{\text{comb}} > 40 \text{ GeV}}^{\text{untagged}}} \quad (5.18)$$

where $N_{\text{bkg}}^{\text{tagged}}$ is the number of tagged background events, whereas $N_{\text{bkg}}^{\text{untagged}}$ is the number of untagged events and it is indicated, that the jet mass is required to be $m^{\text{comb}} > 40 \text{ GeV}$. An additional requirement on the number of constituents $N^{\text{const}} \geq 3$ is applied, to ensure that all jet substructure features are well-defined. The relative signal efficiency, $\epsilon_{\text{sig}}^{\text{rel}}$, is defined in a similar manner.

Figure 5.17 shows the relative background rejection for both the DNN and BDT, which makes it clear, that no significant gain is seen from adding C_2 , τ_1 and τ_3 to the BDT. Hence, they are not included in the final BDT. For the DNN, group 9, with all the variables included, perform the best and is therefore used.

In Figure 5.18, it is seen, that the DNN and BDT top tagger perform equally well, but significantly better than the two-variable tagger. The DNN and BDT is giving an improvement on the background rejection of roughly a factor of two over the full p_T range. It is also seen, that the background rejection gets worse at higher p_T . This is due to the subjects getting closer and closer together, making the substructure variables less well-defined.

Another way to compare the performance of different taggers is by looking at the *ROC curves*.

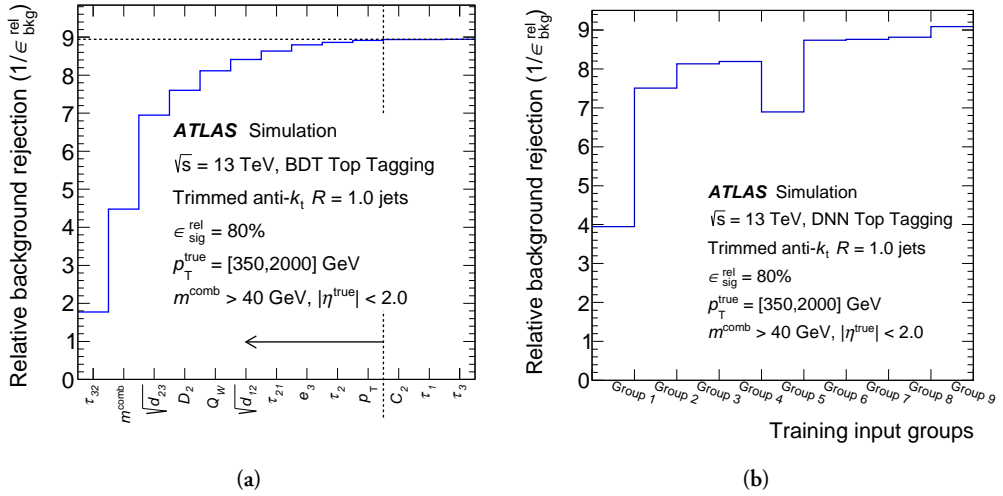


Figure 5.17: Background rejection of (a) the BDT and (b) the DNN as a function of the included variables [91].

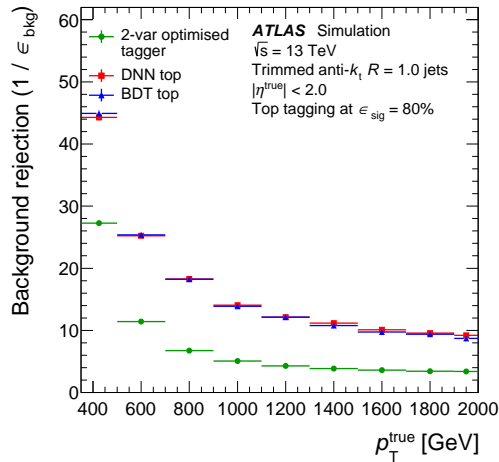
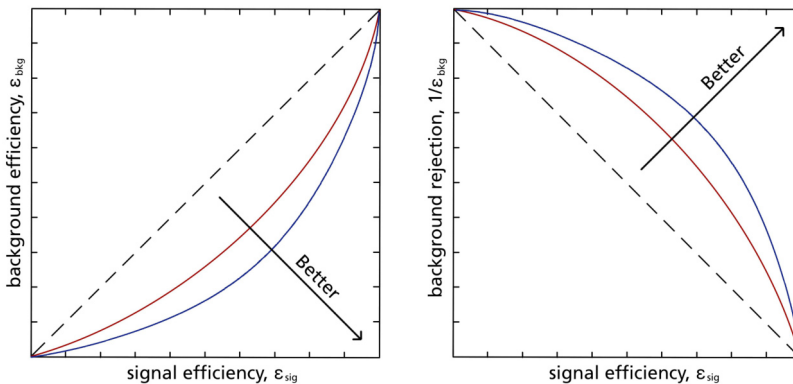


Figure 5.18: Background rejection as a function of p_T for the simple two-variable top tagger as well as the more advanced BDT and DNN tagger [91].

Question 5.5: What is a ROC curve?

A Receiver Operating Characteristic (ROC) curve is usually showing the background efficiency ϵ_{bkg} as a function of the signal efficiency ϵ_{sig} (left), but sometimes the background rejection, $1/\epsilon_{\text{bkg}}$, is showed instead (right). It is used to compare the performance of different taggers or classifiers.

The optimal tagger will have an infinitesimal background efficiency, corresponding to a very high background rejection, for any value of the signal efficiency. However, in practice the background efficiency (rejection) will steeply rise (fall) at high signal efficiency. It is not possible to accept all signal events without also accepting all background events.



The ROC curves for the DNN and BDT tagger, as well as a number of other taggers, are seen in Figure 5.19. Among the other taggers are the shower deconstruction [101] and the HEPTopTagger [102, 103], which will not be discussed further here, since they do not perform nearly as good as the DNN and BDT tagger.

However, the topocluster-based DNN tagger (TopoDNN) [104] is performing slightly better than the multivariate taggers at high p_T , so it deserves some attention. This DNN takes topo-cluster information as input instead of the substructure variables. The idea is that this low-level information might include some additional features, which are not captured by the current substructure variables. It is optimized for high- p_T top quarks with $p_T > 450$ GeV, but even though some gain is seen, it should be noted, that it is not that significant at a signal efficiency of 80%. In ATLAS the multivariate DNN is the recommended top tagger and is the one used in this thesis.

The last step is to validate the tagger on data. The modeling of the top tagging is studied by using a sample of data enriched in $t\bar{t}$ events, where one top quark decays hadronically and

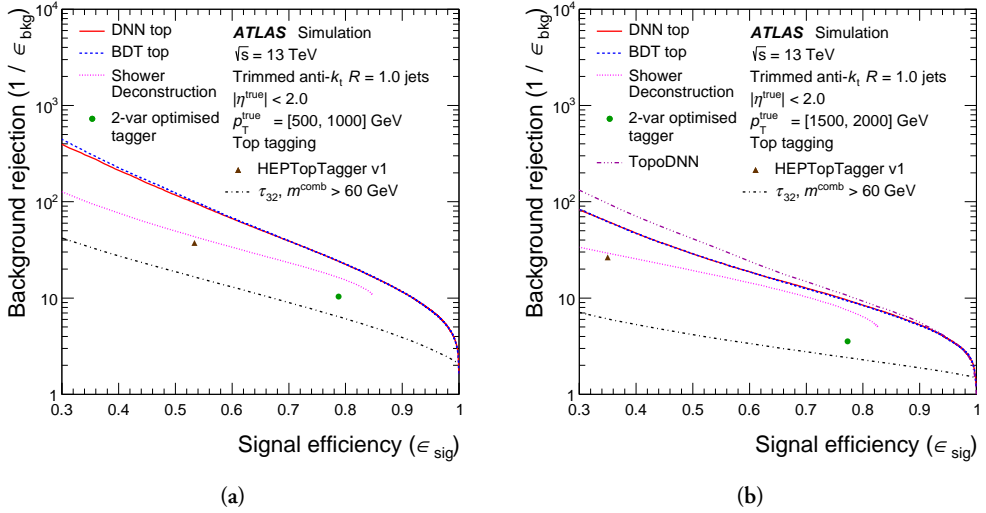


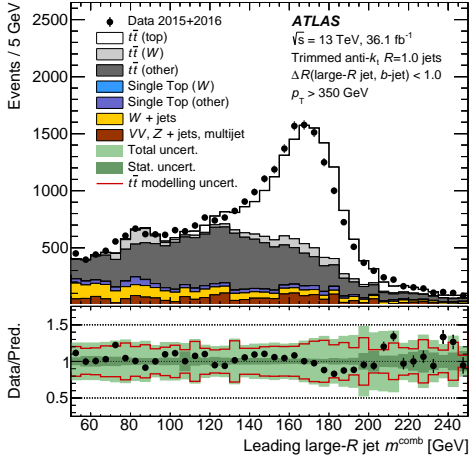
Figure 5.19: ROC curves for the different top taggers for (a) $p_T^{\text{true}} = [500, 1000]$ GeV and (b) $p_T^{\text{true}} = [1500, 2000]$ GeV [91].

the other leptonically. A set of requirements are placed on the samples² in order to increase the purity, including $\Delta R(\text{large-}R \text{ jet}, b\text{-jet}) < 1.0$. A comparison of data and Monte Carlo is done for the key observables and the signal efficiency is measured for the 80% working point.

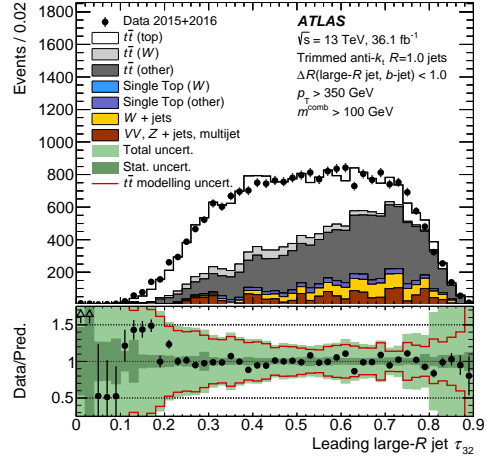
Figure 5.20 shows a comparison of data and Monte Carlo for the mass of the leading large- R jet, τ_{32} and the DNN discriminant for top tagging. The distributions agree within the uncertainty and the disagreement between the mass peak positions in data and Monte Carlo is attributed to a mismodeling of the jet mass scale [88]. Furthermore, it is seen that there is a high purity of fully-contained top-quark jets at high values of the DNN discriminant.

It is possible to measure the signal efficiency in data, due to the relatively high purity of top-quark jets in the selected sample. It is measured by requiring $m^{\text{comb}} > 40$ GeV and a selection on the DNN discriminant, tuned to give a fixed 80% signal efficiency as a function of p_T for fully-contained top-quark jets. The number of signal-like events in data that pass and fail these requirements are obtained from a chi-square template fit of “signal” and “background” distributions predicted by Monte Carlo simulations to the data to correct for mismodeling of the cross-section of the various processes contributing to the phase space of interest. Here the “signal” is the fully-contained top-quark jets and the rest is regarded as background. The fit is performed using distributions of the mass of the leading anti- k_T trimmed jet and the distribution of the events, that pass and fail, are fitted simultaneously. The normalization of the signal distribution in each of the passed

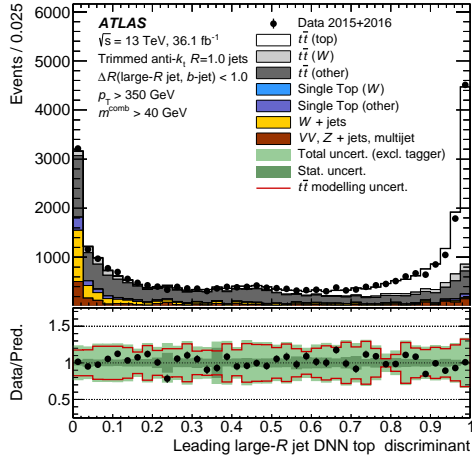
²For the other requirements see Section 6.1.1 of [91].



(a)



(b)



(c)

Figure 5.20: Comparison of data and Monte Carlo distributions for the leading large- R jet (a) mass, m^{comb} , (b) τ_{32} and (c) the DNN discriminant for top tagging. The simulated distribution is normalized to data [91].

and fail category, $N_{\text{fitted signal}}^{\text{tagged}}$ and $N_{\text{fitted signal}}^{\text{untagged}}$, are extracted from the fit, such that the signal efficiency in data is

$$\epsilon_{\text{data}} = \frac{N_{\text{fitted signal}}^{\text{tagged}}}{N_{\text{fitted signal}}^{\text{tagged}} + N_{\text{fitted signal}}^{\text{untagged}}} \quad (5.19)$$

This can then be compared to the signal efficiency in Monte Carlo, which is given by

$$\epsilon_{\text{MC}} = \frac{N_{\text{signal}}^{\text{tagged}}}{N_{\text{signal}}^{\text{tagged}} + N_{\text{signal}}^{\text{untagged}}} \quad (5.20)$$

where $N_{\text{signal}}^{\text{tagged}}$ and $N_{\text{signal}}^{\text{untagged}}$ is the numbers of predicted signal events that pass and fail the tagging requirement, respectively.

Figure 5.21 shows the comparison of the signal efficiency in data and Monte Carlo as a function of the leading large- R jet p_T and the average number of interactions per bunch crossing, μ . They agree within the uncertainties and it is seen, that the signal efficiency is quite robust as a function of μ .

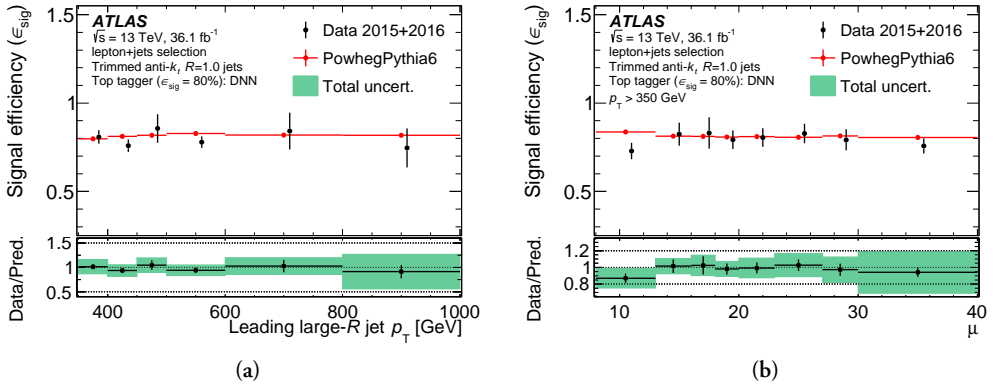


Figure 5.21: Comparison of data and Monte Carlo distributions for the signal efficiency as a function of (a) leading large- R jet p_T , and (b) the average number of interactions per bunch crossing, μ [91].

This comparison between data and Monte Carlo can be used to estimate the systematic uncertainty of the DNN top tagger, when it is applied in an independent analysis, like the all-hadronic $t\bar{t}$ resonance search in Chapter 8. It can also be used to provide an *in situ* correction in the form of jet-by-jet efficiency scale factors.

In a similar way, the background rejection in data is tested as well by using two different samples: a γ + jet sample enriched in light-quark jets and the multijet sample, which probes a mixture of light-quark and gluon jets. The background rejection comparison of data and Monte Carlo is seen in Figure 5.22 for the two different samples.

Since the top quark decays into a W boson and a b quark, it is possible to further increase the separation between top jets and light-quark jets by requiring the top-tagged large- R jet to be matched to a b -tagged jet.

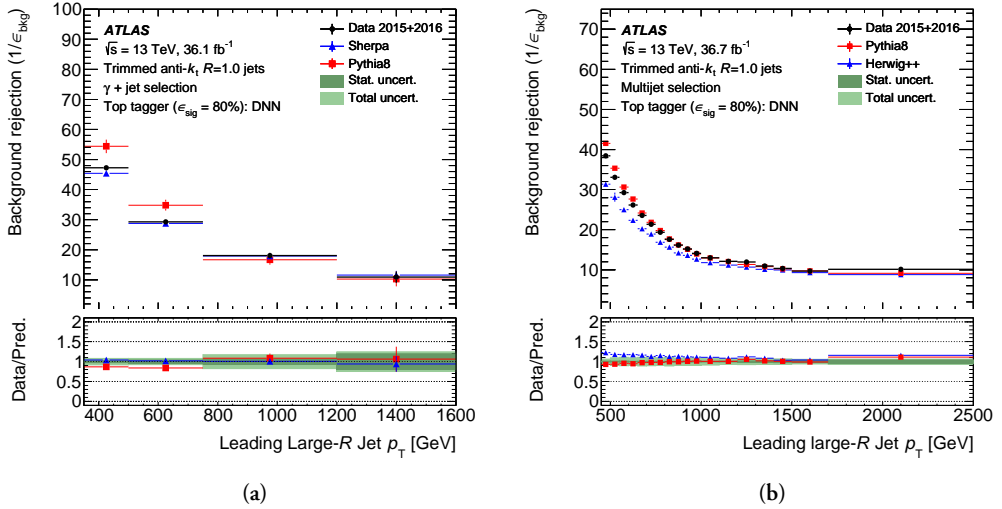


Figure 5.22: Comparison of data and Monte Carlo distributions for the background rejection as a function of leading large- R jet p_T for (a) the $\gamma + \text{jet}$ sample and (b) the multijet sample [91].

5.3.3 b tagging

In ATLAS, b tagging is done in two steps [105]. Firstly, low-level algorithms reconstruct the characteristic features of the b jets using different approaches. The IP2D and IP3D algorithms [106] are exploiting the large impact parameters of the tracks originating from the b -hadron decay. Here the transverse impact parameter, d_0 , is defined as the distance of closest approach in the r - ϕ plane of the track to the primary vertex (PV) and the longitudinal impact parameter, $z_0 \sin \theta$, is defined as the distance of the track to the PV in the longitudinal plane at the point of closest approach in r - ϕ . The IP2D algorithm uses the transverse impact parameter significance, d_0/σ_{d_0} , as a discriminating variable, whereas IP3D uses both the transverse and longitudinal impact parameter significance in a two-dimensional template to account for their correlation.

Before describing the other two low-level algorithms, we need to introduce the concept of *probability density functions* and *likelihood functions*.

Question 5.6: What is probability density and likelihood functions?

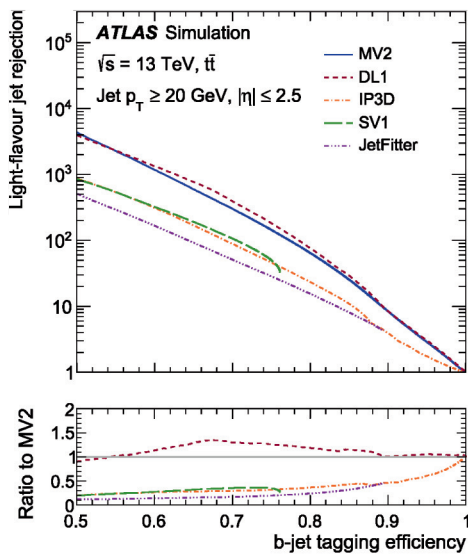
A *probability density function (PDF)* is a function of the data point x and tells you how likely it is, certain data points appear. By integrating the PDF over a certain range you will get the probability, that the variable will fall in that range.

A *likelihood function* or just likelihood, on the other hand, takes the data set as a given and represent the likeliness of different parameter values given the data. It is then possible to test whether a given parameter value fits the data better than another by comparing their likelihoods.

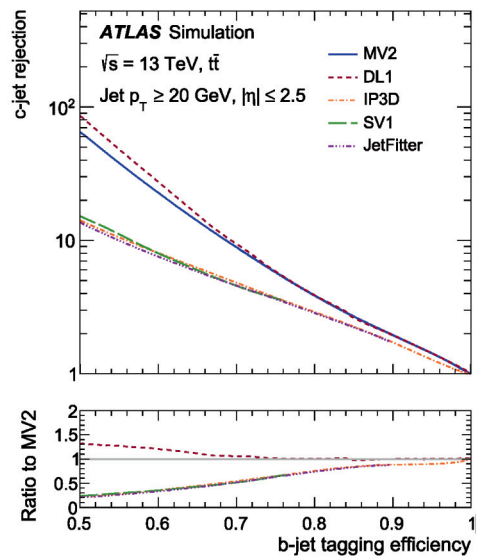
The SV1 algorithm [107] is attempting to reconstruct a single displaced secondary vertex (SV), which it then uses to discriminate between light-quark and b jets using a *likelihood ratio test* (see more in Section 6.5.2). The corresponding probability density functions are constructed using four variables: the total invariant mass of all tracks associated to the SV, the ratio of the sum of the energies of the tracks associated to the SV to the energy of all tracks in the jet, the number of two-track vertices and the ΔR distance between the SV-PV direction and the jet direction.

The JETFITTER algorithm [108] is aiming to reconstruct the full b - and c -hadron decay chain. It uses a likelihood ratio test, similar to the one for SV1, to discriminate between light-quark, b and c jets.

Secondly, the results from these algorithms are combined using one of two different multivariate classifiers: the MV2, which is using a BDT, or the DL1, which is using a DNN [106]. In addition to the inputs from the low-level algorithms, the jet kinematics, namely p_T and $|\eta|$, are also included to take advantage of the correlations with the other variables. The DL1 algorithm takes c -tagging variables from the JETFITTER, which is not true for the MV2 algorithm. This explains, why the DL1 performs slightly better than the MV2 as seen in Figure 5.23, which shows the light-quark jet and c -jet rejection as a function of the b -jet tagging efficiency (ROC curves). It is also seen, that the rejection gets significantly better by combining the results from the low-level algorithms with either the MV2 or DL1. In this thesis, the DL1 algorithm will be used.



(a)



(b)

Figure 5.23: ROC curves for the different b taggers for (a) light-quark jet rejection and (b) c -jet rejection [105].

Dijets

The analyses, presented in this thesis, are considering systems of two jets, also called *dijets*. We start by considering the $2 \rightarrow 2$ parton scattering process sketched in Figure 6.1, where p_1 and p_2 are the four-momenta of the incoming partons and p_3 and p_4 are the four-momenta of the outgoing partons. From these the Mandelstam variables can be defined as

$$\hat{s} = (p_1 + p_2)^2 \quad (6.1)$$

$$\hat{t} = (p_1 - p_3)^2 \quad (6.2)$$

$$\hat{u} = (p_1 - p_4)^2 \quad (6.3)$$

where \hat{s} is the square of the center-of-mass energy, which is related to the proton-proton collision center-of-mass energy, \sqrt{s} , and the Bjorken x of the incoming partons by $\hat{s} = x_1 x_2 s$. Whereas, \hat{t} is also known as the square of the four-momentum transfer.

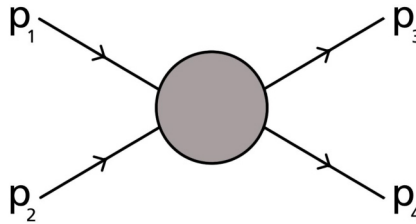


Figure 6.1: Feynman diagram for $2 \rightarrow 2$ process.

6.1 Dijet invariant mass distribution

We notice, that the dijet is formed by the two outgoing partons, so by adding the four-momenta p_3 and p_4 , we get the four-momentum of the dijet, p_{jj} . Furthermore, we have,

that the four-momentum squared equals the invariant mass squared, $p_i^2 = m_i^2$, as well as four-momentum conservation, $p_1 + p_2 = p_3 + p_4$, which leads to

$$\hat{s} = (p_3 + p_4)^2 = p_{jj}^2 = m_{jj}^2 \quad (6.4)$$

where m_{jj} is the *dijet invariant mass*.

Question 6.1: What is the invariant mass?

When a variable is *invariant*, it means, it remains unchanged under some transformation. When we talk about the invariant mass, m , we refer to the part of the total mass, that does not change under any Lorentz transformation. It is a characteristic of a system's total energy, E , and momentum, \vec{p} ,

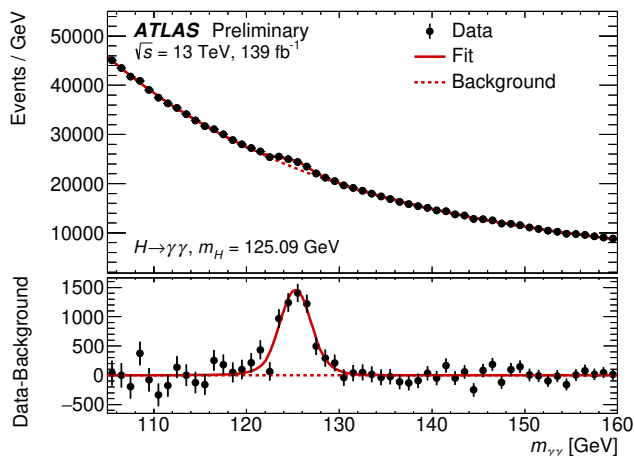
$$m^2 = E^2 - \vec{p}^2 \quad (6.5)$$

The dijet invariant mass is an extremely interesting observable, when searching for new resonances. As described in Chapter 2, a new resonance, like the Z' boson, would lead to an increase in the cross section at the mass of the particle. This would lead to a bump in the otherwise smoothly falling invariant mass distribution coming from QCD interactions.

Question 6.2: What is bump hunting?

When we are searching for new resonances, it is sometimes referred to as *bump hunting*. This is due to the fact, that a new resonance, which is decaying quickly, will lead to a bump in the invariant mass spectrum of the decay products.

As an example, the Higgs boson was found by looking at the invariant mass of two photons. The discovery was announced the 4th of July 2012, but now with the data collected in the full Run 2, the bump is even more evident as seen below [109].



However, not all Beyond Standard Model (BSM) theories result in resonances. This is for example true for the contact interaction described in Chapter 2. For such non-resonant signals, it is useful to instead look at the angular distribution of the dijet system.

6.2 Dijet angular distribution

If we assume massless partons, we can rewrite the Mandelstam \hat{t} and \hat{u} to be expressed in terms of \hat{s} :

$$\hat{t} = -\frac{1}{2}\hat{s}(1 - \cos \hat{\theta}) \quad (6.6)$$

$$\hat{u} = -\frac{1}{2}\hat{s}(1 + \cos \hat{\theta}) \quad (6.7)$$

where $\hat{\theta}$ is the scattering angle in the center-of-mass frame of the colliding partons.

The QCD $2 \rightarrow 2$ cross section is dominated by the t-channel exchange of a gluon, so we have

$$\frac{d\hat{\sigma}}{d\hat{t}} \propto \frac{\alpha_s^2}{\hat{t}^2} \quad (6.8)$$

where $\hat{\sigma}$ is the partonic cross section. We see, that this corresponds to the angular behavior of Rutherford scattering, since

$$\frac{d\hat{\sigma}}{d \cos \hat{\theta}} = \frac{d\hat{\sigma}}{d\hat{t}} \frac{d\hat{t}}{d \cos \hat{\theta}} \propto \frac{\alpha_s^2 \hat{s}}{\hat{t}^2} \frac{\hat{s}}{2} = \frac{2\alpha_s^2}{\hat{s}(1 - \cos \hat{\theta})^2} = \frac{\alpha_s^2}{2\hat{s} \sin^4(\hat{\theta}/2)} \quad (6.9)$$

where we have used the half-angle identity $1 - \cos \hat{\theta} = 2 \sin^2(\hat{\theta}/2)$. So for a fixed \hat{s} , the cross section clearly peaks at small angles, $\hat{\theta}$ (forward).

We now turn to what we can measure in the experiment. Here the two outgoing partons will manifest themselves as jets, but they will be surrounded by other activity, like more jets. We therefore define the dijet as the *leading* and *subleading* jet in the event, which means the jets with the highest and next-to-highest p_T .

As discussed earlier, the two colliding partons do not necessarily have equal and opposite momenta, which means the lab frame and the center-of-mass frame may differ. Here the kinematic variable called *rapidity* is convenient.

Question 6.3: What is rapidity?

Rapidity is defined from the energy, E , and the longitudinal momentum component, p_z , as

$$y \equiv \frac{1}{2} \ln \frac{E + p_z}{E - p_z} \quad (6.10)$$

which has the nice feature, that it changes additively under Lorentz boosts along the z -axis, so rapidity differences are Lorentz invariant.

We denote the rapidity of the leading and subleading jet with y_1 and y_2 , respectively and introduce

$$y_B = \frac{y_1 + y_2}{2} \quad (6.11)$$

$$y^* = \frac{y_1 - y_2}{2} \quad (6.12)$$

where a longitudinal boost, y_B , will bring the lab frame to the center-of-mass frame, giving the jets equal, but opposite, rapidities, $\pm y^*$, as seen in Figure 6.2.

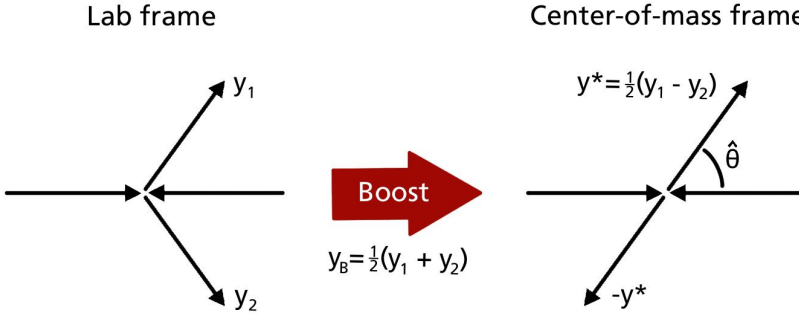


Figure 6.2: Sketch showing a longitudinal boost, y_B , to the lab frame with jet rapidities y_1 and y_2 , bringing it to the center-of-mass frame, where the jets have rapidities $\pm y^*$.

Then we can also define the rapidity difference measure,

$$\chi = e^{|y_1 - y_2|} = e^{2|y^*|} \quad (6.13)$$

where we note, that since y^* is Lorentz invariant, so is χ and that by construction $\chi \geq 1$. Since y^* can be related to the scattering angle by $\cos \hat{\theta} = \tanh y^*$, we get

$$\chi = \frac{1 + |\cos \hat{\theta}|}{1 - |\cos \hat{\theta}|} \propto \frac{1}{1 - |\cos \hat{\theta}|} = -\frac{\hat{s}}{2\hat{t}} \quad (6.14)$$

where we in the last step have used the expression for \hat{t} in Equation 6.6. We can then rewrite the cross section in Equation 6.8 as

$$\frac{d\hat{\sigma}}{d\chi} = \frac{d\hat{\sigma}}{d\hat{t}} \frac{d\hat{t}}{d\chi} \propto \frac{\alpha_s^2 \hat{t}^2}{\hat{t}^2 \hat{s}} = \frac{\alpha_s^2}{\hat{s}} \quad (6.15)$$

which is very illuminating. It tells us that from leading order QCD, where t-channel exchange is dominant, we expect the differential production cross section, $d\hat{\sigma}/d\chi$, to be approximately flat as a function of χ for a fixed $\hat{s} = m_{jj}^2$.

This is contrary to what would be expected for a new phenomena, which is produced via s-channel and is therefore more isotropic. This means, it is independent of $\hat{\theta}$ or equivalently that $d\hat{\sigma}/d\cos\hat{\theta}$ will be constant. From this follows

$$\frac{d\hat{\sigma}}{d\hat{t}} \propto \frac{1}{\hat{s}} \quad (6.16)$$

and therefore

$$\frac{d\hat{\sigma}}{d\chi} = \frac{d\hat{\sigma}}{d\hat{t}} \frac{d\hat{t}}{d\chi} \propto \frac{1}{\hat{s}} \frac{\hat{t}^2}{\hat{s}} = \frac{\hat{t}^2}{\hat{s}^2} \propto \frac{1}{\chi^2} \quad (6.17)$$

so the distribution will peak at low χ .

This means, that when we are searching for a BSM signal, it is very useful to look at the χ distribution in bins of m_{jj} . To this matter, it is also useful to know the relationship between m_{jj} , p_T and χ , which to leading order is

$$m_{jj} = p_T \left(\sqrt{\chi} + \frac{1}{\sqrt{\chi}} \right) \quad (6.18)$$

so we see, that for a given m_{jj} , high p_T values correspond to low χ values and vice versa.

The cross section, we have considered so far, $d\hat{\sigma}/d\chi$, is on the partonic level. However, what we will be measuring with the detector is on the hadronic level. We therefore have to multiply the partonic cross section with the parton distribution function (PDF) and integrate over the momentum fractions as described in Section 2.7. We then get

$$\frac{d\sigma}{d\chi} = \int dx_1 f_i(x_1, Q^2) \int dx_2 f_j(x_2, Q^2) \frac{d\hat{\sigma}}{d\chi} \quad (6.19)$$

so at leading order, the hadronic cross section is determined by the Bjorken x_1 and x_2 as well as χ . We can rewrite $dx_1 dx_2$ as $d\tau dy_B$, where $\tau = x_1 x_2 = \hat{s}/s$ and $y_B = 1/2 \ln(x_1/x_2)$. So the hadronic cross section can equally well be described by $\hat{s} = m_{jj}$, y_B and χ . Then for a fixed \hat{s} in a given bin of χ only y_B can vary and since the partonic cross section does not depend on y_B , it means the difference in the hadronic cross section is coming from the PDFs. However, what we really want to investigate is the partonic cross section over the whole range of χ and therefore it is desirable to keep the y_B range small by applying a cut. Such a cut is applied in the angular dijet analysis presented in Section 9.1.

6.3 QCD dijets as background

Dijets are produced in abundance through QCD processes. These are seen as backgrounds when searching for BSM phenomena. It is therefore very important to be able to estimate these and this can be done in many different ways, which will be outlined below.

6.3.1 Monte Carlo simulations

A common method to estimate Standard Model processes is Monte Carlo simulations as already introduced in Chapter 2. These, however, have some drawbacks. First of all, it requires huge computational resources to produce and store the Monte Carlo samples. Especially when it comes to final states like dijets, which are produced in magnificent numbers especially at low invariant mass.

Another problem is that the data and Monte Carlo agreement is not always great due to inadequate theoretical knowledge, like missing higher order corrections. Therefore, Monte Carlo simulation is sometimes corrected with a factor derived from data. Either way the Monte Carlo samples often come with large systematic uncertainties.

6.3.2 ABCD method

It is instead possible to fully derive the background in a data-driven way. A useful way to estimate the background in the *signal region* from the *control regions* is to use the *ABCD method*.

Question 6.4: What are signal and control regions?

In physics analyses, it is common to divide the data into *signal* and *control* regions using the selection criteria. The signal regions are the parts of phase space, where the signal is expected to be present and the signal to background ratio is optimized. Then by inverting some cut(s), control regions, which are close in phase space to the signal region, but where little signal is expected, are obtained. The control regions can be used to estimate (or control) the background in the signal regions.

Question 6.5: What is the ABCD method?

The *ABCD method* is used to estimate the background in the signal region A from the control regions B , C and D . The signal region is (partly) defined by two selections, which can be inverted to define the control regions, which should have minimal signal contamination. The selections can either be binary (like a veto on electrons) or a cut on a continuous variable (like transverse momentum or invariant mass).

The important assumption, that needs to be true for the ABCD method to work, is that the two selection observables are reasonable uncorrelated for the background events. In this case the following will be true

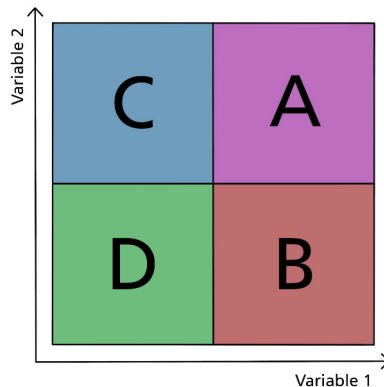
$$\frac{N_C^{\text{bkg}}}{N_D^{\text{bkg}}} = \frac{N_A^{\text{bkg}}}{N_B^{\text{bkg}}} \quad (6.20)$$

where N_i^{bkg} is the number of background events in region i . If we then further assume that the signal contamination in the control regions is negligible such that the total number of events in control region j is $N_j = N_j^{\text{bkg}}$, we get

$$N_A^{\text{bkg}} = \frac{N_C}{N_D} N_B \quad (6.21)$$

and it is possible to calculate the expected number of background events in the signal region A from the data in the three control regions.

In the case of non-negligible signal contributions in the control regions, it is still possible to use the ABCD method by using a *likelihood-based* approach to estimate the relative rates in the four regions.



6.3.3 Global fit

Another background estimation method, which has shown to be useful, when looking at dijet invariant mass distributions, is to perform a global fit on the distribution. This is possible, because the distribution is expected to be smoothly falling without any structures. A functional form, that has proven to describe dijet invariant mass distribution well, is

$$f(x) = p_0(1-x)^{p_1} x^{p_2+p_3 \ln x+p_4(\ln x)^2+\dots} \quad (6.22)$$

where p_i are free parameters and $x = m_{jj}/\sqrt{s}$. It is used in e.g. the $t\bar{t}$ all-hadronic analysis (see Chapter 8), the dijet plus initial state radiation analysis [110] and many more.

6.3.4 Sliding Window Fit

The global fit described above is however not always sufficient, especially with the large integrated luminosity available in Run 2, since the smaller statistical uncertainties reveals structures, that were not visible before. Therefore, a new method is needed. The *sliding window fit* (SWiFt) was developed for the dijet resonance analysis [111], but has been used by several analysis since. It is e.g. used in the full Run 2 dijet and di- b -jet resonance analysis, which is presented in Chapter 9.

Question 6.6: What is SWiFt?

The *sliding window fit* (SWiFt) is applying the fit function in small *windows* rather than on the whole distribution. In this way each bin content is estimated by fitting the distribution around it. So the algorithm *slides* over the distribution, estimating one bin at the time.

The size of the fitting windows has to be optimized. While smaller windows makes it easier to describe the distribution well with the fit, too small windows could give too much flexibility. The size is optimized by performing multiple fits with different window sizes and choosing the window size with the best χ^2 p-value.

6.4 Dijet searches

As we have seen earlier in this chapter, depending on the signal we are searching for, two different variables, m_{jj} and χ , are extremely useful.

For resonance searches looking at the m_{jj} distribution, new BSM signal will manifest itself as a bump on the otherwise smoothly falling QCD background, which can be estimated

in a data-driven way by fitting the distribution with a functional fit as described above. In these searches, tagging of the dijets can be advantageous, if the signal has a larger coupling to e.g. top quarks. This is indeed the strategy used in the search presented in Chapter 8.

For non-resonance searches on the other hand, the χ distribution is of interest. Here we expect from LO QCD, that the distribution will be approximately flat, when divided in narrow m_{jj} bins. However, at higher orders and when including non-perturbative effects, it will no longer be completely flat, so a comparison to Monte Carlo simulation is needed. A BSM signal is expected to be seen at low χ values as discussed above and the angular search is therefore done as a comparison of the shape in data and simulation. The angular search is presented in Chapter 9.

In order to perform these analyses, we need some statistical tools, which will be the last topic of this chapter.

6.5 Statistical tools

The statistical analysis can roughly be divided in two categories. First the distribution(s) are examined for any significant deviations from the background model. This can be done both in a model-dependent and independent way. If no significant deviation is found, the next step is to compute limits on the benchmark signal(s).

6.5.1 Model-independent resonance search

There is a large number of statistical tests, which check whether the data is consistent with a given hypothesis. We will focus on the Pearson's χ^2 test and BUMP HUNTER [112], which are used in the all-hadronic $t\bar{t}$ search presented in Chapter 8. These kind of tests are called *hypothesis tests* or *goodness of fit tests*. It is possible to check, whether the data follow any kind of hypothesis, but it is common to choose the hypothesis to be the *null* or *background* hypothesis, H_0 . In this way, a discovery can be claimed from just saying, that the data is not in agreement with the standard theory without having to show, which theory is the correct one. The big advantage of that is, that it makes the search *model-independent*. The first step in a hypothesis test is to define the *test statistic*.

Question 6.7: What is a test statistic?

The *test statistic* is a single number, that quantifies the difference between data, D , and the background hypothesis, H_0 . It is always defined such that a larger difference between D and H_0 will lead to a larger test statistic. It is often denoted by t .

The second step is to construct the test statistic distribution for H_0 by generating *pseudo-experiments*. The hypothesis test is then made by reading the *p-value* from that distribution, for the test statistic measured in the data.

Question 6.8: What is a pseudo-experiment?

In reality, we often only get one outcome of an experiment, but we know, that the outcome is subject to some uncertainty. We can therefore generate *pseudo-experiments*, which represent other likely outcomes to the experiment. For a counting experiment, this can be done by varying the number of measured events within the Poisson uncertainty.

Pseudo-experiments are also sometimes called *toys* or *pseudo-data*.

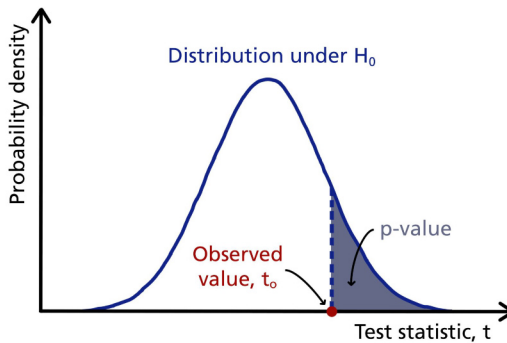
Question 6.9: What is a *p-value*?

The *p-value* or probability value is the probability to obtain a test statistic, t , that is equal to or greater than the observed test statistic, t_o , assuming the background hypothesis, H_0 , is correct. Or mathematically

$$p\text{-value} \equiv P(t \geq t_o | H_0) \quad (6.23)$$

which is also shown graphically in the sketch below.

The *p-value* is a false-discovery probability. If e.g. the hypothesis test returns a $p\text{-value} = 10^{-2}$, we can say that the most reliable decision, which would rule out H_0 , based on *this* hypothesis test, would have a probability of 1% of being wrong.



It is important to realize, that different statistical tests can be sensitive to different features and therefore give very different *p-values*. It can therefore be very useful to apply more than one. However, it is clearly easier to find *one* statistical test, that will reject the background hypothesis, if you perform a lot of tests. It is therefore important to take into account this *trials factor*, which is also called the *look-elsewhere effect*.

Question 6.10: What is the look-elsewhere effect?

The *look-elsewhere effect* or *trials factor* is the phenomenon, that it is possible to get a result, that is looking significant, but is merely caused by the huge size of the parameter space and happens by chance. This effect should be acknowledged and taken into consideration, when performing the statistical analysis.

It is possible to take into account the look-elsewhere effect by performing a *hypertest*, which in itself is also a hypothesis test. It is a union of many hypothesis tests, since it uses their p -values as the test statistic. More specifically, the test statistic is

$$t = -\ln(\min_i p\text{-value}_i) \quad (6.24)$$

or in words: the negative logarithm of the smallest p -value in the set. The negative logarithm is used to make sure t is monotonically increasing, but it could of course be replaced by any other monotonically increasing function.

The p -value of the hypertest quantifies, how often such a small or smaller p -value would be returned by at least one of the N hypothesis tests included in the set, given H_0 is correct. BUMPHUNTER is such a hypertest, but before we start discussing that, we will first have a look at a much simpler hypothesis test, Pearson's χ^2 test.

Pearson's χ^2 test

The most commonly used hypothesis test is probably Pearson's χ^2 test. It uses the test statistic

$$t = \sum_i \left(\frac{d_i - b_i}{\sqrt{b_i}} \right)^2 \quad (6.25)$$

where d_i is the observed events and b_i is the background events expected by H_0 in bin i . The distribution of the test statistic from the pseudo-experiments will follow a χ^2 distribution and the observed test statistic can therefore directly be used to calculate the p -value from the χ^2 distribution.

BUMPHUNTER

A hypothesis test, that has shown to be very useful when searching for resonances in an invariant mass distribution, is BUMPHUNTER. It is designed to find the most significant excess in data compared to the background hypothesis, H_0 . It scans the data using windows of varying width and keeps the window with the largest excess.

It is a hypertest, that combines the several hypothesis tests, which focus on bumps of various widths at different positions of the spectrum, taking the look-elsewhere effect into account.

This is done by calculating a *local* p -value for each of the windows, which is given by

$$p\text{-value} = \begin{cases} 1 & \text{if } d \leq b \\ \Gamma(d, b) & \text{otherwise} \end{cases} \quad (6.26)$$

where $\Gamma(d, b)$ is the normalized lower incomplete Gamma function, d is the observed data events and b is the background events expected from H_0 . The *global* p -value, which takes into account the look-elsewhere effect, is then calculated by using the test statistic given in Equation 6.24 and create pseudo-experiments as explained above.

A thing that should be noticed is, that when the background hypothesis depends on the data, as is the case when using a global fit or SWiFt, the fit needs to be performed for each of the pseudo-experiments in order to find the corresponding background distribution.

6.5.2 Model-dependent search

If we instead are interested in testing the compatibility of data with a specific signal model, we can do a model-dependent search. In this case, we have a signal plus background (s+b) hypothesis, so the expected number of events in bin i is given by

$$\nu_i = \mu s_i(\boldsymbol{\theta}) + b_i(\boldsymbol{\theta}) \quad (6.27)$$

where μ is the signal strength, which is our parameter of interest (POI), $s_i(\boldsymbol{\theta})$ and $b_i(\boldsymbol{\theta})$ are the expected number of signal and background events given the nuisance parameters, $\boldsymbol{\theta}$.

Question 6.11: What is a nuisance parameter?

A *nuisance parameter* is any parameter, which is not the main parameter of interest, but needs to be accounted for in the analysis. Usually the parameter of interest is the mean value of an observable, whereas the variance of the observable is merely a *nuisance*. In a statistical analysis, uncertainties are taking into account by applying nuisance parameters for each of them.

The probability of observing n_i events in bin i , when ν_i is expected, is given by the Poisson probability, so the *likelihood* for a distribution with N bins will be the product of N Poisson terms

$$L(\mu, \boldsymbol{\theta}) = \prod_{i=1}^N P_{\text{pois}}(n_i | \nu_i(\boldsymbol{\theta})) = \prod_{i=1}^N \frac{(\mu s_i(\boldsymbol{\theta}) + b_i(\boldsymbol{\theta}))^{n_i}}{n_i!} e^{-(\mu s_i(\boldsymbol{\theta}) + b_i(\boldsymbol{\theta}))}. \quad (6.28)$$

It is possible to add an external constraint in the likelihood for the nuisance parameters, θ , which are not constrained by the data by definition. This constraint term $C(\theta)$ is given by the product of, usually, Gaussian terms and is multiplied with the likelihood in Equation 6.28 to give the final likelihood.

Now it is possible to test a hypothesized value of μ by considering the profile likelihood ratio [113]

$$\lambda(\mu) = \frac{L(\mu, \hat{\hat{\theta}})}{L(\hat{\mu}, \hat{\theta})} \quad (6.29)$$

where $\hat{\hat{\theta}}$ is the value of θ , that maximizes the likelihood for the specified μ . In other words, it is the conditional maximum-likelihood estimator of θ and is therefore a function of μ . $L(\hat{\mu}, \hat{\theta})$ in the denominator is on the other hand maximized in an unconstrained way and $\hat{\mu}$ and $\hat{\theta}$ are the true maximum-likelihood estimators. The profile likelihood ratio, $\lambda(\mu)$, can take values between 0 and 1, where values close to 1 means, the hypothesized value of μ is in good agreement with data.

We can now define a test statistic from the profile likelihood ratio

$$t_\mu = -2 \ln \lambda(\mu) \quad (6.30)$$

where the logarithm is chosen for computational reasons and the minus is in order to again make sure the test statistic is monotonically increasing as the disagreement between data and the hypothesis gets larger.

Furthermore, we can define the test statistic for discovery of a positive signal. We notice, that the rejection of $\mu = 0$, or the background-only (b-only) hypothesis, effectively is the same as a discovery of a new signal. The special test statistic for this case is

$$q_0 = \begin{cases} -2 \ln \lambda(0) & \text{if } \hat{\mu} \geq 0 \\ 0 & \text{if } \hat{\mu} < 0 \end{cases} \quad (6.31)$$

which can be used to calculate a local p_0 -value, defined as the probability to observe an excess at least as large as the one observed in data, under the background-only hypothesis. A global p_0 -value can also be calculated by taking into account the look-elsewhere effect.

Question 6.12: When can we claim a discovery?

In particle physics, a discovery can be claimed, when the global p_0 -value is less than $3 \cdot 10^{-7}$, which means the probability of observing such an excess (or larger), given the background-only hypothesis is true, is roughly 1 in 3.5 million. This corresponds to a 5σ deviation, where σ is the standard deviation of the Gaussian probability distribution seen in Question 6.9.

6.5.3 Limit setting

In a similar way, we can define a test statistic for setting an upper limit on the signal strength μ . It is

$$q_\mu = \begin{cases} -2 \ln \lambda(\mu) & \text{if } \hat{\mu} \leq \mu \\ 0 & \text{if } \hat{\mu} > \mu \end{cases} \quad (6.32)$$

where it is important to notice that q_0 is not a special case of q_μ . More specifically, q_0 is zero, if the data fluctuates downward ($\hat{\mu} < 0$), whereas q_μ is zero, if the data fluctuates upward ($\hat{\mu} > \mu$). The reason for setting $q_\mu = 0$, when the data fluctuates upward, is that, when setting an upper limit, the upward fluctuation should not be seen as less compatible with μ than the data obtained.

For an observed test statistic, $q_{\mu,\text{obs}}$, the p -value is

$$p_\mu = \int_{q_{\mu,\text{obs}}}^{\infty} f(q_\mu | \mu, \hat{\theta}_\mu) dq_\mu \quad (6.33)$$

where $f(q_\mu | \mu, \hat{\theta}_\mu)$ is the probability density function of q_μ assuming the hypothesized μ and the nuisance parameter values, that maximized the likelihood, $\hat{\theta}_\mu$, for that μ . Then the upper limit on μ is the largest μ with $p_\mu < \alpha$, where α is the specified threshold, e.g. $\alpha = 0.05$ for a 95% confidence level (CL).

Calculating the limit in this way, however, has the unfortunate property, that if too few events are observed to account for the expected background, then any signal, and even the background itself, may be excluded at a high confidence level.

It is therefore instead common to use the CL_s method [114] for the limit setting, where we define the variable

$$\text{CL}_s = \frac{p_\mu}{1 - p_0} = \frac{\int_{q_{\mu,\text{obs}}}^{\infty} f(q_\mu | \mu, \hat{\theta}_\mu) dq_\mu}{\int_{-\infty}^{q_{\mu,\text{obs}}} f(q_\mu | 0, \hat{\theta}_0) dq_\mu} \quad (6.34)$$

from which the confidence level can be calculated as $\text{CL} = 1 - \text{CL}_s$. The integrals of the equation are shown graphically in Figure 6.3.

The probability density function f can be described by an analytic asymptotic formula referred to as the *asymptotic approximation*. This heavily decrease the time it takes to calculate the limit and is therefore often used. It is, however, good practice to check, that the approximation is valid by sampling the distribution from pseudo-experiments and compare the results, if the number of events is small.

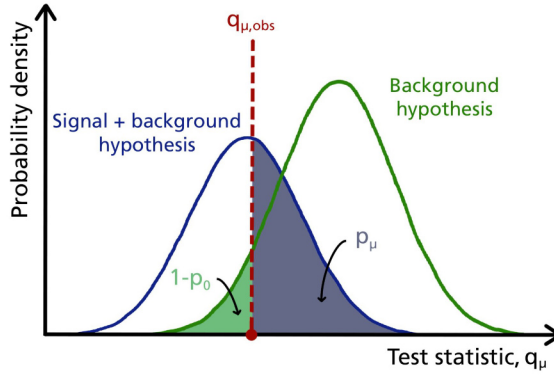


Figure 6.3: Calculation of the CL_s variable shown graphically.

In this approximation [115], it is easy to calculate the significance, Z_μ , from the test statistic by

$$Z_\mu = \sqrt{q_\mu} \quad (6.35)$$

where Z_μ often is given in terms of the standard deviation σ .

6.5.4 Wilks' test

The BUMP HUNTER and χ^2 p -values, introduced above, are also used to assess whether the fit describes the background well, when investigating, how many parameters are needed in the functional form in Equation 6.22. If several of the fits have acceptable BUMP HUNTER and χ^2 p -values, *Wilks' test* can be used to decide on the preferred number of parameters.

Question 6.13: What is Wilks' test?

Wilks' test checks, whether adding another parameter to a fit makes it significantly better at describing the distribution. The test statistic is given as

$$t = -2 \cdot \ln \left(\frac{L_{\text{FP}}}{L_{\text{MP}}} \right) \quad (6.36)$$

where L_{FP} (L_{MP}) is the likelihood of the fewest (most) parameters model. The test statistics will follow a χ^2 distribution with $N_{\text{MP}} - N_{\text{FP}}$ degrees of freedom, where N_{FP} (N_{MP}) is the number of degrees of freedom in the model with fewest (most) parameters. The p -value can then be calculated as the complementary cumulative distribution function (CCDF) of the χ^2 distribution evaluated at the observed test statistic.

If the p -value is more than the threshold α , the fit with the fewest parameters is favored, since the additional parameter is not giving a significantly better description of the distribution.

Single Particle Jet Energy Scale Uncertainty

The jet energy scale (JES) uncertainty is estimated using different methods at different p_T ranges, as we saw in Chapter 5. In-situ techniques exploiting the p_T balance between a jet and a reference object (Z , γ or multijet) are used at lower p_T , but at very high p_T (> 2 TeV) there is not enough statistics for such in-situ techniques.

Therefore, another approach is taken at the highest p_T . The JES uncertainty is estimated from the calorimeter response to single hadrons. In this approach, the jet is seen as a superposition of energy depositions coming from single particles. An uncertainty is applied to each energy deposition belonging to the particles within the jet and propagated to the final JES uncertainty.

This approach is also working at low p_T , but results in a bigger JES uncertainty than the in-situ techniques, so it is only used for the highest p_T jets. However, the calibrations, obtained with the two methods, should be in agreement, so this is checked. The results presented here are for Run 2 data. Similar results were seen in Run 1 [116].

7.1 Data sets and object selection

The jet energy response and uncertainty is derived by examining simulated dijet events using PYTHIA8 [27] with the NNPDF23LO parton distribution function set [23] and the A14 tune [117].

In these events, the reconstructed jets are formed from topological clusters of energy using the anti- k_t algorithm with distance parameter $R = 0.4$. The reconstructed jets are matched to the closest particle jets in $\eta - \phi$ space. The particle jets are formed with the same anti- k_t algorithm as the reconstructed jets but from particles instead of clusters. In this way, the energy depositions in the cells are assigned to individual particles. The energy can then be smeared according to the specifics of the particle.

7.2 Jet energy response and uncertainty

The composition of particles will vary from jet to jet due to hadronization effects. Therefore, the calorimeter response will also vary. Figure 7.1 shows the average spectra of particles inside a jet. The jet is dominated by charged pions and photons, where the spectrum of photons is softer than the spectrum of pions, since the photons are predominantly coming from decay of neutral pions, which have a similar spectrum to the charged pions.

The high energy particles contribute to a substantial part of the total jet energy, even though the jet clearly contains a lot more low energy particles. It is therefore interesting to look at the average energy fraction different types of particles contribute to the total jet energy. This is seen in Figure 7.2. As expected, the energy spectra are not as steep as the particle spectra and it becomes flatter for more energetic jets.

However, the jet energy response and uncertainty is not directly dependent on the energy of the particles, but the amount of energy the particles deposit in the calorimeter. It is therefore more interesting to look at the average energy fraction deposited in the calorimeter by different particles. This is seen in Figure 7.3.

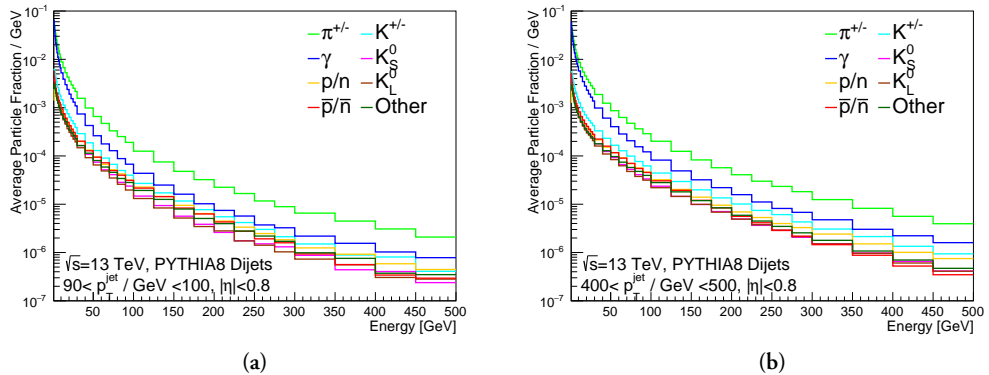
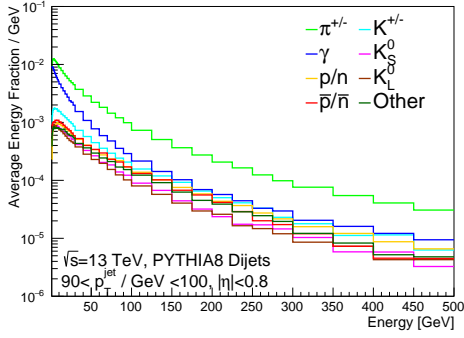


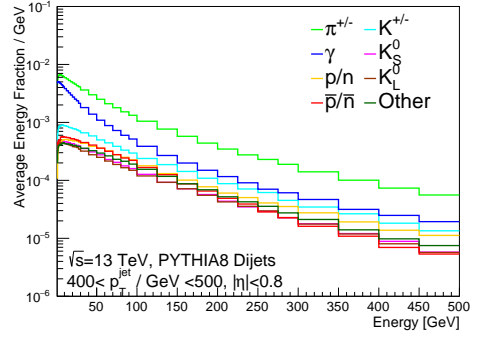
Figure 7.1: Average particle fraction as a function of the particle energy for different types of particles for jets with (a) $90 < p_T[\text{GeV}] < 100$ and (b) $400 < p_T[\text{GeV}] < 500$.

7.2.1 Jet energy scale uncertainty

The uncertainties, applied to the deposited energy in the calorimeter, can be divided into five different categories: E/p, Combined Test Beam, Out of Range, Electromagnetic Scale and Neutral. They are all treated as independent Gaussian-distributed uncertainties. They can potentially have an offset, which describe the average relative difference in the scale

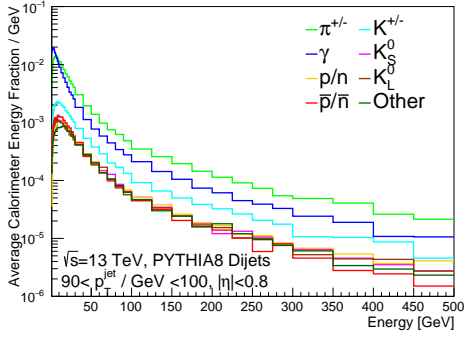


(a)

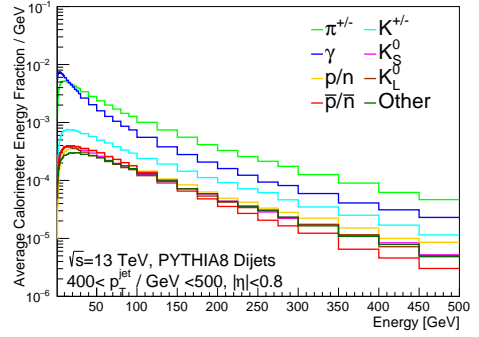


(b)

Figure 7.2: Average energy fraction as a function of the particle energy for different types of particles for jets with (a) $90 < p_T [\text{GeV}] < 100$ and (b) $400 < p_T [\text{GeV}] < 500$.



(a)



(b)

Figure 7.3: Average calorimeter energy fraction as a function of the particle energy for different types of particles for jets with (a) $90 < p_T [\text{GeV}] < 100$ and (b) $400 < p_T [\text{GeV}] < 500$.

between data and simulation. In the following, only the main contributors are described, but the full list of the different terms is given in Appendix C.

E/p : The energy response given by E/p is calculated by taking the ratio of the energy deposited in the calorimeter by a hadron to the momentum measured by the inner detector from its track. These measurements are available in the range $0.5 < p [\text{GeV}] < 30$ and $|\eta| < 2.3$. One of the major uncertainties assigned to the particles in this range is to account for the discrepancy in the energy response in data and Monte Carlo (*In situ E/p*). Another uncertainty accounts for the discrepancy in the fraction of tracks matched to zero or negative energy clusters in data and Monte Carlo (*E/p Zero Fraction*).

An uncertainty in the momentum measurement is coming from the misalignment of the

inner detector [118, 119] (*E/p Misalignment*) and yet another to account for the potential mismodeling of threshold effects in topological clustering (*E/p Threshold*).

Combined Test Beam (CTB): Measurements of the barrel calorimeter response to hadrons were done with the combined test beam [120]. They are available in the range $20 < p[\text{GeV}] < 400$ and $|\eta| < 0.8$. If a particle is in the overlap region of the E/p and CTB regions, the CTB uncertainties are applied. Here the major uncertainty also comes from the discrepancy in the energy response in data and Monte Carlo (*CTB*).

Out of Range: When a particle is outside both the E/p and CTB region, it is said to be “out of range”. In this case no measurements are available and we have to apply a conservative uncertainty to make sure, we account for the effects of saturation, punchthrough, and nonlinearity at high energy [121]. This is done by applying a 10% uncertainty to all particles in this region (*Out of Range*).

Neutral: Additional uncertainties are needed for neutral particles, since the calorimeter response in Monte Carlo depends on the physics model used [122]. An uncertainty of either 5 or 10% is applied to all neutral particles depending on whether the momentum is above or below 3 GeV (*Neutral*). For long-lived neutral kaons a bigger uncertainty of 20% is applied (K_L). This uncertainty is a bit conservative, because of the limited measurements, that were available at the time.

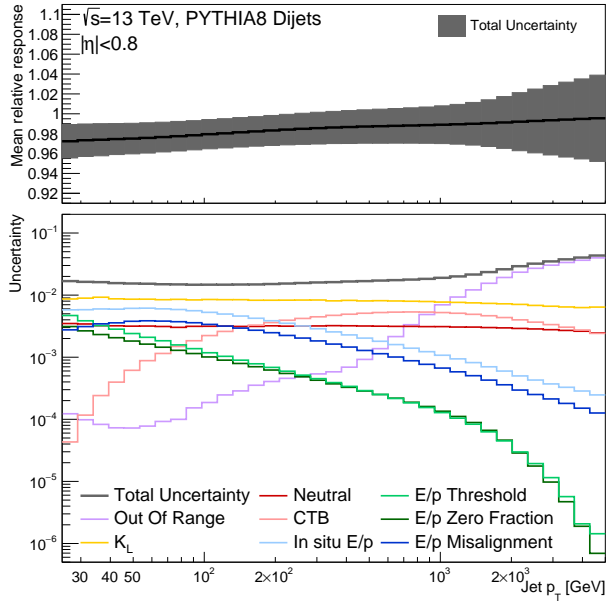
The jet energy scale response and uncertainty is seen in Figure 7.4. The upper panel shows the mean relative response with the total uncertainty as a gray band. The lower panel shows a breakdown of the most dominant contributions. At low $|\eta|$ (Figure 7.4a), the uncertainty is less than 2% for jets with $p_T < 1$ TeV, where the K_L uncertainty is dominant. Above this point the “Out of Range”-uncertainty becomes dominant. At higher $|\eta|$ (Figure 7.4b) the ‘Out of Range’-uncertainty becomes dominant already at $p_T = 80$ GeV. Below this point the “E/p Threshold”-uncertainty is the largest contributor.

The fact that two of the most dominant uncertainties are the “Out of Range” and K_L uncertainty, which both are rather conservative, calls for further investigations, such that the overall uncertainty can be reduced. However, that goes beyond the scope of these studies.

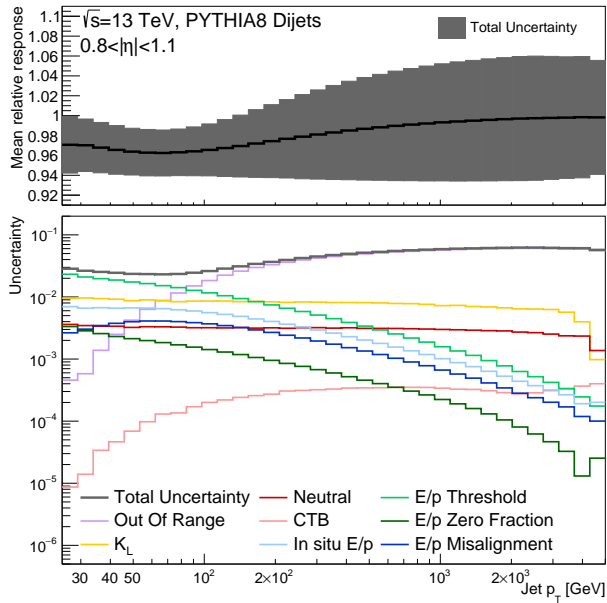
The correlations in uncertainty of jets with different p_T and $|\eta|$ is shown in Figure 7.5. As expected the uncertainty of jets, which are close in p_T and $|\eta|$ are almost fully correlated. The same is true for high p_T jets with different $|\eta|$ due to the “Out of Range”-uncertainty being the dominant uncertainty for all high p_T jets.

In Figure 7.6, a comparison between the relative response derived with this method (single hadron response) and the normal in-situ p_T balance techniques is shown. It is seen, that the methods are consistent, but this method gives an uncertainty, which is about twice as big as the normal method. However, the p_T balance method is not available for jets with

$p_T > 2$ TeV, so here the single hadron response needs to be used. We saw the effect of this change in method in Figure 5.6.



(a)



(b)

Figure 7.4: Mean relative response and JES uncertainty for jets with (a) $|\eta| < 0.8$ and (b) $0.8 < |\eta| < 1.1$.

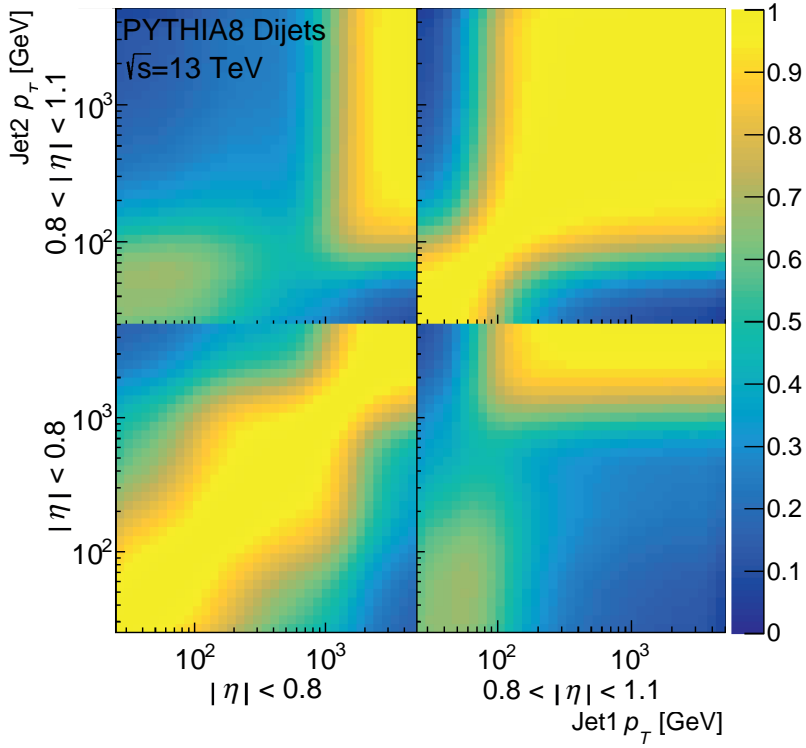


Figure 7.5: Correlation between jets with difference p_T and $|\eta|$.

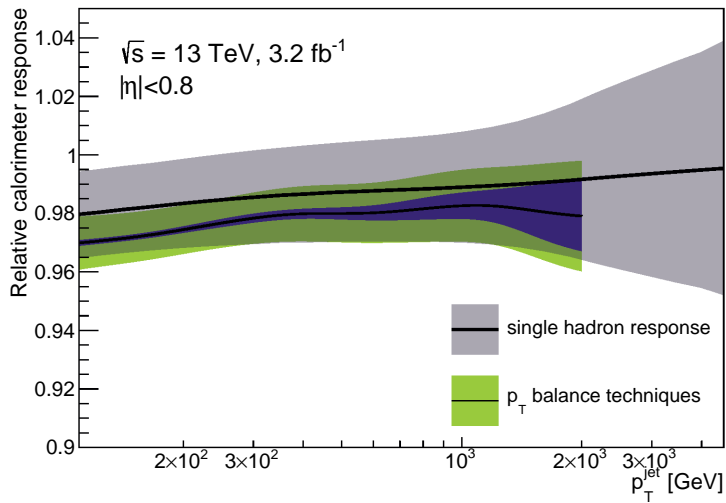


Figure 7.6: Comparison between the single hadron response and p_T balance method.

All-hadronic $t\bar{t}$ Resonance Analysis

Many observed phenomena cannot be explained by the Standard Model, like the ones highlighted in Section 2.11. One of the main interests of particle physicists today is therefore to find any hints on how to explain physics beyond the Standard Model (BSM). Here the top quark, being the heaviest elementary particle, could be of particular interest, because of its large coupling to the Higgs boson. It could therefore play a special role in the theory of electroweak symmetry breaking and help solving the hierarchy problem of the Higgs mass.

In this analysis, the final state, we are looking for, is two top quarks decaying in the all-hadronic channel. These could be decay products of the topcolor-assisted-technicolor Z'_{TC2} boson, which was introduced in 2.11.1. However, they could also origin from any other resonance that can decay into top quarks. The analysis therefore includes a model-independent search step on top of the model-dependent search for the Z'_{TC2} benchmark signal. A Feynman diagram, showing one possible outcome of a Z' boson decaying to two top quarks, which then decay hadronically, is seen in Figure 8.1.

In other words, the aim of this analysis is to localize any deviation from the smoothly falling background in the invariant mass spectrum of the two top quark candidates, $m_{t\bar{t}}$. This is done by firstly optimizing the event selection using a Monte Carlo sample of $Z'_{TC2} \rightarrow t\bar{t}$. Then applying top and b tagging in order to improve the signal to background ratio and thereby the sensitivity to a new resonance. The signal is modeled by fitting the Monte Carlo sample with an appropriate function and perform a *signal morphing*, which makes it possible to predict the signal shape at any mass. The background is also modeled by performing a functional fit. This is tested on Monte Carlo samples first, but is eventually done on data. Finally the statistical analysis is performed in order to either claim a discovery or set limits on current models.

This analysis strategy is significantly different from the one used in the previous all-hadronic $t\bar{t}$ analysis [123], which used 36.1 fb^{-1} of $\sqrt{s} = 13 \text{ TeV}$ data. The new strategy is more sensitive to the benchmark signal, as we will see in Section 8.7.3. A search in the lepton+jets

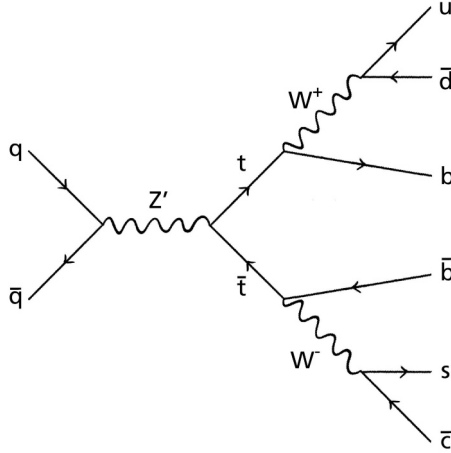


Figure 8.1: Example of the decay of a Z' boson in the all-hadronic $t\bar{t}$ channel.

channel on the same data set has also been performed in ATLAS [124], whereas CMS has made a combination of all three final states including the dilepton channel [125]. The all-hadronic analysis, presented here, is the first $t\bar{t}$ result to become public with the full Run 2 data.

A visualization of one of the highest $m_{t\bar{t}}$ events is seen in Figure 8.2. The two blue cones represent the large- R jets, where the leading jet has $p_T = 1.96$ TeV, $\eta = 0.64$, $\phi = 0.41$ and $m = 152$ GeV and the subleading jet has $p_T = 1.92$ TeV, $\eta = -0.72$, $\phi = -2.71$ and $m = 173$ GeV. They are both top tagged and the invariant mass of them is $m_{t\bar{t}} = 4.83$ TeV. The green and yellow boxes represent the energy deposits in the electromagnetic and hadronic calorimeters, respectively. Each of the large- R jets have three associated variable-radius track-jets of which one is b tagged. In the top left corner the same event is displayed, but with a higher energy thresholds to remove low- p_T particle contributions. The three-prong substructure expected for the hadronic decay of top quarks is clearly visible in the electromagnetic calorimeter.

8.1 Data and simulation

Even though this analysis is data-driven, which means, the background is estimated from data instead of relying on Monte Carlo simulations, a number of Monte Carlo samples are used in addition to the data. A list of the samples and data containers are given in Appendix D.

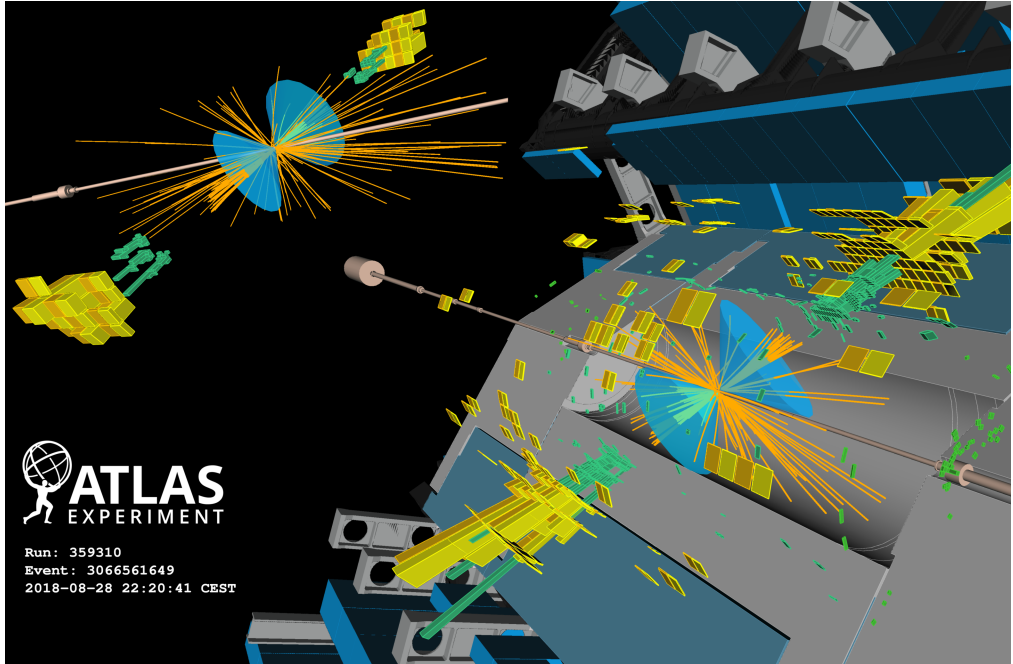


Figure 8.2: Visualization of $t\bar{t}$ event (Run=359310, Event=3066561649) [126].

8.1.1 Monte Carlo samples

Monte Carlo simulations are used to model both signal and background processes, but the background samples are only used to validate the analysis strategy, since the background is eventually estimated directly from data.

The signal samples for the Z'_{TC2} , which were introduced in Section 2.11.1, are generated using PYTHIA v8.186 [27] with the leading order (LO) NNPDF2.3 parton distribution function (PDF) set [23] and the A14 set of tuned parameters for parton shower and hadronization [117]. To bring the production cross section to next-to-leading order (NLO), it is multiplied by 1.3 [127]. The Z'_{TC2} couples only to first- and third-generation quarks and is primarily produced by quark annihilation. The model parameters are chosen, such that the $Z'_{TC2} \rightarrow t\bar{t}$ branching fraction is maximized, which means it reaches 33%. The samples are generated at different masses, which have different cross sections as summarized in Table 8.1. Furthermore, the width of the resonances are set to 1% of the mass, which is smaller than the detector resolution, as we will see in Section 8.3.4.

The background samples consist of both Standard Model $t\bar{t}$ and multijet samples. These are used to validate the analysis strategy, as mentioned above, but are also used to optimize the selection criteria and for top and b tagging studies.

Table 8.1: Masses and leading order (LO) cross sections, σ_{LO} , for the generated Z'_{TC2} samples.

$Z'_{\text{TC2}} \text{ mass [TeV]}$	1.75	2	2.25	2.5	2.75	3	4	5	6
$\sigma_{\text{LO}} \text{ [pb]}$	0.334	0.172	0.0924	0.0511	0.0289	0.0167	$2.13 \cdot 10^{-3}$	$3.31 \cdot 10^{-4}$	$7.17 \cdot 10^{-5}$

Table 8.2: Single high- p_{T} large- R jet triggers used in all-hadronic $t\bar{t}$ analysis.

Year	Name	Jet p_{T} threshold	Jet trimming
2015	HLT_j360_a10_lcw_sub_L1J100	> 360 GeV	Untrimmed
2016	HLT_j420_a10_lcw_L1J100	> 420 GeV	Untrimmed
2017-18	HLT_j460_a10t_lcw_jes_L1J100	> 460 GeV	Trimmed

The Standard Model $t\bar{t}$ events are generated using the NLO Monte Carlo generator POWHEG-Box v2 [128] with the NLO NNPDF3.0 PDF set [129]. The cross section is scaled to next-to-next-to-leading-order (NNLO) in QCD including resummation of next-to-next-to-leading logarithmic soft gluon terms with Top++2.0 [130]. Furthermore, the parton showering, hadronization and underlying event are modeled using PYTHIA v8.230 [27] with the LO NNPDF2.3 PDF set and the A14 set of tuned parameters. A few more technical details on these samples are found in Appendix D.

The multijet events are like the Z'_{TC2} events generated using PYTHIA v8.186 with the LO NNPDF2.3 PDF set and the A14 tune.

8.1.2 Data samples

The data samples used in this analysis is recorded by ATLAS from pp collisions at $\sqrt{s} = 13$ TeV in 2015-2018 (Run 2). Only data, collected during stable beam conditions and with the relevant detector components operational, is used, resulting in a integrated luminosity of 139 fb^{-1} .

In order to record the events, a number of triggers are used as described in Chapter 4. In this analysis a set of unrescaled single high- p_{T} large- R jet triggers are used. They vary for the different data-taking years and are summarized in Table 8.2. The unrescaled trigger with the lowest jet p_{T} threshold in each data-taking period is chosen, which is why it varies for the different years. Similarly, the trimmed jet triggers¹ are preferred over the untrimmed triggers, since they have better turn-on curves. However, these were not available in 2015 and 2016, so the untrimmed triggers were used.

To ensure almost 100% efficient triggers, the leading large- R jet (the one with the highest p_{T}) is required to have $p_{\text{T}} > 500$ GeV.

¹For triggers, the trimming is using $f_{\text{cut}} = 0.04$ instead of 0.05, which is used in the offline algorithm as described in Section 5.2.2. The lower value is used to avoid inefficiencies.

8.2 Event selection

Before the selection criteria are investigated, a few pre-selections are applied to the samples. First of all, each event is required to have at least one vertex associated with two or more tracks with $p_T > 500$ MeV. As mentioned in Question 4.3, the vertex with the largest $\sum p_T^2$ of associated tracks is chosen as the primary vertex. Furthermore, events are removed, if they contain electrons or muons, in order to avoid any overlap with the $t\bar{t}$ lepton+jets and dilepton analyses. The object definitions used for the electrons, muons and other physics objects are given in Appendix E.

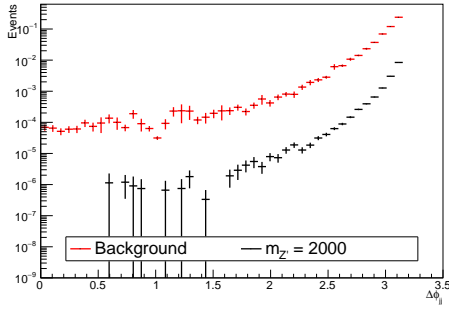
8.2.1 Kinematic selection

Since we are searching for events, where a resonance decays into two top-quarks, the main requirement is that the leading and subleading large- R jets are top tagged (see Section 8.2.2 about top tagging). In addition to this requirement, the two leading large- R jets, which we will now refer to as top jets, need to have $p_T > 350$ GeV. This requirement is necessary to enhance the presence of jets, that fully contain the top-quark decay products and to be able to use the provided tagger calibrations. Furthermore, the leading large- R jet is required to have $p_T > 500$ GeV, to ensure it is on the plateau of the trigger turn-on curve as mentioned above.

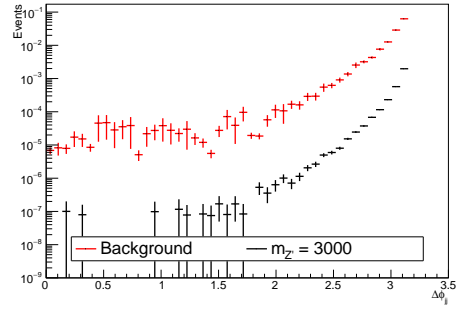
A number of variables have been investigated for finding the optimal selection cuts. This was done by applying a mass window of 20% below and above the signal peak value in both the background and signal samples and then calculating the significance given by $\frac{s}{\sqrt{b}}$ as a function of the variable cut. Here s is the number of signal events and b is the number of background events. For the background, the multijet and inclusive all-hadronic $t\bar{t}$ samples are used here. The mass window of 20% captures the main part of the signal especially at low masses. It goes from 98% at 1750 GeV to 77% at 4000 TeV, but only 60% at 5000 GeV, because of the low mass tail.

Figure 8.3 shows the azimuthal angle separation between the two top jets, $\Delta\phi_{jj}$, for a number of different Z'_{TC2} masses. It is seen that in all cases, the two top jets are reasonable back-to-back. Therefore, it is required, that the two top jets have an azimuthal angle separation larger than 1.6. It is seen from Figure 8.4, that this cut does not lower the significance for any Z'_{TC2} mass as expected. However, it does also not improve the significance either, but it can act as a quality check of the data.

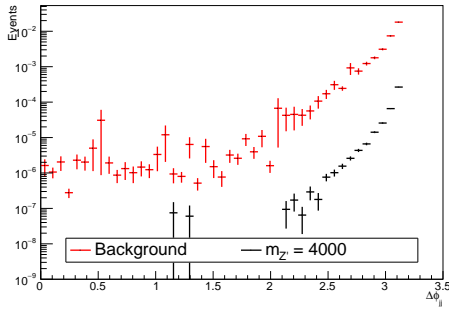
Figure 8.5 shows the rapidity difference between the two top jets, Δy_{jj} , for a number of different Z'_{TC2} masses. It is seen that for high mass, the signal jets have a smaller separation in rapidity than the background jets. In Figure 8.6 it is seen that for high Z'_{TC2} masses, the



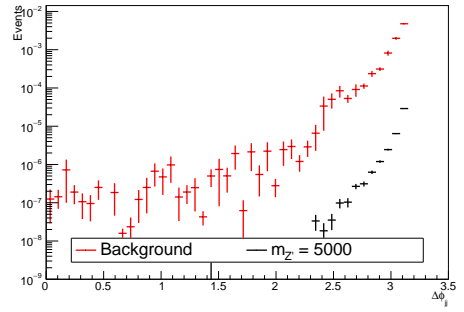
(a)



(b)

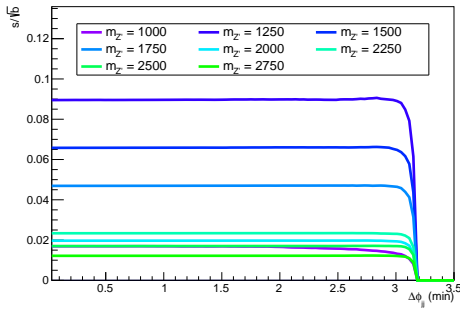


(c)

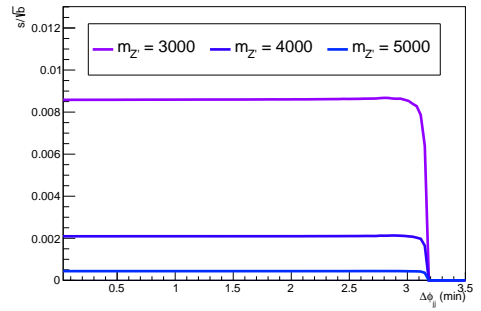


(d)

Figure 8.3: Distribution of the azimuthal angle separation, $\Delta\phi_{ij}$, for Z'_{TC2} mass of (a) 2000 GeV, (b) 3000 GeV, (c) 4000 GeV and (d) 5000 GeV.

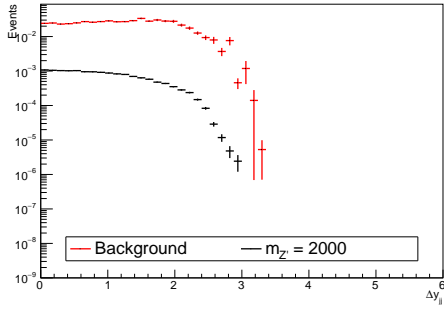


(a)

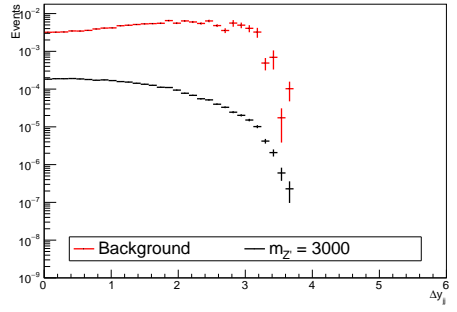


(b)

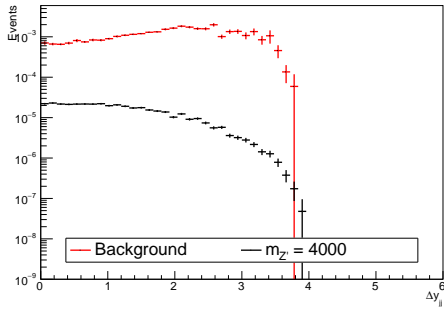
Figure 8.4: Significance as a function of the minimum cut value of the azimuthal angle separation, $\Delta\phi_{ij}$, for Z'_{TC2} signal for (a) low masses and (b) high masses.



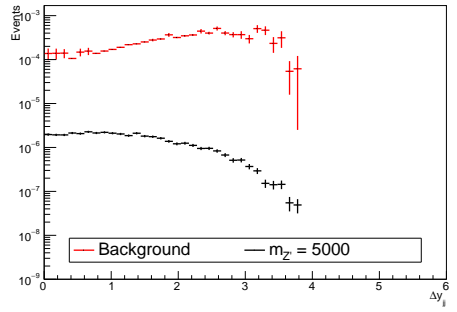
(a)



(b)

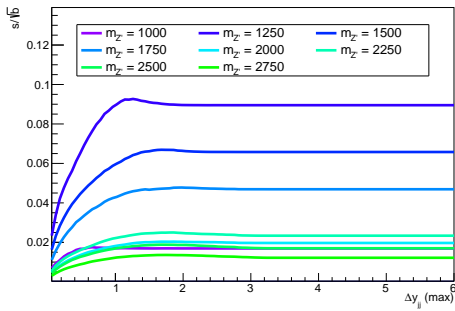


(c)

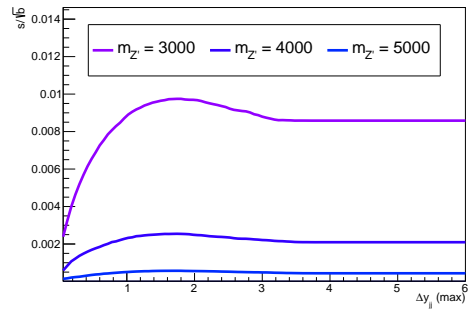


(d)

Figure 8.5: Distribution of the rapidity difference, Δy_{jj} , for Z'_{TC2} mass of (a) 2000 GeV, (b) 3000 GeV, (c) 4000 GeV and (d) 5000 GeV.



(a)



(b)

Figure 8.6: Significance as a function of the maximum cut value of the rapidity difference, Δy_{jj} , for Z'_{TC2} for (a) low masses and (b) high masses.

significance is highest with a cut of $\Delta y_{jj} < 1.8$. Therefore, the two top jets are required to have a rapidity difference smaller than 1.8 to better reject the Standard Model background produced in t -channel processes.

Other variables such as the transverse momentum of the two top jets (Figure 8.7), the p_T balance, $A = \frac{p_{T1} - p_{T2}}{p_{T1} + p_{T2}}$ (Figure 8.8a) and the rapidity boost, $y_B = \frac{y_1 + y_2}{2}$ (Figure 8.8b) were also investigated, but it was decided to not apply cuts on any of them.

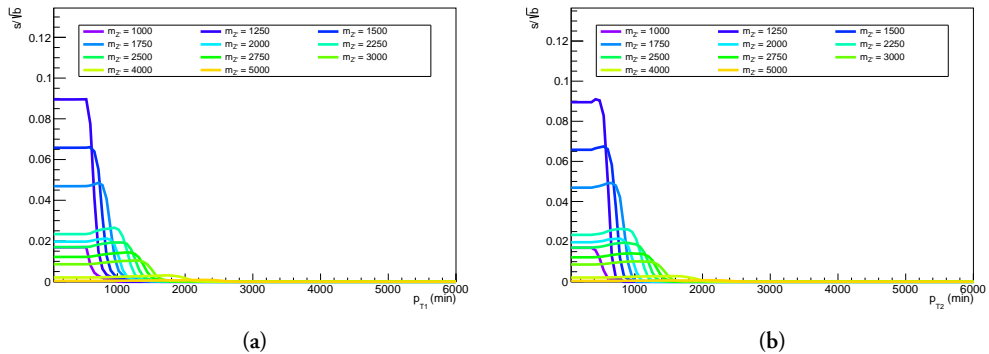


Figure 8.7: Significance as a function of the minimum cut value of (a) transverse momentum of the leading top jet, p_{T1} , and (b) transverse momentum of the subleading top jet, p_{T2} .

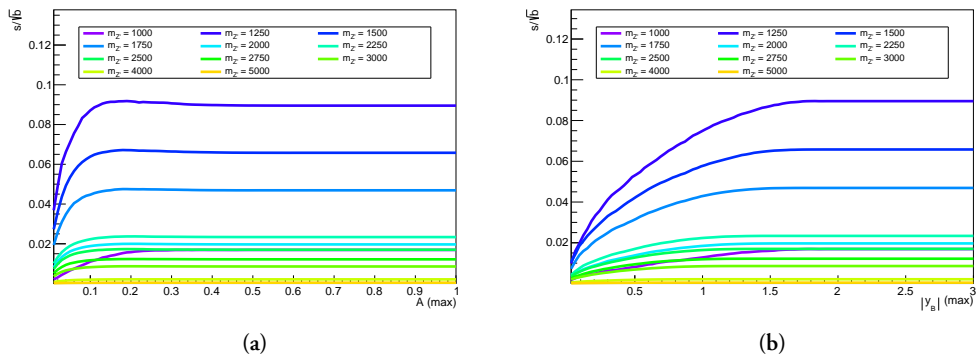


Figure 8.8: Significance as a function of the maximum cut value of (a) the p_T balance, A , and (b) the rapidity boost, y_B .

8.2.2 Top tagging

The deep neural network (DNN) top tagger, that was introduced in Section 5.3, has been optimized for this analysis. It was retrained in the newest software release (R21) and the fixed signal efficiency working points were derived for the fully-contained configuration.

Signal significance based working points were studied, but the fixed 80% efficiency working point was found to provide similar sensitivity across the full mass range and was therefore used. The 80% efficiency working point corresponds to a rejection of light-quark and gluon jets of approximately 30 at a large- R jet $p_T = 500$ GeV and 12 at $p_T = 3000$ GeV.

8.2.3 b tagging

For the b tagging, the DL1 algorithm, which was also introduced in Section 5.3, is used with the 77% efficiency working point on variable-radius (VR) track jets, which were defined in Section 5.1.5. This requirement has corresponding rejection factors of approximately 5 and 128 for jets containing c -hadrons and light-quark jets, respectively.

The b tagging requirement is used to define two *signal regions*. In the $1b$ signal region, either the leading or the subleading top jet is matched to a b -tagged VR track jet within a cone of radius $\Delta R < 1.0$. Whereas in the $2b$ signal region, both top jets are matched to a b -tagged jet.

8.2.4 Summary

Table 8.3 gives a summary of the selection criteria, which were presented above. As also mentioned above, the analysis has two signal regions: the $1b$ signal region and the $2b$ signal region. The $2b$ signal region is expected to provide a better sensitivity, but as we will see later, the contribution to the sensitivity from the $1b$ signal region is not negligible.

Table 8.3: Event selection criteria for the all-hadronic $t\bar{t}$ analysis.

Observable	Requirement
Leading large- R jet transverse momentum	$p_{T,1} > 500$ GeV
Subleading large- R jet transverse momentum	$p_{T,2} > 350$ GeV
Azimuthal angle separation	$\Delta\phi_{jj} > 1.6$
Rapidity difference	$\Delta y_{jj} < 1.8$
Top tagging	
Both leading large- R jets should fulfill the DNN 80% working point	
b tagging	
Either one ($1b$) or both ($2b$) leading large- R jets should be matched to a VR track jet that fulfill the DL1 77% working point	

The acceptance of Z'_{TC2} signal events is calculated at the truth (or generator) level. The four kinematic cuts given in Table 8.3 are for this study applied to the truth variables instead of the reconstructed variables. The acceptance is defined as the fraction of Z'_{TC2} signal events, that fulfill the kinematic requirements, have the top decay products contained inside the

leading large- R truth jets (fully-contained requirement) and do not include any electrons or muons with $p_T > 25$ GeV and $\eta < 2.5$.

The acceptance times efficiency is the fraction of events that fulfill the full analysis selection on the reconstructed variables including the top- and b -tagging requirements. This means the events that pass the acceptance times efficiency requirements are not necessarily a subset of the events that pass the acceptance requirements, since some *fake* contribution can occur.

The acceptance and the acceptance times efficiency is seen for the two signal regions as a function of the invariant mass of the top-quark pair at the generator level, $m_{t\bar{t}}^{\text{gen}}$, in Figure 8.9. It is seen, that the acceptance increase at higher invariant mass values, which is mostly due to the fact, that the top quarks get more boosted and the fully-contained requirement gets fulfilled easier. It is also seen, that the acceptance times efficiency is approximately 5%.

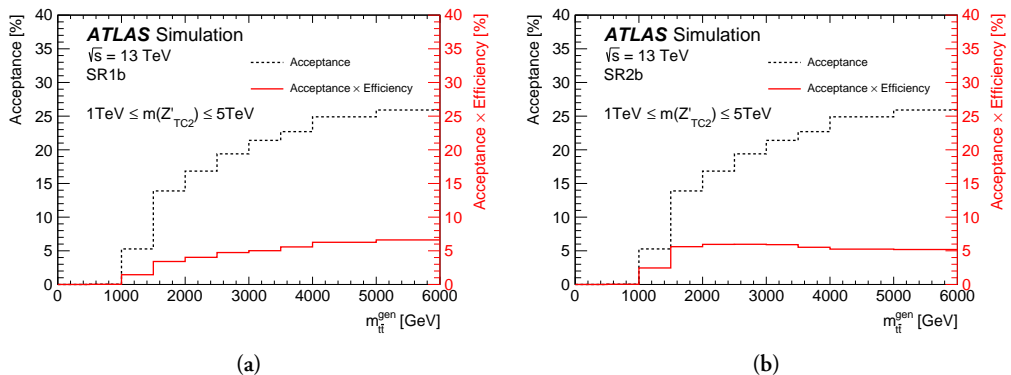


Figure 8.9: The acceptance (black) and the acceptance times efficiency (red) as a function of the invariant mass $m_{t\bar{t}}^{\text{gen}}$ for (a) the $1b$ signal region and (b) the $2b$ signal region [131].

8.3 Background modeling

The background modeling is done by making a global fit to the invariant mass, $m_{t\bar{t}}$, distribution. In order to test the background modeling procedure and estimate the uncertainties on it, a sample, which is similar to what is expected in data, is needed. This is the case, because the data in the signal regions is *blinded*.

Question 8.1: What is a blind analysis?

To do a *blind analysis* means you are setting up and testing your analysis from start to finish without looking at the data in the region, where you expect a signal. This is done to make sure you are not being biased by what you see. It also means, that you are not allowed to make any changes to the event selection, tagger or fitting procedure after the *unblinding* of the data.

The sample used for testing the analysis can either be a Monte Carlo sample or a data-driven sample. In our case, we are using a combination of both. The background Monte Carlo samples have been introduced above, so we will now discuss the data-driven sample.

8.3.1 ABCD method

The data-driven sample used to estimate the multijet background in the signal region is derived with an *ABCD method*. The ABCD method used for this analysis is a bit more complicated, than what was introduced in Chapter 6, since it includes two selection variables for two leading large- R jets, such that the result is a 4×4 matrix and not just a 2×2 matrix.

The selections are the top tagging requirement of the large- R jets and the matching of the large- R jet to a b -tagged VR track jet. Furthermore, the calculations are done *bin-by-bin* and are not just a single number. The details on the ABCD method used for this analysis is described in the paper [131]

8.3.2 Effective entries

It is important, that the sample, that is used for the testing of the background modeling, has at least as good statistics as what is expected in data. Otherwise the statistical fluctuations and uncertainties would be larger and make the test unreliable. To check whether the sample has sufficient statistics, it is useful to calculate the *effective entries*, which are defined as

$$N_{\text{effective}} = \left(\frac{\text{bin content}}{\text{bin error}} \right)^2. \quad (8.1)$$

It should be noted, that if $N_{\text{effective}}$ was calculated for data, it would be equal to the bin content, since the bin error is the square root of the bin content. The statistics is sufficient, if the number of effective entries is larger than the sample scaled to the expected luminosity in data.

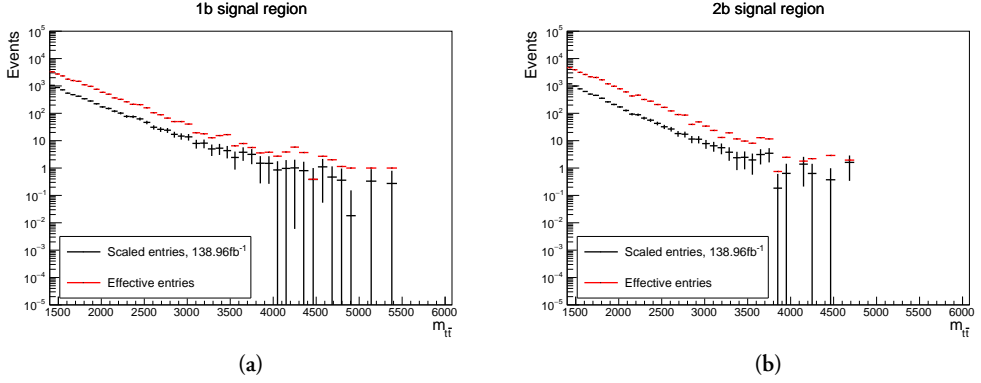


Figure 8.10: The effective entries (red) compared to the Monte Carlo $t\bar{t}$ distribution scaled to the expected luminosity in data (black) for the (a) $1b$ signal region and (b) $2b$ signal region.

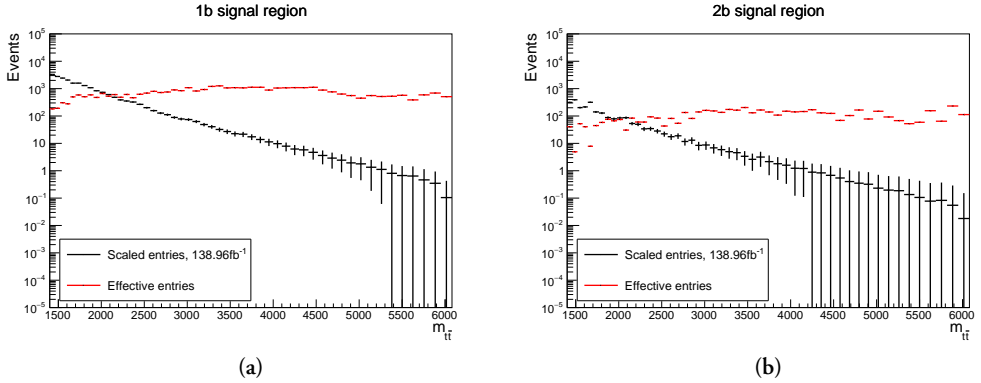


Figure 8.11: The effective entries (red) compared to the Monte Carlo multijet distribution scaled to the expected luminosity in data (black) for the (a) $1b$ signal region and (b) $2b$ signal region.

Figure 8.10 shows the effective entries compared to the scaled sample for the Monte Carlo $t\bar{t}$ background. It is seen, that there is sufficient statistics over the whole range. Unfortunately, that is not the case for the Monte Carlo multijets sample, which is seen in Figure 8.11. Below approximately 2.1 TeV the effective entries is less than the scaled multijet sample in both the $1b$ and $2b$ signal region.

Looking at the effective entries compared to the scaled sample for the data-driven multijets in Figure 8.12, it is seen that for this distribution the statistics is much better at low mass. However, the statistics is instead insufficient above 3.3 TeV in the $1b$ signal region and above 4.3 TeV in the $2b$ signal region.

Since neither the Monte Carlo or data-driven multijet sample have enough statistics over the full range, they have been combined.

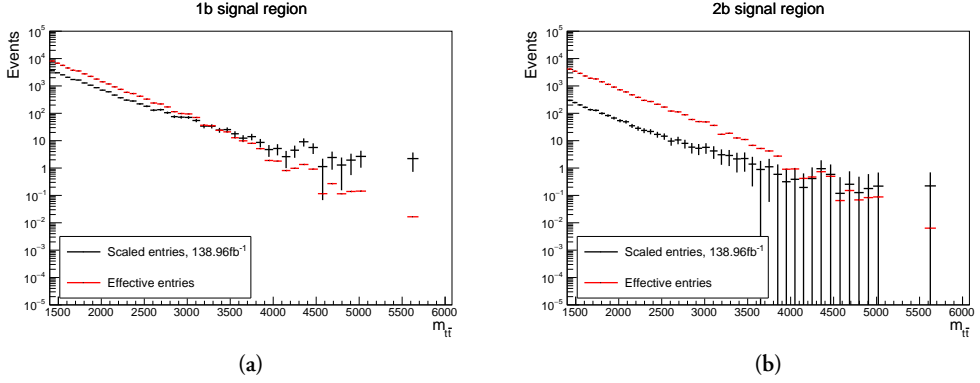


Figure 8.12: The effective entries (red) compared to the data-driven multijet distribution scaled to the expected luminosity in data (black) for the (a) $1b$ signal region and (b) $2b$ signal region.

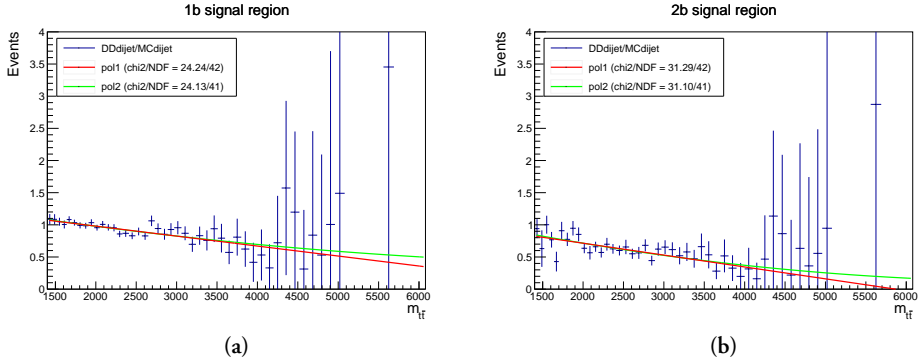


Figure 8.13: Ratio of the mass spectrum from the data-driven and Monte Carlo samples for the (a) $1b$ signal region and (b) $2b$ signal region fitted with a first order (red) and second order (green) polynomial.

8.3.3 Combined multijet sample

The data-driven sample can be used at low mass, but at higher mass, the Monte Carlo sample has much better statistics. However, the data-driven sample has a shape that resembles the expected data better than the Monte Carlo. Therefore, the Monte Carlo needs to be corrected with a factor derived from the ratio of the data-driven sample and the Monte Carlo sample. This correction factor is found by fitting the ratio with a polynomial as seen in Figure 8.13. Both a first and second order polynomial was tried.

Figure 8.14 shows a comparison of the corrected mass spectra with first and second order polynomial corrections to the original Monte Carlo and data-driven spectra. It is clear that the correction is needed to be able to stitch the data-driven and Monte Carlo samples.

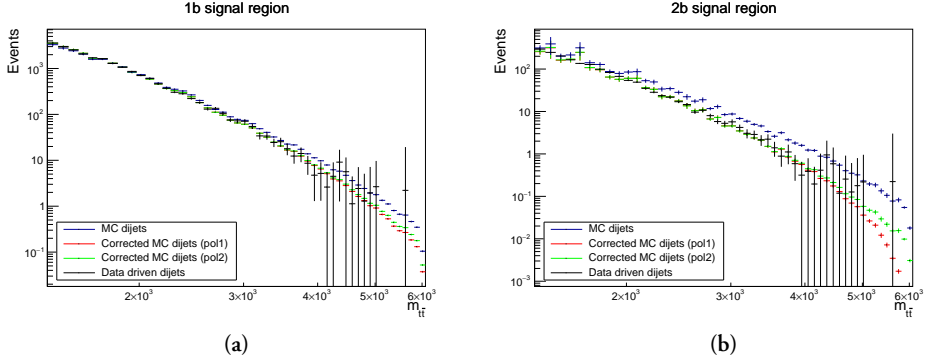


Figure 8.14: Comparison of corrected Monte Carlo samples to the original Monte Carlo and data-driven samples for the (a) $1b$ signal region and (b) $2b$ signal region.

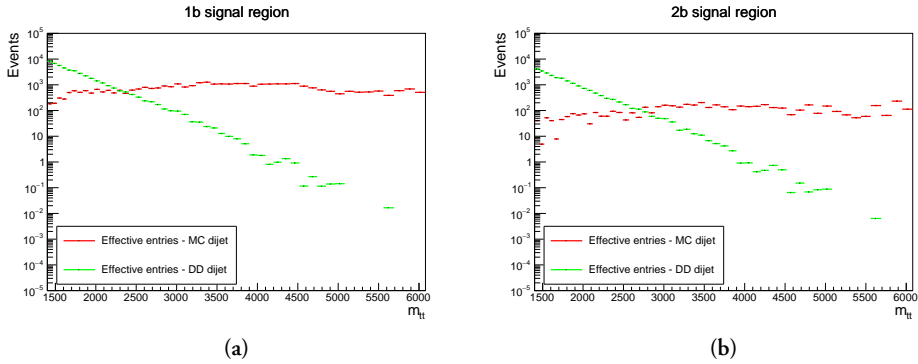


Figure 8.15: Comparison of the effective entries of the Monte Carlo and data-driven samples for the (a) $1b$ signal region and (b) $2b$ signal region.

To decide at which mass the switch, from the data-driven to the corrected Monte Carlo sample, should happen, the effective entries of the samples are compared. This is seen in Figure 8.15. It is seen, that the statistics is better for the Monte Carlo sample above 2410 GeV and 2730 GeV for the $1b$ and $2b$ signal regions, respectively. These values are therefore used for the stitch points. So for the combined samples, the data-driven sample is used below the stitch point and the corrected Monte Carlo is used above.

A comparison of the combined multijet samples (with Poisson errors) and the data-driven sample is seen in Figure 8.16. Within the uncertainty there is no difference between the first and second order polynomial correction, so the first order polynomial is used.

Figure 8.17 shows the effective entries of the combined multijet sample and Monte Carlo $t\bar{t}$ combined. It is evident, that the statistics is sufficient and this spectrum is therefore well-suited to test the background estimation procedure.

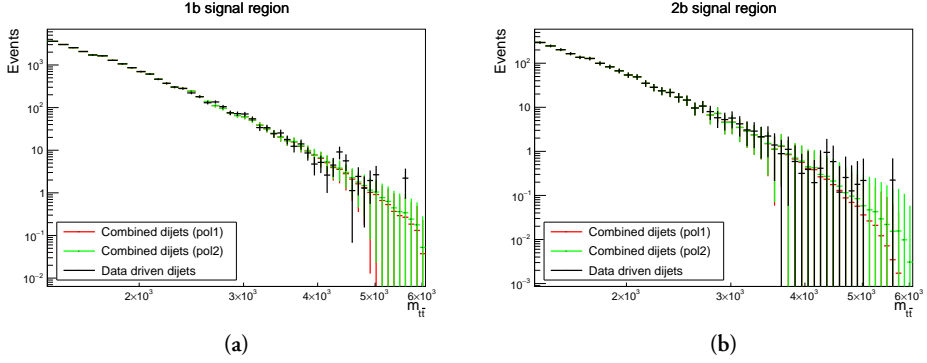


Figure 8.16: Comparison of the combined multijet samples and the data-driven sample for the (a) $1b$ signal region and (b) $2b$ signal region.

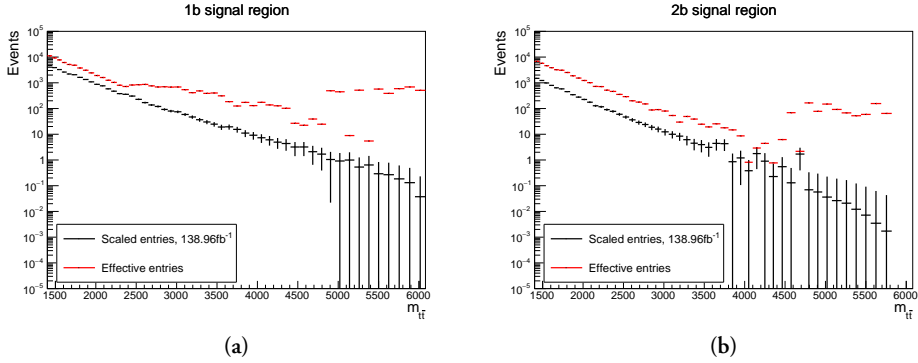


Figure 8.17: The effective entries (red) compared to the combined multijet and Monte Carlo $t\bar{t}$ distribution scaled to the expected luminosity in data (black) for the (a) $1b$ signal region and (b) $2b$ signal region.

Figure 8.18 shows the the combined multijet sample (red) and Monte Carlo $t\bar{t}$ sample (purple) in a stacked histogram. It is seen, that in the $2b$ signal region, the two components are equally important, whereas in the $1b$ signal region, the multijets are dominant.

8.3.4 Fitting range and binning

Before the fitting procedure can be tested on the sample, the fitting range and the $m_{t\bar{t}}$ binning has to be determined. It was decided to start the fitting at 1400 GeV, since the $m_{t\bar{t}}$ distribution is affected by the leading large- R jet p_T cut of 500 GeV below this point, which makes it harder to fit the distribution.

The end point of the fitting is set to 6910 GeV, but it will only fit up until the last non-empty bin, so since there are no events above 5820 GeV in the $2b$ signal region, the fitting

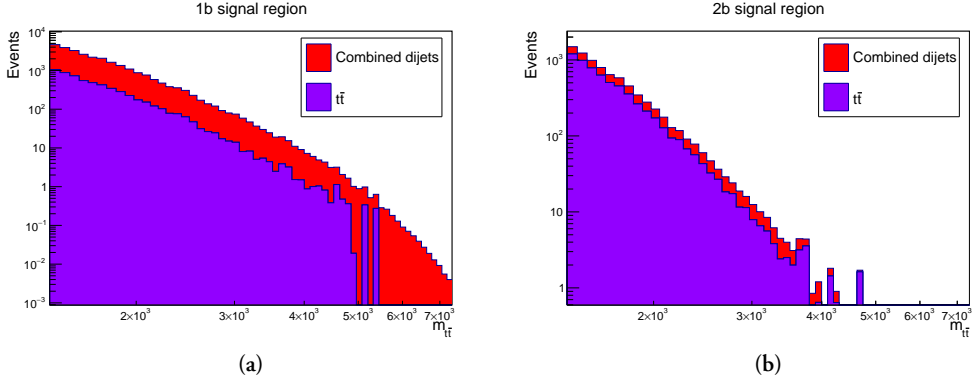


Figure 8.18: The background sample with the combined multijet (red) and Monte Carlo $t\bar{t}$ (purple) for the (a) $1b$ signal region and (b) $2b$ signal region. The samples are scaled to 139 fb^{-1} .

range will be 1400 GeV to 5820 GeV in this region for the testing of the fitting procedure. However, if there would have been events in the data above this point, they would also have been included in the fit.

Regarding the $m_{t\bar{t}}$ binning, we want to maximize the number of bins in order to be able to detect as narrow resonances as possible. However, we want the binning to be coarser than the detector resolution in order to limit the effects of bin-to-bin migration. Therefore, a study has been performed to find the detector resolution, so the bin size can be determined accordingly.

To find the detector resolution, the ratio $m_{jj}^{\text{reco}}/m_{jj}^{\text{truth}}$ is plotted for several m_{jj}^{truth} ranges. Here m_{jj}^{reco} is the reconstructed invariant mass of the two leading large- R jets and m_{jj}^{truth} is the invariant mass of the truth large- R jets matched to the reconstructed jets. The ratios are fitted with a Gaussian distribution as seen in the example in Figure 8.19a. The detector resolution is given by the width divided by the mean of the Gaussian, σ/μ .

In Figure 8.19b, the measured detector resolution is plotted as a function of m_{jj}^{truth} . The x -value for each m_{jj}^{truth} range is set to the mean value of m_{jj}^{truth} in that range and the uncertainty on the y -axis is propagated from the Gaussian fits. The points are fitted with a function of the form $\frac{a}{m_{jj}^{\text{truth}}} + \frac{b}{\sqrt{m_{jj}^{\text{truth}}}} + c$.

The bins are derived from this function with the requirements, that the bins should be larger than the detector resolution, the bin width should be a multiple of 10 GeV and start from 1400 GeV. It is seen in Figure 8.20a, that the bin resolution, given by the bin center divided by the bin width, is approximately larger than or equal to the detector resolution as wanted. In fact the bin resolution is between 99-114% of the detector resolution as seen in Figure 8.20b.

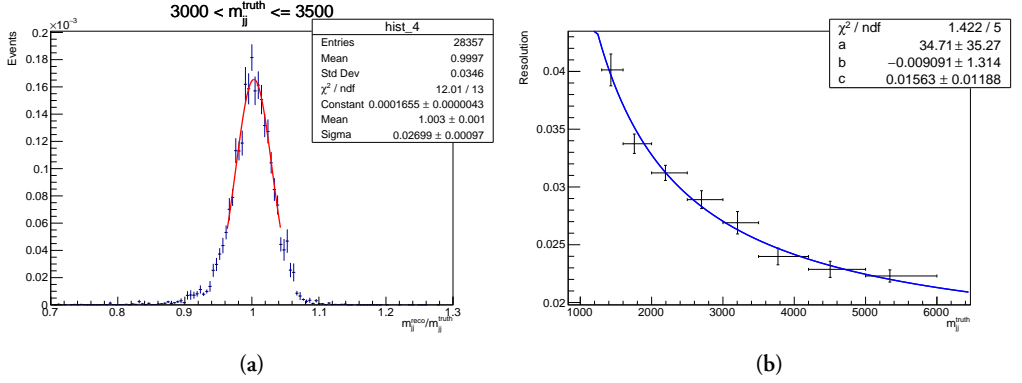


Figure 8.19: The detector resolution is found from a Gaussian fit to $m_{jj}^{\text{reco}}/m_{jj}^{\text{truth}}$. Here (a) shows an example for events with $3000 \text{ GeV} < m_{jj}^{\text{truth}} \leq 3500 \text{ GeV}$ and (b) shows the resolution as a function of the m_{jj}^{truth} fitted with a distribution of the form $\frac{a}{m_{jj}^{\text{truth}}} + \frac{b}{\sqrt{m_{jj}^{\text{truth}}}} + c$

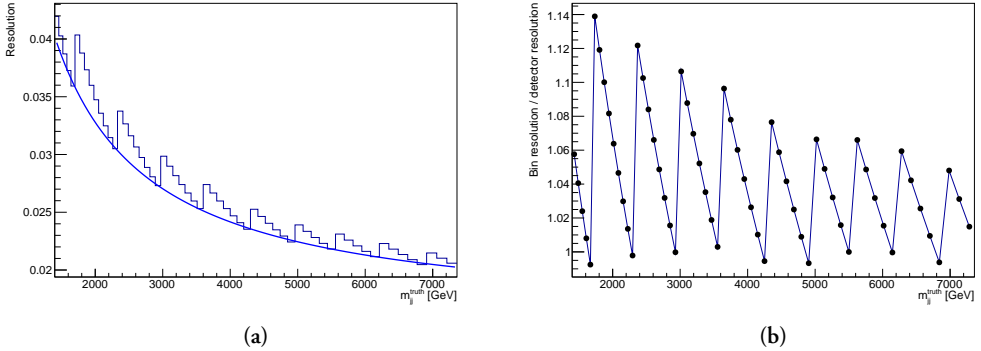


Figure 8.20: The bin resolution (black) is approximately larger than or equal to the fit representing the detector resolution (blue). Here (a) shows a comparison as a function of the m_{jj}^{truth} and (b) shows the ratio.

8.3.5 Global fit requirements

The functional form, that was introduced in Equation 6.22, is tested for this analysis in the 3-, 4- and 5-parameter form:

$$f_3(x) = p_0(1-x)^{p_1}x^{p_2}, \quad (8.2)$$

$$f_4(x) = p_0(1-x)^{p_1}x^{p_2+p_3 \ln x}, \quad (8.3)$$

$$f_5(x) = p_0(1-x)^{p_1}x^{p_2+p_3 \ln x+p_4(\ln x)^2}. \quad (8.4)$$

Table 8.4: Requirements on the various p-values for the fit.

P-value	Requirement
χ^2	> 0.05
BUMPHUNTER	> 0.01
Wilks'	> 0.10

The number of parameters needed, usually depends on the number of events. In the dijet analysis, it has been seen, that as the integrated luminosity grows, more parameters are needed in order to give a good description of the distribution.

The quality of the fit can be evaluated by looking at the χ^2 and BUMPHUNTER p-values, which were introduced in Chapter 6. Furthermore, Wilks' test can be used to decide on the number of parameters, if several of the functions fulfill the χ^2 and BUMPHUNTER p-value requirements. The requirements on the p-values for this analysis have been inspired by those used in similar analyses and are summarized in Table 8.4.

8.3.6 Pseudo-experiments

It is possible to check the fitting procedure directly on the combined multijet and Monte Carlo $t\bar{t}$ sample, which was presented in Section 8.3.3, however the data will fluctuate around these values, so in order to assess the robustness of the method, it is tested on pseudo-experiments thrown from the original distribution.

A pseudo-experiment is produced by fluctuating each bin content by assigning a random value from a Poisson distribution with a mean of the original bin content. The error is set as the square root of the new bin content. A set of 1000 pseudo-experiments is created.

The set of pseudo-experiments is used to determine the amount of fit parameters, that is expected to be needed to describe the data well. It is also used to estimate the background modeling systematic uncertainties, which will be described in Section 8.5.

8.3.7 Choice of fit function

The Wilks' p-value is calculated for each of the pseudo-experiments for the 3-parameter fit compared to the 4-parameter fit and for the 4-parameter fit compared to the 5-parameter fit, where the fits fulfill the χ^2 and BUMPHUNTER p-value requirements given in Table 8.4. The distribution of the Wilks' p-values is seen in Figure 8.21 and 8.22.

As mentioned above, if the p-value is less than 0.1, the fit with more parameters is preferred. It is seen that for the $1b$ signal region, 3 parameters are almost never enough, since 4 parameters are preferred over 3 in 92% of the cases. Whereas 4 parameters are the preferred

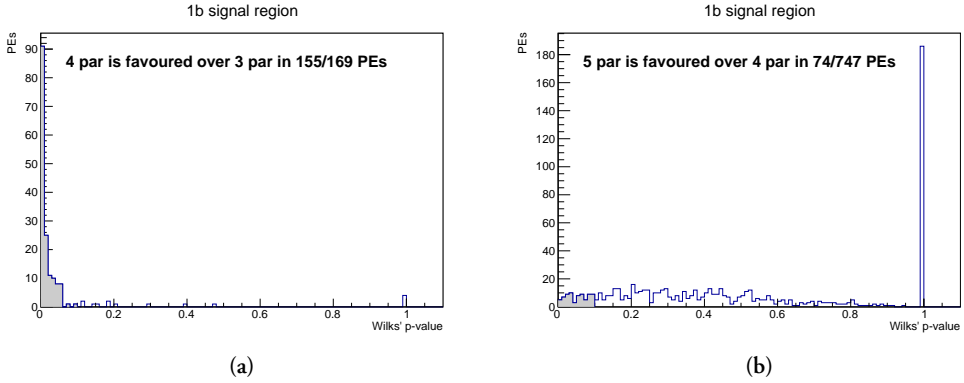


Figure 8.21: Wilks' p-value for the pseudo-experiments comparing good fits with (a) 3 and 4 parameters and (b) 4 and 5 parameters in the $1b$ signal region. The gray histogram indicates the pseudo-experiments, where the higher number of parameters are favored.

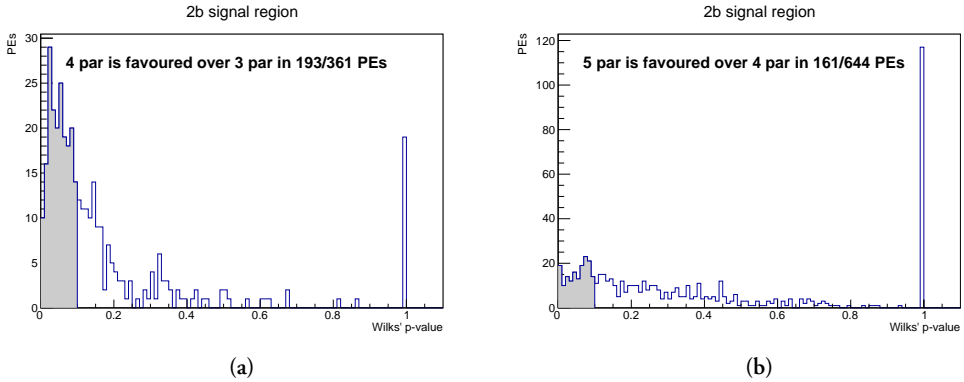


Figure 8.22: Wilks' p-value for the pseudo-experiments comparing good fits with (a) 3 and 4 parameters and (b) 4 and 5 parameters in the $2b$ signal region. The gray histogram indicates the pseudo-experiments, where the higher number of parameters are favored.

number over 5 parameters in 90% of the cases. In the $2b$ signal region, the result is not as clear. In 53% of the cases the 4-parameter fit is favored over the 3-parameter fit. But in a significant fraction, 25%, of the pseudo-experiments the 5-parameter fit is also favored over the 4-parameter fit. It is therefore quite hard to predict, how many parameters are needed in the data, especially in the $2b$ signal region. However, it was decided based on this study combined with the spurious signal study, which will be described below, that the 4-parameter fit will be used in data in both signal regions. In addition, it was checked that the background estimation procedure is able to detect an injected signal in a so-called *signal injection test*. The test showed a good agreement between the injected and subtracted signal, but with a slight overestimation, that however was below 10% at all masses.

8.4 Signal modeling

As explained in Section 8.1.1, the signal is generated for a number of Z'_{TC2} masses listed in Table 8.1. We would however like to do the statistical analysis for masses in between those points as well. Therefore, a functional form is used to model the signal $m_{\tilde{t}}$ distribution and create interpolated signal templates for masses where Monte Carlo samples are not available.

The modeling was first done with the sum of a reversed Landau and a Gaussian function. The Landau function is given by

$$l(x; \mu_L, c) = \frac{1}{\pi c} \int_0^\infty e^{-t} \cos \left[t \left(\frac{x - \mu_L}{c} \right) + \frac{2t}{\pi} \ln \left(\frac{t}{c} \right) \right] dt \quad (8.5)$$

and has two free parameters, a location parameter, μ_L , which corresponds approximately to the most probable value and a scale parameter, c . The Gaussian function is given by

$$g(x; \mu, \sigma) = \frac{1}{\sqrt{2\pi\sigma^2}} e^{-\frac{(x-\mu)^2}{2\sigma^2}} \quad (8.6)$$

and it also has two free parameters, the mean value μ and the standard deviation σ . The resulting fit function is then

$$f_{\text{RL+G}}(x; k, \mu, \sigma, \mu_L, c) = k \cdot g(x; \mu, \sigma) + (1 - k) l(-x; \mu_L, c) \quad (8.7)$$

where $0 < k < 1$ is a fractional coefficient and we see the Landau function is reversed by substituting $x \rightarrow -x$. The reversed Landau describes the signal peak and the low mass tail, whereas the Gaussian helps describe the high mass tail.

However, it turned out that the sum of a Crystal Ball function [132, 133] and a Gaussian function describes the distribution even better. The Crystal Ball function is essentially a Gaussian distribution at the core connected with a power-law distribution describing the lower tail. It is given by

$$h(x; \alpha_{\text{CB}}, n_{\text{CB}}, \mu_{\text{CB}}, \sigma_{\text{CB}}) = N \cdot \begin{cases} \exp\left(-\frac{(x-\mu_{\text{CB}})^2}{2\sigma_{\text{CB}}^2}\right), & \text{for } \frac{x-\mu_{\text{CB}}}{\sigma_{\text{CB}}} > -\alpha_{\text{CB}} \\ A \cdot \left(B - \frac{x-\mu_{\text{CB}}}{\sigma_{\text{CB}}}\right)^{-n_{\text{CB}}}, & \text{for } \frac{x-\mu_{\text{CB}}}{\sigma_{\text{CB}}} \leq -\alpha_{\text{CB}} \end{cases} \quad (8.8)$$

where

$$A = \left(\frac{n_{\text{CB}}}{|\alpha_{\text{CB}}|} \right)^{n_{\text{CB}}} \cdot \exp \left(-\frac{|\alpha_{\text{CB}}|^2}{2} \right) \quad (8.9)$$

$$B = \frac{n_{\text{CB}}}{|\alpha_{\text{CB}}|} - |\alpha_{\text{CB}}| \quad (8.10)$$

$$N = \frac{1}{\sigma_{\text{CB}}(C + D)} \quad (8.11)$$

$$C = \frac{n_{\text{CB}}}{|\alpha_{\text{CB}}|} \cdot \frac{1}{n_{\text{CB}} - 1} \cdot \exp \left(-\frac{|\alpha_{\text{CB}}|^2}{2} \right) \quad (8.12)$$

$$D = \sqrt{\frac{\pi}{2}} \left(1 + \operatorname{erf} \left(\frac{|\alpha_{\text{CB}}|}{\sqrt{2}} \right) \right) \quad (8.13)$$

where erf is the error function. It is seen, that the function has four free parameters, α_{CB} , n_{CB} , μ_{CB} and σ_{CB} . The fit function then instead takes the form

$$f'_s(x; k, \mu, \sigma, \alpha_{\text{CB}}, n_{\text{CB}}, \mu_{\text{CB}}, \sigma_{\text{CB}}) = k \cdot g(x; \mu, \sigma) + (1 - k) b(x; \alpha_{\text{CB}}, n_{\text{CB}}, \mu_{\text{CB}}, \sigma_{\text{CB}}). \quad (8.14)$$

So in total, the fit function has seven shape parameters and an additional normalization parameter. A restriction is put on the Gaussian μ to always be larger than μ_{CB} . This is done to ensure, that the Gaussian does not move to low $m_{\tilde{t}\bar{t}}$ values to fit the low-mass tail for the high $Z'_{\text{TC}2}$ masses.

The fits to the Monte Carlo samples are seen in Figure 8.23 and 8.24 for the $1b$ and $2b$ signal region, respectively. It is seen, that the low-mass tail is not well described for the 5 and 6 TeV signal (Figure 8.23h, 8.23i, 8.24h and 8.24i), but this is not expected to have a large effect on the limit due to the steeply falling background. This is confirmed by the following studies.

The eight free parameters are either linear interpolated between or fitted with a polynomial function to estimate the value of the parameters at masses not available in the Monte Carlo samples. The distribution of the variables are seen in Figure 8.25 and 8.26 for the $1b$ and $2b$ signal region, respectively.

Both the Gaussian μ and μ_{CB} are fitted with a first order polynomial, whereas the Gaussian σ is fitted with a second order polynomial and the normalization is fitted with a third order polynomial. The rest of the parameters are linear interpolated. For n_{CB} , the logarithm of the value is taken before doing the interpolation, since it makes the distribution more linear.

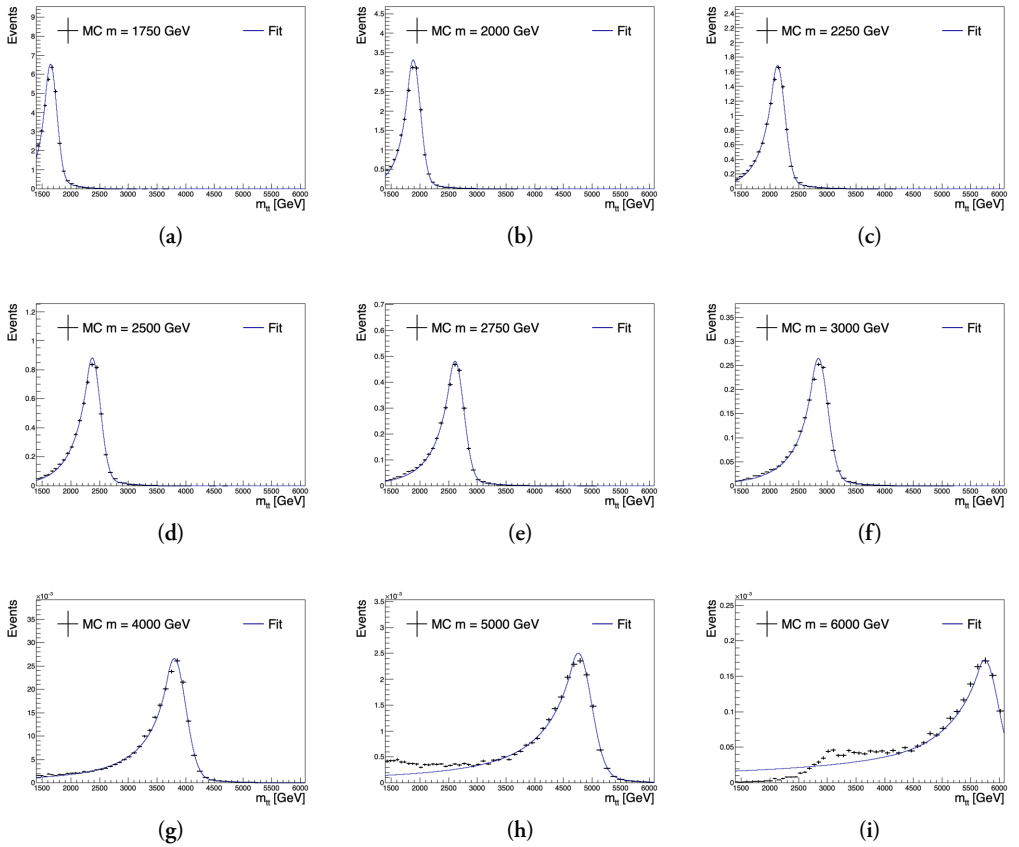


Figure 8.23: Crystal Ball plus Gaussian function fit to the mass distribution of Z'_{CC2} samples in the $1b$ signal region. The low mass tail is not well described for the 5 and 6 TeV signal, but this does not have a large effect on the limit due to the steeply falling background (see discussion in text).

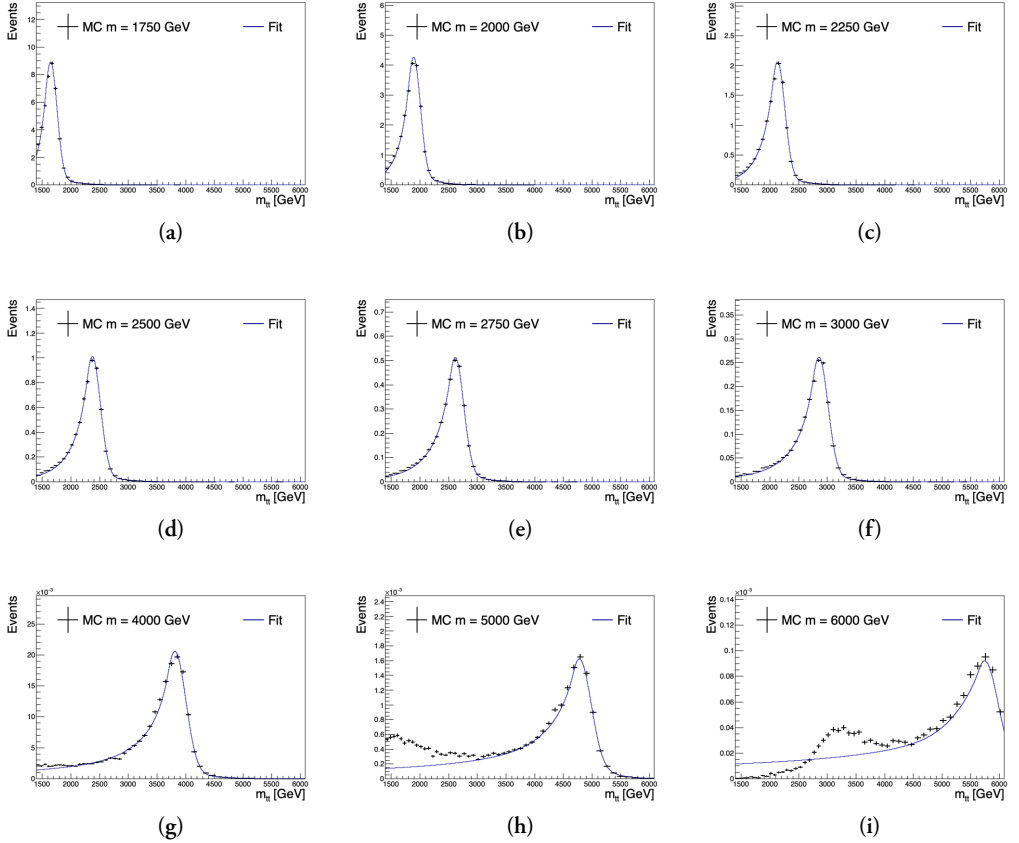


Figure 8.24: Crystal Ball plus Gaussian function fit to the mass distribution of Z'_{CC2} samples in the $2b$ signal region. The low mass tail is not well described for the 5 and 6 TeV signal, but this does not have a large effect on the limit due to the steeply falling background (see discussion in text).

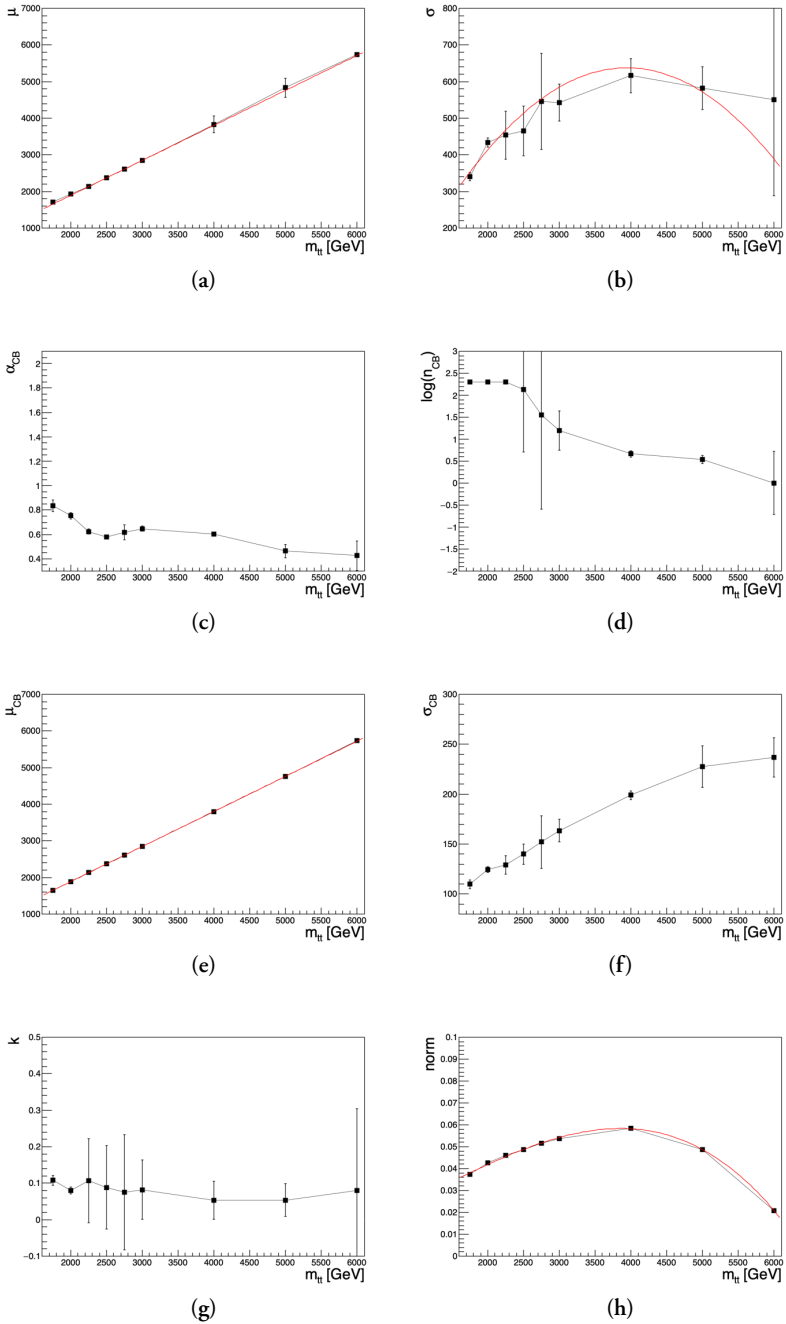


Figure 8.25: Linear interpolation of and polynomial fits to the parameters of the Crystal Ball plus Gaussian function for the $1b$ signal region.

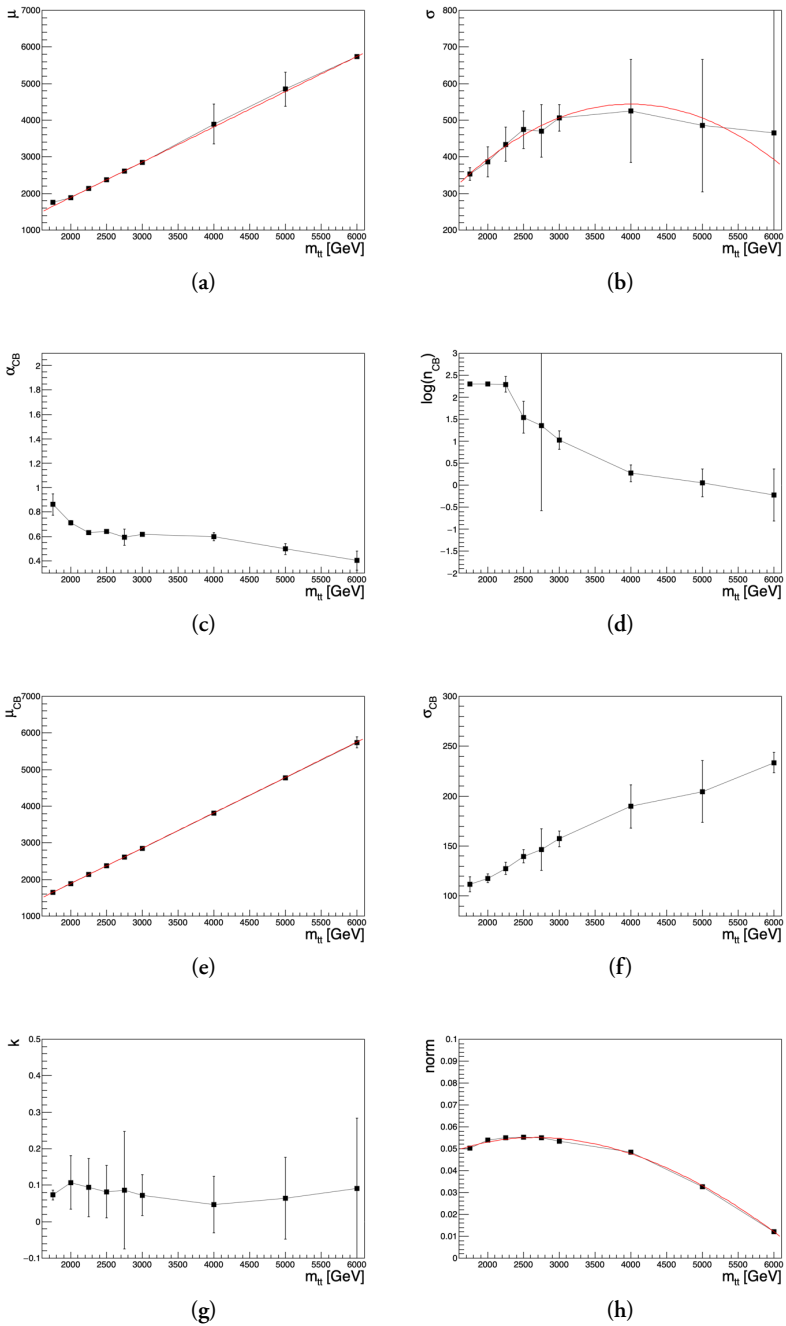


Figure 8.26: Linear interpolation of and polynomial fits to the parameters of the Crystal Ball plus Gaussian function for the $2b$ signal region.

8.4.1 Closure test

A closure test is performed to make sure, the interpolated samples are a good representation of what we would have gotten with Monte Carlo simulation. This is done by using the same procedure as described above, but now removing the points for each of the Monte Carlo samples one at a time to estimate the interpolated value at that point. An example for the signal mass of 4 TeV in the $2b$ signal region is seen in Figure 8.27.

The interpolated signal is shown together with the fit to the Monte Carlo in Figure 8.28 and 8.29. It is only possible to do the closure test from 2 to 5 TeV since the end points needs to be used for the interpolation.

The closure test result is seen in Figure 8.30. It is found by calculating the limit with the Monte Carlo samples and the interpolated samples respectively and taking the ratio of the results. It is seen, that the difference is at maximum 5%, which is acceptable, but to take this into account, a systematic uncertainty of 5% is added to the mass points, where the interpolated signal is used.

8.5 Systematic uncertainties

The systematic uncertainties are divided in signal and background uncertainties. Since the background is estimated by a functional fit as described above, the only systematic uncertainties on the background distributions are related to the fit. They are the uncertainty on the fit parameters and the spurious signal caused by the choice of the functional form.

8.5.1 Fit parameter uncertainty

Due to the statistical fluctuations in each pseudo-experiment (or data sample), the fit parameters vary and result in slightly different fits. This variation of the fits is seen in Figure 8.31, which shows the fits to the 1000 pseudo-experiments in red and the fit to the nominal background template (combined multijet sample and Monte Carlo $t\bar{t}$ sample) in black. It is clear, that there is a larger variation in the fits at high $m_{t\bar{t}}$ in the $2b$ signal region due to lower statistics.

The variation in the fits is transformed into an uncertainty by taking the root mean square (RMS) of the fit values divided by the mean value in each of the bins. The result is seen in Figure 8.32.

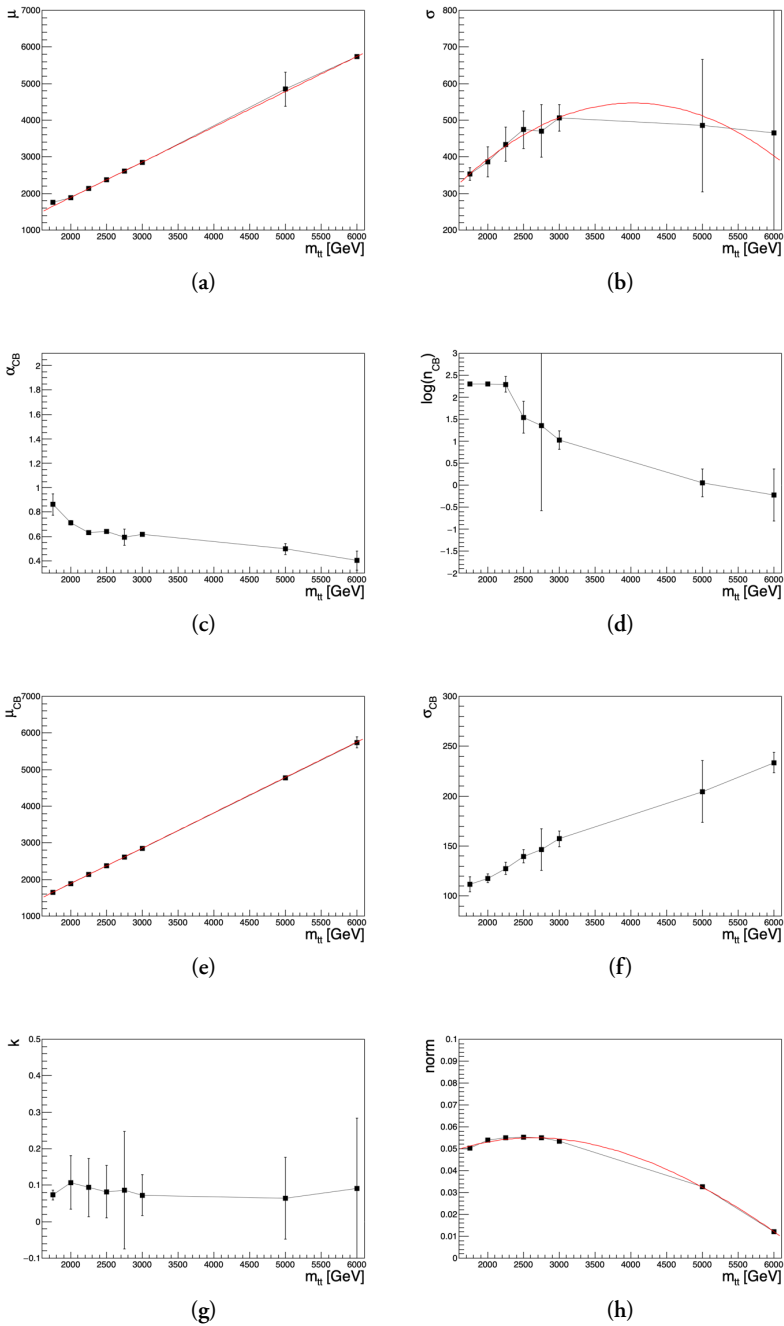


Figure 8.27: Linear interpolation of and polynomial fits to the parameters of the Crystal Ball plus Gaussian function for the $2b$ signal region with the 4 TeV sample removed for the closure test.

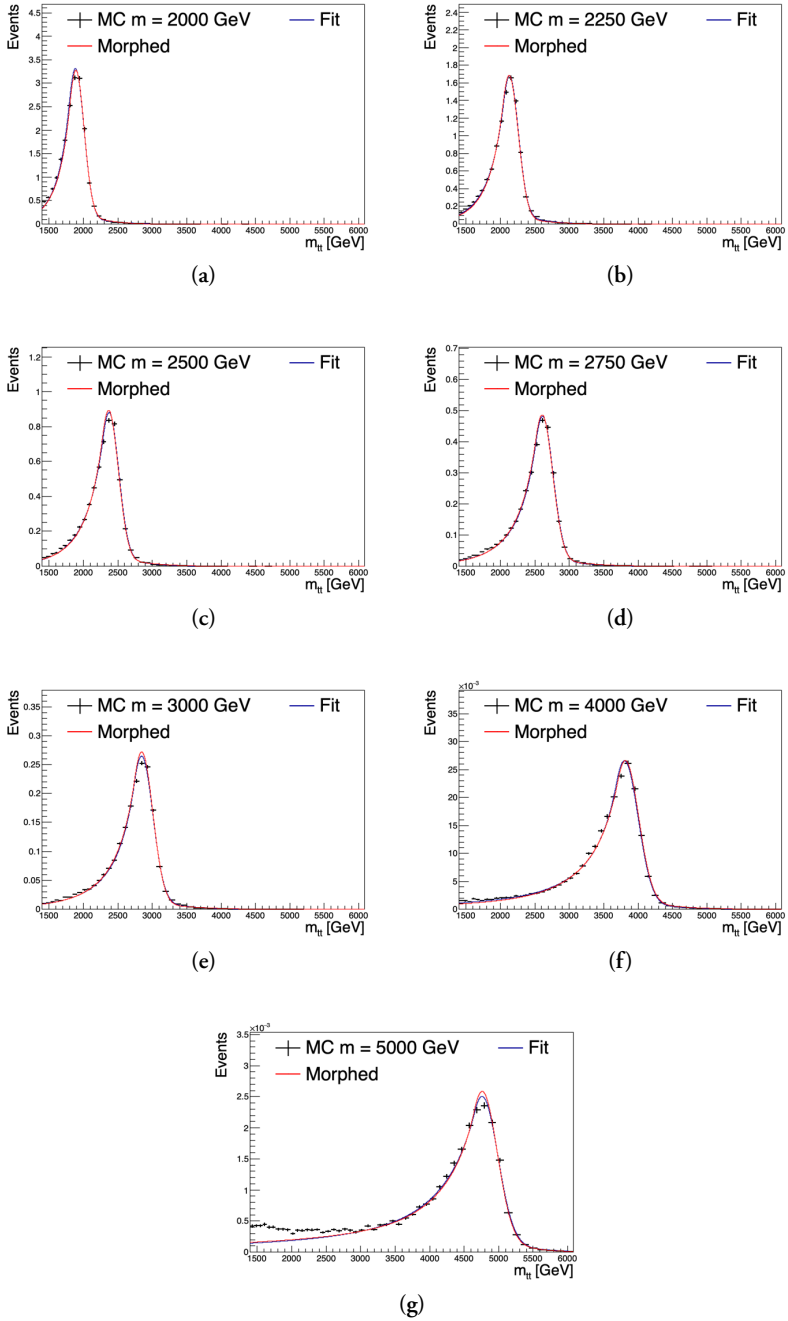


Figure 8.28: Comparison of the fitted and interpolated signal samples in the $1b$ signal region.

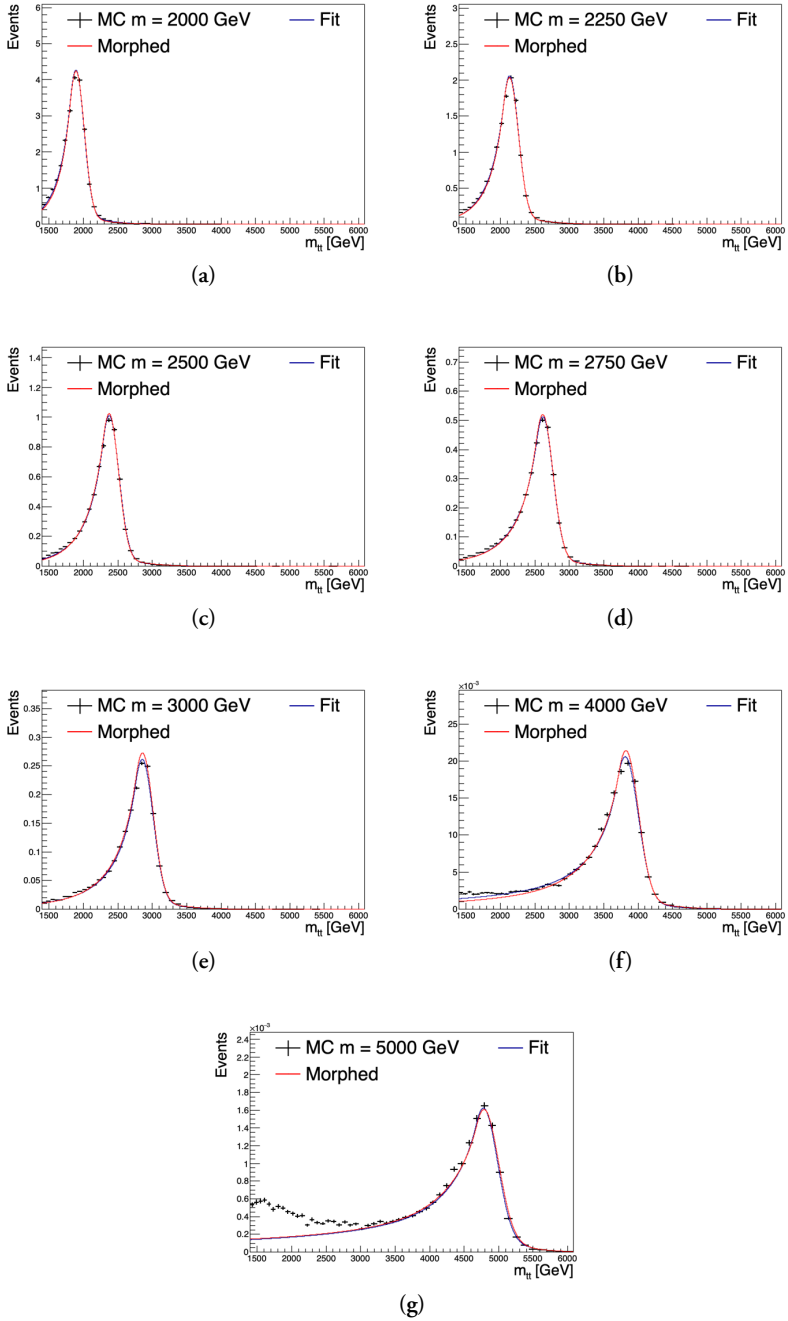
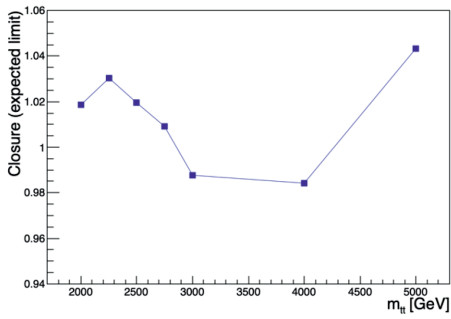
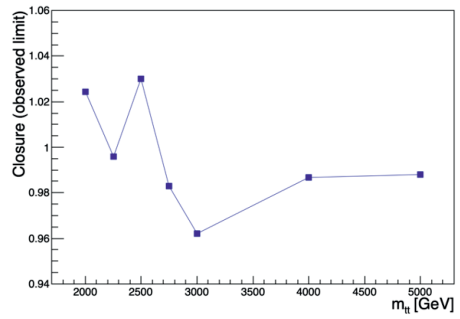


Figure 8.29: Comparison of the fitted and interpolated signal samples in the $2b$ signal region.

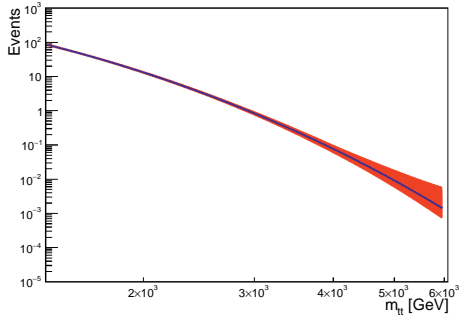


(a)

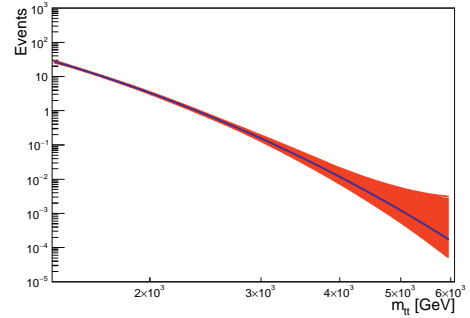


(b)

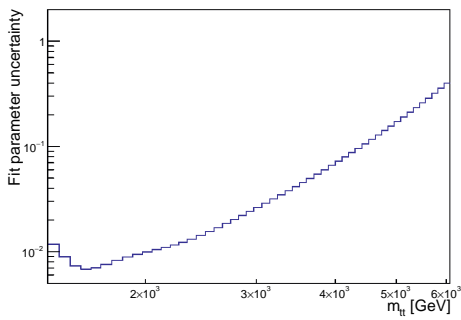
Figure 8.30: Closure test with the (a) expected and (b) observed limits.



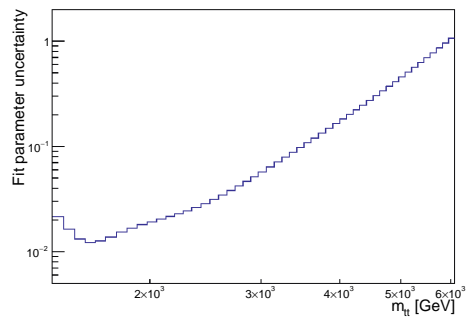
(a)



(b)

Figure 8.31: Fits to set of 1000 pseudo-experiments in the (a) $1b$ signal region and (b) $2b$ signal region. The black line is the fit to the nominal background template.

(a)



(b)

Figure 8.32: Fit parameter uncertainty in the (a) $1b$ signal region and (b) $2b$ signal region.

8.5.2 Spurious signal

To evaluate the bias on the extracted signal yield caused by the choice of background modeling function, a *spurious signal* is evaluated by fitting the background-only (b-only) $m_{t\bar{t}}$ distribution with a signal plus background (s+b) model for a number of signal masses.

The s+b function is given by

$$f_{s+b}(x) = f_4(x) + \mu_{\text{sp}} \cdot f_s(x) \quad (8.15)$$

where μ_{sp} is the spurious signal strength, $f_4(x)$ is the 4-parameter background function given in Equation 8.3 and $f_s(x)$ is the signal function given in Equation 8.14. The parameters of the signal functions are kept fixed during this process, such that only the parameters of the background function and μ_{sp} can vary.

For the background-only sample the pseudo-experiments from the combination of combined multijet and Monte Carlo $t\bar{t}$ is used. To make sure the point, where the two samples are stitch, referred to as the stitching point, will not affect the spurious signal result, it was decided to take the average of calculating the spurious signal from pseudo-experiments from samples with 6 different stitching points. The stitching points are 2260, 2410, 2570, 2730, 2890 and 3060 GeV in both signal regions. It is seen from Figure 8.11 and 8.12, that for these stitching points both the data-driven and Monte Carlo multijet have better statistics, than what is expected in data. The averaged results are seen in the following.

In addition to the spurious signal strength, it can be interesting to look at the spurious signal pull, $N_{\text{sp}}/\sigma_{\text{bkg}}$, which compare the spurious signal events in a window of 20% around the signal peak, N_{sp} , to the background uncertainty calculated as the square-root of the number of background events in the same window of 20% around the signal peak, σ_{bkg} . The mass window is selected to capture the main part of the signal. The spurious signal strength and pull is seen in Figure 8.33 and 8.34, respectively.

For both variables the value and error is taken as the mean and width of a Gaussian fit to the pseudo-experiments. An example of this (for the spurious signal pull in the $1b$ signal region for the 4-parameter fit with a stitching point at 2570 GeV) is seen in Figure 8.35. Similar Gaussian fits are done for the spurious signal strength in both signal regions and for all stitching points.

To get the average result, which are shown here, the mean value is simply the average of the 6 results (with different stitching point) and the error is $\sqrt{\sum \sigma_x^2}/\sqrt{6}$, where σ_x is the error on the variable taken from the Gaussian fit described in the previous paragraph.

The pull is relatively large, compared to what is seen in other analyses, like the dijet analysis. This can be explained by the different method used here. If instead the pseudo-experiments

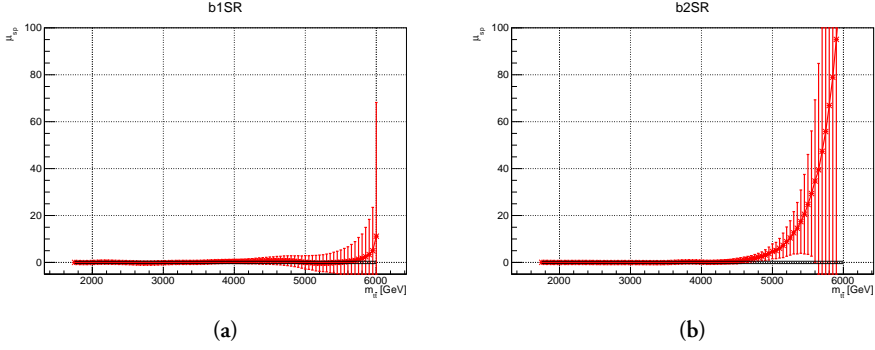


Figure 8.33: Spurious signal strength, μ_{sp} , as function of $Z'_{\text{TC}2}$ mass using the 4-parameter dijet functions for background modeling in the (a) $1b$ signal region and (b) $2b$ signal region.

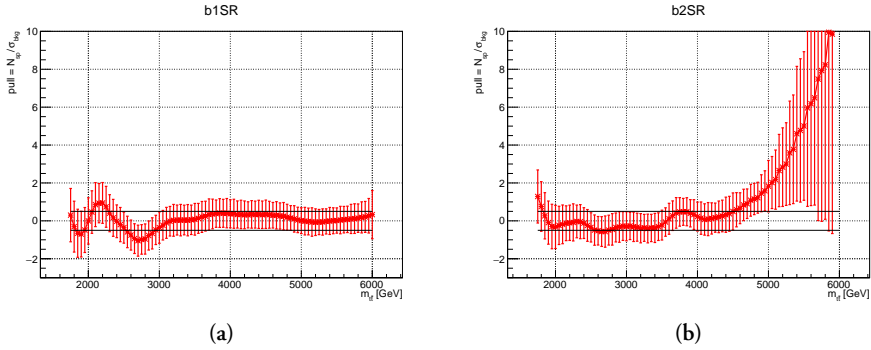


Figure 8.34: Spurious signal pull, $N_{\text{sp}}/\sigma_{\text{bkg}}$, as function of $Z'_{\text{TC}2}$ mass using the 4-parameter dijet functions for background modeling in the (a) $1b$ signal region and (b) $2b$ signal region.

were created from an initial fit to the combination of combined dijet and Monte Carlo $t\bar{t}$ a much smaller spurious signal is seen.

It is also catching the eye, that the spurious signal gets very large especially at high mass in the $2b$ region. This difference between the two signal regions is partly due to the $2b$ signal region having less events, but is mainly due to the $m_{t\bar{t}}$ distribution in the $2b$ signal region falling off more steeply than in the $1b$ region.

It is seen, that the spurious signal is fluctuating quite a lot, which is likely due to the statistical fluctuations in the background sample, so in order to get a more smooth result, it was decided to fit the spurious signal strength, μ_{sp} , with a suitable function to describe the trend. Before this was done the signal strength was first symmetrized by taking the absolute values to get $|\mu_{\text{sp}}|$. The chosen fit is

$$f(x) = p_0 \cdot \exp(p_1 + \exp(p_2 + p_3 \cdot x)) \quad (8.16)$$

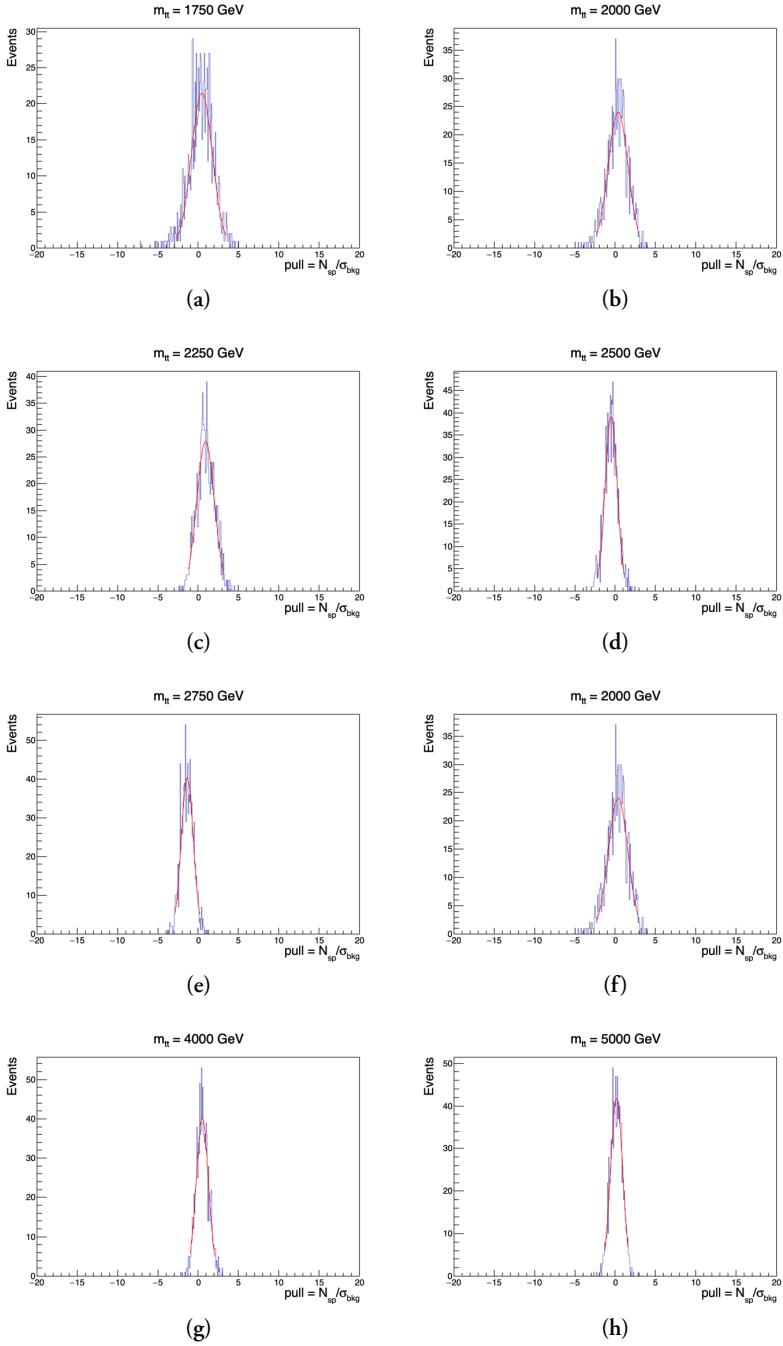


Figure 8.35: Gaussian fits to spurious signal pull in $1b$ signal region for 4-parameter fit for the different signal masses.

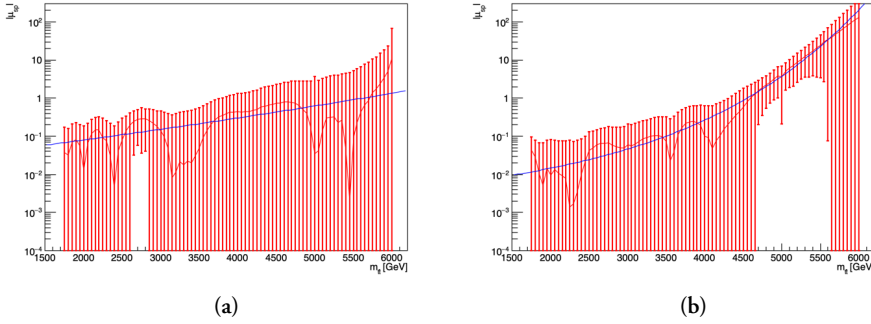


Figure 8.36: Absolute value of spurious signal strength, $|\mu_{\text{sp}}|$, as function of $Z'_{\text{TC}2}$ mass fitted to make a smooth spurious signal estimate in the (a) $1b$ signal region and (b) $2b$ signal region.

and the result is seen in Figure 8.36. The blue fits are used for the spurious signal uncertainty in the statistical analysis, which is calculated in the following way.

The signal templates, which were described in Section 8.4, are multiplied with the estimated μ_{sp} to get the scaled signal template, ϵ_{sp} , which therefore varies as a function of $m_{T\bar{T}}$. Since the spurious signal uncertainty is treated as a background uncertainty, the $+1\sigma$ (-1σ) variation is created by adding (subtracting) ϵ_{sp} to the nominal background template obtained from the background-only fit. It should be noted, that this uncertainty is calculated for each of the signal masses considered in the statistical analysis.

8.5.3 Large- R jet uncertainties

The systematic uncertainties related to the large- R jets are derived with the R_{trk} method, which was introduced in Section 5.2.2. The uncertainties are divided in jet energy scale (JES) and jet mass scale (JMS) uncertainties and consist of four components. The *baseline* component, which is based on the difference between data and PYTHIA8 simulations and the *modeling* component, which covers the differences between different event generators (PYTHIA, HERWIG and SHERPA). The *tracking* component, where tracks are being used as reference and the *statistical* component, which comes from the statistical limitations of the method.

Furthermore, a jet energy response (JER) and jet mass response (JMR) uncertainty is applied. The JER uncertainty is found by applying a 2% uncertainty to the large- R jet p_{T} and propagate it to the $m_{T\bar{T}}$ distribution. Whereas, the JMR uncertainty, which is derived specifically in the context of top-quark jets, is obtained by applying a 20% uncertainty to the jet mass.

8.5.4 Top and b tagging uncertainties

The uncertainties related to top and b tagging are handled in a similar way. The tagging efficiencies are calculated both in data and Monte Carlo and the ratio between them is applied to the Monte Carlo samples as a *scale factor* as explain in Section 5.3.2. It is then possible to propagate the various uncertainties through these scale factors.

For the top tagging, the efficiency for hadronically decaying top quarks is measured using samples, which are enriched in $t\bar{t}$ events with the lepton+jets final state. The uncertainty in the correction factor is estimated to be 10 – 15% per jet depending on the p_T of the jet.

An additional uncertainty is considered at high p_T , where the scale factor is not measured due to low statistics in data. Instead, the Monte Carlo samples are varied by applying different conditions to the GEANT4 calorimeter shower model and the detector material. The uncertainty is added in quadrature to the scale factor uncertainty at the highest available p_T bin to obtain the uncertainty above that point. The components of the large- R jet and top tagging uncertainties, that are associated with the same sources of systematic uncertainties, are varied together in the statistical analysis.

For the b tagging, the efficiency for b -quark-induced jets is measured in samples with $t\bar{t}$ events in the dilepton final state. The uncertainties are divided in the effects from b , c and light-quark jets. Again an additional uncertainty is applied at high p_T using an extrapolation technique.

8.5.5 Other uncertainties

The uncertainties described above are the most dominant. However, an uncertainty on the integrated luminosity of 1.7% [134] is applied as well. Uncertainties related to the pile-up modeling and the lepton reconstruction and identification are also applied, even though they are negligible compared to the others. Furthermore, the uncertainty on the interpolated signal templates of 5%, which were calculated in Section 8.4.1 are applied at the masses, where the interpolated signal is used.

8.6 Statistical analysis

The statistical analysis consist of three steps. First a model-independent search is done with BUMP HUNTER and then a hypothesis test based on the benchmark signal (model-dependent search) is performed using the profile likelihood ratio method described in Section 6.5.2. If neither of the two tests show any significant deviation, the CL_s method is used to compute the observed and expected upper limits for the benchmark signal production cross section.

8.6.1 BUMP HUNTER

BUMP HUNTER is able to identify any resonant signal, with an acceptable width, regardless of the source, as explain in 6.5.1. In this search, the minimum search window is set to two bins and the maximum to half of the number of bins in the full spectrum.

8.6.2 Likelihood

The likelihood used in the profile likelihood ratio is given, similarly to Equation 6.28, by

$$L(\mu, \boldsymbol{\theta}) = \prod_{i=1}^N P_{\text{pois}}(n_i | \nu_i(\boldsymbol{\theta}, \theta_{\text{sp}})) \times C(\boldsymbol{\theta}) \quad (8.17)$$

where $\nu_i(\boldsymbol{\theta}, \theta_{\text{sp}}) = \mu s_i(\boldsymbol{\theta}) + b_i(\boldsymbol{\theta}) + m_i(\theta_{\text{sp}})$ is the number of expected events in bin i including the $m_i(\theta_{\text{sp}})$ events, which are coming from the spurious signal uncertainty, θ_{sp} . $C(\boldsymbol{\theta})$ is a series of Gaussian distributions for the nuisance parameters, $\boldsymbol{\theta}$, which represent the systematic uncertainties presented in Section 8.5. The signal systematic uncertainties are treated as fully correlated between the two signal regions, whereas the background systematic uncertainties are treated as uncorrelated, since they are estimated from statistically independent samples.

8.6.3 Limit setting

The 95% confidence level (CL) upper limit on the signal strength, μ , is found by scanning over values of μ until a CL_s value of 0.05 is found. This is then converted into an upper limit on the cross section times branching fraction, $\sigma \times B$, by using the relation

$$\sigma \times B \times A \times \epsilon = \frac{\mu \times N_s}{L} \quad (8.18)$$

where A is the acceptance, ϵ is the efficiency, N_s is the total signal yield estimated from the signal templates and L is the integrated luminosity.

The asymptotic approximation mentioned in Section 6.5.3 is used in this analysis, but a check with the test statistic sampled using pseudo-experiments is performed in the high-mass region from 3 TeV and up. It is found that the $\sigma \times B$ limit from the asymptotic approximation is stronger than those from the pseudo-experiments by at most 20% at masses above 4 TeV. Furthermore, the impact on the mass limit from this approximation is estimated to be below 100 GeV.

8.7 Results

The results are divided in three parts following the steps of the statistical analysis. However, it is interesting to first compare the data to the nominal background template, we derive in Section 8.3.3, since the derived background template is the foundation for the choice of fitting function and background systematic uncertainties. It is clear from the comparison in Figure 8.37, that the agreement is really good.

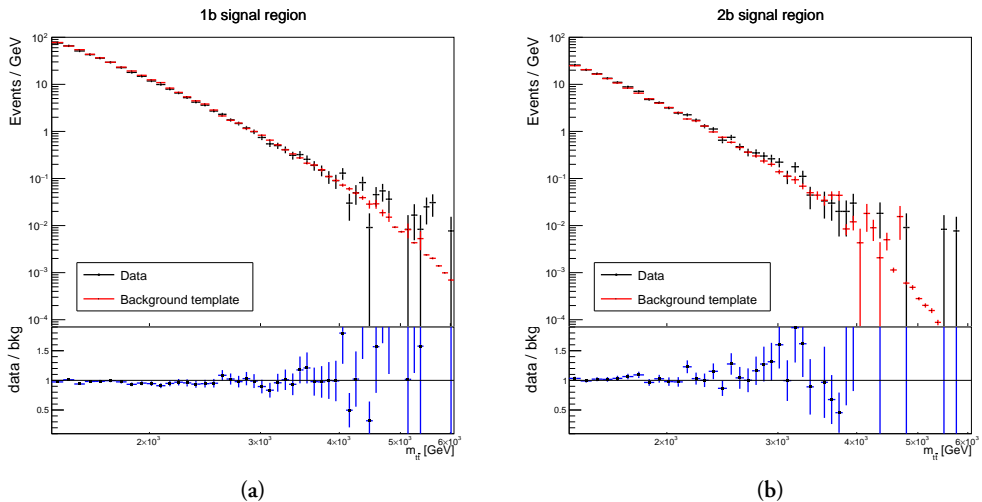


Figure 8.37: The $m_{t\bar{t}}$ distribution for the data compared to the background template from the combined multijet and Monte Carlo $t\bar{t}$ sample in the (a) $1b$ signal region and (b) $2b$ signal region.

8.7.1 Model-independent search

The data is fitted with the 4-parameter function described in Equation 8.3 and BUMPHUNTER is used to perform the model-independent search. As seen in Figure 8.38, the data is described well by the fit with BUMPHUNTER (BH) p -values of 0.45 and 0.56 for the $1b$ and $2b$ signal region, respectively.

The figure also shows, what a Z'_{TC2} signal with five times the nominal signal strength would look like, if it had a mass of 2 TeV or 4 TeV. From comparing these bumps in the two signal regions, it is easy to see, that the $2b$ signal region is more sensitive to the signal, but that the sensitivity in the $1b$ signal region is not negligible.

Furthermore, the fit parameter uncertainty is shown as a band around the fit to show the variation, that is expected especially at high mass. This uncertainty, or any of the other systematic uncertainties for that matter, are however not included, when the BUMPHUNTER

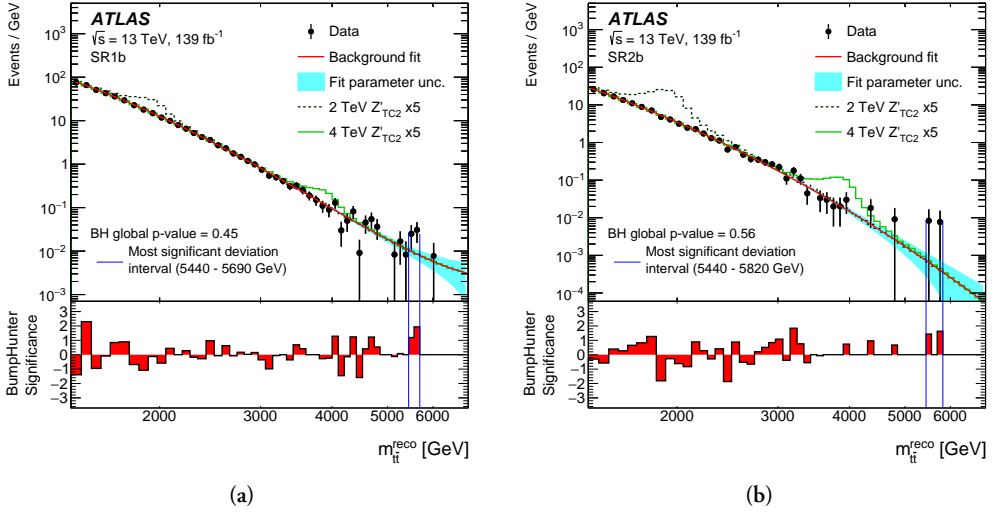


Figure 8.38: The $m_{t\bar{t}}$ distribution for data including the 4-parameter fit in the (a) $1b$ signal region and (b) $2b$ signal region [131].

p -values are calculated. Therefore it is also not surprising, that the most significant deviation interval is seen at high mass in both signal regions. The interval is marked by vertical lines and are 5440–5690 GeV and 5440–5820 GeV in the $1b$ and $2b$ signal region, respectively.

To conclude, BUMP HUNTER did unfortunately not find any significant deviation from the expected smoothly falling background, but on the positive side the 4-parameter fit has proven to describe the data distribution well.

8.7.2 Model-dependent search

We now continue by performing the model-dependent search taking into account the templates for the Z'_{TC2} signal and all the systematic uncertainties. The investigated mass points are

- 1750, 1875, **2000**, 2125, 2250, 2375, **2500**, 2625, 2750, 2875, **3000**, 3250, 3500, 3750, **4000**, 4250, 4500, 4750 and 5000 GeV

where the masses in bold are the Monte Carlo samples and the others are the interpolated samples, which were introduced in Section 8.4. The first mass is 1750 GeV to make sure the full peak is included in the mass spectrum, that starts at 1400 GeV.

The local p_0 -value for the background-only hypothesis is calculated in order to see, whether we can reject the background-only hypothesis and thereby effectively claim a discovery. This

is done by using the test statistic, q_0 , stated in Equation 6.31 with the likelihood given in Equation 8.17. The result is seen in Figure 8.39, which also shows the corresponding local significance given by

$$Z_0 = \sqrt{q_0}. \quad (8.19)$$

The largest deviation is at 1875 GeV and has $p_0 = 0.06$, which corresponds to a significance of 1.6σ . So the model-dependent search did also not find any significant deviation as expected from the result of the model-independent search.

Before we move on to the limit setting, it is interesting to look at the effects of the nuisance parameters in the profile likelihood fit for the signal plus background (s+b) hypothesis. Figure 8.40 shows the post-fit nuisance parameter pulls at Z'_{TC2} masses of 2 TeV and 4 TeV. It is seen, that the fit parameter uncertainty is constrained more than 50% in both signal regions and where it is pulled a bit downwards in the $1b$ signal region, it is pulled a bit upwards in the $2b$ signal region. The largest uncertainty on the signal, the JES R_{trk} modeling uncertainty, is also constrained at both 2 TeV and 4 TeV, as well as pulled at 4 TeV.

That the JES R_{trk} modeling uncertainty is the most dominant signal uncertainty is seen in Figure 8.41, which shows the ranking of the twenty most dominant systematic uncertainties at Z'_{TC2} masses of 2 TeV and 4 TeV. At 2 TeV, the fit parameter uncertainty in the $2b$ signal region has the largest post-fit impact, followed by the spurious signal uncertainty in the $2b$ signal region and the JES R_{trk} modeling uncertainty. At 4 TeV the situation is a bit different. Here the spurious signal uncertainty in the $2b$ signal region has the largest post-fit impact, followed by the JES R_{trk} modeling uncertainty and then the fit parameter uncertainty in the $2b$ signal region.

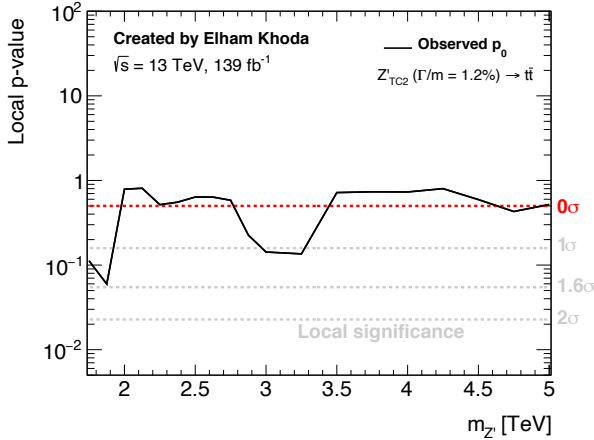


Figure 8.39: The observed p_0 -value as a function of the Z'_{TC2} mass (created by Elham Khoda).

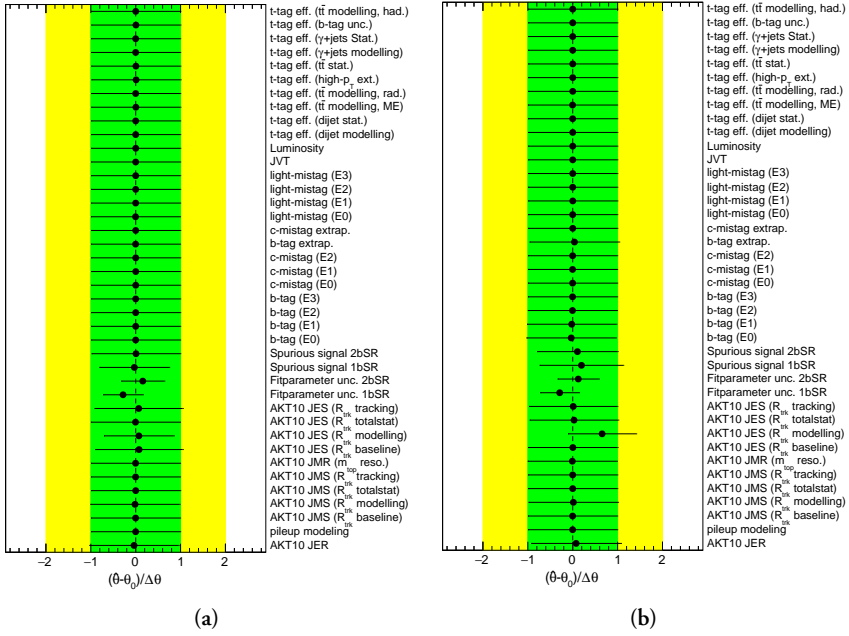


Figure 8.40: Post-fit nuisance parameter pull plot for a Z'_{TC2} mass of (a) 2 TeV and (b) 4 TeV.

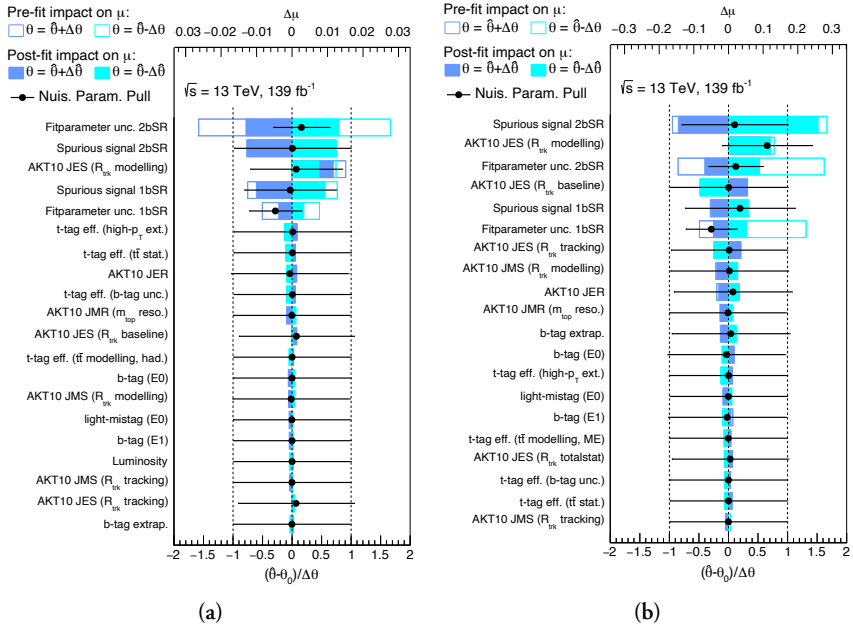


Figure 8.41: Systematic uncertainty ranking plot for a Z'_{TC2} mass of (a) 2 TeV and (b) 4 TeV.

To understand these systematic uncertainties a bit better, we can look at the variation plots for these uncertainties. In Figure 8.42, the $\pm 1\sigma$ variation of the JES R_{trk} modeling uncertainty is seen for a Z'_{TC2} mass of 4 TeV. It is clear, that this uncertainty is huge and affects both the normalization and shape of the signal. It can also be seen, that the $+1\sigma$ and -1σ variations are very asymmetrical, since it is not possible to have downwards variations of less than 0 events, corresponding to -100% , but upwards fluctuations of more than 1000% is fully possible. Figure 8.43 shows variations of the spurious signal uncertainty at 4 TeV and the fit parameter uncertainty in the $2b$ signal regions. These are much more symmetrical for the $+1\sigma$ and -1σ variations.

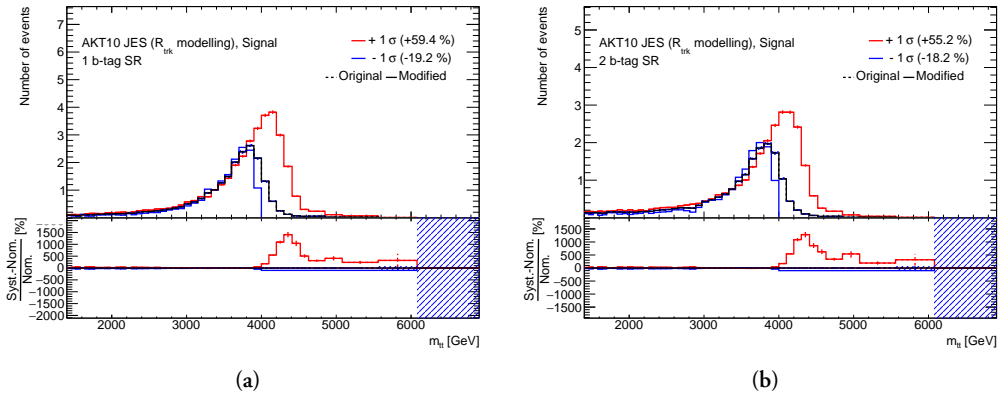


Figure 8.42: The m_{ii} distribution of the Z'_{TC2} signal with a mass of 4 TeV with the JES R_{trk} modeling uncertainty applied in the (a) $1b$ signal region and (b) $2b$ signal region.

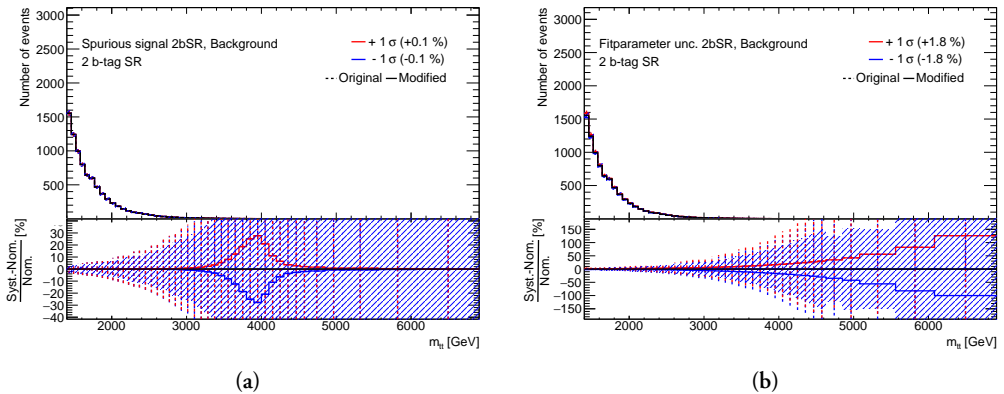


Figure 8.43: The m_{ii} background distribution in the $2b$ signal region with (a) the spurious signal uncertainty at 4 TeV and (b) the fit parameter uncertainty applied.

Table 8.5: Summary of the expected and observed mass exclusion limits of Z'_{TC2} signals with $\Gamma = 1.2\%$, 1% , 3% . The Z'_{TC2} masses are excluded at 95% confidence level (CL).

Signal		Mass exclusion limit	
	Width	Expected [GeV]	Observed [GeV]
Z'_{TC2}	$\Gamma/m = 1.2\%$	4027	4141
	$\Gamma/m = 1\%$	3801	3903
	$\Gamma/m = 3\%$	4724	4726

8.7.3 Limits

Since no significant deviations are seen either in the model-independent or model-dependent search, upper limits on the cross section times branching fraction, $\sigma \times B$, are set on the benchmark Z'_{TC2} signal. The result for the observed and expected upper limits is seen in Figure 8.44, which also shows the theory lines at next-to-leading order (NLO) for the Z'_{TC2} with $\Gamma/m = 1\%$ and 3% . Furthermore, the theory line at NLO, obtained by multiplying the leading order (LO) theory cross-section times branching fraction by a factor 1.3, with $\Gamma/m = 1.2\%$ is shown. The mass exclusion limit are summarized in Table 8.5.

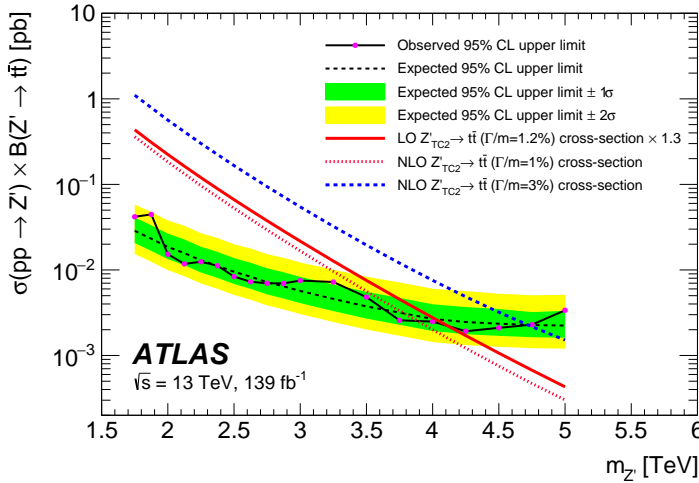


Figure 8.44: The observed and expected upper limit on the cross section times branching fraction [131].

The limits can also be done separately for the two signal regions to see, how they each contribute, which is shown in Figure 8.45. It was not possible to get the limit for the $1b$ signal region to converge at 4 TeV and up with all the systematic uncertainties included, but a study showed, that if two of the b -tagging uncertainties ($E0$ and extrapolation) were excluded, the limit converged. These uncertainties are however not dominant, so the limits at lower masses are almost identical with and without them included as seen in the figure. It is furthermore seen, that the main sensitivity is coming from the $2b$ signal region, but a

none negligible improvement is seen from combining the two signal regions, especially at high mass, where we are running out of events in the $2b$ signal region.

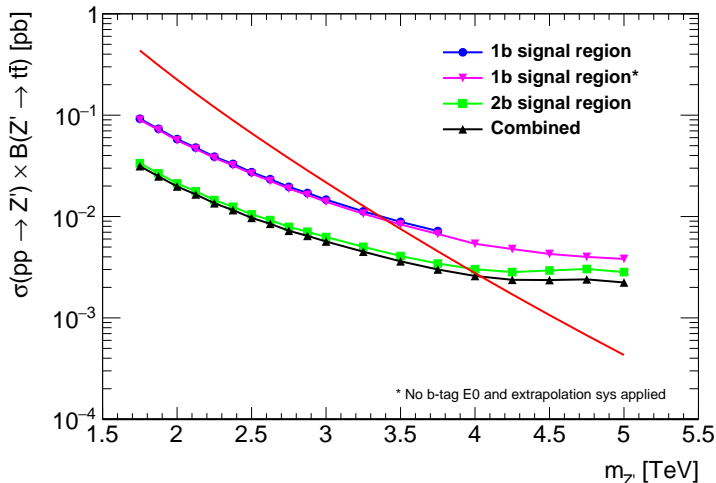


Figure 8.45: The expected upper limit on the cross section times branching fraction separate for the signal regions as well as combined.

8.7.4 Comparison to previous analysis

It is very interesting to see, how the limit compares to the one, that was found in the previous analysis [123], which was using a very different analysis strategy. It was divided in a resolved (low mass) and a boosted (high mass) part. We will focus on the boosted part here, since it gives a clearer comparison to the current analysis. The previous analysis was using the simple two-variable top tagger, which use one-sided cuts on m^{comb} and τ_{32} . We saw in Section 5.3.2, that the DNN top tagger, used in the current analysis, has more than a factor of two better background rejection.

The previous analysis also used a less effective b tagger. It used an old version [135] of the MV2 algorithm, which was performing worse than the one presented in Section 5.3.3.

The last major difference between the two analyses is the background estimation technique. Instead of the fitting technique, the previous analysis was using Monte Carlo samples for the $t\bar{t}$ background and a data-driven sample, found using an ABCD method, for the multijet background.

In order to do a fair comparison of the two analyses, by taking the increase in integrated luminosity out of the equation, the current analysis is performed on the same data set with 36.1 fb^{-1} . It is seen in Figure 8.46, that about half of the improvement in the mass

exclusion limit is coming from the upgraded analysis strategy and the other half is coming from the increase in integrated luminosity.

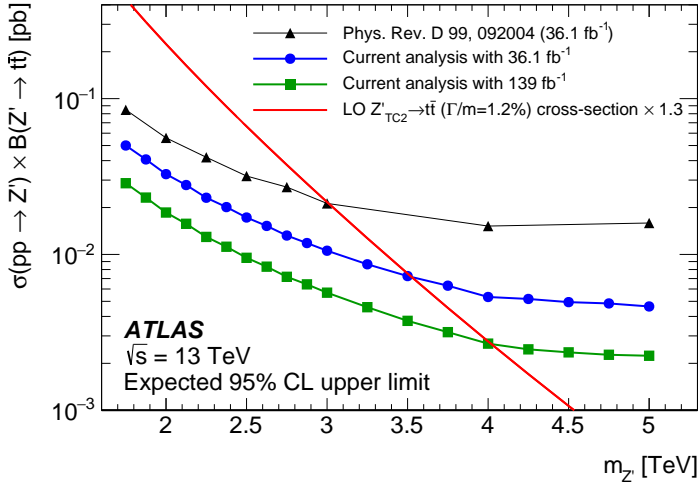


Figure 8.46: The expected upper limit on the cross section times branching fraction compared to the result from the previous analysis [131].

8.8 Discussion

As seen above, the analysis strategy has improved significantly compared to the previous analysis. However, there are still a few things, which can be improved in the future.

The largest systematic uncertainty on the signal is the JES R_{trk} modeling uncertainty. This uncertainty could be reduced by, instead of calibrating the large- R jets using the R_{trk} method, using the newer in situ combination technique, which was presented in Section 5.2.2. This was not done in this analysis, since the R_{trk} method was used for the top tagging uncertainty, so to be consistent and to be able to vary the uncertainties together, the R_{trk} method was used for both. In the future, the top tagging uncertainty should be found using the in situ combination technique, such that a smaller uncertainty can be applied for the JES.

Furthermore, it could be interesting to investigate other signal models and repeat the kinematic selection studies to see, if other choices would be optimal for different signals and thereby make the analysis more sensitive. It is however possible to simply use the current analysis strategy and set limits on similar signal models, like a dark matter mediator Z' .

8.8.1 Dark matter summary plot

It is possible to reweight the benchmark Z'_{TC2} signal to a dark matter leptophobic axial-vector Z'_A signal by applying event-by-event weights. The obtained upper limit on this signal is compared to the limits provided by other analyses as seen in Figure 8.47, which shows the upper limit on the coupling to quarks, g_q , as a function of the resonance mass, $m_{Z'_A}$. The limit is comparable to the ones obtained in the dijet angular and resonance searches, which will be presented in Chapter 9.

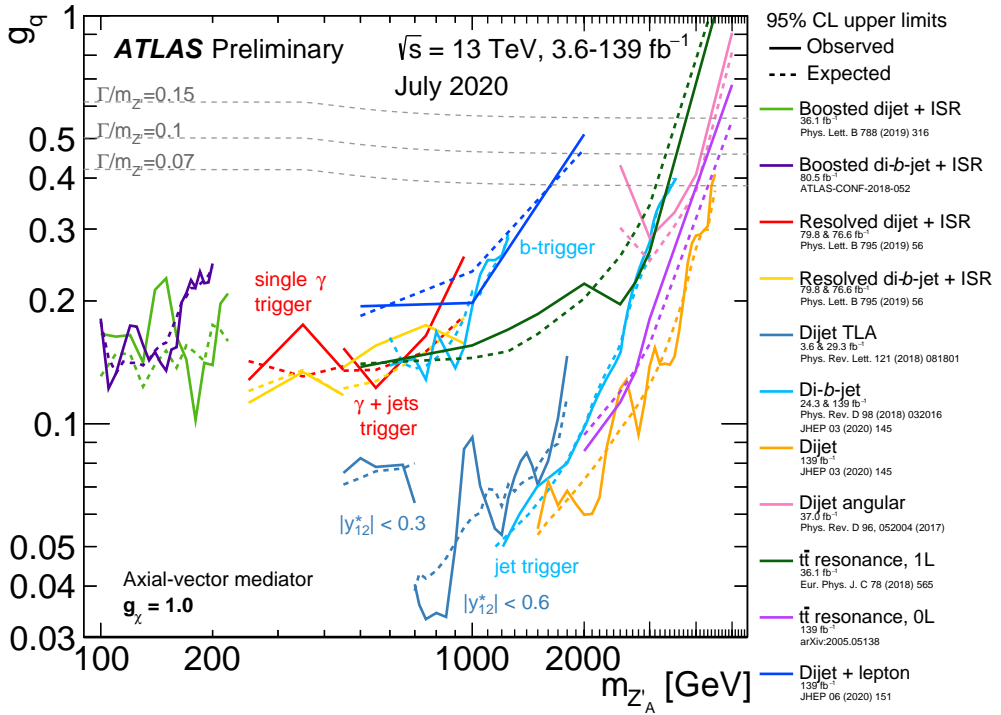


Figure 8.47: 95% CL upper limits on the coupling, g_q , as a function of the resonance mass, $m_{Z'_A}$, for the leptophobic axial-vector Z'_A model [136].

Dijet Analysis

In this chapter, several dijet studies will be discussed, including the published angular analysis on 37 fb^{-1} of data [111] and the resonance analysis on 139 fb^{-1} of data [137]. Furthermore, initial studies for an angular analysis on 139 fb^{-1} of data, will be highlighted.

As described in Chapter 6, the resonance analysis is investigating the m_{jj} distribution, where the angular analysis is looking at the $\chi = e^{|\gamma_1 - \gamma_2|} = e^{2|\gamma^*|}$ distribution in different m_{jj} ranges.

The resonance and angular analyses are complementary. Where the resonance analysis is, not surprisingly, more sensitive to (narrow) resonances, the angular analysis is more sensitive to non-resonant phenomena and broad resonances. It therefore makes great sense to investigate both. In case of a discovery of a new beyond the Standard Model (BSM) signal in the resonance analysis, the angular analysis can also be used to give more information about the discovered particle.

9.1 Angular analysis on 37 fb^{-1}

The dijet analysis using the data collected at $\sqrt{s} = 13 \text{ TeV}$ in 2015 and 2016, corresponding to 37 fb^{-1} , included both a resonance and angular analysis [111]. Only the angular analysis will be presented here. CMS has also performed a similar search [138].

The angular analysis is optimal, when searching for contact interactions (CI), which were introduced in Section 2.11.2. Contact interactions with a nonzero left-chiral color-singlet coupling ($\eta_{LL} = \pm 1, \eta_{RL} = \eta_{RR} = 0$) are chosen as the benchmark signal. These couplings are preferred, since they give rise to angular distributions similar to those of other BSM models (e.g. Z'). It is worth noting that the angular analysis is purely a shape analysis, which means, the background prediction is normalized to the data.

9.1.1 Simulation

This analysis uses the same PYTHIA multijet sample, that is used in the $t\bar{t}$ analysis and presented in Section 8.1.1. However, in this analysis it is not only used for tests and systematic uncertainty estimation, but as the background template. Therefore, it is important to apply corrections, called k -factors, to bring the distribution to next-to-leading order (NLO), such that the agreement between data and Monte Carlo gets better. The NLO calculations are done with NLOJET++ [139, 140, 141] and will be described in greater detail in Section 9.5.

The contact interactions are simulated at leading order (LO) using PYTHIA 8.816. Interference of the signal model with the Standard Model process $q\bar{q} \rightarrow q\bar{q}$ is included, such that events are simulated for both constructive ($\eta_{LL} = -1$) and destructive ($\eta_{LL} = +1$) interference with $\Lambda = 7$ TeV.

Angular distributions for other Λ values are produced from this sample, by taken advantage of the fact that the interference term is proportional to $1/\Lambda^2$ and the pure contact-interaction cross section (called CI term in the following) is proportional to $1/\Lambda^4$ [39].

It is possible to isolate the two terms by adding or subtracting the two interference modes. When they are added, the interference terms cancel and we are left with $2(\sigma_{\text{QCD}} + \sigma_{\text{CI}})$, where the QCD term is known from the multijet sample and can be subtracted. In a similar way, we can isolate the interference term, σ_{int} , by subtracting the two interference modes. The samples derived this way, were compared to a simulated sample at $\Lambda = 10$ TeV and they agreed withing 4%, with the largest deviation in the high- χ region, where the signal contribution is negligible [142].

To bring the samples to NLO, k -factors are applied as will be described next.

9.1.2 NLO corrections for signal

The NLO k -factors for the CI signal are derived using CIJET [143]. The program can calculate both the LO and NLO cross sections as a function of m_{jj} and χ . As for the leading order calculations above, the CI and interference terms can be separated. However, in this case there is no QCD term, that needs to be subtracted. The k -factors, for each of the terms, are found as $k = \sigma_{\text{NLO}}/\sigma_{\text{LO}}$ and the results for two different m_{jj} ranges are seen in Figure 9.1.

It is seen, that a larger χ dependence is present in the higher m_{jj} range and for the interference term. Furthermore, the distributions are very smooth as a function of χ , but also Λ . The k -factors are applied bin-by-bin to bring the signal distributions to NLO.

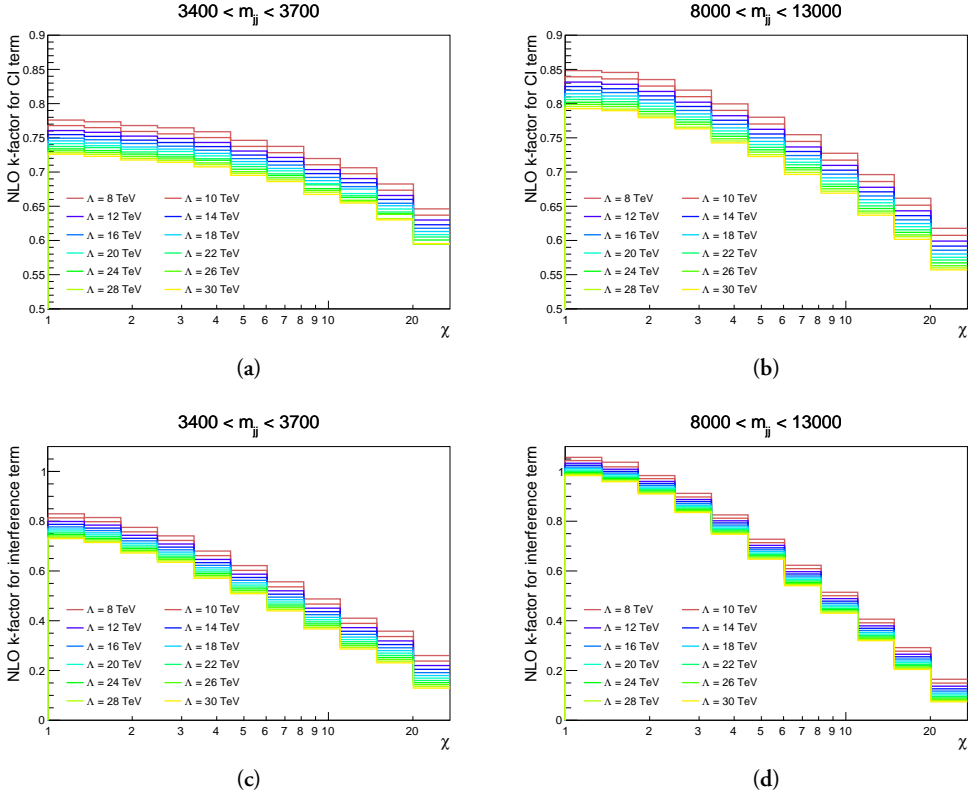


Figure 9.1: NLO k -factors as a function of χ for the CI term in the mass range (a) $3.4 \text{ TeV} < m_{jj} < 3.7 \text{ TeV}$ and (b) $8 \text{ TeV} < m_{jj} < 13 \text{ TeV}$ and for the interference term in the mass range (c) $3.4 \text{ TeV} < m_{jj} < 3.7 \text{ TeV}$ and (d) $8 \text{ TeV} < m_{jj} < 13 \text{ TeV}$.

9.1.3 Event selection

This analysis is using small- R ($R = 0.4$) topo-cluster jets on the EM scale. The leading and sub-leading jets are required to have $p_T > 440 \text{ GeV}$ and $p_T > 60 \text{ GeV}$, respectively. This ensures a trigger efficiency of at least 99.5%. As discussed in Section 6.2, a limited range of $y_B = (y_1 + y_2)/2$ is preferable, in order to limit the dependence of the cross section on the parton distribution functions (PDFs). The chosen value is $|y_B| < 1.1$. Furthermore, a cut of $|y^*| < 1.7$, which is equivalent to $\chi < 30$ is applied.

Using Equation 6.18, we see that, we will lose events at the highest χ for $m_{jj} < 2.5 \text{ TeV}$ due to the leading p_T cut, so therefore only events with $m_{jj} > 2.5 \text{ TeV}$ is allowed. The event selection is summarized in Table 9.1.

Table 9.1: Selections for the angular search with 37 fb^{-1} of data.

Category	Angular
Leading jet p_T	$> 440 \text{ GeV}$
Subleading jet p_T	$> 60 \text{ GeV}$
$ y^* $	< 1.7
$ y_B $	< 1.1
m_{jj}	$> 2500 \text{ GeV}$

9.1.4 Systematic uncertainties

The systematic uncertainties can be divided in theoretical and experimental uncertainties. The theoretical uncertainties include PDF, scale and tune uncertainties, where the dominant experimental uncertainty is the jet energy scale (JES) uncertainty.

The PDF uncertainty is found by using NLOJET++ with three different parton distribution function (PDF) sets (CT10 [144], MSTW2008 [145] and NNPDF2.3 [23]) and finding the variation. Since the choice of PDF set mainly affects the total cross section, rather than the shape of the χ distribution, the uncertainty is small ($< 1\%$) for this analysis.

The scale uncertainty is also found by using NLOJET++. Here the renormalization and factorization scales are varied independently up and down by a factor of 2. The uncertainty is taken as the variation in the normalized χ distributions and is highest at low χ and high m_{jj} with values of 12% and 8% for the renormalization and factorization scales, respectively.

The tune uncertainty takes into account the uncertainties in the tuned parameters for parton shower and hadronization in the A14 tune set used for the multijet simulations. On the normalized χ distribution, the uncertainty is at most 6% [142].

The JES uncertainty is represented by three orthogonal nuisance parameters [146], which together lead to the most dominant systematic uncertainty, which is up to 15% at high m_{jj} .

9.1.5 Statistical analysis

The statistical analysis is performed as a combined profile likelihood fit to the χ distributions in seven coarse m_{jj} regions starting at 3.4 TeV. The $2.5 \text{ TeV} < m_{jj} < 3.4 \text{ TeV}$ region is not included, since it does not provide any sensitivity to the benchmark signal in ranges, which have not yet been excluded.

As mentioned above, the Monte Carlo simulation is normalized to the data separately in each m_{jj} bin, which makes the analysis a shape comparison.

The likelihood function includes nuisance parameters corresponding to the systematic uncertainties, which were described in the previous section. The systematic uncertainties are treated as fully correlated in m_{jj} . This assumption was cross checked with other correlation models for e.g. the tune uncertainties, but proved to not make any significant difference.

A p -value, with the background-only hypothesis, is calculated in order to check for any deviations from the Standard Model. If no significant deviations are found, the limit is set using the CL_s method described in 6.5.3.

9.1.6 Results

Figure 9.2 shows the χ distributions for the seven m_{jj} regions before and after the profile likelihood fit to data. In this visualization, both the Monte Carlo and data distributions are normalized to unity, but in the limit setting, the Monte Carlo is normalized to data. There is a clear discrepancy between data and Monte Carlo before the profile likelihood fit as seen in Figure 9.2b.

The uncertainty bands are split between the theoretical uncertainties and the total uncertainty (green/blue) and examples of the CI signal is shown both for the constructive (red) and destructive (orange) interference model at 22 and 15 TeV, respectively. It should be noted that for the destructive interference signal, the expected distribution is smaller than the Standard Model at low χ and m_{jj} .

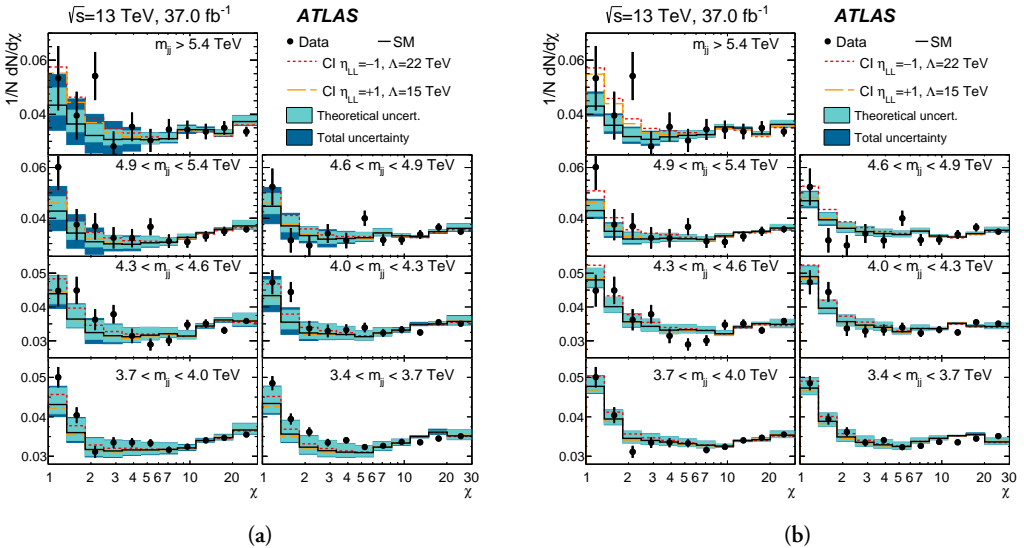
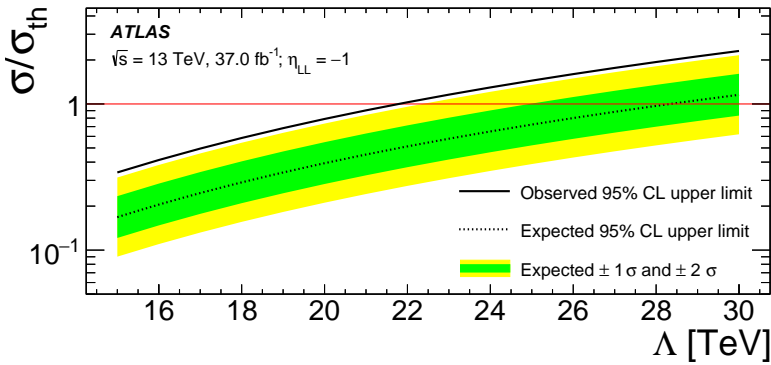


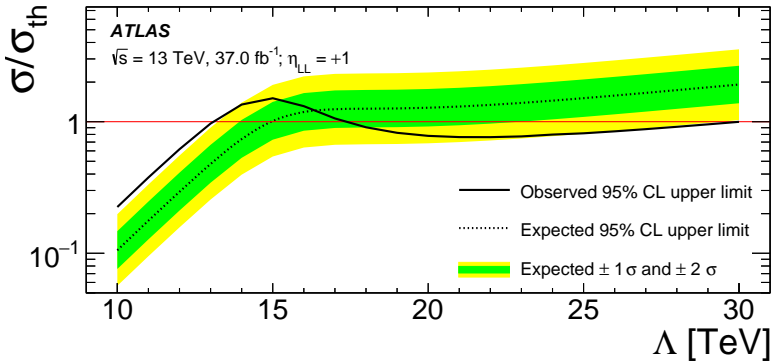
Figure 9.2: Angular distribution with 37 fb^{-1} of data with Standard Model prediction and systematic uncertainties (a) before [147] and (b) after the fit to data [111].

The fit to data is strongly constrained by the lowest m_{jj} regions, which have very good statistical precision and negligible contributions from the benchmark signal. It therefore provides constraints of 20 – 40% on the uncertainties at the higher m_{jj} regions as seen in Figure 9.2b. The background-only p -value is found to be 0.06.

The 95% confidence level (CL) observed and expected limits as a function of Λ are shown in Figure 9.3. Due to some excesses at low χ , the observed limit for the CI signal with constructive interference ($\eta_{LL} = -1$) is weaker than the expected. However, for the CI signal with destructive interference ($\eta_{LL} = +1$), the limit is weaker at low Λ values and gets stronger at higher values. This is due to the fact that the signal can result in less events at low χ , but this depends on the value of Λ and m_{jj} . The 95% CL exclusion limits for Λ is seen in Table 9.2.



(a)



(b)

Figure 9.3: Ratio $\sigma/\sigma_{\text{th}}$ of the observed and expected 95% CL upper limits on the cross-section in the contact interaction model to the predicted cross-section as a function of the compositeness scale Λ for (a) constructive ($\eta_{LL} = -1$) and (b) destructive ($\eta_{LL} = +1$) interference with QCD processes. The Λ regions where the 95% CL line is below one are excluded [111].

Table 9.2: 95% CL exclusion limits for Λ with 37 fb^{-1} of data [111].

Signal Model	Observed	Expected
CI ($\eta_{LL} = -1$)	21.8 TeV	28.3 TeV
CI ($\eta_{LL} = +1$)	13.1 TeV and 17.4 – 29.5 TeV	15.0 TeV

9.2 Dijet and di- b -jet resonance search

An analysis similar to the one presented in Chapter 8, has been performed on inclusive dijet and b -tagged final states on the complete Run 2 data set corresponding to 139 fb^{-1} . This result is an extension to the previous inclusive dijet [111] and b -tagged dijet searches [148], which were performed on the 2015 and 2016 data only.

An abundance of signal models has been investigated for several event categories, but in this section, we will focus on the inclusive and $2b$ category and the limits set on excited quarks q^* and Z' Dark Matter mediators. Information on the remaining event categories (W^* and $1b$) and signal models can be found in the paper [137]. CMS has also performed an inclusive dijet search on the complete Run 2 data set [149], whereas the most recent b -tagged dijet search is on Run 1 data [150].

A visualization of the dijet event with the highest m_{jj} (in the W^* category) is seen in Figure 9.4. It has $m_{jj} = 9.5 \text{ TeV}$ and the two leading jets have $p_T = 3.0$ and 2.9 TeV , one is at $\eta = -1.2$ and the other at $\eta = 0.9$. The two yellow cones represent the reconstructed jets.

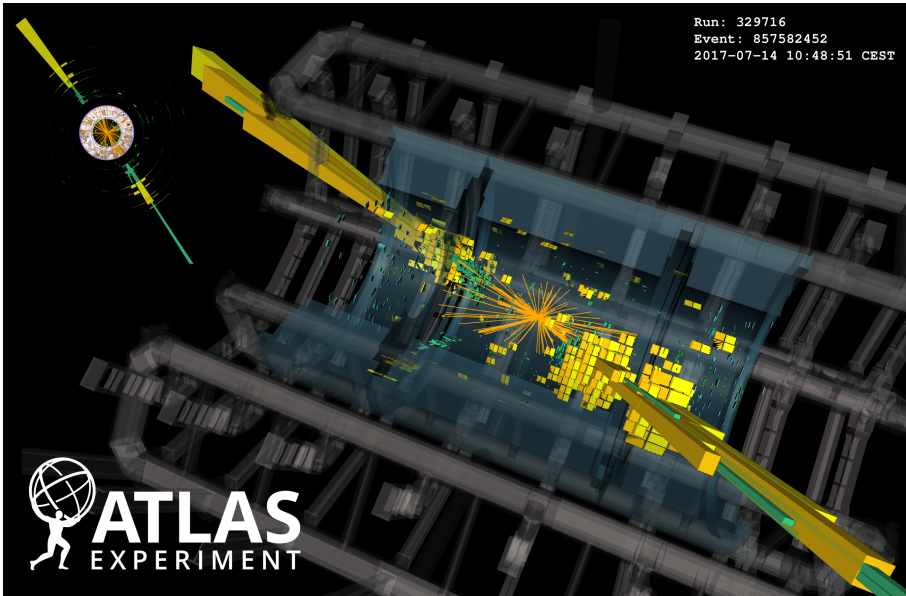


Figure 9.4: Visualization of a dijet event (Run=329716, Event=857582452) [151].

9.2.1 Simulation

In order to estimate the expected QCD background, the PYTHIA multijet samples, presented in Section 8.1.1, are again used and they are corrected with NLO k -factors as in the angular analysis [139, 140, 141]. The Monte Carlo simulation is found to be in agreement with the data, with a difference up to approximately 20% in the tail regions. These samples, do however not have sufficient statistical precision especially at low m_{jj} , so they are not used as the final background estimation, where instead the SWiFt algorithm is used, as will be described in Section 9.2.3.

The excited quark q^* signal is generated with PYTHIA 8.186, assuming spin- $\frac{1}{2}$ excited quarks with the same coupling constants as Standard Model quarks. Only decays into gluons and up or down quarks are included, since this is the dominant process in the dijet final state with a branching ratio of 85%.

The DM Z' decaying into $q\bar{q}$ is generated with MADGRAPH5_aMC@NLO 2.4.3 with the DM mass fixed to $m_\chi = 10$ TeV and the DM coupling set to $g_\chi = 1.5$ and the coupling to Standard Model quarks g_q varying from 0.1 to 0.5. The coupling of $g_q = 0.5$ corresponds to a width of the resonance of 12%. Dedicated samples of $Z' \rightarrow b\bar{b}$ is created with the same generator setup with a branching fraction of 18.9%.

9.2.2 Event selection

Like the angular analysis presented above, this analysis uses small- R EM topo-cluster jets and data is collected using the lowest- p_T non-prescaled single-jet trigger, which requires at least one jet with $p_T > 420$ GeV. The two leading jets are only required to have at least $p_T > 150$ GeV, but to ensure fully efficient triggers, a cut on m_{jj} is included, depending on the y^* cut. Furthermore, the azimuthal angle between the two leading jets has to fulfill $|\Delta\phi_{jj}| > 1.0$.

The y^* cut depends on the category, since it is optimized for different signals. In the inclusive category $|y^*| < 0.6$, whereas in the $2b$ category, where the two leading jets are required to have $|\eta| < 2.0$, a less strict cut of $|y^*| < 0.6$ is used. This cut helps reject the Standard Model background produced mostly in t -channel processes, like it was the case in the all-hadronic $t\bar{t}$ analysis in Chapter 8.

As for the angular analysis, the m_{jj} cut is determined using the relation in Equation 6.18 with the maximum allowed value of $|y^*|$. The values are seen in Table 9.3, which summarizes the selections for the inclusive and $2b$ categories.

The b -tagging algorithm used for the $2b$ category is called DL1r, which is similar to the DL1 algorithm used for the $t\bar{t}$ analysis in Chapter 8, but includes inputs from a recurrent

Table 9.3: Selections for the inclusive and $2b$ category in the resonance search. The requirements only apply to the two leading jets.

Category	Inclusive	$2b$
Jet p_T	> 150 GeV	
Jet ϕ	$ \Delta\phi_{jj} > 1.0$	
Jet $ \eta $	-	< 2.0
$ y^* $	< 0.6	< 0.8
m_{jj}	> 1100 GeV	> 1133 GeV
b tagging	No requirement	2 b -tagged jets

neural network [152]. A b -tagging working point of 77% is used to maximize the signal sensitivity across the different signal models.

9.2.3 Background modeling

As mentioned above, the sliding window fit (SWiFt) algorithm, which was introduced in Section 6.3.4, is used to estimate the background. The four-parameter version of Equation 6.22 is used as the nominal function for both the inclusive and $2b$ category.

Several data-driven m_{jj} distributions are used to validate the background fitting strategy. For the inclusive category, the fit obtained in the resonance analysis on 37 fb^{-1} [111] is used to make a background template by scaling it to 139 fb^{-1} and Poisson fluctuated each bin. Whereas for the $2b$ category, the template is created from control regions using an ABCD method.

Like in the $t\bar{t}$ analysis, signal injection and spurious signal tests are performed to validate the method. The signal injection test shows good agreement between the injected and subtracted signal within the statistical uncertainty.

The spurious signal test shows no bias for the signals in the inclusive category and no dedicated uncertainty is therefore needed. However, for the $2b$ category the observed spurious signal yield is between 10% and 20% of the statistical uncertainty of the estimated background fit and a corresponding systematic uncertainty is therefore included in the limit setting.

9.2.4 Resolution study

As in the $t\bar{t}$ analysis, the m_{jj} binning is based on the resolution. Therefore, a resolution study, similar to the one presented in 8.3.4, is performed. The resolution as a function of m_{jj}^{truth} is fitted with a function of the form $\frac{a}{m_{jj}^{\text{truth}}} + \frac{b}{\sqrt{m_{jj}^{\text{truth}}}} + c$ as seen in Figure 9.5.

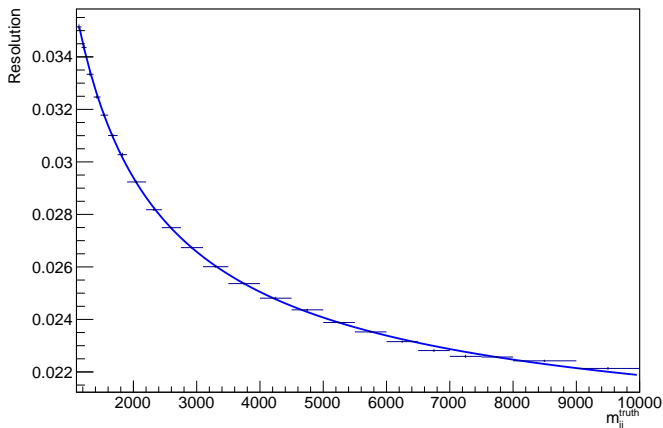


Figure 9.5: Resolution as a function of m_{jj}^{truth} fitted with a distribution of the form $\frac{a}{m_{jj}^{\text{truth}}} + \frac{b}{\sqrt{m_{jj}^{\text{truth}}}} + c$.

Comparing this to the resolution for the large- R jets in Figure 8.19b, it is seen that the resolution for the small- R jet in this analysis is a bit better at low mass, but gets worse at higher mass. This is explained by several factors. First of all the simulated small- R jets are corrected to match the jet energy resolution (JER) found in data and the large- R jets are not. However, a smaller need to do this is seen for the large- R jets, since the data and Monte Carlo agree within the uncertainty. A better JER modeling is also expected for large- R jets at high p_T , since it contains the entire jet energy profile, whereas small- R jets has a truncated energy distribution. However at small p_T , where the noise term of Equation 4.3 has a larger impact, the large- R jets will have a worse resolution, since they are more susceptible to noise, due to their larger size. Furthermore, the topo-clusters are on the LCW scale for the large- R jets, whereas they are on the EM scale for the small- R jets, which also yields a better mass resolution at high p_T for the large- R jets.

9.2.5 Systematic uncertainties

The systematic uncertainties are divided in background and signal uncertainties as for the $t\bar{t}$ analysis in Chapter 8. The fit parameter uncertainty is derived in a similar way, to what was explained in Section 8.5.1, however with 10000 pseudo-experiments and of course using the SWiFt algorithm. The uncertainty increase from approximately 0.1% at $m_{jj} = 2$ TeV to 30 – 40% at the highest m_{jj} .

A spurious signal uncertainty is only applied in the b -tagged region as explained above. However, an additional background uncertainty is applied for all categories in this analysis, which covers the uncertainty from the choice of background parameterization. It is

Table 9.4: 95% CL mass exclusion limits with 139 fb^{-1} of data [137].

Category	Signal Model	Observed	Expected
Inclusive	q^*	6.7 TeV	6.4 TeV
	DM mediator Z' $g_q = 0.20$	3.8 TeV	3.8 TeV
	DM mediator Z' $g_q = 0.50$	4.6 TeV	4.9 TeV
$2b$	DM mediator Z' $g_q = 0.20$	2.8 TeV	2.8 TeV
	DM mediator Z' $g_q = 0.25$	2.9 TeV	3.0 TeV

estimated by the difference to another parametric function, which also fulfill the fit quality criteria, but gives the largest difference to the nominal function. It is approximately 10% at the highest m_{jj} .

The main signal uncertainties are the jet energy scale (JES), jet energy resolution (JER) and b -tagging uncertainties. The JES uncertainty is around 4% at the highest mass and the JER uncertainty varies from 3 – 6%. In the $2b$ category, the b -tagging uncertainty is the most dominant with approximately 20% for a jet with $p_T = 3 \text{ TeV}$.

Smaller uncertainties come from the luminosity measurement, PDF and scale choices.

9.2.6 Statistical analysis

The statistical analysis is very similar to what was presented in Section 8.6 with a model-independent search using BUMP HUNTER and limit setting using the CL_s method with the asymptotic approximation used at low mass and pseudo-experiments used at high mass.

9.2.7 Results

The m_{jj} distributions for the inclusive and $2b$ category are seen in Figure 9.6 including the fit from the SWiFt algorithm and examples of q^* and DM mediator Z' signals. The most significant regions found by BUMP HUNTER is marked with vertical lines. The data is consistent with the Standard Model with p -values of 0.89 and 0.83, respectively for the two categories.

Since no significant deviations are found, limits are set on the benchmark signals. The 95% CL upper limits for the q^* in the inclusive category and the DM mediator $Z' \rightarrow b\bar{b}$ in the $2b$ signal region are seen in Figure 9.7. The corresponding mass limits are summarized in Table 9.4, which also includes the limit on the DM mediator Z' from the inclusive category.

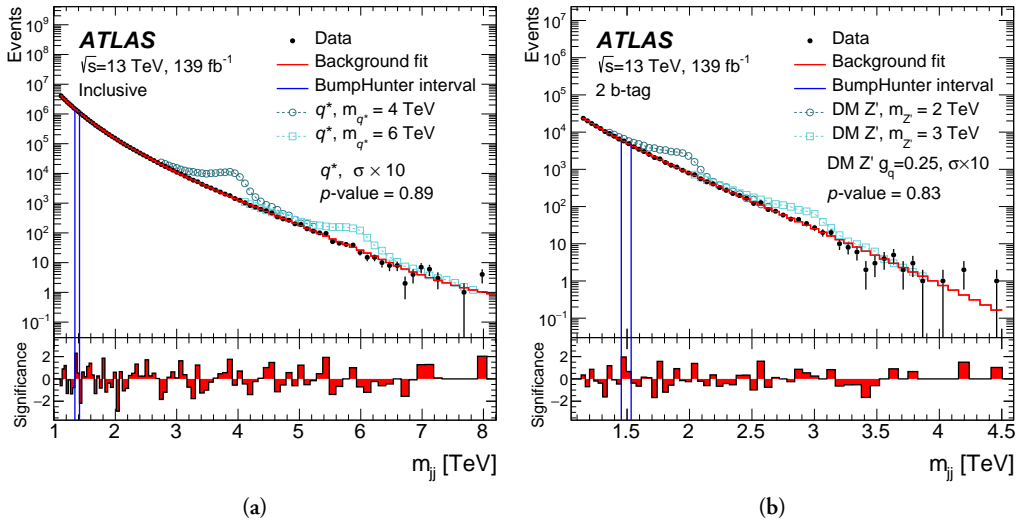


Figure 9.6: The m_{jj} distribution for (a) the inclusive dijet selection and (b) the $2b$ category [137].

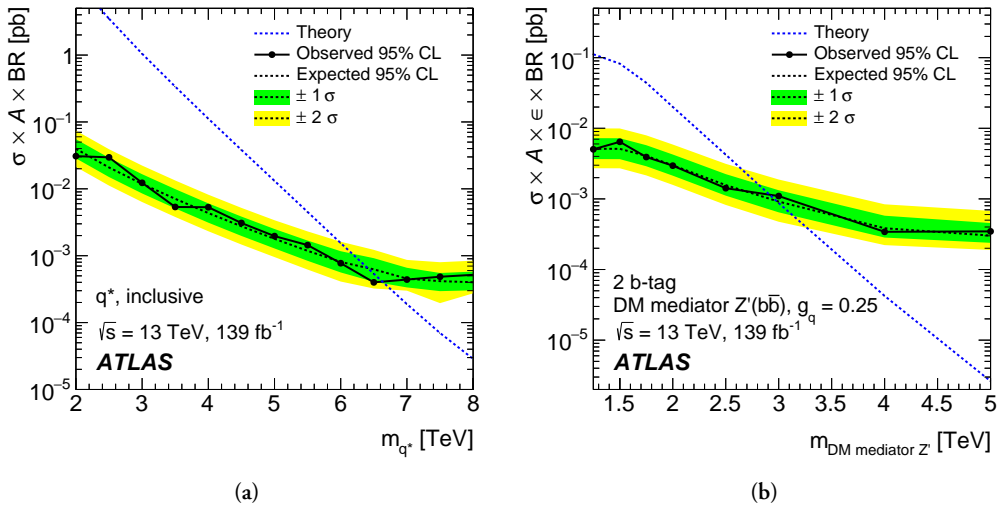


Figure 9.7: The 95% CL upper limits on the cross-section times acceptance (times b -tagging efficiency) times branching ratio as a function of the signal mass for (a) a q^* using the inclusive dijet selection and (b) a Dark Matter (DM) mediator Z' with $g_q = 0.25$ using the $2b$ selection [137].

9.3 Initial studies for angular analysis on 139 fb^{-1}

The rest of this chapter is dedicated to different studies meant to be used for the angular analysis on 139 fb^{-1} of data collected in Run 2. They include small studies like the calculation of the angular resolution, but also more complex studies like the development of more smooth NLO k -factors and the investigation of a ratio method, which removes the discrepancy between data and Monte Carlo.

9.4 Angular resolution study

The angular resolution can be calculated in a similar way to the m_{jj} resolution by fitting $\chi^{\text{reco}}/\chi^{\text{truth}}$ in bins of χ and m_{jj} . As seen in Figure 9.8, the resolution varies up and down as a function of χ , especially at high m_{jj} , but is less than 0.73% in all bins. The difference between the m_{jj} regions is somewhat expected due to the relation between χ , m_{jj} and p_T seen in Equation 6.18.

According to this study, the χ binning can be made finer, than it was in the previous analysis presented in 9.1, without any problem, but the statistical precision of the Monte Carlo simulations will be a limiting factor.

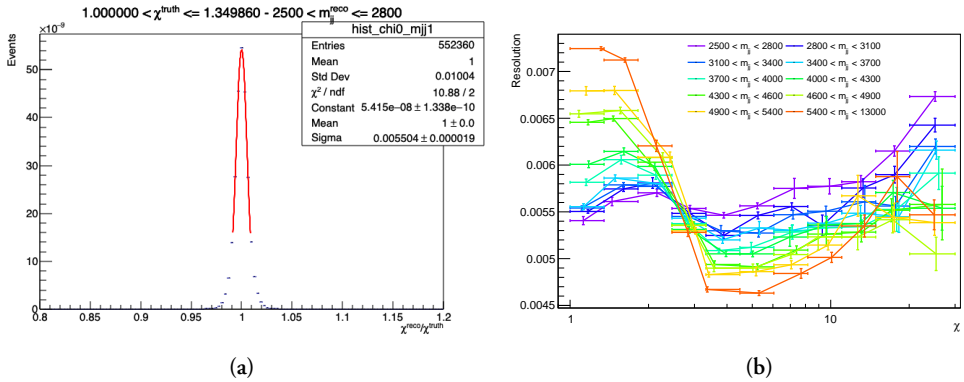


Figure 9.8: The angular resolution is found from a Gaussian fit to $\chi^{\text{reco}}/\chi^{\text{truth}}$. Here (a) show an example of the fit for events with $1.0 < \chi \leq 1.35$ and $2.5 \text{ TeV} < m_{jj}^{\text{reco}} \leq 2.8 \text{ TeV}$ and (b) shows the resolution as a function of χ for the different m_{jj} bins.

9.5 QCD NLO corrections

As mentioned above, the next-to-leading order (NLO) calculations of the dijet cross section are done with NLOJET++ [139, 140, 141]. In order to correct the leading order (LO) PYTHIA simulations, k -factors are applied.

9.5.1 NLO k -factors

When wanting to bring the LO PYTHIA simulations to NLO by applying k -factors, it is not enough to just apply the difference between NLO and LO hard scatter cross sections, as one would think, since PYTHIA is a complete event generator. This means that some of the missing higher order processes are partially made up for in the parton shower already.

We therefore need to take this into account, when applying the k -factors. This is done by producing a special PYTHIA simulation with only the hard process and the parton shower included, but no hadronization. The NLO contribution in the nominal PYTHIA simulation is given by $K_{\text{part}} = (\text{LO}_{\text{show}}/\text{LO})^{\text{PYTHIA}}$, where $\text{LO}^{\text{PYTHIA}}$ is the hard scatter cross section and $\text{LO}_{\text{show}}^{\text{PYTHIA}}$ also includes the parton shower. The correctly NLO corrected PYTHIA prediction is then given by

$$\text{PYTHIA}_{\text{corr}} = \frac{(\text{NLO}/\text{LO})^{\text{NLOJET++}}}{(\text{LO}_{\text{show}}/\text{LO})^{\text{PYTHIA}}} \cdot \text{PYTHIA}_{\text{reco}} \quad (9.1)$$

$$= \frac{\text{NLO}^{\text{NLOJET++}}}{\text{LO}_{\text{show}}^{\text{PYTHIA}}} \cdot \text{PYTHIA}_{\text{reco}} \quad (9.2)$$

$$= k \cdot \text{PYTHIA}_{\text{reco}} \quad (9.3)$$

where we have assumed that $\text{LO}^{\text{NLOJET++}} = \text{LO}^{\text{PYTHIA}}$, which has been shown to be a fair assumption [142].

So besides the special PYTHIA simulation, we need to calculate the NLO hard scatter cross section with NLOJET++.

9.5.2 NLOJET++

The NLOJET++ program is based on the Catani-Seymour dipole subtraction method [141], which is a general version of the *subtraction algorithm*. It introduces a set of universal *counter terms*, that can be used for any NLO QCD calculation.

Question 9.1: What is the subtraction method?

When discussing NLO calculations, the *subtraction method* is a way to calculate the NLO cross section by introducing a local *counter term*, $d\sigma^A$, for the real contribution $d\sigma^R$ such that the NLO cross is given by

$$\sigma^{NLO} = \int_{m+1} d\sigma^R + \int_m d\sigma^V = \int_{m+1} [d\sigma^R - d\sigma^A] + \int_{m+1} d\sigma^A + \int_m d\sigma^V \quad (9.4)$$

where m is the number of final-state partons and $d\sigma^V$ is the virtual contribution. The idea is now that since $d\sigma^A$ has the same pointwise singular behavior as $d\sigma^R$, the integral over the subtraction of the two terms can be performed safely in the divergent limit $\epsilon \rightarrow 0$. If it, furthermore, is possible to analytically integrate $d\sigma^A$ over the one-parton subspace, which is leading to the divergences, it can be combined with the divergences in $d\sigma^V$ and thereby cancel them. The final NLO cross section is then

$$\sigma^{NLO} = \int_{m+1} [(d\sigma^R)_{\epsilon=0} - (d\sigma^A)_{\epsilon=0}] + \int_m \left[d\sigma^V + \int_{+1} d\sigma^A \right]_{\epsilon=0} \quad (9.5)$$

This formula can easily be implemented in a Monte Carlo program, which generates appropriately weighted partonic events with $m + 1$ and m final-state partons.

In the Catani-Seymour dipole subtraction method, the counter term $d\sigma^A$ is developed from the knowledge of how the $m + 1$ -parton matrix elements behave in the soft and collinear limits, that produce the divergences. It contains several dipole terms, which each corresponds to a different kinematic configuration of $m + 1$ partons matching the ones leading to divergences in $d\sigma^R$.

The calculations are however not perfect. Unfortunately, it sometimes happens that a large positive weight for $d\sigma^R$ goes into another bin, than the large negative weight for the subtraction term $d\sigma^A$. This leads to fluctuations, especially at high χ as seen in Figure 9.9, which shows the nominal NLO calculations with NLOJET++.

9.5.3 Improvement of NLO calculation

The weights, which are supposed to cancel, can end up in different bins, because soft radiation with a large angle is not always being captured by the jet algorithm, which therefore leads to a change in the kinematics.

NLOJet++

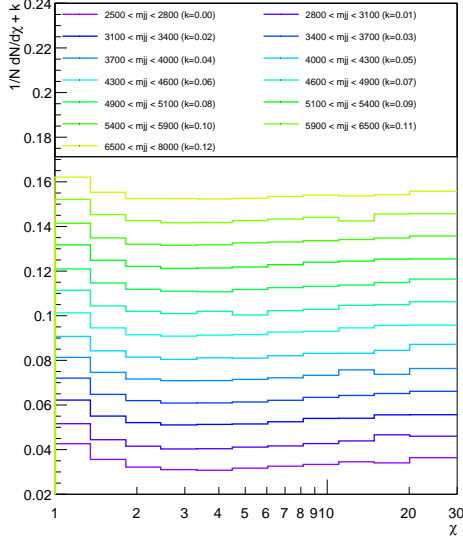


Figure 9.9: Nominal NLO calculations done with NLOJet++. A constant k is added to the distributions in the figure in order to better see the features.

A new method was invented, together with Johan Rathsman, to minimize this effect. If the weights are treated like Gaussian distributions taking up a range of values of the kinematic variable(s) under consideration, it is possible to get significantly smoother distributions. For a kinematic variable x , the partial weight is given by

$$w_{nk}(x) = w_{nk} \frac{1}{\sqrt{2\pi\sigma_x^2}} \exp \left[-\frac{(x - x_{nk})^2}{2\sigma_x^2} \right] \quad (9.6)$$

where w_{nk} is the k th partial weight for the n th fill calculated by NLOJET++ and x_{nk} and σ_x are the Gaussian mean and width, respectively. The contribution to a given bin i , which is defined by the interval $x \in [x_{i-1}, x_i]$ is then given by

$$f_{nki} = \frac{\int_{x_{i-1}}^{x_i} w_{nk}(x') dx'}{\int_{-\infty}^{\infty} w_{nk}(x') dx'}. \quad (9.7)$$

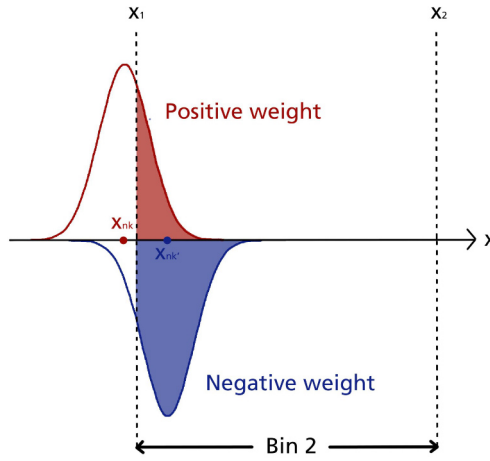
If we now consider a width of the Gaussian, which is much smaller than the bin size, $\sigma_x \ll x_i - x_{i-1}$, we will only expect non-negligible contributions in two neighboring bins. In the case of just two bins, which are separated at x_1 , the contributions in bin 1 and 2 will be

$$f_{nk1} = \frac{\int_{-\infty}^{x_1} w_{nk}(x') dx'}{\int_{-\infty}^{\infty} w_{nk}(x') dx'} = \frac{1}{2} \left(1 + \operatorname{erf} \left[\frac{x_1 - x_{nk}}{\sqrt{2}\sigma_x} \right] \right) \quad (9.8)$$

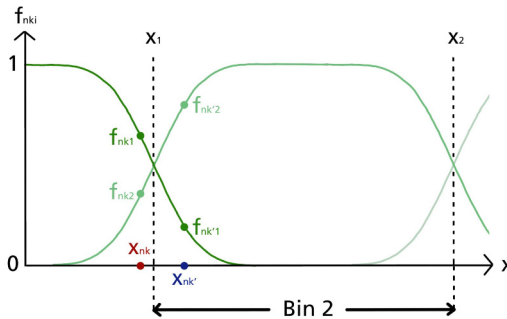
$$f_{nk2} = 1 - f_{nk1} \quad (9.9)$$

In our implementation, we use this formula for each bin edge throughout, leading to what we call “error function” bins. This means, that each partial weight can contribute to at most three bins in one kinematic variable.

The method is sketched in Figure 9.10. A large positive partial weight w_{nk} with the kinematic value x_{nk} is falling into bin 1, whereas the corresponding negative partial weight $w_{nk'}$ with kinematic value $x_{nk'}$ falls into bin 2. This would with the old method lead to large fluctuations in the two bins, but by introducing the Gaussian-distributed partial weight, the two weights will be divided in fractions f_{nk1} , $f_{nk'1}$, f_{nk2} and $f_{nk'2}$ for the two bins and the cancellation will still happen to some extent.



(a)



(b)

Figure 9.10: The new method for NLO calculations in NLOJet++ introduces (a) Gaussian-distributed partial weights, which lead to (b) “error function” bins.

In our application of this method, we use the “error function” bins for both the m_{jj} and χ distributions. For the m_{jj} bins we use

$$f_{nki}^m = \frac{1}{2} \left(\operatorname{erf} \left[\frac{m_i - m_{nk}}{\sqrt{2}\sigma_{m_i}} \right] - \operatorname{erf} \left[\frac{m_{i-1} - m_{nk}}{\sqrt{2}\sigma_{m_{i-1}}} \right] \right) \quad (9.10)$$

with $\sigma_{m_i} = 0.0002/\sqrt{2}m_i$, whereas for the χ bins

$$f_{nki}^\chi = \frac{1}{2} \left(\operatorname{erf} \left[\frac{\chi_i - \chi_{nk}}{\sqrt{2}\sigma_{\chi_i}} \right] - \operatorname{erf} \left[\frac{\chi_{i-1} - \chi_{nk}}{\sqrt{2}\sigma_{\chi_{i-1}}} \right] \right) \quad (9.11)$$

with $\sigma_{\chi_i} = 0.0005\chi_i^2$ is used.

A direct comparison of the NLO χ distributions in two different m_{jj} regions calculated using normal bins and “error function” bins is seen in Figure 9.11. It is clear, that the “error function” bins do not change the overall trend of the distribution, but makes it a lot smoother.

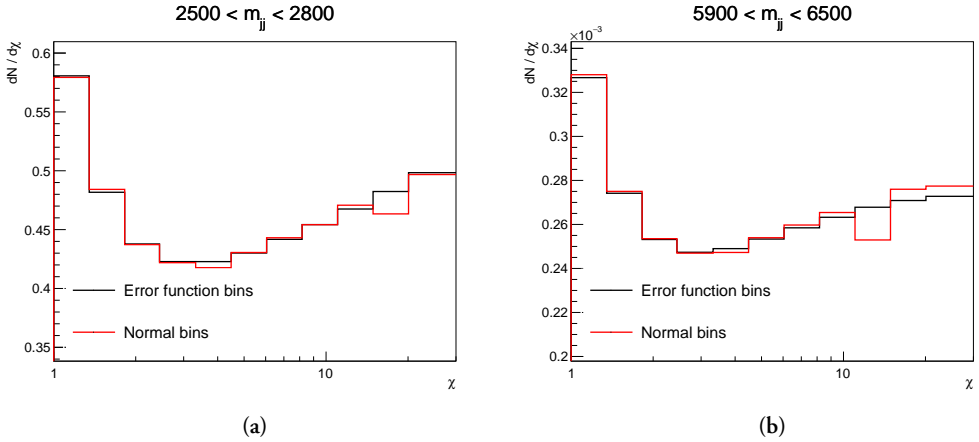


Figure 9.11: Comparison of NLO calculations done with NLOJet++ with normal bins and “error function” bins for (a) $2500 < m_{jj} < 2800$ GeV and (b) $5900 < m_{jj} < 6500$ GeV.

It is important to note that for the normal binning, there is a point, where an increase in the number of generated events, will not lead to an improvement of the distribution, since generating an extra event, could introduce a new fluctuation from non-canceling weights, so it is not just a question of generating enough events.

9.5.4 Final k -factors

The improved NLO calculations using the “error function” bins are seen in Figure 9.12 together with the LO calculations including parton showering, but no hadronization done

with PYTHIA. As described above the bin-by-bin k -factor is given by the ratio of the two distributions

$$k = \frac{\text{NLO}^{\text{NLOJET++}}}{\text{LO}^{\text{PYTHIA}}_{\text{show}}} \quad (9.12)$$

and is displayed in Figure 9.13. It is seen that even though the distributions from both NLOJET++ and PYTHIA look smooth, the k -factors do have some fluctuations. These can be smoothed using the ROOT method `TH1::Smooth()` before applying them to the nominal PYTHIA simulations as was done in [142].

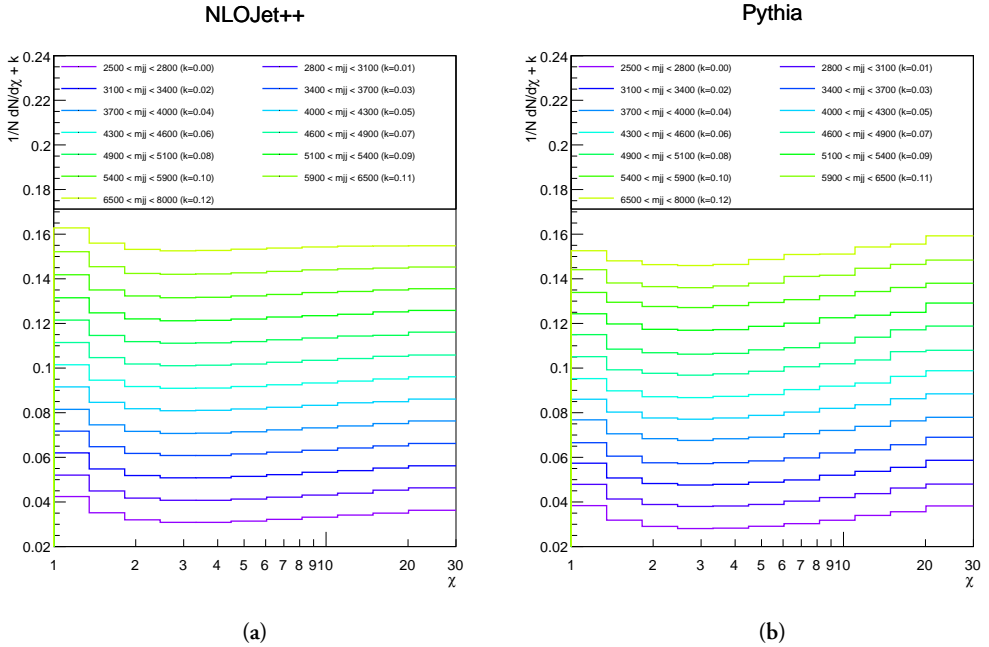


Figure 9.12: The inputs for NLO k -factor calculations are (a) NLO calculations from NLOJet++ with “error function” bins and (b) LO calculations including parton showering from Pythia. A constant k is added to the distributions in the figure in order to better see the features.

9.6 Systematic uncertainties

As seen in Section 9.1.4, several systematic uncertainties are included in the angular analysis. The derivation of them is covered below.

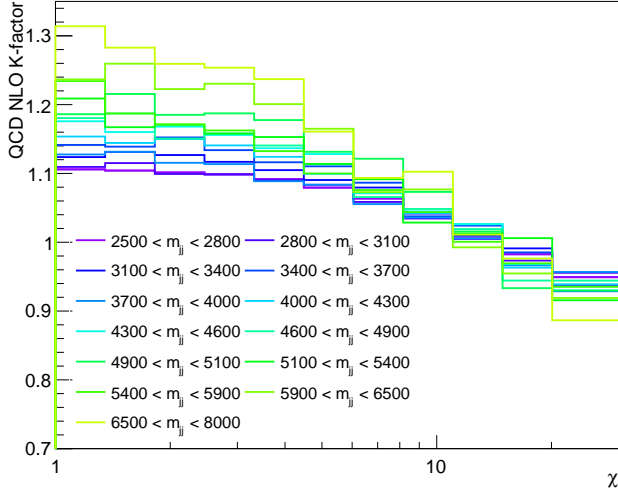


Figure 9.13: NLO QCD k -factors as function of χ for various m_{jj} regions.

9.6.1 Scale uncertainty

The uncertainties related to the choice of renormalization and factorization scales are derived using NLOJET++. The scales are usually set to the momentum transfer, Q , however this can not be exactly experimentally measured, so instead the average of the leading and subleading jet p_T is used as a proxy, $\mu_R = \mu_F = \frac{p_T^{\text{lead}} + p_T^{\text{sublead}}}{2}$. The uncertainty on this choice is found by varying μ_R and μ_F up and down by a factor of two. The envelope of the variations is taken as the uncertainty. The result is seen in Figure 9.14.

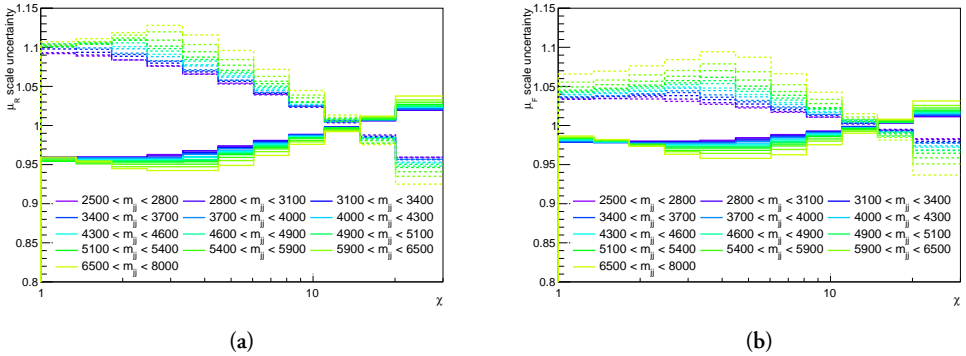


Figure 9.14: Relative uncertainty related to the (a) renormalization scale, μ_R , and (b) factorization scale, μ_F . The solid and dashed lines are the $+1\sigma$ and -1σ variations.

9.6.2 PDF uncertainty

The uncertainty related to the choice of parton distribution function (PDF) is also derived using NLOJET++. Three different parton distribution function (PDF) sets (CT10, MSTW2008 and NNPDF2.3) are investigated and the variation is found. The result is seen in Figure 9.15.

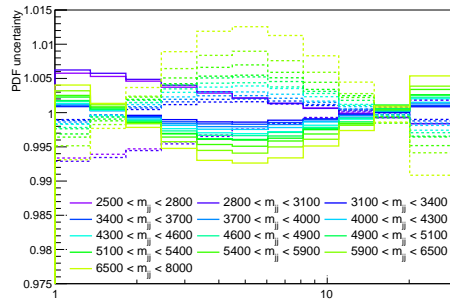


Figure 9.15: Relative uncertainty related to the parton distribution function (PDF). The solid and dashed lines are the $+1\sigma$ and -1σ variations.

9.6.3 JES uncertainty

The jet energy scale (JES) uncertainty is derived as a function of p_T , as we saw in Figure 5.6c. As mentioned above, the uncertainty is represented by three orthogonal nuisance parameters NP1, NP2 and NP3. We recall, that the uncertainty increases rapidly above 2.5 TeV, which is caused by the change of method used to derive the uncertainty. Below 2.5 TeV, the in situ balancing method is used, which gives a very small uncertainty, but above 2.5 TeV, the single particle method described in Chapter 7 is used, which introduce much larger uncertainties. This high- p_T uncertainty is included in NP3.

The uncertainty as a function of p_T is migrated to an uncertainty as a function of χ in the different m_{jj} regions as seen in Figure 9.16. This results in the $\pm 1\sigma$ variations of NP3 crossing each other, such that the $+1\sigma$ variation is sometimes above the -1σ variation and sometimes below. This is caused by the high p_T jets with large uncertainties being present at different χ in different m_{jj} regions combined with bin migrations. As expected, the uncertainty is larger in the high m_{jj} regions, where more high- p_T jets are present.

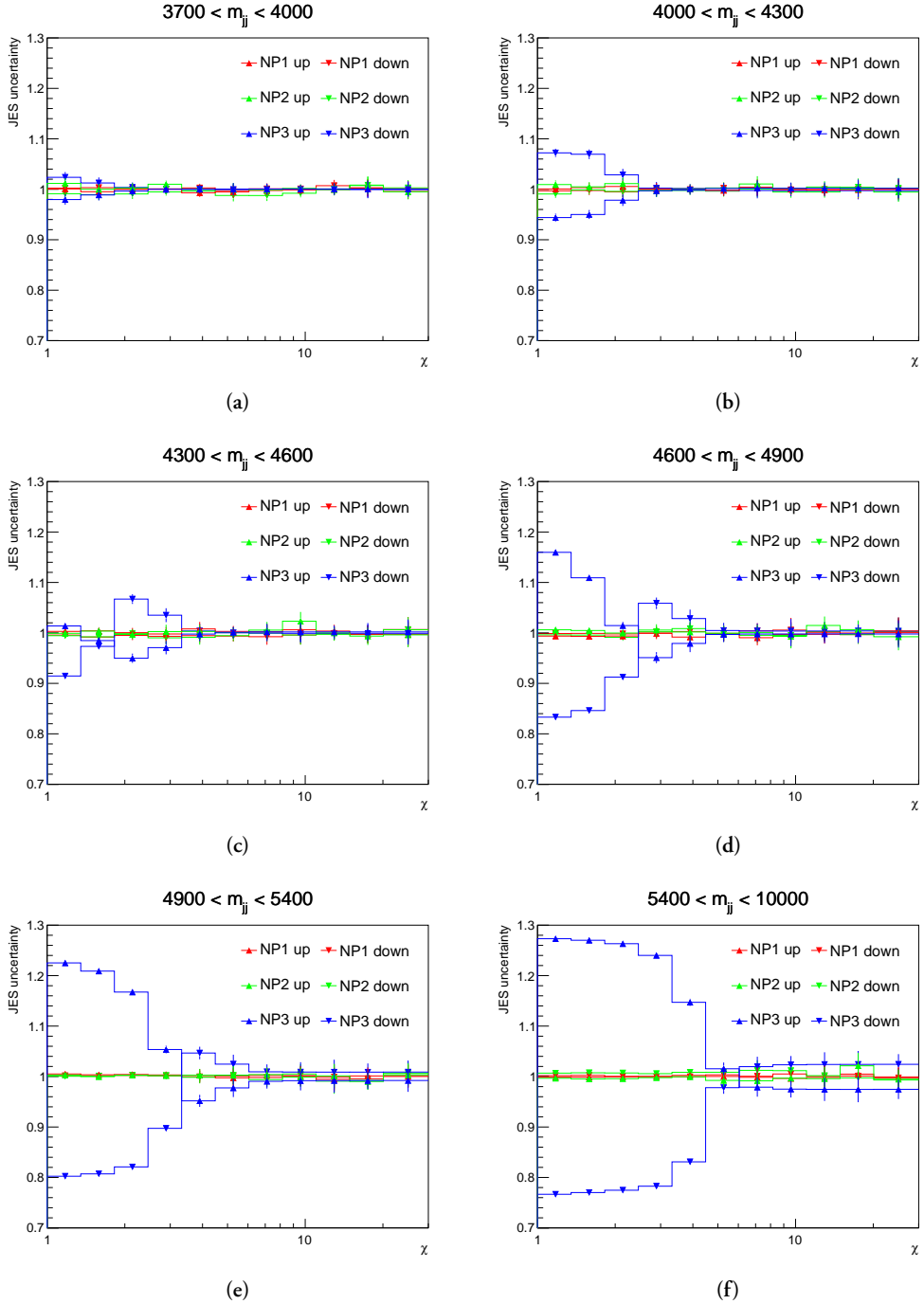


Figure 9.16: Relative JES uncertainty for (a) $3.7 < m_{jj} < 4.0$ TeV, (b) $4.0 < m_{jj} < 4.3$ TeV, (c) $4.3 < m_{jj} < 4.6$ TeV, (d) $4.6 < m_{jj} < 4.9$ TeV, (e) $4.9 < m_{jj} < 5.4$ TeV and (f) $5.4 < m_{jj} < 10.0$ TeV.

9.7 Ratio method

We saw in the angular analysis on 37 fb^{-1} in Section 9.1, that there is a large discrepancy between data and Monte Carlo even after applying NLO k -factors (Figure 9.2a). Figure 9.17a shows the angular distribution for the same data, but with the improved k -factors from Section 9.5.4 applied to the Monte Carlo. Note, that only the JES uncertainty is shown and not any of the other systematic uncertainties. The Monte Carlo distributions are smoother, due to the improved k -factors, but we still see a poor agreement with data, especially in the two lowest m_{jj} regions.

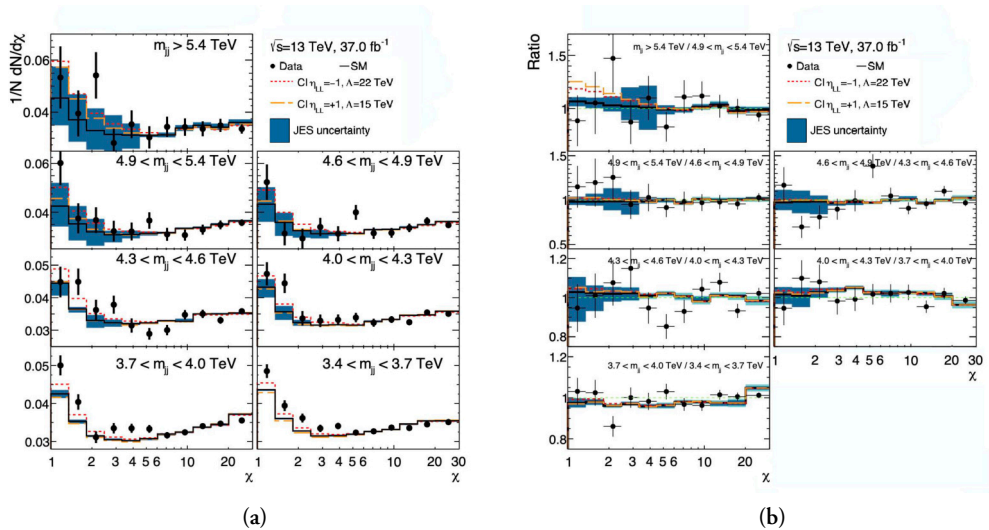


Figure 9.17: Angular distributions with improved k -factors only including JES uncertainty for the (a) nominal method and (b) ratio method.

Since the discrepancy looks similar in the neighboring m_{jj} regions, taking the ratio of them, seems like a good way of removing the discrepancy. The result of taking the ratio of the distribution in each m_{jj} region, with the distribution in the m_{jj} region below is seen in Figure 9.17. Looking at the ratio of the distributions with $3.7 < m_{jj} < 4.0 \text{ TeV}$ and $3.4 < m_{jj} < 3.7 \text{ TeV}$, we can see that the clear discrepancy between data and Monte Carlo is gone.

Furthermore, we can see that in some bins, the JES uncertainty has decreased, while in others it has increased. This is not a surprise, since we are taking the ratio of e.g. the $+1\sigma$ variations of NP3 in Figure 9.16. Since the $+1\sigma$ variation is crossing unity at different χ in the neighboring m_{jj} regions, the ratio method will result in larger uncertainties at a few χ values.

However, the other dominant uncertainty, the scale uncertainty, will to a large degree cancel, since it is very similar in neighboring m_{jj} regions as seen in Figure 9.14. The same is true for the PDF uncertainty in Figure 9.15.

9.7.1 Limit setting

The original idea was to set upper limits on the benchmark signals directly from these ratio distributions, which have better agreement between data and Monte Carlo and in many bins smaller uncertainties than the nominal distributions. However, this is not trivial, since the normal tool for setting limits, HISTFACTORY [153], expects bins with number of events following Poisson statistics. It might however be possible to include the ratio information in the form of a so-called ShapeFactor. This needs to be further investigated.

9.8 Discussion

It is clear that there is still room for improvement of the angular analysis. The discrepancy between data and Monte Carlo in the low m_{jj} regions should be further investigated. One idea is to compare the current background prediction to NLO POWHEG+PYTHIA simulations.

Furthermore, the correlations between the systematic uncertainties in each m_{jj} region should be investigated further. As a starting point, it would be interesting to see the effect of applying separate nuisance parameters for each set of neighboring m_{jj} regions for each systematic uncertainty instead of just having one fully-correlated nuisance parameter for all m_{jj} regions for each uncertainty.

It could also be interesting to look at optimizing the analysis for different signal models, like very broad resonances, which would not be detected by the current resonance search due to the background estimation technique. The angular analysis has indeed been used to set limits on dark matter leptophobic axial-vector Z'_A signal as was seen in Figure 8.47 in the previous chapter.

Another search strategy, that has not been tried before, is to do a top- or b -tagged dijet angular search. Here the sensitivity to e.g. broad resonances, that primarily couple to heavy quarks, could be improved.

Conclusions and Outlook

When protons collide in the LHC, we expect to see an abundance of dijet events, as predicted by QCD. However, such events could also be a sign of physics beyond the Standard Model. In this thesis, analyses searching for such new phenomena are presented.

Using the data collected by the ATLAS experiment during 2015-2018 at a center-of-mass energy of $\sqrt{s} = 13$ TeV, the invariant mass of the two jets with the highest p_T has been studied. In the all-hadronic $t\bar{t}$ analysis, large- R jets, which have been identified as coming from top quarks, are used to search for a Z'_{TC2} boson predicted by the topcolor assisted technicolor model. However, the data was in good agreement with the Standard Model prediction found by fitting the distribution with a smoothly falling function, so limits were set on the model.

In the dijet and di- b -jet resonance analysis, inclusive and b -tagged small- R jets, were used to search for various phenomena beyond the Standard Model, including dark matter mediators, Z' , and excited quarks, q^* . Again no significant deviation from the expected smooth distribution was seen, so limits were set.

An angular analysis of the dijets were also presented, which however only include the data collected in 2015 and 2016. This analysis is complementary to the resonance search in the way, that it is sensitive to non-resonant signals, like contact interactions. Further studies, done as a preparation for the analysis of the full Run 2 data set, are also shown. These include the development of more smooth next-to-leading order calculations and a ratio method, which removes the discrepancy between data and Monte Carlo.

An idea for the future could be to combined the experience gathered from the all-hadronic $t\bar{t}$ resonance analysis and the dijet angular analysis in a top-tagged dijet angular search for e.g. broad resonances, which has never been performed before.



Popular Scientific Description

In this appendix, you will find a popular scientific introduction to each of the chapters. This is meant for friends and family as well as other people, whom are not too familiar with particle physics, as a help to understand, what the thesis is about. I hope, it will be useful.

Standard Model and Beyond

The ultimate goal of the research described in this thesis is to find something new and interesting, we have not seen before. The hope is that this new thing can help us describe some of the weird phenomena, we have observed, but cannot explain at the moment. In this sense, we are on a treasure hunt with the treasure being a better understanding of the Universe.

It might very well be, that we will not find anything new, but then we can at least scratch out the part of the map, where we have already looked, such that the next adventurer does not need to look in the same place. In addition, we do also learn something from not finding anything, since it tells us, that the searched areas of the map then cannot solve the unexplained mysteries of the Universe.

Before we can start looking for something new, we need to understand what other adventurers have found on previous treasure hunts. Otherwise, how would we know, that what we have found, is indeed something new and not just something new to us.

Therefore, in Chapter 2, we start by covering the knowledge, we have on particle physics today. We will learn about the different particles and the forces acting on them. We will also see what happens, when two particles are smashed together in a collision. This is interesting, since these collisions are our most valuable tool in our quest of finding something new.

In order to have an idea of what we are looking for on this quest, we will also cover some of

the phenomena, that we see, but do not yet understand. A few theories, which will be able to explain some of these phenomena, if they turn out to be true, are also introduced. These theories will be our guidelines, when we later have to decide, in which way we should do our treasure hunt.

Below you find a small introduction to the Standard Model of Particle Physics, which hopefully, will help you understand the foundation, this thesis build upon.

The fundamental forces of nature

To our current knowledge, there are four fundamental forces of nature: Electromagnetism, the weak force, the strong force and gravity.

- *Electromagnetism* is a well-known phenomena in everyday life. It describes the sun light hitting your window in the morning, the electricity that makes it possible to charge your phone over night and the magnetism that keeps the pictures of your loved ones stuck to your refrigerator with a small magnet.
- *The weak force* is much less obvious in everyday life. It is however accountable for the radioactive β decay, which transforms a neutron into a proton, an electron and a particle called the neutrino.
- *The strong force* is keeping together the atomic nuclei (protons and neutrons) in the nucleus of the atoms. It also keeps together the constituents of the nuclei called quarks.
- *Gravity* is also easy to observe in the world around us. Just try to jump and you will feel the gravitational field of the whole earth work against you. No wonder jumping squats are so tiring!

Particle physicists have managed to combine the first three of these in what is called the Standard Model of Particle Physics. This model also includes all the fundamental particles, we know exists.

The fundamental particles

There are two kind of particles, matter particles called fermions and force carrier particles called bosons. The fermions are further divided into quarks and leptons as seen in Figure A.1a and A.1b. All the matter around us are made of only up and down quarks and electrons as sketched in Figure A.1c. The up and down quarks make up protons and neutrons, which

are at the core of the atoms with the electrons circling around. The other quarks (charm, strange, top and bottom) are essentially just heavier versions of the up and down quarks. Similarly, the muon and tau are heavier versions of the electron. The neutrinos are almost massless and sometimes called ghost particles. They are very interesting in themselves, but I will leave that for another time.

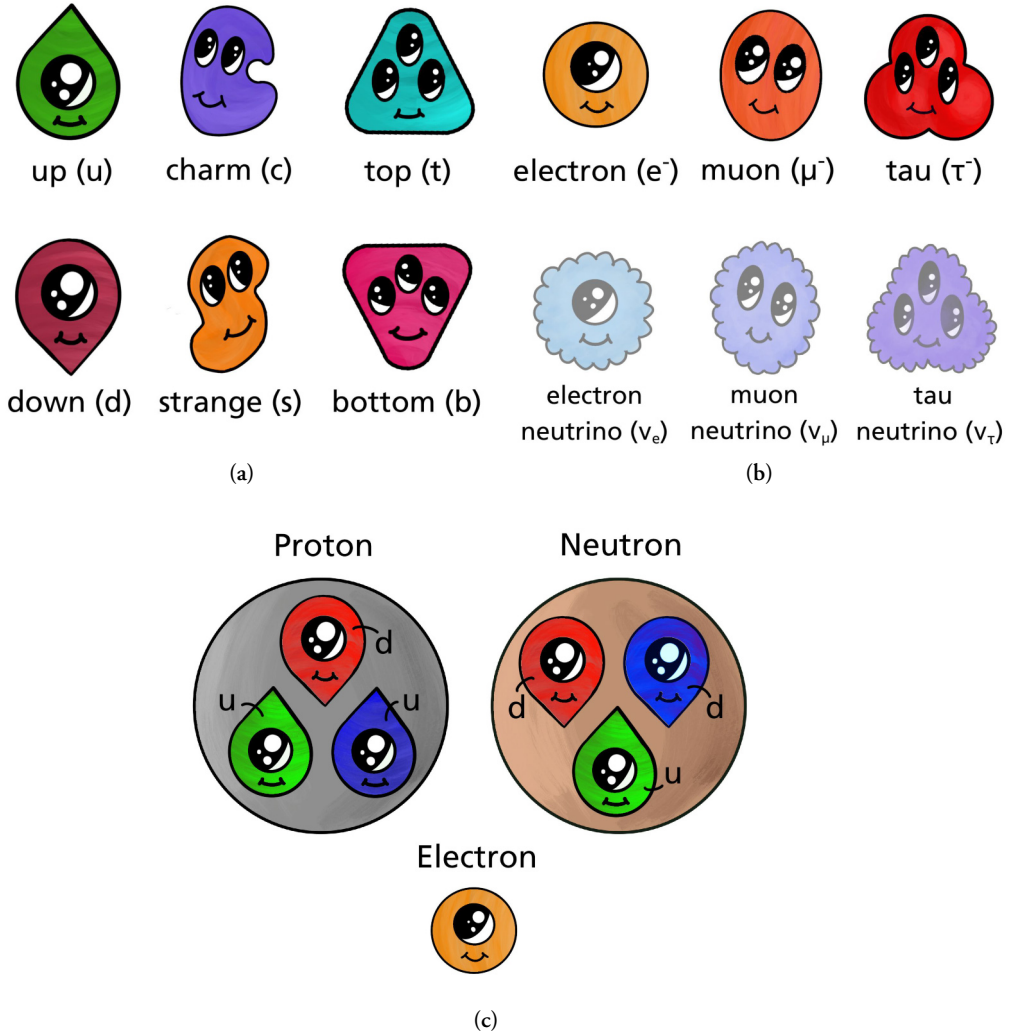


Figure A.1: The fundamental fermions are (a) quarks and (b) leptons and (c) a few of them (up quark, down quark and electron) make up all the ordinary matter around us.

The force carrier particles or bosons are seen in Figure A.2. Electromagnetism is carried by the photon, the weak force by the Z and W bosons and the strong force by the gluon. The last boson, the Higgs boson, is a bit different. It does not carry any force, but it is

responsible for giving the particles mass. The heavier a particle is, the more it couples to the Higgs boson. This boson was the last fundamental particle to be found. It was discovered by the ATLAS and CMS experiments by using the Large Hadron Collider, which is the topic of the next chapter.

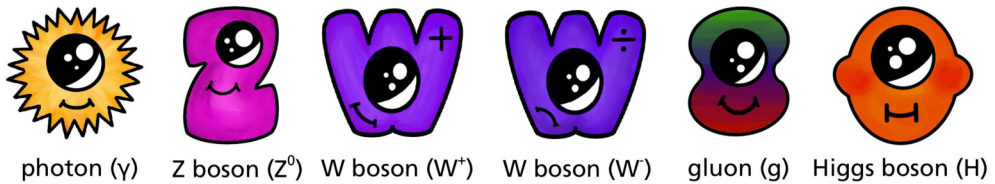


Figure A.2: The fundamental bosons.

Large Hadron Collider

The Large Hadron Collider is an enormous machine placed underground at CERN outside Geneva, Switzerland. The reason it is useful is closely related to Einstein's famous equation $E = mc^2$. It says that energy can be changed into massive particles and vice versa. This means that if we smash together very fast moving particles, which have big kinetic energy, we can create massive particles out of that energy. That is exactly the purpose of the Large Hadron Collider, to accelerate protons to velocities very close to the speed of light and smash them together to create a plethora of different particles. Chapter 3 explains how the Large Hadron Collider works and is operated to provide collisions for the four major experiments: ATLAS, CMS, ALICE and LHCb.

The ATLAS Experiment

It is not enough to create a lot of particles, we also need to detect them. One of the machines that are built to do this is the ATLAS experiment, which is the topic of Chapter 4. You can think of it as a huge digital camera. However, the output is not just a simple picture, but consists of millions of signals, which together provide a three-dimensional snapshot of the proton collisions.

It consists of several layers, which are optimized to detect different types of particles. The innermost part is a tracking detector, which means it can detect the path of electrically charged particles, as they move out from the collision point. Surrounding the tracking detector is the calorimeters. Their purpose is to measure the energy of the particles by stop-

ping them with chunks of dense material. The outermost part is the muon spectrometer, which helps determine the tracks of the muons, which are not absorbed in the calorimeter.

Jets

One of the things, that are mentioned *a lot* in this thesis, is jets. A jet is a spray of particles moving in approximately the same direction. All the particles in a jet origin from one single gluon or quark and measuring the jets precisely is therefore very important in order to determine, which kind of particles were created in the collision.

Chapter 5 is dedicated to explain, how the jets are reconstructed and calibrated in ATLAS. It also covers the topic of jet substructure. It is possible for a large jet to consist of several small jets. We say, that the jets have prongs. It is e.g. possible to recognize a jet, which is originating from a top quark, since it will have three prongs. The three prongs belongs to each of the three quarks, the top quark can decay into as seen in Figure A.3.

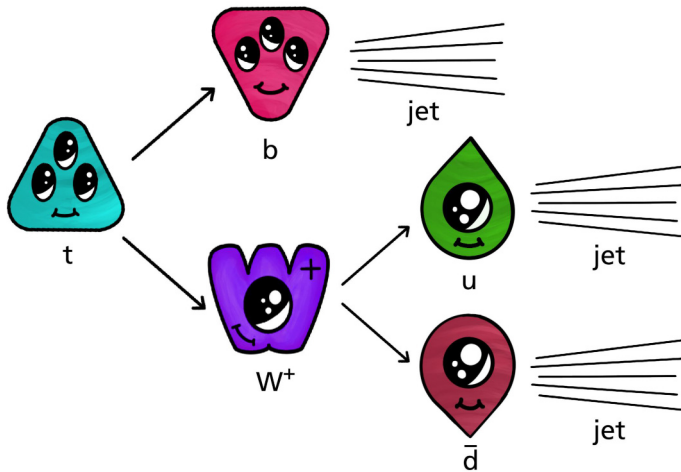


Figure A.3: Example of the decay of a top quark.

Dijets

Another word, that is used a lot in the thesis, is dijets. A dijet is simply a pair of jets. It is very common for a collision in the Large Hadron Collider to result in a dijet and that is expected from the Standard Model, but they could also be the decay products of a new

particle. Therefore, we want to study the collisions, that result in dijets very carefully. The tools to do so are presented in Chapter 6.

We can study the dijets by either looking at their mass or the angle between them. When we look at the mass of the dijets, m_{jj} , we expect a smoothly falling distribution. However, if we see a bump, it is a sign of something new. For some theories though, we do not expect a bump, but would instead be able to see a change in the angular distribution, χ . The difference between the expected distributions, given by the Standard Model and some new phenomena, is sketched in Figure A.4.

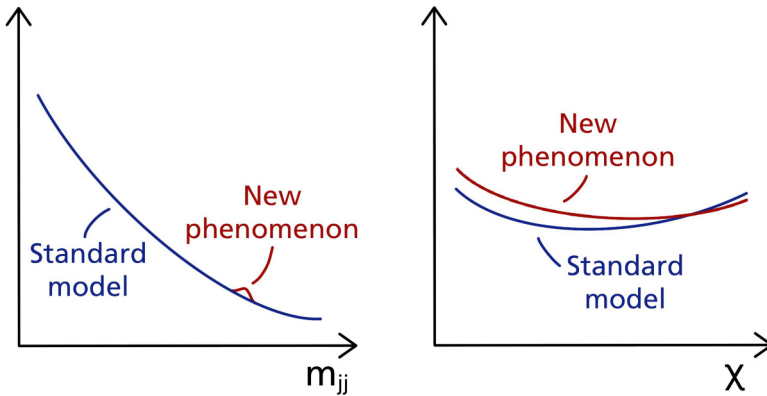


Figure A.4: Difference between the Standard Model and a theory including a new phenomenon in the mass, m_{jj} , and angular, χ , distributions.

Single Particle Jet Energy Scale Uncertainty

As mentioned above, a jet is made up of a lot of particles. These particles do not behave in the same way in the detector. Where some are easy to detector, others are harder. In Chapter 7, the detector's ability, to measure the energy of the different types of particles, is investigated. The end result is an uncertainty on the energy of the jet.

All-hadronic $t\bar{t}$ Resonance Analysis

In Chapter 8, the first major result of the thesis is presented. Here we are looking for a new particle called Z' . It is predicted by a theory called *topcolor assisted technicolor*, that the Z' would, among others, decay to a top and an anti-top quark. We are therefore looking for a dijet system, where both jets are identified as coming from top quarks.

We are then looking at the mass distribution of the dijets, where we would expect a bump at the mass of the Z' , if it exists. But how do we know, that if we see a bump, that it actually is coming from a Z' ? The short answer is, we do not. It is a bit like, if you were hiding under a blanket. I would be able to see the bump, but I could not be sure, that it was you or someone else or just a stack of pillows. However, if I get closer, I can investigate more. I can try to poke you and see, if you will make a sound. I can also measure the size of the bump and see, if it is in agreement with your size. Nevertheless, the first task is to even find the bump, which is also the case, when we are looking for a new particle, and then any further investigations will come later.

Spoiler alert: Unfortunately, no such bump was found and the result is instead a limit plot, which can be understood as a map, where we scratch out the places, we already have looked.

Dijet Analysis

The last chapter, Chapter 9, includes several studies, which all have in common, that they are done on dijets. One study is very similar to the one presented in the previous chapter, but here more narrow jets are used and the jets are not required to be identified as coming from top quarks. Instead no requirement is given, which is called an inclusive search, or the jets are required to be identified as coming from bottom quarks. Again we are looking at the mass distribution, but do unfortunately not see any sign of a new particle.

Another part of the studies in Chapter 9 is focused on the angular distribution of the dijets, which is complementary to the mass search, since it would be able to detect different kinds of new phenomena. However, we do not see any large deviation from what we expect here either and we have to settle for just scratching out more parts of the map by setting limits on specific models.

B

List of Question Boxes

1.1	What are question boxes?	2
2.1	What are the elementary particles?	6
2.2	What is helicity?	9
2.3	What is color charge?	12
2.4	What is confinement?	13
2.5	What is the Lagrangian of the Standard Model?	16
2.6	What is a cross section?	18
2.7	What is a jet?	22
2.8	What is an event?	22
2.9	What is a resonance?	26
2.10	What is an effective field theory?	27
3.1	What is luminosity?	30
3.2	What is pile-up?	33
4.1	Which coordinate system does ATLAS use?	38
4.2	What is missing transverse energy?	39
4.3	What is a vertex?	41

4.4	What is a sampling calorimeter?	43
4.5	What is the radiation length?	44
4.6	What is the absorption length?	45
4.7	What is a compensating calorimeter?	46
4.8	What is the energy resolution of the ATLAS calorimeter?	48
4.9	What is a trigger?	52
4.10	What is a prescaled trigger?	52
5.1	What is infrared and collinear safety?	61
5.2	What is EM and LCW scale?	63
5.3	What is jet substructure?	71
5.4	What is jet tagging?	71
5.5	What is a ROC curve?	80
5.6	What is probability density and likelihood functions?	85
6.1	What is the invariant mass?	88
6.2	What is bump hunting?	88
6.3	What is rapidity?	90
6.4	What are signal and control regions?	92
6.5	What is the ABCD method?	93
6.6	What is SWiFt?	94
6.7	What is a test statistic?	95
6.8	What is a pseudo-experiment?	96
6.9	What is a p -value?	96
6.10	What is the look-elsewhere effect?	97
6.11	What is a nuisance parameter?	98
6.12	When can we claim a discovery?	99

6.13	What is Wilks' test?	102
8.1	What is a blind analysis?	119
9.1	What is the subtraction method?	169



Single Particle Uncertainties

The uncertainties applied to the deposited energy in the calorimeter (Figure 7.3) are describe below.

E/p

The E/p measurements are available for particles with $0.5 < p [\text{GeV}] < 30$ and $|\eta| < 2.3$ (E/p region). For particles in this region:

- An uncertainty binned in p and $|\eta|$ is applied to all energy depositions in the calorimeter system to account for the discrepancy in the energy response in data and Monte Carlo (*In situ E/p*).
- An uncertainty binned in p and $|\eta|$ is applied to all energy depositions in the calorimeter system to account for the discrepancy in the fraction of tracks matched to zero or negative energy clusters in data and Monte Carlo (*E/p Zero Fraction*).
- A flat 0.5% uncertainty is applied to all energy depositions in the calorimeter system to account for possible pile-up effects.
- A flat 2% uncertainty is applied to energy depositions in the tile and electromagnetic end cap calorimeters if the particle has $p < 10$ GeV to account for the potential mis-modelling of threshold effects in topological clustering.
- A flat 3% uncertainty is applied to all energy depositions in the calorimeter system if the particle has $p < 2$ GeV to account for the uncertainty in $\langle E/p \rangle_{COR}$ at the electromagnetic scale introduced by the background subtraction scheme.
- A flat 1% uncertainty is applied to all energy depositions in the calorimeter system if the particle has $p > 2$ GeV to account for the uncertainty in $\langle E/p \rangle_{COR}$ at the electromagnetic scale introduced by the background subtraction scheme.

- A flat 0.15% uncertainty is applied to all energy depositions in the calorimeter system if the particle has $p_T > 5$ GeV to account for the uncertainty in the p measurement introduced by the misalignment of the inner detector [118, 119] (*E/p Misalignment*).
- A parametrized uncertainty is applied to energy depositions in the LAr calorimeter (barrel, presampler and electromagnetic end cap) if the particle has $|\eta| < 0.8$ to account for the potential mismodeling of threshold effects in topological clustering (*E/p Threshold*).
- Another parametrized uncertainty is applied to energy depositions in the LAr calorimeter (barrel, presampler and electromagnetic end cap) if the particle has $|\eta| > 0.8$ to account for the potential mismodeling of threshold effects in topological clustering (*E/p Threshold*).

Combined Test Beam

The combined test beam measurements of the barrel calorimeter response to hadrons [120] are available for particles with $20 < p[\text{GeV}] < 400$ and $|\eta| < 0.8$ (CTB region). If a particle is in the overlap region of the E/p and CTB regions, the CTB uncertainties are applied. So for particles in the CTB region:

- An uncertainty binned in p and $|\eta|$ is applied to all energy depositions in the calorimeter system to account for the discrepancy in the energy response in data and Monte Carlo (*CTB*).
- A flat 0.7% uncertainty is applied to energy depositions in the LAr calorimeter (barrel, presampler and electromagnetic end cap) to account for the uncertainty in the electromagnetic energy scale.
- A flat 0.5% uncertainty is applied to energy depositions in the tile calorimeter to account for the uncertainty in the electromagnetic energy scale.
- A flat 0.4% uncertainty is applied to energy depositions in the LAr calorimeter (barrel, presampler and electromagnetic end cap) to account for the difference in non-uniformity of the energy response in data and Monte Carlo.
- A flat 1.5% uncertainty is applied to energy depositions in the tile calorimeter to account for the difference in non-uniformity of the energy response in data and Monte Carlo.
- A flat 1% uncertainty is applied to all energy depositions in the calorimeter system to account for the difference in the measured test beam energy and the nominal test beam energy due to the inner detector material (*CTB*).

Out Of Range

When a particle is outside both the E/p and CTB region, it is said to be “out of range”. In this case no measurements are available and we have to apply a conservative uncertainty to make sure we account for the effects of saturation, punch-through, and non-linearity at high energy. For particles in this region:

- A flat 10% uncertainty is applied to all energy depositions in the calorimeter system (*Out of Range*).

Electromagnetic scale

The uncertainties on the electromagnetic energy scale have been directly measured. For the LAr calorimeter $Z \rightarrow e^+e^-$ decays were used [154], whereas energy loss of minimum ionising muons were used in the tile calorimeter [155]. The uncertainties in this category are the only ones applied to $e^{+/-}$, γ and π^0 since they lose their energy electromagnetically. They are applied to all other particles as well unless they are in the E/p region since the E/p measurements already covers these uncertainties. For the above mentioned particles:

- A flat 3% uncertainty is applied to energy depositions in the tile calorimeter.
- A flat 1.5% uncertainty is applied to energy depositions in the LAr barrel.
- A flat 5% uncertainty is applied to energy depositions in the LAr presampler.
- A flat 2% uncertainty is applied to energy depositions in the LAr electromagnetic end cap calorimeter.
- A flat 3% uncertainty is applied to energy depositions in the LAr hadronic end cap calorimeter.

Neutral

Additional uncertainties are applied to neutral particles since the calorimeter response varies as function of the physics model. This was shown in GEANT4 studies [122]. So for neutral particles:

- A flat 10% uncertainty is applied to all energy depositions in the calorimeter system if the hadron has $p < 3$ GeV (Neutral).
- A flat 5% uncertainty is applied to all energy depositions in the calorimeter system if the hadron has $p > 3$ GeV (Neutral).
- A flat 20% uncertainty is applied to all energy depositions in the calorimeter system if the particle is a long-lived neutral kaon (K_L).

Samples for All-hadronic $t\bar{t}$ Resonance Analysis

The sample used for the all-hadronic $t\bar{t}$ resonance analysis described in Chapter 8 are summarized below. Table D.1 lists the names of the Monte Carlo (MC) samples and Table D.2 the data period containers.

For the Standard Model $t\bar{t}$ samples, a h_{damp} parameter equal to the top quark mass is used [156] and the top-quark kinematics were corrected to account for electroweak higher-order effects [157]. This correction was applied to the generated events as a function of the flavor and center-of-mass energy of the initial partons, and of the decay angle of the top quarks in the center-of-mass frame of the initial partons.

Table D.1: List of MC samples, where \square = Pythia8EvtGen_A14NNPDF23LO and \diamond = PhPy8EG_A14_ttbar_hdamp258p75.

Process	Name
Z'_{TC2}	mc16_13TeV.301328. \square _zprime1750_tt.deriv.DAOD_EXOT7.e4061_s3126
	mc16_13TeV.301329. \square _zprime2000_tt.deriv.DAOD_EXOT7.e4061_s3126
	mc16_13TeV.301330. \square _zprime2250_tt.deriv.DAOD_EXOT7.e4061_s3126
	mc16_13TeV.301331. \square _zprime2500_tt.deriv.DAOD_EXOT7.e4061_s3126
	mc16_13TeV.301332. \square _zprime2750_tt.deriv.DAOD_EXOT7.e4061_s3126
	mc16_13TeV.301333. \square _zprime3000_tt.deriv.DAOD_EXOT7.e3723_s3126
	mc16_13TeV.301334. \square _zprime4000_tt.deriv.DAOD_EXOT7.e3723_s3126
	mc16_13TeV.301335. \square _zprime5000_tt.deriv.DAOD_EXOT7.e3723_s3126
SM $t\bar{t}$	mc16_13TeV.410471. \diamond _allhad.deriv.DAOD_EXOT7.e6337_e5984_s3126
	mc16_13TeV.410284. \diamond _allhad_mtt_1100_1300.deriv.DAOD_EXOT7.e6603_s3126
	mc16_13TeV.410285. \diamond _allhad_mtt_1300_1500.deriv.DAOD_EXOT7.e6686_s3126
	mc16_13TeV.410286. \diamond _allhad_mtt_1500_1700.deriv.DAOD_EXOT7.e6686_s3126
	mc16_13TeV.410287. \diamond _allhad_mtt_1700_2000.deriv.DAOD_EXOT7.e6686_s3126
	mc16_13TeV.410288. \diamond _allhad_mtt_2000_14000.deriv.DAOD_EXOT7.e6686_s3126
	mc16_13TeV.410470. \diamond _nonallhad.deriv.DAOD_TOPQ1.e6337_s3126
	mc16_13TeV.410633. \diamond _nonallhad_1100_1300.deriv.DAOD_EXOT7.e6602_s3126
	mc16_13TeV.410634. \diamond _nonallhad_1300_1500.deriv.DAOD_EXOT7.e6602_s3126
	mc16_13TeV.410635. \diamond _nonallhad_1500_1700.deriv.DAOD_EXOT7.e6685_s3126
	mc16_13TeV.410636. \diamond _nonallhad_1700_2000.deriv.DAOD_EXOT7.e6685_s3126
	mc16_13TeV.410637. \diamond _nonallhad_2000_14000.deriv.DAOD_EXOT7.e6685_s3126
Multijet	mc16_13TeV.361020. \square _jetjet_JZ0W.deriv.DAOD_EXOT7.e3569_s3126
	mc16_13TeV.361021. \square _jetjet_JZ1W.deriv.DAOD_EXOT7.e3569_s3126
	mc16_13TeV.361022. \square _jetjet_JZ2W.deriv.DAOD_EXOT7.e3668_s3126
	mc16_13TeV.361023. \square _jetjet_JZ3W.deriv.DAOD_EXOT7.e3668_s3126
	mc16_13TeV.361024. \square _jetjet_JZ4W.deriv.DAOD_EXOT7.e3668_s3126
	mc16_13TeV.361025. \square _jetjet_JZ5W.deriv.DAOD_EXOT7.e3668_s3126
	mc16_13TeV.361026. \square _jetjet_JZ6W.deriv.DAOD_EXOT7.e3569_s3126
	mc16_13TeV.361027. \square _jetjet_JZ7W.deriv.DAOD_EXOT7.e3668_s3126
	mc16_13TeV.361028. \square _jetjet_JZ8W.deriv.DAOD_EXOT7.e3569_s3126
	mc16_13TeV.361029. \square _jetjet_JZ9W.deriv.DAOD_EXOT7.e3569_s3126
	mc16_13TeV.361030. \square _jetjet_JZ10W.deriv.DAOD_EXOT7.e3569_s3126
	mc16_13TeV.361031. \square _jetjet_JZ11W.deriv.DAOD_EXOT7.e3569_s3126
	mc16_13TeV.361032. \square _jetjet_JZ12W.deriv.DAOD_EXOT7.e3668_s3126

Table D.2: List of data period containers.

Year	Name
2015	data15_13TeV.periodD.physics_Main.PhysCont.DAOD_EXOT7.grp15_v01_p3841 data15_13TeV.periodE.physics_Main.PhysCont.DAOD_EXOT7.grp15_v01_p3841 data15_13TeV.periodF.physics_Main.PhysCont.DAOD_EXOT7.grp15_v01_p3841 data15_13TeV.periodG.physics_Main.PhysCont.DAOD_EXOT7.grp15_v01_p3841 data15_13TeV.periodH.physics_Main.PhysCont.DAOD_EXOT7.grp15_v01_p3841 data15_13TeV.periodJ.physics_Main.PhysCont.DAOD_EXOT7.grp15_v01_p3841
2016	data16_13TeV.periodA.physics_Main.PhysCont.DAOD_EXOT7.grp16_v01_p3841 data16_13TeV.periodB.physics_Main.PhysCont.DAOD_EXOT7.grp16_v01_p3841 data16_13TeV.periodC.physics_Main.PhysCont.DAOD_EXOT7.grp16_v01_p3841 data16_13TeV.periodD.physics_Main.PhysCont.DAOD_EXOT7.grp16_v01_p3841 data16_13TeV.periodE.physics_Main.PhysCont.DAOD_EXOT7.grp16_v01_p3841 data16_13TeV.periodF.physics_Main.PhysCont.DAOD_EXOT7.grp16_v01_p3841 data16_13TeV.periodG.physics_Main.PhysCont.DAOD_EXOT7.grp16_v01_p3841 data16_13TeV.periodI.physics_Main.PhysCont.DAOD_EXOT7.grp16_v01_p3841 data16_13TeV.periodK.physics_Main.PhysCont.DAOD_EXOT7.grp16_v01_p3841 data16_13TeV.periodL.physics_Main.PhysCont.DAOD_EXOT7.grp16_v01_p3841
2017	data17_13TeV.periodB.physics_Main.PhysCont.DAOD_EXOT7.grp17_v01_p3841 data17_13TeV.periodC.physics_Main.PhysCont.DAOD_EXOT7.grp17_v01_p3841 data17_13TeV.periodD.physics_Main.PhysCont.DAOD_EXOT7.grp17_v01_p3841 data17_13TeV.periodE.physics_Main.PhysCont.DAOD_EXOT7.grp17_v01_p3841 data17_13TeV.periodF.physics_Main.PhysCont.DAOD_EXOT7.grp17_v01_p3841 data17_13TeV.periodH.physics_Main.PhysCont.DAOD_EXOT7.grp17_v01_p3841 data17_13TeV.periodI.physics_Main.PhysCont.DAOD_EXOT7.grp17_v01_p3841 data17_13TeV.periodK.physics_Main.PhysCont.DAOD_EXOT7.grp17_v01_p3841
2018	data18_13TeV.periodB.physics_Main.PhysCont.DAOD_EXOT7.grp18_v01_p3841 data18_13TeV.periodC.physics_Main.PhysCont.DAOD_EXOT7.grp18_v01_p3841 data18_13TeV.periodD.physics_Main.PhysCont.DAOD_EXOT7.grp18_v01_p3841 data18_13TeV.periodF.physics_Main.PhysCont.DAOD_EXOT7.grp18_v01_p3841 data18_13TeV.periodI.physics_Main.PhysCont.DAOD_EXOT7.grp18_v01_p3841 data18_13TeV.periodK.physics_Main.PhysCont.DAOD_EXOT7.grp18_v01_p3841 data18_13TeV.periodL.physics_Main.PhysCont.DAOD_EXOT7.grp18_v01_p3841 data18_13TeV.periodM.physics_Main.PhysCont.DAOD_EXOT7.grp18_v01_p3841 data18_13TeV.periodO.physics_Main.PhysCont.DAOD_EXOT7.grp18_v01_p3841 data18_13TeV.periodQ.physics_Main.PhysCont.DAOD_EXOT7.grp18_v01_p3841

Object Definitions for All-hadronic $t\bar{t}$ Resonance Analysis

The most relevant physics objects in the $t\bar{t}$ all-hadronic analysis is large- R jets for top tagging, variable-radius track jets for b tagging and electrons and muons for vetoing in order to be orthogonal to the $t\bar{t}$ lepton+jets analysis. The object selections are summarized in the tables below.

Table E.1: Large-R jet selections

Jet reconstruction parameters	
Parameter	Value
Jet algorithm	Anti- k_T
R -parameter	1.0
Input constituent	LCTopo
Grooming algorithm	Trimming
f_{cut}	0.05
R_{trim}	0.2
AnalysisTop release number	21.2.87
CalibArea tag	00-04-82
Calibration configuration	JES_MC16recommendation_FatJet_Trimmed_JMS_comb_17Oct2018.config
Calibration sequence (Data)	EtaJES_JMS_Insitu
Calibration sequence (MC)	EtaJES_JMS
Selection requirements	
Observable	Requirement
p_T	> 350 GeV
$ \eta $	< 2.0

Table E.2: Variable-radius track jet selections

Jet reconstruction parameters	
Parameter	Value
Jet algorithm	Anti- k_T
R -parameter	$R_{\text{eff}}(p_T)$ in Equation 5.4
Input constituent	Track
AnalysisTop release number	21.2.87
CalibArea tag	00-04-81
Calibration configuration	JES_data2017_2016_2015_Recommendation_Feb2018_rel21.config
Calibration sequence (Data)	JetArea_Residual_EtaJES_GSC_Insitu
Calibration sequence (MC)	JetArea_Residual_EtaJES_GSC
Selection requirements	
Observable	Requirement
p_T	$> 10 \text{ GeV}$
$ \eta $	< 2.5

Table E.3: Electron selections

Electron selection	
Parameter	Value
Identification	Tight
Isolation	Not applied
Energy calibration	“es2018_R21_v0” (ESModel)
Object quality	Not from a bad calorimeter cluster (BADCLUSELECTRON) Remove clusters from regions with EMEC bad HV (2016 data only)
Impact parameter cuts	$ d_0^{\text{BL}} \text{significance} < 5$ $ \Delta z_0^{\text{BL}} \sin \theta < 0.5 \text{ mm}$
Selection requirements	
Observable	Requirement
p_T	$> 25 \text{ GeV}$
$ \eta $	< 2.47 , excluding $1.37 < \eta < 1.52$

Table E.4: Muon selections

Muon selection	
Parameter	Value
Selection	Medium
Isolation	Tight
Momentum calibration	Sagitta correction used
Impact parameter cuts	$ d_0^{\text{BL}} \text{significance} < 5$ $ \Delta z_0^{\text{BL}} \sin \theta < 0.5 \text{ mm}$
Selection requirements	
Observable	Requirement
p_T	$> 25 \text{ GeV}$
$ \eta $	< 2.5

References

- [1] S. H. Neddermeyer and C. D. Anderson. Note on the nature of cosmic-ray particles. *Phys. Rev.*, 51:884–886, May 1937.
- [2] C. M. G. Lattes, H. Muirhead, G. P. S. Occhialini, and C. F. Powell. Processes Involving Charged Mesons. *Nature*, 159(4047):694–697, May 1947.
- [3] C. M. G. Lattes, G. P. S. Occhialini, and C. F. Powell. Observations on the Tracks of Slow Mesons in Photographic Emulsions. *Nature*, 160(4066):453–456, October 1947.
- [4] E. D. Bloom, D. H. Coward, H. Destaebler, J. Drees, G. Miller, L. W. Mo, R. E. Taylor, M. Breidenbach, J. I. Friedman, G. C. Hartmann, and H. W. Kendall. High-Energy Inelastic e-p Scattering at 6° and 10°. *Phys. Rev. Lett.*, 23(16):930–934, October 1969.
- [5] M. Breidenbach, J. I. Friedman, H. W. Kendall, E. D. Bloom, D. H. Coward, H. Destaebler, J. Drees, L. W. Mo, and R. E. Taylor. Observed Behavior of Highly Inelastic Electron-Proton Scattering. *Phys. Rev. Lett.*, 23(16):935–939, October 1969.
- [6] CDF collaboration. Observation of Top Quark Production in $\bar{p}p$ Collisions with the Collider Detector at Fermilab. *Phys. Rev. Lett.*, 74(14):2626–2631, April 1995.
- [7] DØ collaboration. Observation of the Top Quark. *Phys. Rev. Lett.*, 74(14):2632–2637, April 1995.
- [8] K. Kodama et al. Observation of tau neutrino interactions. *Physics Letters B*, 504(3):218–224, Apr 2001.
- [9] ATLAS Collaboration. Observation of a new particle in the search for the Standard Model Higgs boson with the ATLAS detector at the LHC. *Physics Letters B*, 716(1):1–29, Sep 2012.
- [10] CMS Collaboration. Observation of a new boson at a mass of 125 GeV with the CMS experiment at the LHC. *Physics Letters B*, 716(1):30–61, Sep 2012.

- [11] Dr. Quantum - Double Slit Experiment. <https://www.youtube.com/watch?v=Q1YqgPatzho>.
- [12] D. J. Griffiths. *Introduction to elementary particles; 2nd rev. version*. Physics textbook. Wiley, New York, NY, 2008.
- [13] D. Carlsmith. *Particle physics*. Pearson, Boston, USA, 2013.
- [14] Y. Nagashima. *Elementary particle physics: Foundations of the standard model, volume 2*. Wiley-VCH, Weinheim, 2010.
- [15] M. Tanabashi et al. (Particle Data Group). Review of Particle Physics. *Phys. Rev. D*, 98:030001, Aug 2018 and 2019 update.
- [16] F. Englert and R. Brout. Broken Symmetry and the Mass of Gauge Vector Mesons. *Phys. Rev. Lett.*, 13:321–323, 1964.
- [17] P. W. Higgs. Broken Symmetries and the Masses of Gauge Bosons. *Phys. Rev. Lett.*, 13:508–509, 1964.
- [18] T. Yanagida. Horizontal Symmetry and Masses of Neutrinos. *Progress of Theoretical Physics*, 64(3):1103–1105, 09 1980.
- [19] ATLAS Collaboration. Measurement of dijet azimuthal decorrelations in pp collisions at $\sqrt{s} = 8$ TeV with the ATLAS detector and determination of the strong coupling. *Phys. Rev.*, D98(9):092004, 2018.
- [20] J. Woithe, G. J. Wiener, and F. F. Van der Veken. Let’s have a coffee with the Standard Model of particle physics! *Physics Education*, 52(3):034001, mar 2017.
- [21] V. Bertone, S. Carrazza, and J. Rojo. APFEL: A PDF evolution library with QED corrections. *Computer Physics Communications*, 185(6):1647–1668, Jun 2014.
- [22] S. Carrazza, A. Ferrara, D. Palazzo, and J. Rojo. APFEL Web: a web-based application for the graphical visualization of parton distribution functions, 2014.
- [23] R. D. Ball, V. Bertone, S. Carrazza, C. S. Deans, L. [Del Debbio], S. Forte, A. Guffanti, N. P. Hartland, J. I. Latorre, J. Rojo, and M. Ubiali. Parton distributions with LHC data. *Nuclear Physics B*, 867(2):244 – 289, 2013.
- [24] J. C. Collins, D. E. Soper, and G. Sterman. Factorization of hard processes in QCD. *Advanced Series on Directions in High Energy Physics*, page 1–91, Jul 1989.
- [25] B. Andersson, G. Gustafson, G. Ingelman, and T. Sjöstrand. Parton Fragmentation and String Dynamics. *Phys. Rept.*, 97:31–145, 1983.

- [26] R. D. Field and S. Wolfram. A QCD Model for $e^+ e^-$ Annihilation. *Nucl. Phys. B*, 213:65–84, 1983.
- [27] T. Sjöstrand, S. Mrenna, and P. Z. Skands. A brief introduction to PYTHIA 8.1. *Comput. Phys. Commun.*, 178:852–867, 2008.
- [28] J. Bellm et al. Herwig 7.0/Herwig++ 3.0 release note. *Eur. Phys. J. C*, 76(4):196, 2016.
- [29] E. Bothmann et al. Event generation with Sherpa 2.2. *SciPost Physics*, 7(3), Sep 2019.
- [30] S. Jindariani. Measurements of top quark properties in top pair production and decay at the LHC using the CMS detector. *Nucl. Part. Phys. Proc.*, 273-275:2299–2306, 2016.
- [31] P. Langacker. The physics of heavy Z' gauge bosons. *Rev. Mod. Phys.*, 81:1199–1228, Aug 2009.
- [32] C. T. Hill and S. J. Parke. Top production: Sensitivity to new physics. *Phys. Rev. D*, 49:4454–4462, 1994.
- [33] C. T. Hill. Topcolor assisted technicolor. *Physics Letters B*, 345(4):483 – 489, 1995.
- [34] R. M. Harris and S. Jain. Cross Sections for Leptophobic Topcolor Z' Decaying to Top-Antitop. *Eur. Phys. J. C*, 72:2072, 2012.
- [35] M. Fairbairn, J. Heal, F. Kahlhoefer, and P. Tunney. Constraints on Z' models from LHC dijet searches and implications for dark matter. *JHEP*, 09:018, 2016.
- [36] D. Abercrombie et al. Dark Matter benchmark models for early LHC Run-2 Searches: Report of the ATLAS/CMS Dark Matter Forum. *Physics of the Dark Universe*, 27:100371, 2020.
- [37] Jalal A. et al. Simplified models for dark matter searches at the LHC. *Physics of the Dark Universe*, 9-10:8 – 23, 2015.
- [38] E. Eichten, I. Hinchliffe, K. Lane, and C. Quigg. Supercollider physics. *Rev. Mod. Phys.*, 56:579–707, Oct 1984.
- [39] P. Chiappetta and M. Perrottet. Possible bounds on compositeness from inclusive one jet production in large hadron colliders. *Physics Letters B*, 253(3):489 – 493, 1991.
- [40] U. Baur, I. Hinchliffe, and D. Zeppenfeld. Excited Quark Production at Hadron Colliders. *Int. J. Mod. Phys. A*, 2:1285, 1987.

- [41] U. Baur, M. Spira, and P. M. Zerwas. Excited Quark and Lepton Production at Hadron Colliders. *Phys. Rev. D*, 42:815–824, 1990.
- [42] O. S. Brüning, P. Collier, P. Lebrun, S. Myers, R. Ostojic, J. Poole, and P. Proudlock. *LHC Design Report*. CERN Yellow Reports: Monographs. CERN, Geneva, 2004.
- [43] L. Evans and P. Bryant. LHC machine. *Journal of Instrumentation*, 3(08):S08001–S08001, aug 2008.
- [44] G. Bachy, A. Hofmann, S. Myers, E. Picasso, and G. Plass. The LEP collider: construction, project status and outlook. *Part. Accel.*, 26:19–32, 1990.
- [45] ATLAS Collaboration. The ATLAS Experiment at the CERN Large Hadron Collider. *JINST*, 3:S08003, 2008.
- [46] CMS Collaboration. The CMS Experiment at the CERN LHC. *JINST*, 3:S08004, 2008.
- [47] LHCb Collaboration. The LHCb Detector at the LHC. *JINST*, 3:S08005, 2008.
- [48] ALICE Collaboration. The ALICE experiment at the CERN LHC. *JINST*, 3:S08002, 2008.
- [49] J. Wenninger. LHC status and performance. *PoS*, CHARGED2018:001. 9 p, 2018.
- [50] E. Mobs. The CERN accelerator complex - 2019. Complexe des accélérateurs du CERN - 2019. Technical report, CERN, Jul 2019. General Photo.
- [51] B. J. Holzer. Introduction to Transverse Beam Dynamics. Technical Report arXiv:1404.0923, CERN, Apr 2014.
- [52] ATLAS Collaboration. ATLAS data quality operations and performance for 2015–2018 data-taking. *Journal of Instrumentation*, 15(04):P04003–P04003, Apr 2020.
- [53] M. S. Camillocci. LHC nominal cycle. In *6th Evian Workshop on LHC beam operation*, pages 45–48, Geneva, 2016. CERN.
- [54] J. Pequeno. Computer generated image of the whole ATLAS detector. Mar 2008.
- [55] J. Pequeno and P. Schaffner. How ATLAS detects particles: diagram of particle paths in the detector. Jan 2013.
- [56] ATLAS Collaboration. ATLAS Phase-II Upgrade Scoping Document. Technical Report CERN-LHCC-2015-020. LHCC-G-166, CERN, Geneva, Sep 2015.

- [57] M. Capeans, G. Darbo, K. Einsweiler, M. Elsing, T. Flick, M. Garcia-Sciveres, C. Gemme, H. Pernegger, O. Rohne, and R. Vuillermet. ATLAS Insertable B-Layer Technical Design Report. Technical Report CERN-LHCC-2010-013. ATLAS-TDR-19, Sep 2010.
- [58] K. Potamianos. The upgraded Pixel detector and the commissioning of the Inner Detector tracking of the ATLAS experiment for Run-2 at the Large Hadron Collider. Technical Report ATL-PHYS-PROC-2016-104, CERN, Geneva, Aug 2016. 15 pages, EPS-HEP 2015 Proceedings.
- [59] R. L. Gluckstern. Uncertainties in track momentum and direction, due to multiple scattering and measurement errors. *Nuclear Instruments and Methods*, 24:381 – 389, 1963.
- [60] H. Kolanoski and N. Wermes. *Particle Detectors: Fundamentals and Applications*. Oxford University Press, 2020.
- [61] J. Pequena. Computer Generated image of the ATLAS calorimeter. Mar 2008.
- [62] U. H. Stolzenberg. *Radiation length measurements with high-resolution telescopes*. PhD thesis, Gottingen U., 2019.
- [63] H. Abreu, M. Aharrouche, M. Aleksa, L. Bella, J. P. Archambault, S. Arfaoui, O. Arnaez, E. Auge, M. Aourousseau, S. Bahinipati, J. Bán, D. Banfi, A. Barajas, T. Barilari, A. Bazan, F. Bellachia, O. Beloborodova, D. Benchekroun, K. Benslama, and L. Zivkovic. Performance of the electronic readout of the ATLAS liquid argon calorimeters. *Journal of Instrumentation*, 5, 09 2010.
- [64] A. Hrynevich. Performance of the ATLAS Tile Calorimeter. *Journal of Instrumentation*, 12(06):C06021–C06021, jun 2017.
- [65] G. Avoni et al. The new LUCID-2 detector for luminosity measurement and monitoring in ATLAS. *JINST*, 13(07):P07017, 2018.
- [66] ATLAS Collaboration. Measurement of beam background in special high- β^* LHC runs at $\sqrt{s} = 900$ GeV using the ATLAS–ALFA detectors. Technical Report ATL-FWD-PUB-2020-001, CERN, Geneva, May 2020.
- [67] ATLAS Collaboration. Total Integrated Luminosity and Data Quality in 2015-2018. <https://twiki.cern.ch/twiki/bin/view/AtlasPublic/LuminosityPublicResultsRun2>.
- [68] ATLAS Collaboration. Performance of the ATLAS trigger system in 2015. *The European Physical Journal C*, 77(5), May 2017.

- [69] ATLAS Collaboration. Comparison of jet trigger in 2015 and 2016. Technical Report ATL-COM-DAQ-2016-087, CERN, Geneva, Jul 2016.
- [70] S. Agostinelli et al. GEANT4: A Simulation toolkit. *Nucl. Instrum. Meth. A*, 506:250–303, 2003.
- [71] ATLAS Collaboration. *ATLAS Computing: technical design report*. Technical Design Report ATLAS. CERN, Geneva, 2005.
- [72] ATLAS Collaboration. Topological cell clustering in the ATLAS calorimeters and its performance in LHC Run 1. *Eur. Phys. J. C*, 77:490, 2017.
- [73] ATLAS Collaboration. Jet energy scale and resolution measured in proton-proton collisions at $\sqrt{s} = 13$ TeV with the ATLAS detector, 2020.
- [74] ATLAS Collaboration. Performance of the ATLAS track reconstruction algorithms in dense environments in LHC Run 2. *The European Physical Journal C*, 77(10):673, 2017.
- [75] R. Frühwirth. Application of Kalman filtering to track and vertex fitting. *Nuclear Instruments and Methods in Physics Research Section A: Accelerators, Spectrometers, Detectors and Associated Equipment*, 262(2):444 – 450, 1987.
- [76] T. Cornelissen, M. Elsing, I. Gavrilenko, W. Liebig, E. Moyses, and A. Salzburger. The new ATLAS track reconstruction (NEWT). *Journal of Physics: Conference Series*, 119(3):032014, jul 2008.
- [77] ATLAS Collaboration. Jet reconstruction and performance using particle flow with the ATLAS Detector. *The European Physical Journal C*, 77(7):466, 2017.
- [78] ATLAS Collaboration. Improving jet substructure performance in ATLAS using Track-CaloClusters. Technical Report ATL-PHYS-PUB-2017-015, CERN, Geneva, Jul 2017.
- [79] G. P. Salam. Towards jetography. *The European Physical Journal C*, 67(3-4):637–686, May 2010.
- [80] S. D. Ellis and D. E. Soper. Successive combination jet algorithm for hadron collisions. *Phys. Rev. D*, 48:3160–3166, 1993.
- [81] S. Catani, Y. L. Dokshitzer, M.H. Seymour, and B.R. Webber. Longitudinally-invariant k_t -clustering algorithms for hadron-hadron collisions. *Nuclear Physics B*, 406(1):187 – 224, 1993.
- [82] M. Cacciari, G. P. Salam, and G. Soyez. The anti- k_t jet clustering algorithm. *Journal of High Energy Physics*, 2008(04):063–063, apr 2008.

- [83] Y. L. Dokshitzer, G.D. Leder, S. Moretti, and B.R. Webber. Better jet clustering algorithms. *JHEP*, 08:001, 1997.
- [84] M. Wobisch and T. Wengler. Hadronization corrections to jet cross-sections in deep inelastic scattering. In *Monte Carlo generators for HERA physics. Proceedings, Workshop, Hamburg, Germany, 1998-1999*, pages 270–279, 4 1998.
- [85] M. Cacciari, G. P. Salam, and G. Soyez. Fastjet user manual. *The European Physical Journal C*, 72(3), Mar 2012.
- [86] D. Krohn, J. Thaler, and L.-T. Wang. Jets with variable R . *Journal of High Energy Physics*, 2009(06):059–059, Jun 2009.
- [87] ATLAS Collaboration. Variable Radius, Exclusive- k_T , and Center-of-Mass Subject Reconstruction for Higgs($\rightarrow b\bar{b}$) Tagging in ATLAS. Technical Report ATL-PHYS-PUB-2017-010, CERN, Geneva, Jun 2017.
- [88] ATLAS Collaboration. In situ calibration of large- R jet energy and mass in 13 TeV proton-proton collisions with the ATLAS detector. *Eur. Phys. J. C*, 79(arXiv:1807.09477. 2):135. 70 p, Jul 2018. Submitted to Eur.Phys.J.
- [89] ATLAS Collaboration. In situ large- R jet energy scale calibration and uncertainties in 2015-2017 data. <https://atlas.web.cern.ch/Atlas/GROUPS/PHYSICS/PLOTS/JETM-2019-05/>.
- [90] S. Marzani, G. Soyez, and M. Spannowsky. Looking Inside Jets: an introduction to jet substructure and boosted-object phenomenology. *Lecture Notes in Physics*, 2019.
- [91] ATLAS Collaboration. Performance of top-quark and W -boson tagging with ATLAS in Run 2 of the LHC. *The European Physical Journal C*, 79, 05 2019.
- [92] ATLAS Collaboration. Jet mass reconstruction with the ATLAS Detector in early Run 2 data. Technical Report ATLAS-CONF-2016-035, CERN, Geneva, Jul 2016.
- [93] Roman Kogler et al. Jet Substructure at the Large Hadron Collider. Jet Substructure at the Large Hadron Collider : Experimental Review. *Rev. Mod. Phys.*, 91(arXiv:1803.06991):045003. 44 p, Mar 2018. 52 figures.
- [94] A. J. Larkoski, G. P. Salam, and J. Thaler. Energy correlation functions for jet substructure. *Journal of High Energy Physics*, 2013(6), Jun 2013.
- [95] A. J. Larkoski, I. Moulton, and D. Neill. Power counting to better jet observables. *Journal of High Energy Physics*, 2014(12), Dec 2014.
- [96] J. Thaler and K. Van Tilburg. Identifying boosted objects with n -subjettiness. *Journal of High Energy Physics*, 2011(3), Mar 2011.

- [97] J. Thaler and K. Van Tilburg. Maximizing boosted top identification by minimizing n-subjettiness. *Journal of High Energy Physics*, 2012(2), Feb 2012.
- [98] ATLAS Collaboration. Measurement of k_T splitting scales in $w \rightarrow l\nu$ events at $\sqrt{s} = 7$ TeV with the atlas detector. *The European Physical Journal C*, 73(5), May 2013.
- [99] J. Thaler and L.-T. Wang. Strategies to identify boosted tops. *Journal of High Energy Physics*, 2008(07):092–092, Jul 2008.
- [100] ATLAS Collaboration. Performance of jet substructure techniques for large-R jets in proton-proton collisions at $\sqrt{s} = 7$ TeV using the ATLAS detector. *Journal of High Energy Physics*, 2013(9), Sep 2013.
- [101] D. E. Soper and M. Spannowsky. Finding top quarks with shower deconstruction. *Physical Review D*, 87(5), Mar 2013.
- [102] T. Plehn, G. P. Salam, and M. Spannowsky. Fat jets for a light higgs boson. *Physical Review Letters*, 104(11), Mar 2010.
- [103] T. Plehn, M. Spannowsky, M. Takeuchi, and D. Zerwas. Stop reconstruction with tagged tops. *Journal of High Energy Physics*, 2010(10), Oct 2010.
- [104] J. Pearkes, W. Fedorko, A. Lister, and C. Gay. Jet constituents for deep neural network based top quark tagging, 2017.
- [105] ATLAS Collaboration. ATLAS b -jet identification performance and efficiency measurement with $t\bar{t}$ events in pp collisions at $\sqrt{s} = 13$ TeV. *The European Physical Journal C*, 79(11), Nov 2019.
- [106] ATLAS Collaboration. Optimisation and performance studies of the ATLAS b -tagging algorithms for the 2017-18 LHC run. Technical Report ATL-PHYS-PUB-2017-013, CERN, Geneva, Jul 2017.
- [107] ATLAS Collaboration. Secondary vertex finding for jet flavour identification with the ATLAS detector. Technical Report ATL-PHYS-PUB-2017-011, CERN, Geneva, Jun 2017.
- [108] ATLAS Collaboration. Topological b -hadron decay reconstruction and identification of b -jets with the JetFitter package in the ATLAS experiment at the LHC. Technical Report ATL-PHYS-PUB-2018-025, CERN, Geneva, Oct 2018.
- [109] ATLAS Collaboration. Measurements and interpretations of Higgs-boson fiducial cross sections in the diphoton decay channel using 139 fb1 of pp collision data at $\sqrt{s} = 13$ TeV with the ATLAS detector. Technical Report ATLAS-CONF-2019-029, CERN, Geneva, Jul 2019.

- [110] ATLAS Collaboration. Search for low-mass resonances decaying into two jets and produced in association with a photon using pp collisions at $\sqrt{s} = 13$ TeV with the ATLAS detector. *Physics Letters B*, 795:56 – 75, 2019.
- [111] ATLAS Collaboration. Search for new phenomena in dijet events using 37 fb^{-1} of pp collision data collected at $\sqrt{s} = 13$ tev with the atlas detector. *Physical Review D*, 96(5), Sep 2017.
- [112] G. Choudalakis. On hypothesis testing, trials factor, hypertests and the BumpHunter, 2011.
- [113] G. Ranucci. The profile likelihood ratio and the look elsewhere effect in high energy physics. *Nuclear Instruments and Methods in Physics Research Section A: Accelerators, Spectrometers, Detectors and Associated Equipment*, 661(1):77–85, Jan 2012.
- [114] A. L. Read. Presentation of search results: The CL_s technique. *J. Phys. G*, 28:2693–2704, 2002.
- [115] G. Cowan, K. Cranmer, E. Gross, and O. Vitells. Asymptotic formulae for likelihood-based tests of new physics. *The European Physical Journal C*, 71(2), Feb 2011.
- [116] ATLAS Collaboration. A measurement of the calorimeter response to single hadrons and determination of the jet energy scale uncertainty using LHC Run-1 pp-collision data with the ATLAS detector. *The European Physical Journal C*, 77, 01 2017.
- [117] ATLAS Collaboration. ATLAS Pythia 8 tunes to 7 TeV datas. Technical Report ATL-PHYS-PUB-2014-021, CERN, Geneva, Nov 2014.
- [118] ATLAS Collaboration. Alignment of the ATLAS Inner Detector and its Performance in 2012, 2014.
- [119] ATLAS Collaboration. Studies of radial distortions of the ATLAS Inner Detector. Technical Report ATL-PHYS-PUB-2018-003, CERN, Geneva, Mar 2018.
- [120] ATLAS Collaboration. Study of energy response and resolution of the ATLAS barrel calorimeter to hadrons of energies from 20-GeV to 350-GeV. *Nucl. Instrum. Meth.*, A621:134–150, 2010.
- [121] ATLAS Collaboration. Measurement of pion and proton response and longitudinal shower profiles up to 20 nuclear interaction lengths with the ATLAS Tile calorimeter. *Nuclear Instruments and Methods in Physics Research Section A: Accelerators, Spectrometers, Detectors and Associated Equipment*, 615(2):158 – 181, 2010.

- [122] ATLAS Collaboration. Single hadron response measurement and calorimeter jet energy scale uncertainty with the ATLAS detector at the LHC. *Eur. Phys. J.*, C73(3):2305, 2013.
- [123] ATLAS Collaboration. Search for heavy particles decaying into a top-quark pair in the fully hadronic final state in pp collisions at $\sqrt{s} = 13$ TeV with the atlas detector. *Phys. Rev. D*, 99:092004, May 2019.
- [124] ATLAS Collaboration. Search for heavy particles decaying into top-quark pairs using lepton-plus-jets events in proton–proton collisions at $\sqrt{s} = 13$ TeV with the atlas detector. *The European Physical Journal C*, 78(7), Jul 2018.
- [125] CMS Collaboration. Search for resonant $t\bar{t}$ production in proton-proton collisions at $\sqrt{s} = 13$ TeV. *Journal of High Energy Physics*, 2019(4):31, 2019.
- [126] ATLAS Collaboration. Search for $t\bar{t}$ resonances in fully hadronic final states in pp collisions at $\sqrt{s} = 13$ TeV with the ATLAS detector (Auxiliary). <https://atlas.web.cern.ch/Atlas/GROUPS/PHYSICS/PAPERS/EXOT-2018-48/>.
- [127] R. Bonciani, T. Ježo, M. Klasen, F. Lyonnet, and I. Schienbein. Electroweak top-quark pair production at the LHC with Z' bosons to NLO QCD in POWHEG. *Journal of High Energy Physics*, 2016(2), Feb 2016.
- [128] S. Alioli, P. Nason, C. Oleari, and E. Re. A general framework for implementing NLO calculations in shower Monte Carlo programs: the POWHEG BOX. *Journal of High Energy Physics*, 2010(6), Jun 2010.
- [129] R. D. Ball et al. Parton distributions for the LHC Run II. *Journal of High Energy Physics*, 2015(4), Apr 2015.
- [130] M. Czakon and A. Mitov. Top++: A program for the calculation of the top-pair cross-section at hadron colliders. *Computer Physics Communications*, 185(11):2930–2938, Nov 2014.
- [131] ATLAS Collaboration. Search for $t\bar{t}$ resonances in fully hadronic final states in pp collisions at $\sqrt{s} = 13$ TeV with the ATLAS detector, 2020.
- [132] M. J. Oreglia. *A Study of the Reactions $\psi' \rightarrow \gamma\gamma\psi$* . PhD thesis, Stanford University, 1980.
- [133] T. Skwarnicki. *A study of the radiative CASCADE transitions between the Upsilon-Prime and Upsilon resonances*. PhD thesis, Cracow, INP, 1986.
- [134] ATLAS Collaboration. Luminosity determination in pp collisions at $\sqrt{s} = 13$ TeV using the ATLAS detector at the LHC. Technical Report ATLAS-CONF-2019-021, CERN, Geneva, Jun 2019.

- [135] ATLAS Collaboration. Measurements of b-jet tagging efficiency with the ATLAS detector using $t\bar{t}$ events at $\sqrt{s} = 13$ TeV. *Journal of High Energy Physics*, 2018(8):89, 2018.
- [136] ATLAS Collaboration. Dark matter summary plots : update July 2020. Technical Report ATL-PHYS-PUB-2020-021, CERN, Geneva, Jul 2020.
- [137] ATLAS Collaboration. Search for new resonances in mass distributions of jet pairs using 139 fb^{-1} of pp collisions at $\sqrt{s} = 13$ TeV with the ATLAS detector. *Journal of High Energy Physics*, 2020(3), Mar 2020.
- [138] CMS Collaboration. Search for new physics in dijet angular distributions using proton–proton collisions at $\sqrt{s} = 13$ tev and constraints on dark matter and other models. *The European Physical Journal C*, 78(9), Sep 2018.
- [139] Z. Nagy. Three jet cross-sections in hadron hadron collisions at next-to-leading order. *Phys. Rev. Lett.*, 88:122003, 2002.
- [140] Z. Nagy. Next-to-leading order calculation of three-jet observables in hadron-hadron collisions. *Physical Review D*, 68(9), Nov 2003.
- [141] S. Catani and M. H. Seymour. A general algorithm for calculating jet cross sections in NLO QCD. *Nuclear Physics B*, 485(1-2):291–419, Feb 1997.
- [142] L. Bryngemark. *Search for new phenomena in dijet angular distributions at $\sqrt{s} = 8$ and 13 TeV*. PhD thesis, Feb 2016. Presented 18 Mar 2016.
- [143] J. Gao. Cijet: A program for computation of jet cross sections induced by quark contact interactions at hadron colliders. *Computer Physics Communications*, 184(10):2362–2366, Oct 2013.
- [144] H.-L. Lai, M. Guzzi, J. Huston, Z. Li, P. M. Nadolsky, J. Pumplin, and C.-P. Yuan. New parton distributions for collider physics. *Phys. Rev. D*, 82:074024, Oct 2010.
- [145] A. D. Martin, W. J. Stirling, R. S. Thorne, and G. Watt. Parton distributions for the LHC. *The European Physical Journal C*, 63(2):189–285, Jul 2009.
- [146] ATLAS Collaboration. A method for the construction of strongly reduced representations of ATLAS experimental uncertainties and the application thereof to the jet energy scale. Technical Report ATL-PHYS-PUB-2015-014, CERN, Geneva, Jul 2015.
- [147] ATLAS Collaboration. Search for new phenomena in dijet events using 37 fb^{-1} of pp collision data collected at $\sqrt{s} = 13$ TeV with the ATLAS detector (Auxiliary). <https://atlas.web.cern.ch/Atlas/GROUPS/PHYSICS/PAPERS/EXOT-2016-21/>.

- [148] ATLAS Collaboration. Search for resonances in the mass distribution of jet pairs with one or two jets identified as b -jets in proton-proton collisions at $\sqrt{s} = 13$ TeV with the ATLAS detector. *Physical Review D*, 98(3), Aug 2018.
- [149] CMS Collaboration. Search for high mass dijet resonances with a new background prediction method in proton-proton collisions at $\sqrt{s} = 13$ TeV. *Journal of High Energy Physics*, 2020(5), May 2020.
- [150] CMS Collaboration. Search for Narrow Resonances in the b -tagged Dijet Mass Spectrum in Proton-Proton Collisions at $\sqrt{s} = 8$ TeV. *Physical Review Letters*, 120(20), May 2018.
- [151] ATLAS Collaboration. Search for new resonances in mass distributions of jet pairs using 139 fb^{-1} of pp collisions at $\sqrt{s} = 13$ TeV with the ATLAS detector (Auxiliary). <https://atlas.web.cern.ch/Atlas/GROUPS/PHYSICS/PAPERS/EXOT-2019-03/>.
- [152] ATLAS Collaboration. Identification of Jets Containing b -Hadrons with Recurrent Neural Networks at the ATLAS Experiment. Technical Report ATL-PHYS-PUB-2017-003, CERN, Geneva, Mar 2017.
- [153] K. Cranmer, G. Lewis, L. Moneta, A. Shibata, and W. Verkerke. HistFactory: A tool for creating statistical models for use with RooFit and RooStats. Technical Report CERN-OPEN-2012-016, New York U., New York, Jan 2012.
- [154] ATLAS Collaboration. Electron performance measurements with the ATLAS detector using the 2010 LHC proton-proton collision data. *Eur. Phys. J.*, C72:1909, 2012.
- [155] ATLAS Collaboration. Readiness of the ATLAS Tile Calorimeter for LHC collisions. *Eur. Phys. J.*, C70:1193–1236, 2010.
- [156] ATLAS Collaboration. Studies on top-quark Monte Carlo modelling for Top2016. Technical Report ATL-PHYS-PUB-2016-020, CERN, Geneva, Sep 2016.
- [157] J. H. Kühn, A. Scharf, and P. Uwer. Weak interactions in top-quark pair production at hadron colliders: An update. *Physical Review D*, 91(1), Jan 2015.